THE UNIVERSITY OF
WARWICK

University of Warwick institutional repository: http://go.warwick.ac.uk/wrap

A Thesis Submitted for the Degree of PhD at the University of Warwick

http://go.warwick.ac.uk/wrap/55927

This thesis is made available online and is protected by original copyright.

Please scroll down to view the document itself.

Please refer to the repository record for this item for information to help you to cite it. Our policy information is available from the repository home page.

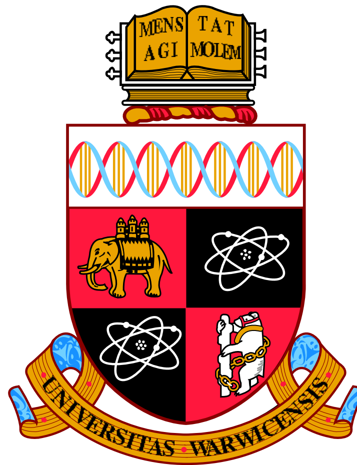

Growth and Characterisation of MnSb Thin Films and Interfaces

by

Christopher William Burrows

Thesis

Submitted to the University of Warwick

for the degree of

Doctor of Philosophy

Department of Physics

August 2012

THE UNIVERSITY OF
WARWICK

Contents

List of Figures v

List of Tables ix

Acknowledgements xi

Declarations xiii

Abstract xvi

Abbreviations xvii

Chapter 1 Introduction 1

1.1 Motivation 1

1.1.1 Spintronics 2

1.2 Organisation of the thesis 6

1.3 Properties of MnSb 7

1.4 Surface notation and reconstructions 10

1.4.1 Wood Notation 12

1.4.2 Electron counting rules 15

Chapter 2 Experimental techniques 19

2.1 Molecular beam epitaxy 19

2.2 Electron diffraction techniques 30
2.2.1 Reflection high-energy electron diffraction 30
2.2.2 Low-energy electron diffraction 37
2.3 Microscopy techniques 38
2.3.1 Scanning tunnelling microscopy 38
2.3.2 Atomic force microscopy 39
2.3.3 Transmission electron microscopy 43
2.4 X-ray techniques 44
2.4.1 X-ray photoelectron spectroscopy 44
2.4.2 X-ray diffraction 47
2.4.3 Interpretation of X-ray diffraction data 50
2.5 Bulk magnetometry 58

Chapter 3 Manganese on III-V semiconductor surfaces 59

3.1 Introduction 59
3.2 Experimental Details 60
3.3 Results 62
3.3.1 InSb 62
3.3.2 GaAs 68
3.4 Discussion 73
3.4.1 Thermodynamics 73
3.4.2 Surface reconstructions 79
3.5 Conclusions 86

Chapter 4 Characterisation of MnSb thin films 88

4.1 Introduction 88
4.2 Growth of MnSb(0001) thin-films on GaAs substrates 91
4.3 Structural overview of MnSb polymorphs 95
4.3.1 J dependence of the polymorphs 98

4.4 Structural characterisation of MnSb polymorphs 100
4.4.1 Niccolite MnSb 101
4.4.2 Cubic MnSb 113
4.4.3 Wurtzite MnSb 117
4.4.4 Summary 118
4.5 Reciprocal space map analysis 119
4.5.1 Polymorph identification 119
4.5.2 Quantitative polymorph identification 126
4.6 Conclusions 130

Chapter 5 Heteroepitaxial growth of MnSb on Ge **132**
5.1 Introduction 132
5.2 Surface preparation of Ge substrates 133
5.2.1 Electron diffraction 134
5.2.2 X-ray photoelectron spectroscopy 138
5.3 Growth of MnSb layers on Ge(001) substrates 141
5.4 Characterisation of MnSb/Ge(001) samples 146
5.4.1 Transmission electron microscopy 146
5.4.2 X-ray photoelectron spectroscopy 147
5.4.3 X-ray diffraction 150
5.4.4 Atomic force microscopy 153
5.4.5 Magnetometry 155
5.5 Growth of MnSb layers on Ge(111) substrates 157
5.6 Characterisation of MnSb/Ge(111) samples 159
5.6.1 X-ray photoelectron spectroscopy 159
5.6.2 X-ray diffraction 162
5.6.3 Atomic force microscopy 164
5.6.4 Magnetometry 166
5.7 Conclusions 167

Chapter 6 Conclusions and future work **169**

6.1 Conclusions 169

6.2 Future work 172

Appendix A Predicted X-ray diffraction reflection positions **175**

Appendix B Heteroepitaxial growth of MnSb on InSb and NaCl **179**

References **183**

List of Figures

1.1 Illustrative band structures of a ferromagnet and a half-metal. 5
1.2 MnSb unit cell and surface directions. 8
1.3 Unit cells and stacking order schematics for the three MnSb polymorphs. 9
1.4 Schematics of the zincblende unit cell, (001) and (111)A surfaces. . . . 14
1.5 Schematic of the GaAs(001)-$\beta2(2\times4)$ surface reconstruction. 16

2.1 Schematic of the Warwick MBE growth chamber. 20
2.2 Representation of the atomistic surface processes during growth. 22
2.3 Schematic of the three idealised growth modes. 23
2.4 Illustration of the Warwick MBE chamber indicating cell height offsets. 26
2.5 Behaviour of the Sb cell beam equivalent pressure with time. 28
2.6 Ewald sphere construction in 3D and 2D. 31
2.7 Example RHEED pattern and illustration of a MnSb(0001) (2×2) surface. 32
2.8 Geometric construction used for RHEED lattice parameter determination. 33
2.9 Schematic of surface crystallinity and the resulting RHEED patterns. . . 36
2.10 Schematic of the optical detection of AFM cantilever movement. 39
2.11 Example AFM of a NiSb(0001) surface. 41
2.12 Geometric construction of the scattering vector $\mathbf{Q}$. 49
2.13 Example XRD data for a NiSb(0001) thin film. 51
2.14 Illustrative diagram of mosaic and correlation length dominated structures. 56

3.1 InSb(001) RHEED showing Mn-induced reconstruction changes. 64
3.2 InSb(111)A RHEED showing Mn-induced reconstruction changes. . . . 64
3.3 InSb(111)B RHEED showing Mn-induced reconstruction changes. . . . 65
3.4 θ_{Mn} required to change InSb surface reconstructions as function of Δ_{Sb}. 66
3.5 Surface morphology of InSb(001) surfaces before and after Mn deposition. 67
3.6 GaAs(001) RHEED showing Mn-induced reconstruction changes. 70
3.7 AFM of GaAs(001) surface following Mn deposition. 71
3.8 STM of GaAs(001)-β2(2×4) surface at 0, 0.8, 1.2, 1.8 and 2.4 ML of Mn. 72
3.9 STM of GaAs(001)-c(4×4) surface at 0, 0.8, 1.2, and 1.8 ML of Mn. . 73
3.10 Illustrative diagram of surface reactivity in the Mn-InSb system. 76
3.11 GECR compliant models for Mn substitution into GaAs(001)-c(4×4). . 81
3.12 GECR compliant models for Mn substitution into GaAs(001)-β2(2×4). 86

4.1 HRTEM images showing polymorph crystallites in n-MnSb framework. . 89
4.2 RHEED patterns for GaAs(111)B, MnSb(0001) and Sb(0001). 91
4.3 Magnetometry measurements of MnSb thin films on GaAs(111)B. . . . 93
4.4 Sb 4d region XPS data for MnSb films grown on GaAs(111). 94
4.5 Symmetric XRD data from a MnSb film grown on GaAs(111). 96
4.6 TEM image showing the presence of GaSb features at the interface. . . 97
4.7 Schematic showing the relative polymorph content of MnSb thin films. . 99
4.8 n-MnSb c lattice parameter variation with grain size. 102
4.9 n-MnSb c lattice parameter variation with J_{corr} and BEP_{Mn}. 102
4.10 Behaviour of relative polymorph content with n-MnSb c lattice parameter. 104
4.11 Strain dispersion variation with sample thickness for n-MnSb crystallites. 104
4.12 Uniaxial strain dispersion behaviour for n-MnSb with J_{corr} and BEP_{Mn}. . 105
4.13 XRD diffraction data showing thickness evolution of MnSb films from 2 to 30 nm thick films. 107
4.14 n-MnSb(0002) rocking curves for film thicknesses between 2 and 190 nm. 109
4.15 Schematic of island relaxation in n-MnSb thin films. 112

4.16 Typical XRD data of a capped and uncapped Sample Around the GaAs(111) reflection. 113
4.17 c-MnSb a lattice parameter variation with crystallite size and J_{corr}. . . . 114
4.18 Strain dispersion behaviour with crystallite size and J_{corr} for c-MnSb. . . 115
4.19 Variation in rocking curve FWHM for c-MnSb crystallites. 116
4.20 Strain dispersion behaviour of w-MnSb with crystallite size and J_{corr}. . . 118
4.21 Asymmetric RSM about the GaAs(422) reflection for Sample A. 120
4.22 Out-of-plane and in-plane diffraction data for Sample A. 123
4.23 Asymmetric RSMs around GaAs(422) reflection for Samples B, C and D. 127
4.24 n-MnSb:c-MnSb ratio variation with n-MnSb c lattice parameter and J_{corr}.128

5.1 LEED and RHEED from the clean Ge(001)-(2×1) surface. 135
5.2 Models for the higher-order reconstructions present on Ge(001). 136
5.3 Schematic of the intersection of the Ewald sphere with two intensity sheets.138
5.4 RHEED of the clean Ge(111)-c(2×8) structure. 139
5.5 XPS spectra for clean Ge(001) and Ge(111) substrates. 140
5.6 RHEED transmission patterns from MnSb on Ge(001). 143
5.7 Schematic showing transmission through MnSb(11$\bar{2}$0) crystallite. 145
5.8 TEM of MnSb/Ge(001) interface revealing the irregular layer structure and presence of multiple crystallites. 146
5.9 Shallow core, Ge 2p and Sb 4d region XPS spectra for MnSb on Ge(001).148
5.10 Symmetric XRD data for a MnSb layer on Ge(001). 151
5.11 AFM images of MnSb/Ge(001) with layer thicknesses of 5.5, 27 and 70 nm.154
5.12 SQUID magnetometry of a MnSb/Ge(001) film showing M-T and M-H. 156
5.13 RHEED images of MnSb(0001) on Ge(111) after growth was stopped and following Mn deposition. 158
5.14 Shallow core, Ge 2p and Sb 4d region XPS spectra for MnSb on Ge(001).160
5.15 XRD data of a MnSb(0001) on Ge(111) film. 163
5.16 AFM of a MnSb(0001) film at 5 × 5 μm and 15 × 15 μm scan sizes. . 165

5.17 SQUID magnetometry of MnSb(0001)/Ge(111) film showing M-T and M-H. 166

B.1 RHEED patterns for InSb(001) and a MnSb film grown on InSb(001). . 180

B.2 Symmetric XRD data for 5 nm MnSb film on InSb(001). 181

B.3 RHEED patterns for NaCl(001) and a MnSb thin film grown on NaCl(001). 182

B.4 Symmetric XRD data for 20 nm MnSb film on NaCl(001). 184

List of Tables

1.1 SADP derived lattice parameters for the MnSb polymorphs. 9
1.2 Example electron counting for the GaAs(001)-β2(2×4) reconstruction. . 16
2.1 Binding energies for Mn, Sb, Ga, As and Ge between 19 and 48 eV. . . 47
3.1 Reconstructions on the InSb(001), (111)A and (111)B surfaces. 63
3.2 Stoichiometry changes observed on the Sb terminated surface of InSb. . 65
3.3 Reconstructions on the GaAs(001) surface. 68
3.4 Enthalpies of formation for various binary compounds. 75
3.5 Enthalpies of reaction for various metal/semiconductor combinations. . 78
3.6 Charge compensation for GECR compliant Mn-substituted c(4×4) models. 82
4.1 SADP derived lattice parameters for the MnSb polymorphs. 90
4.2 Lattice parameters and crystallites sizes for ultra-thin MnSb films. . . . 107
4.3 θ and Q values for the FWHM of the two rocking curves components observed in the ultra-thin limit. 110
4.4 A summary of the MnSb samples studied using asymmetric RSMs. . . . 119
4.5 Candidate reflections for the in-plane data shown in Figure 4.22(c). . . 124
4.6 Summary of the lattice parameters derived for Sample A. 126
4.7 Ratios of the c-MnSb(133) and n-MnSb($1\bar{1}05$) reflections for Samples A through D. 128

5.1 Real space separations for the transmission features observed in MnSb on Ge(001). 144
5.2 Sb 4d XPS fitting values for a MnSb film on Ge(001). 150
5.3 Normalised peak areas of the C 1s, O 1s, Mn 3p and Sb 4d regions for a MnSb film on Ge(001). 150
5.4 Normalised peak areas of the C 1s, O 1s, Mn 3p and Sb 4d regions for a MnSb(0001) film on Ge(111). 161
5.5 Sb 4d XPS fitting values for a MnSb(0001) film on Ge(111). 162
5.6 XRD fitting details for n-MnSb{0002} reflections from a MnSb/Ge(111) film. 162

A.1 Lattice parameters of materials relevant to the growth of MnSb thin films. 176
A.2 Predicted Q_z for cubic materials relevant to MnSb thin films. 177
A.3 Predicted Q_z for hexagonal materials relevant to MnSb thin films. . . . 177
A.4 Lattice parameters of materials trialled to account for unidentified peaks. 178
A.5 Predicted values of Q_z for materials trialled to account for unidentified peaks. 178

Acknowledgements

A great many thanks need to go out to the large number of people who have been involved in getting me to this stage. Firstly, thanks should go to Dr Gavin Bell for giving me the chance to work on these materials and techniques. Gavin is also thanked for his endless supply of prog-rock trivia and 'awe'-'inspiring' Randy Savage impressions. Prof Chris McConville is thanked for introducing me to ultra-high vacuum during my undergraduate final year project and to the interests of antimony-related science.

In every surface science Ph.D there comes that dreaded time: the Vent. And there is but one man, just one, with the inner strength to hold off the tides of terror that come with such a thing. That man is Rob Johnston. An overwhelming amount of thanks goes to Rob for fixing practically everything on MADGE at least once, for his wisdom and for the time spent in sorting out some rather unfortunate 'incidents'...

Further thanks go to Dr Tom Hase (a.k.a Dr Errors!) for his vast knowledge and his assistance with all things synchrotron. His wide collection of phrases should be noted (for all of eternity): 'cheesy poooooofs!', 'peeeeeeeeeps' and 'bikky?!'. Cheers Tom!

Special thanks (or should that be commiserations?) go to the members of Team Brasso: Dr James Aldous, Dan Higgins and Mo Saghir. Their help over the years, in various forms and guises, has been exemplary! Thanks goes to Jim for teaching me the ups-and-downs, the ins-and-outs and the general wibbles of MADGE. Both Dan and Mo are (greatly) thanked for their tireless sample mounting skills, obeying my whimsical requests and surviving the near constant abuse - good show chaps!

The current iteration of Team Real Space (a.k.a CAICISS) are thanked for providing copious amounts of entertainment in an otherwise dark and solemn lab. Liam Fishwick, for having put up with me since the undergraduate days (sorry!) and Dr Marc Walker for his vacuum knowledge, wealth of Portuguese golf information and (deeply) suspicious liking of Spanish club music. Although he's not a member of Team Real Space they are perhaps the best sorts to associate him with and so the Daresbury pub quiz guy also receives an honourable mention. Thank you for at least considering a drum'n'bass music round - *'I might as well throw my speaker down the stairs'*.

The (past and present) members of P449, P459, and 'the other office' are also thanked for tolerating my inane jokes (Hur Hur!): Dr Louise "Lolly" Bailey, Dr Matthew

Bradley, Earl Davis, Dr Dave Duncan, Nessa Fereshteh-Saniee, Dr Phil King, Wojciech Linhart, James Mudd (Mr. Labview/Igor), Dr Dan "Saturday conversations" Sheppard and Sepehr Vashegani-Farahani.

In any surface physics Ph.D, where would you be without the Compton Scattering group? It is for precisely this reason that Matthew Butchers, Ian Maskery, David Kersh and David Pickup are *not* thanked for their scientific contributions but, instead, for the continual eroding of my Friday work ethic - "Pub?"

Further work-ethic erosion was performed by the following individuals: Rich Beaumont ('Slack it off'), Andy Bennieston, Tom Hill, Mike Lazenby, Matt Kenny and Adam Wall. Cheers guys!

The final thanks go to my family: my parents, brother and grandparents. Thank you for tirelessly supporting me, for encouraging me and for getting me to where I am now. Thank you!

Declarations

I declare that this thesis reports my work between October 2008 and August 2012 under the supervision of Dr Gain Bell. The research reported here has not been submitted either wholly or in part in this or any other academic institution for the admission to a higher degree.

The NiSb samples used in Chapter 2 were grown by Dr James Aldous, while MnSb samples with thicknesses greater than 50 nm, as used in Chapter 4, were also grown with the assistance of Dr James Aldous. The XRD data presented throughout this thesis were obtained with the assistance of Dr Thomas Hase, while the reciprocal space maps presented were generated with the assistance of Mr Matthew Brewer. The TEM images presented in Chapters 4 and 5 were obtained by Dr Richard Beanland and Dr Ana Sanchez. The XPS spectra and LEED images presented in Chapter 5 were taken with the assistance of Dr Marc Walker and Mr James Mudd. The RHEED and STM shown in Figures 3.1, 3.2, 3.3 and 3.5 were obtained by Dr Stuart Hatfield. The STM images of the GaAs surface, shown in Figures 3.8 and 3.9, were taken by Dr Faebian Bastiman (EPSRC Centre for III-V Materials). The Ge substrates used in Chapter 5 were grown by Dr Andrew Dobbie and Dr Maksym Myronov (University of Warwick). The bulk magnetometry measurements presented in Chapter 5 were obtained with the assistance of Mr Ian Maskery and Dr Martin Lees. All other analysis and data collection has been performed by the author.

Work presented in this thesis but that is currently awaiting submission to a refereed journal:

- *Interaction of Mn with GaAs and InSb reconstructed surfaces*, **C. W. Burrows**, S. A. Hatfield, F. Bastiman and G. R. Bell, *to be submitted to Surf. Sci.*

- *Non-classical early-stage growth of MnSb on GaAs(111)*, **C. W. Burrows**, T. P. A. Hase, S. A. Hatfield, S. B. Wilkins and G. R. Bell, *in preparation for submission to App. Phys. Lett.*

- *Heteroepitaxial growth of MnSb on Ge(111) virtual substrates*, **C. W. Burrows**, A. Dobbie, M. Myronov, T. P. A. Hase, I. Maskery, S. B. Wilkins, D. R. Leadley and G. R. Bell, *in preparation*

The work presented in this thesis has been published in a refereed journal:

- *Growth and characterisation of NiSb(0001)/GaAs(111)B epitaxial films*, J. D. Aldous, **C. W. Burrows**, I. Maskery, M. Brewer, D. Pickup, M. Walker, J. Mudd, T. P. A. Hase, J. A. Duffy, S. Wilkins, C. Sánchez-Hanke, G. R. Bell, *currently in proof in J. Cryst. Growth*

Work carried out by the author during this PhD, but not presented in this thesis has been published in the following refereed journals:

- *Cubic MnSb: epitaxial growth of a predicted room temperature half-metal*, J. D. Aldous, **C. W. Burrows**, A. M. Sánchez, R. Beanland, I. Maskery, M. K. Bradley, M. d-S. Dias, J. B. Staunton, G. R. Bell, *Phys. Rev. B.* **85**, 060403, 2012

- *Depth-dependent magnetism in epitaxial MnSb thin films: effects of surface passivation and cleaning*, J. D. Aldous, **C. W. Burrows**, I. Maskery, M. Brewer, T. P. A. Hase, J. A. Duffy, C. Sánchez-Hanke, T. Decoster, W. Theis, A. Quesada, A. K. Schmid, G. R. Bell, *J. Phys-Condens. Mat.* **24**, 146002, 2012

Work carried out by the author during this Ph.D but not presented in the thesis has also been presented at the following conferences:

- *Structural characterisation of thin-film CrSb grown by MBE*, **C. W. Burrows**, J. D. Aldous, C. F. McConville and G. R. Bell, Poster presentation at Condensed Matter and Materials Physics, 14–16 December 2010, University of Warwick UK
- *Structural characterisation of thin-film CrSb grown by MBE*, **C. W. Burrows**, J. D. Aldous, C. F. McConville and G. R. Bell, Poster presentation at Interdisciplinary Surface Science Conference, 4–7 April 2011, University of Warwick UK

Abstract

The deposition of Mn on to reconstructed InSb and GaAs surfaces has been studied by reflection high-energy electron diffraction (RHEED), atomic force microscopy and scanning tunnelling microscopy. On both Ga- and As-terminated GaAs(001), a Mn-induced (2×2) reconstruction is observed. In contrast, there are no well defined Mn-induced surface reconstructions on InSb. Islands are observed to form on all of the surfaces studied, with islands on the Group III-rich surfaces composed of elemental Mn and of an alloy on the Group V-rich surfaces. The conversion from Group III(V)-rich to Group V(III)-rich surfaces are discussed in terms of basic thermodynamic quantities and a number of models for surface atom substitution are proposed as pathways for MnAs and MnSb island formation.

A high resolution X-ray diffraction study (HRXRD) has been performed on niccolite, cubic and wurtzite crystallites present within MnSb thin films grown on GaAs(111) substrates. It is observed that the lattice parameters of the polymorphs do not depend on the film thickness or the time-corrected beam flux ratio, J. The niccolite phase is found to relax rapidly (within 3 nm) and the average c lattice parameter of these films is 5.791(1) Å. Variations in the c lattice parameter indicate that the average stoichiometry of the films varies on a per sample basis and this may act to promote the formation of polymorphs. Cubic MnSb crystallites exhibit a large strain dispersion of approximately 1 % and a rhombohedral or trigonal distortion is believed to be the origin. Quantitative analysis of asymmetric reciprocal space maps reveals that films grown using the optimised conditions have the highest concentration of the cubic polymorph, with lower values of J in the optimised range promoting this polymorph.

The growth of MnSb on Ge(001) and Ge(111) substrates has been investigated. On Ge(001) growth proceeds through the formation of three dimensional islands and no dependence on the growth conditions is observed. Evidence for $(1\bar{1}02)$ and $(11\bar{2}0)$ crystallites is seen in XRD and RHEED, respectively. The interface between the MnSb islands and the Ge(001) substrate is sharp with no evidence for interfacial reactivity. The epitaxial growth of MnSb on Ge(111) is reported for the first time. The growth orientation is confirmed to be (0001) by X-ray diffraction while the layers are found to be ferromagnetic with a Curie temperature in excess of 300 K.

Abbreviations

AFM atomic force microscopy
bcc body-centred cubic
BEP beam equivalent pressure
CVD chemical vapour deposition
DFT density functional theory
DHCP double hexagonal close packed
DMS dilute magnetic semiconductors
DOS density of states
ECR electron counting rules
fcc face-centred cubic
FWHM full-width at half-maximum
GECR generalised electron counting rules
IBA ion bombardment and annealing
IMFP inelastic mean free path
LEED low-energy electron diffraction
LET layer equivalent thickness
MBE molecular beam epitaxy
RHEED reflection high-energy electron diffraction
RMS root mean square
RSM reciprocal space map
SADP selected area diffraction pattern
SQUID superconducting quantum interference device
STM scanning tunnelling microscope
TEM transmission electron microscope
TOA take-off angle
UHV ultra-high vacuum
XPS X-ray photoelectron spectroscopy
XRD X-ray diffraction

Chapter 1

Introduction

1.1 Motivation

A key area of research within condensed matter physics has been in the study of bulk crystalline materials and their properties. However, as modern semiconductor technologies continue to focus on miniaturisation the surfaces of these crystalline materials have become increasingly important. The nature of a surface gives rise to several phenomena including the formation of surface reconstructions, alloying or impurity segregation. These phenomena strongly affect the behaviour of the interfaces that form when these crystalline materials are combined into heterostructures. As an example, the segregation of Al into GaAs quantum well layers in AlAs/GaAs heterostructures leads to shifts in the observed optical emission spectra [1] (dependent upon the extent of the Al segregation). Consequently, detailed studies of the properties of these surfaces, and the interfaces they form, are then necessary prior to their incorporation into device structures.

One of the problems with decreasing device size is that of leakage currents arising due to quantum mechanical tunnelling effects. Efforts have been made to reduce these currents in the technologically important complementary metal-oxide-semiconductor (CMOS) devices through the use of unconventional materials. New technologies are

also under investigation to help replace or enhance existing methods and one such new technology is that of *spintronics*.

1.1.1 Spintronics

Spintronics, a portmanteau of *spin* and *electronics*, introduces the concept of manipulating the quantum mechanical spin of an electron as well as its charge. The addition of the spin degree of freedom offers new methods of computation or could be used to increase the speed and power efficiency of existing electronic devices. Current spintronic device designs feature operating speeds that are comparable with existing technologies [2]. While the reduced dissipative effects experienced by spin currents result in lower power consumption when compared with existing capacitive electronic technologies. Traditionally, the increase in computing speed and the reduction in power consumption have been achieved through a shrinking of transistor feature sizes, with the current generation of (silicon based) modern desktop central processing units achieving feature sizes of 32 nm or smaller [3]. At these lengthscales, leakage currents arising from quantum mechanical tunnelling become significant and the efficiency of the device decreases rapidly, and so spintronics offers new methodologies for the reduction of these problems.

The first applications of spintronics arose out of the discovery of the giant magnetoresistance (GMR) effect in the late 1980s [4, 5], whereby coupled layers of ferromagnetic materials experience a large change in resistance depending upon their relative magnetisation. This relative magnetisation of the ferromagnetic layers can be changed through the application of an external magnetic field and so enables magnetic control of device resistance. Early commercial hard-drive read heads made extensive use of GMR although modern read heads make use of tunnelling magnetoresistance (TMR) [6, 7], in which quantum mechanical tunnelling between the ferromagnetic layers is instead used. In addition to use in the writing of the magnetic bits of a hard drive, the application of TMR to memory storage applications has resulted in the de-

velopment of magnetic random-access memory (MRAM) [8]. The benefits of MRAM include non-volatile storage and reduced power consumption, and so it could plausibly replace conventional memory in everyday computing applications. Additionally, there are several other unique applications of the spintronics concept including: spin light emitting diodes [9], spin transistors [10] and spin-based batteries [11].

Although there are examples of the commercial use of spintronics (such as the hard drive read heads and MRAM mentioned above), several key issues still remain with its integration into traditional electronics. These issues are reflected by the three main requirements of a spintronic device: 1) a highly polarised *injection* source, 2) long spin coherent lengths and lifetimes (*transport*) and 3) efficient *detection* methodologies. Addressing the second point, a large lifetime is required in order to both successfully manipulate and subsequently detect a spin-polarised current. This lifetime readily translates into a spin diffusion length and values of up to 4 μm have been observed in GaAs [12] (at low temperatures) and up to $\sim$310 nm in Si (at room temperature) [13]. These are larger than most proposed device lengthscales ($\sim$100 nm) and so the second criterion is considered fulfilled.

The third criterion requires a method whereby the spin polarisation of an injected current can be reliably manipulated and measured. One such method for manipulating a spin-polarised current is through the Rashba effect, as proposed in the construction of the spin transistor, where an applied electric field induces a precession in a spin polarised current. Detection methods are broadly generalised into three categories: optical (electro- and photo-luminescence), Andreev reflection and ferromagnetic contacts (transport methods) [14]. Although the first two categories are mature they are relatively bulky and so are unsuitable for inclusion into device applications. Consequently, a solid-state detection method, such as magnetoresistance techniques, is preferred for straightforward incorporation with existing semiconductor technology.

Material considerations for spin injection

The most critical aspect for a spintronic device is then the first criterion, which places strict requirements on the materials used to construct the injection sources for hybrid (semiconductor-ferromagnet) spintronic devices. Any material intended for use as an injection source must: 1) be able to polarise an injected current and 2) be compatible with existing semiconductor technologies. The first point is naturally fulfilled through the use of ferromagnets due to the spin imbalance present at the Fermi level in these materials. However, the second requirement is more complex to fulfil and requires structural and chemical compatibility with a range of cubic materials such as Si, Ge and GaAs. This compatibility is crucial owing to the strong effect that defects such as intermixed layers, misfit dislocations or stacking faults [15] have on the spin polarisation of an injected current.

A simple injection source could be constructed from a layer of an elemental ferromagnet deposited directly onto a semiconductor. However, effects arising from chemical intermixing reduce the effectiveness of these contacts through the introduction of magnetic 'dead-layers' [16] which limit the ultimate spin polarisation. Ferromagnetic alloys, such as the transition-metal pnictides, then provide an attractive alternative to the elemental contacts due to their epitaxial compatibility with III-V substrates and high Curie temperatures [17, 18]. The primary disadvantage of these alloys is their relatively low spin polarisations ($<$20 %) and it is thought that polarisations of close to 100 % are necessary for high efficiency injection [19]. Instead, all-semiconductor structures could be constructed through doping with magnetic ions such as Mn [20] or Gd [21] and could feasibly be achieved within the same growth system. These materials are known as the dilute magnetic semiconductors (DMS) and, as the crystal structure remains unchanged, have excellent epitaxial compatibility. However, the primary disadvantage of DMS is their low Curie temperatures, with values of up to 176 K for (Ga,Mn)As reported [20], precluding them from inclusion into existing electronics.

A fourth class of materials, which have particular relevance to this thesis, are

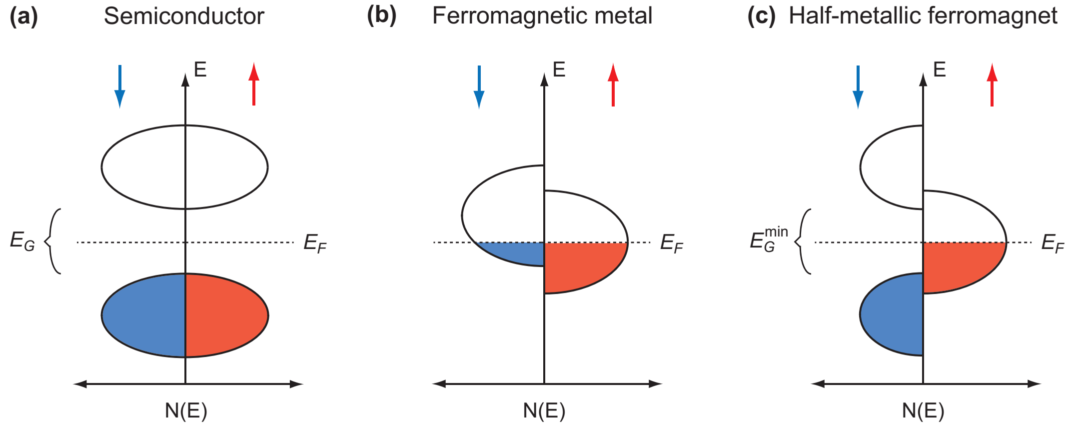

Figure 1.1: Schematic density of states for (a) a direct gap semiconductor with a band gap of E_g, (b) a ferromagnetic metal and (c) a half-metallic ferromagnet with the minority spin band gap, E_G^{min}, indicated. The red and blue arrows denote the majority and minority spin channels, respectively.

the half-metallic ferromagnets (HMFs) which offer high spin polarisations at the Fermi level, good epitaxial compatibility and high Curie temperatures. The interest in these materials initially arose out of theoretical work performed by de Groot [22] on the half-Heusler alloy NiMnSb, which determined that a metallic density of states exists for one spin orientation (the majority spin) and a semiconducting density of states exists for the other (the minority spin). This is illustrated in Figure 1.1(c), Figure 1.1 also shows the density of states for a direct gap semiconductor (panel (a)) and a ferromagnetic metal (panel (b)) for comparison to the spin polarised density of states of the HMF. As a result of this unusual band structure, HMFs have 100 % spin polarisation at the Fermi level and so provide a naturally highly polarised injection source.

The Heusler alloys consist of four interpenetrating face-centred cubic (fcc) lattices that are offset from one another by $\frac{1}{4}$ of a unit cell. The full-Heusler alloys have all four fcc lattices occupied while the half-Heusler alloys have only three lattices occupied, with the fourth remaining vacant. The cubic symmetry of these alloys is important for epitaxial compatibility with the III-V and Group IV semiconductors. Recent theoretical results have shown that the structurally simpler zincblende binary transition-metal pnic-

tides are more robust against the formation of minority states [23] and are half-metallic at the surface for the energetically favoured Sb termination [24]. However, it is thought that the 100 % spin polarisation at the Fermi level, in both the zincblende and Heusler alloys, is significantly reduced by segregation, minority spin states and defects at the surface [25]. As a result, HMF materials within heterostructures can have reduced spin polarisations (due to interface formation) and so their efficiency as injections sources will be reduced.

1.2 Organisation of the thesis

The work presented in this thesis focuses upon the characterisation of MnSb thin films and interfaces, with focus on the effects of Mn on the surfaces of III-V semiconductors. The remainder of the current chapter introduces some general properties of the transition-metal pnictides. The physical origins of surface reconstructions are then explored alongside the conventions and notations used to describe them.

A large number of techniques have been used to investigate the properties of MnSb films and interfaces, and these are introduced in Chapter 2. The background theory of the techniques is described, with experimental schematics, and reference is made to relevant experimental data to aid in the explanation of the analysis procedures used.

Chapter 3 details the behaviour of Mn on the surfaces of GaAs and InSb substrates. A combination of RHEED, STM and AFM is used to investigate the changes in surface morphology and reconstruction with increasing Mn coverage. On the basis of these observations, the effects of bulk thermodynamics and surface reconstructions on the changes observed is discussed.

In Chapter 4, high resolution X-ray diffraction measurements of MnSb overlayers grown on GaAs(111) substrates is presented. The behaviour of the niccolite phase of MnSb under varying growth conditions is investigated and then compared with the observed properties of the cubic and wurtzite phases. Finally, reciprocal space maps

are used in a preliminary study of the polymorph in-plane parameters and their relative abundances.

Chapter 5 details the growth of MnSb on Ge(001) and Ge(111) substrates. The chapter begins with a discussion on the properties of the (2×1) reconstruction of Ge(001) using a combined RHEED-LEED study (Section 5.2). A combined RHEED, AFM, XPS, TEM and SQUID study is then used to determine the properties of MnSb overlayers grown on Ge(001) substrates (Section 5.3). Preliminary work on the previously unreported growth of MnSb on Ge(111) is presented (Section 5.5).

Finally, Chapter 6 summarises the main findings of this work and highlights some of the key outstanding questions found during this project. Directions for future work, including surface structure studies on the transition metal/III-V semiconductor surfaces described in Chapter 3 and more detailed growth studies of the MnSb/Ge system are proposed.

1.3 Properties of MnSb

The binary transition-metal pnictides (TMPs) are intermetallic alloys consisting of a transition-metal atom (such as Cr, Mn or Ni) bonded to a Group V atom (such as As or Sb). These materials can exist in a range of crystallographic and magnetic structures, and of particular interest to this thesis is the manganese pnictide MnSb. In the bulk, MnSb exhibits the double hexagonal close packed (DHCP) niccolite structure (spacegroup $P6_3/mmc$) with an AbAc stacking order and the lattice parameters are $a = 4.115$ Å and $c = 5.769$ Å (see Table 1.1). In the niccolite structure, the Mn atoms occupy the A sites while Sb atoms sit on the alternating b/c sites, although it is possible for atoms of either species to occupy the b/c anti-sites under off-stoichiometric conditions [26]. The hexagonal unit cell of the niccolite structure is shown in Figure 1.2 and highlights the primary crystallographic directions in addition to the AbAc stacking order. Note that truncating the niccolite structure at an 'Ab' site, such that 'b' site Sb atoms are at the surface, results in a rotation of the Sb atoms, and the corresponding bond

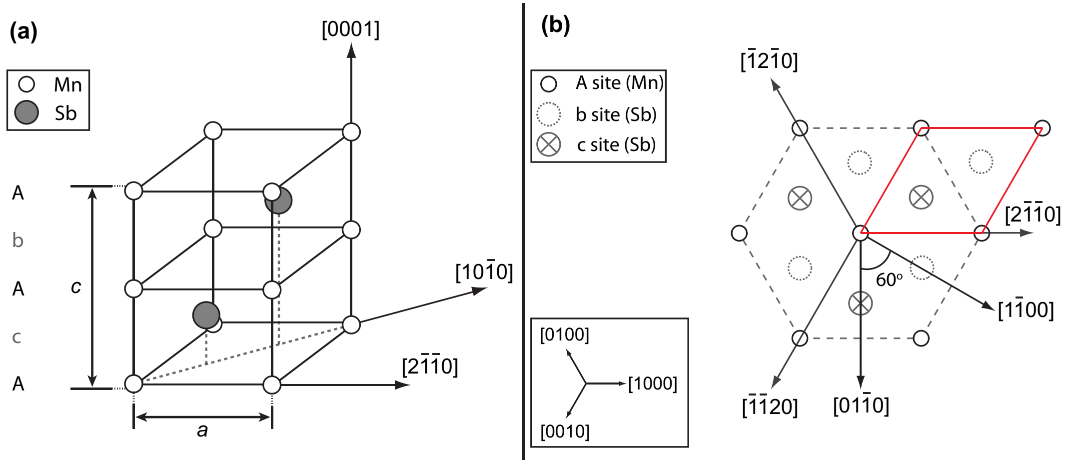

Figure 1.2: (a) Crystal structure of niccolite MnSb showing the hexagonal unit cell. (b) Surface directions for a hexagonal crystal in 4 index notation, the red lines indicate the primitive surface mesh and corresponds to the unit cell shown in (a). Note that families of equivalent directions can be generated through a permutation of the *h*, *k* and *i* indices.

directions, by 60° relative to an 'Ac' termination. This arises due to the position difference of the Sb sub-lattices and this rotation is shown schematically in Figure 1.2(b). In the niccolite phase, MnSb is a p-type semi-metal with a carrier concentration of approximately 10^{22} cm^{-3} [27]. It orders ferromagnetically with a Curie temperature of ∼587 K and the easy axis of magnetisation lies in the plane for both thin-films and bulk crystals [17]. With reference to the first requirement of a spintronic material (compatibility of the injection source, as outlined in Section 1.1.1) MnSb is epitaxially stable on GaAs substrates and forms abrupt, unreacted, interfaces [28]. Of additional interest is the large magneto-optical Kerr rotation observed in MnSb thin films on sapphire [29] which is of use in optoelectronic applications [30].

It is interesting to note that the related transition-metal pnictides CrSb and NiSb share the niccolite structure and have in-plane lattice parameters similar to that of MnSb and GaAs ($a_{\mathrm{GaAs}}\langle 110\rangle = 3.997$ Å [31], $a_{\mathrm{CrSb}} = 4.108$ Å [32] and $a_{\mathrm{NiSb}} = 3.953$ Å [33]). However, they exhibit different magnetic properties to MnSb, where CrSb is an antiferromagnet and NiSb is a paramagnet. Consequently, all-epitaxial single crystal spin valves could be constructed on III-V semiconductor substrates.

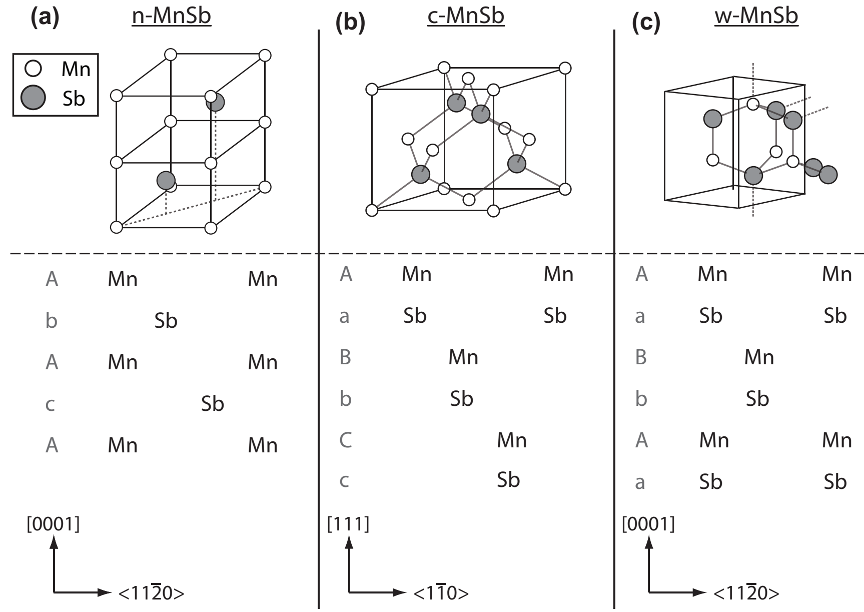

Figure 1.3: Crystal structures and illustrative stacking order schematics for (a) niccolite MnSb (n-MnSb), (b) zincblende MnSb (c-MnSb) and (c) wurtzite MnSb.

Table 1.1: Lattice parameters for the MnSb polymorphs as determined from electron diffraction measurements, values reproduced from Reference [23]. Note that the uncertainty of the values is ±0.5 %.

Polymorph structure	*a* lattice parameter (Å)	*c* lattice parameter (Å)
Niccolite (n-MnSb)	4.115	5.769
Zincblende (c-MnSb)	6.502	-
Wurtzite (w-MnSb)	4.291	7.003

The observation of zincblende and wurtzite MnSb crystallites in thin films of MnSb grown by MBE [34] is of great interest for spintronic applications. The crystal structures of the three MnSb polymorphs (niccolite, zincblende and wurtzite) are shown in Figure 1.3, in addition the stacking orders of the polymorphs in the crystallographic orientations relevant to this thesis are shown. Lattice parameters for the polymorphs are given in Table 1.1 and have been determined from electron diffraction measurements. Note that the zincblende polymorph is referred to as the cubic polymorph (c-MnSb) throughout this thesis.

Studies performed using density functional theory (DFT) have shown that both the cubic and wurtzite polymorphs are half-metallic with minority spin-channel band-gaps greater than 1 eV. Despite this, little exists in the literature on the growth of half-metallic binary pnictides, with the majority of success reported for the Cr-based pnictides CrAs [35] and CrSb [36] on GaAs substrates. However, both materials revert to their more stable bulk crystal forms for films with thicknesses greater than $\sim$3 nm (the bulk phases are an orthorhombic structure for CrAs and the niccolite structure for CrSb) and the half-metallicity is destroyed. Although these additional structures are observed experimentally they are only metastable and, in the case of MnSb, the large equilibrium energies of the cubic and wurtzite polymorphs ($\sim$0.8 eV higher than that of the niccolite phase [23]) suppresses their formation. However, novel substrates may provide a route to the formation of the polymorphs of MnSb through the use of strain engineering.

1.4 Surface notation and reconstructions

The termination of a 3D bulk structure straightforwardly leads to the formation of a surface, although the resulting atomic structure of such a surface may not be the most energetically favoured. Several processes can occur in order to minimise the free energy of the surface and these vary depending upon the type of bonding present in the material: metallic, ionic or covalent. The simplest method for minimising this free energy is for atoms to relax perpendicular to the surface and is commonly seen in metal crystals. The outermost layer of atoms contract inwards as a result of the asymmetric charge density that arises from the bulk truncation. Consequently, the second layer of atoms expand outwards as a result of the charge re-distribution, while the third contracts. This oscillatory behaviour continues into the bulk and is typically damped within five to six atomic layers [37]. For ionic solids the situation is more complex and depends upon the number of atomic species present at the surface [38]. If the truncation of the bulk leads to a surface that is terminated by a single species of ion (such as the rocksalt (111)

surfaces) then this results in an unphysically large dipole energy due to the absence of charge balancing. These surfaces are highly unstable and can relax through the formation of facets of mixed atomic termination which have zero net charge. For surfaces with two atomic species (the rocksalt (100) or (110) surfaces) then it is possible for the surface to charge balance by reconstructing or through relaxation of the surface atoms from bulk positions. Finally, for covalently bonded materials such as the III-V semiconductors, the surface relaxes through the formation of bonds between neighbouring surface atoms and further detail is provided on the reconstructions of these surfaces in Section 1.4.2. The truncation of a real bulk crystal is not perfect and typically features a small angular deviation from normal. The result is the formation of large terraces separated by a regular array of 'steps' with heights related to the size of the material unit cell. The size (width) of these terraces is important when considering the observed electron diffraction patterns (outlined in Section 2.2) from a surface, while steps have a profound effect on the growth of thin films [39].

It is worth briefly discussing the surface direction notation used in this thesis. The directions and planes within a crystal are defined using the Miller indices and for cubic structures a 3-index (hkl) system of notation is used. For a crystal plane h, k and l represent the reciprocal values of the fractional intercepts made by the plane with the three crystallographic directions: a, b and c. For a cubic structure a, b and c are orthogonal to one another and have the same length, representing the lattice parameter (in real space) of the crystal. Consequently, (hkl) is used to denote a plane that intercepts the axes at $\frac{a}{h}$, $\frac{b}{k}$ and $\frac{c}{l}$, while [hkl] denotes the real-space direction perpendicular to the (hkl) plane. There are two further notations that are used throughout this thesis: $\langle hkl \rangle$, which represents all directions equivalent to [hkl] by symmetry; and $\{hkl\}$ which indicates all planes that are related to (hkl) by symmetry. The non-orthogonal basis vectors of the hexagonal crystal structure require a fourth index, i, and give rise to the Miller-Bravais indices: $hkil$. As an example, the directions for a MnSb(0001) surface are shown in Figure 1.2(b). The directions [h000], [0k00]

and $[00i0]$ all lie in the basal plane and the fourth index is given by $i = -(h + k)$. Analogously to the 3-index system, the $[hkil]$ direction is perpendicular to the $(hkil)$ plane and the addition of the fourth, dummy, index aids in determining which directions and planes are related by symmetry. From Figure 1.2(b) it can be seen that the $[2\bar{1}\bar{1}0]$, $[\bar{1}\bar{1}20]$ and $[\bar{1}2\bar{1}0]$ directions are equivalent and so symmetry related directions can be found by permutating h, k and i.

1.4.1 Wood Notation

The reconstruction of a surface results in a new atomic arrangement and a change in the periodicity, defined as the distance between atoms in similar bonding environments, of the surface. One method of relating the periodicity of the bulk structure and the surface periodicity is through the use of matrix notation [40]. If the substrate lattice vectors are defined as **a** and **b** and the surface lattice vectors as $\mathbf{a}'$ and $\mathbf{b}'$ then the relationship between the two can be described as follows:

$$\begin{aligned} \mathbf{a}' &= G_{11}\,\mathbf{a} + G_{12}\,\mathbf{b} \\ \mathbf{b}' &= G_{21}\,\mathbf{a} + G_{22}\,\mathbf{b} \end{aligned} \tag{1.1}$$

where G is a matrix of the form

$$\begin{pmatrix} G_{11} & G_{12} \\ G_{21} & G_{22} \end{pmatrix}. \tag{1.2}$$

The key advantage of matrix notation is that it allows for the description of incommensurate adsorbate layers. A surface structure is incommensurate when there is no simple relation between the adsorbate and the substrate, and they do not share the same translational symmetry.

A more convenient method of representing these changes in surface structure is Wood notation. Here a ratio and a rotation angle are specified between the bulk termination, and the reconstructed surface and is given by

$$X\{hkl\}\text{-}(n \times m)R\theta - A \tag{1.3}$$

where X is the substrate element or alloy, $\{hkl\}$ is the surface plane, $R\theta$ is the angle between the substrate and surface lattice vectors, and A is the adsorbate element, if present. The integers n and m are given by $|\mathbf{a}'| = n\,|\mathbf{a}|$ and $|\mathbf{b}'| = m\,|\mathbf{b}|$ and represent the reconstruction lattice vectors relative to those of the substrate. Note that if there is no rotation in the reconstruction, the -$R\theta$ is omitted, while if the reconstruction is intrinsic to the material and not induced by an adsorbate, then the -A is also omitted. Several prefix letters are often applied to the $(n \times m)$ component of the notation in order to remove ambiguity regarding the reconstruction. For primitive or centred reconstructions 'p' or 'c' are added to denote reconstructions of this form. In this thesis primitive reconstructions have the 'p' prefix omitted and so a p(2×2) reconstruction is given as (2×2). Additionally, if the surface exhibits rotational symmetry then it is possible for a reconstruction to be repeated according to this symmetry. In the case of square surface lattices, this rotation is 90° and is known as 'double domain'. For a hexagonal lattice a 120° rotation occurs and these are known as 'triple domain', and the notation 'td' is used.

III-V semiconductor surfaces

The III-V semiconductors are compounds consisting of a Group III element (Al, Ga, In) bonded to a Group V element (P, As, Sb). These alloys are typically seen to have the zincblende structure and, similarly to the Heusler alloys, consist of interpenetrating fcc lattices. The structure features two lattices that are offset by $\frac{1}{4}$ of a unit cell relative to each other. Figure 1.4(a) illustrates the zincblende unit cell and it can be seen that each atom forms four bonds with its neighbours in a tetrahedral configuration. When truncating the bulk structure, the bonds between atoms are broken and become partially filled. As the bonding is highly directional in zincblende semiconductors, these unfilled bonds are directed away from the bulk and are known as 'dangling' bonds. This is an energetically unfavourable situation and results in neighbouring surface atoms bonding to form dimers.

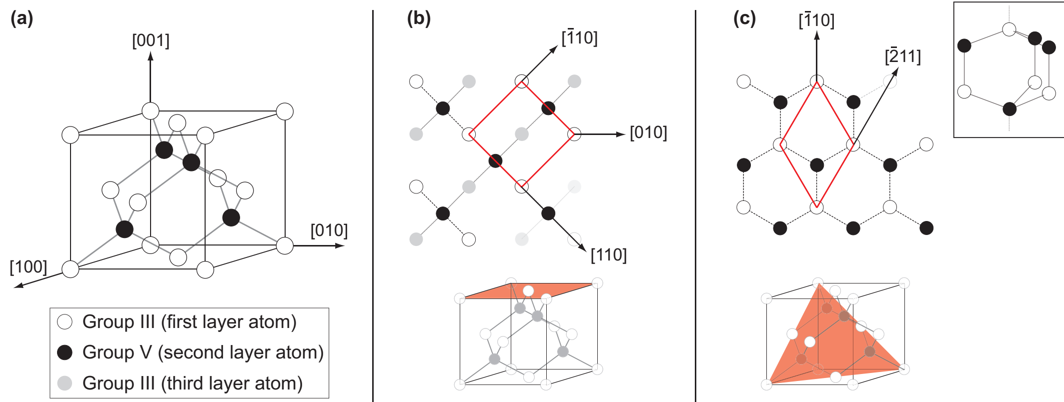

Figure 1.4: Schematics showing the zincblende (a) unit cell (b) (001) surface and (c) (111)A surface, the inset shows a ball and stick model of the GaAs(111) tetrahedral bonding configuration. The red lines and shaded regions indicate the position of the primitive surface mesh and the position of the plane within the unit cell, respectively.

Of relevance to this thesis are the (001) and (111) surfaces which are illustrated in Figures 1.4(b) and (c), respectively. The (001) surface has square symmetry and truncating the bulk in this plane results in the formation of two dangling bonds per atom which, due to the tetrahedral bonding configuration, are aligned along different directions for each atomic species. The Group V bonds are directed along the [1$\bar{1}$0] direction (the *n* periodicity direction) and the Group III bonds are directed along the [110] direction (the *m* periodicity direction). In the cubic system the (001), (010) and (100) faces are equivalent by symmetry and in this thesis the convention is made that the growth surface of a cubic substrate is labelled as the (001) face.

The (111) surface is more complex due to the inequivalent number of dangling bonds present depending upon whether it is cation (Group III) or anion (Group V) terminated [41]. Considering a Group III terminated crystal first, an example of which is shown in Figure 1.4(c), the top layer of Ga atoms has one upward dangling bond and three backbonds to the As layer below. Removing the topmost Ga layer exposes the As layer, in which each atom has three upward dangling bonds and a single backbond, which is energetically unfavourable. The As layer then desorbs and a single dangling bond Ga layer remains, this surface is known as the (111)A surface. If, instead, the

crystal is terminated by a layer of As with one upward bond then removal of this As layer exposes a Ga layer with three dangling bonds, which subsequently desorbs resulting in a As terminated layer, this is known as the (111)B surface.

1.4.2 Electron counting rules

Although a number of quantitative surface structure techniques, including surface X-ray diffraction [42], ion scattering [43, 44] and low energy electron diffraction [45] have been used in the study of III-V semiconductors surfaces, few provide a direct way of identifying the atomic positions on the surface. A trial structure is often required and the reliable identification of physically valid models from either STM images or LEED patterns is non-trivial. One method for determining the plausibility of a model is through the use of the electron counting rules (ECR) [46]. The dangling bonds that are formed at the surface when a crystal is truncated are energetically unfavourable and so a reduction in the number of dangling bonds will minimise the energy of the surface. The III-V semiconductors achieve this via the transfer of charge to and from dangling bonds, where Group V dangling bonds are filled and Group III dangling bonds are emptied. This charge transfer arises due to the sp^3 hybridised bonding orbitals that are present in the zincblende structure and, on this basis, an estimation of the energies of the conduction and valence bands can be made from the energies of the s and p atomic orbitals [46]. In the case of GaAs the Ga dangling bonds lie above the conduction band minimum, and so are emptied, while the As dangling bonds lie below the valence band maximum, and so are filled.

The electron counting rules then ensure that the surface is charge neutral and remains semiconducting as excess charge carries a significant energy cost [47]. Each bond between a Group III and Group V atom consists of two electrons with 2 e^- total charge and so, on average, each Group III atom contributes $\frac{3}{4}$ e^- and each Group V contributes $\frac{5}{4}$ e^-. Dimers contain 2 e^- while charge transfer occurs between the Group III dangling bonds and Group V dangling bonds. To determine if a structure is ECR

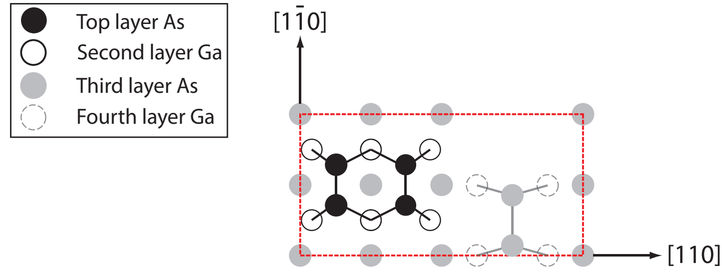

Figure 1.5: GaAs(001)-β2(2×4) surface reconstruction, the red dashed line indicates the reconstruction unit cell. Reproduced from Reference [48].

Table 1.2: Example electron counting for the GaAs(001)-β2(2×4) reconstruction as shown in Figure 1.5.

	Group III bonds	Group V bonds	Dimers	Group III DB	Group V DB	Total e$^-$
Charge excess/deficit	$\frac{3}{4}$ e$^-$	$\frac{5}{4}$ e$^-$	2 e$^-$	0 e$^-$	2 e$^-$	
β2(2×4)	12	12	3	4	6	**42**
Total e$^-$ from Ga						12
Total e$^-$ from As						30
Total valence						**42**

compliant a comparison of the total number of electrons available in the reconstruction, found by summing the total number of valence electrons present in non-bulk bonding configurations (3 e$^-$ from Group III atoms and 5 e$^-$ from Group V atoms), and the number required by the reconstruction is made. The following conditions can be applied:

- Group III bonds contribute $\frac{3}{4}$ e$^-$
- Group V bonds contribute $\frac{5}{4}$ e$^-$
- Group III dangling bonds have 0 e$^-$
- Group V dangling bonds have 2 e$^-$ (from emptied Group III dangling bonds)
- Dimers (and heterodimers) have 2 e$^-$.

Using the β2(2×4) reconstruction of the GaAs(001) surface, shown in Figure 1.5, as an example then there are 6 As atoms and 4 Ga atoms in non-bulk bonding con-

figurations. Each of these atoms has a single dangling bond and three III-V bonds, while there are three dimers formed between the As surface atoms. A summary of the values determined for this structure are given in Table 1.2 and it can be seen that the number of electrons required matches the number of available valence electrons and so the structure is ECR compliant. Substitution of the atoms within dimers is permitted so long as the atom has only one dangling bond. A Group V atom can be replaced by a Group III atom, which decreases the available number of valence electrons by two but the loss of the filled dangling bond on the Group V then provides two electrons and so accounts for the discrepancy in charge. The reverse is also true and so a Group III atom can replace a Group V atom, both of these processes lead to the formation of heterodimers (mixed Group III-Group V dimers) on the III-V surfaces. It should be noted that while the ECR can be used to predict which surface structures are charge neutral, and so are energetically favourable, they cannot be used to determine the lowest energy structure for a given surface. Typically, experimental results in conjunction with DFT studies are then used to determine the true surface structure. In addition, some experimentally observed structures are known to violate the ECR, in particular on the GaSb, AlSb and GaN surfaces [49].

An extension to the ECR was proposed by Zhang et al. [50] to account for the adsorption of metal adatoms due to their variable valence electron number. These modified rules are known as the generalised electron counting rules (GECR) and they are based on three additional constraints:

1. Metal adatom location:
    - d metal adatoms (transition metals) will prefer to occupy interstitial sites
    - sp metals will prefer to occupy substitutional sites
2. An adatom will act as a donor (acceptor) if its electronegativity is lower (higher) than those of the component elements of the semiconductor

3. A metal adatom will try to maximise (minimise) its valence electron number if it behaves as an acceptor (donor) in the system.

Accordingly, metal adatoms are able to donate or accept electrons as required and subsequently the surface then reconstructs according to the ECR outlined above. One possible limitation of the GECR arises from the large number of valence electrons of the transition metals. Although, in the case of Mn, it is assumed that adatoms will act as donors (due to its electronegativity relative to that of Ga and As) whereas the situation is more complex for metals which are amphoteric in the semiconductor. An example of this is Fe, which has an electronegativity value between that of Ga and As. It is plausible that Fe could donate its two 4s electrons to the local structure or accept up to four electrons in its 3d subshell and so this mixed behaviour may complicate the determination of the true structural model.

Chapter 2

Experimental techniques

2.1 Molecular beam epitaxy

Molecular beam epitaxy (MBE) enables the growth of high-quality crystalline films on a variety of substrates and was first successfully applied to III-V compound semiconductors by Arthur and Cho [51] in the 1960s. The primary advantage of MBE is the ability to grow a range of materials, including films showing magnetic behaviour, within the same growth chamber with thicknesses controllable to the atomic level. Additional benefits include independent control of the growth parameters, through variation of the substrate temperature and material fluxes, and the use of strain engineering to manipulate the electronic and structural properties of the resulting thin film. The technological applications for MBE are diverse and are predominantly based on the growth of multilayer heterostructures such as high-speed transistors [52] and solid-state lasers [53]. The inclusion of magnetic layers into these structures opens up new avenues of research into the growth and manipulation of spintronic devices.

The principle behind MBE is the formation of molecular beams due to the sublimation (or evaporation) of material. The formation of molecular beams is only possible under vacuum conditions owing to the large mean free paths possible at such low pressures ($< 10^{-5}$ mbar). For example, at atmospheric pressures the mean free path of a

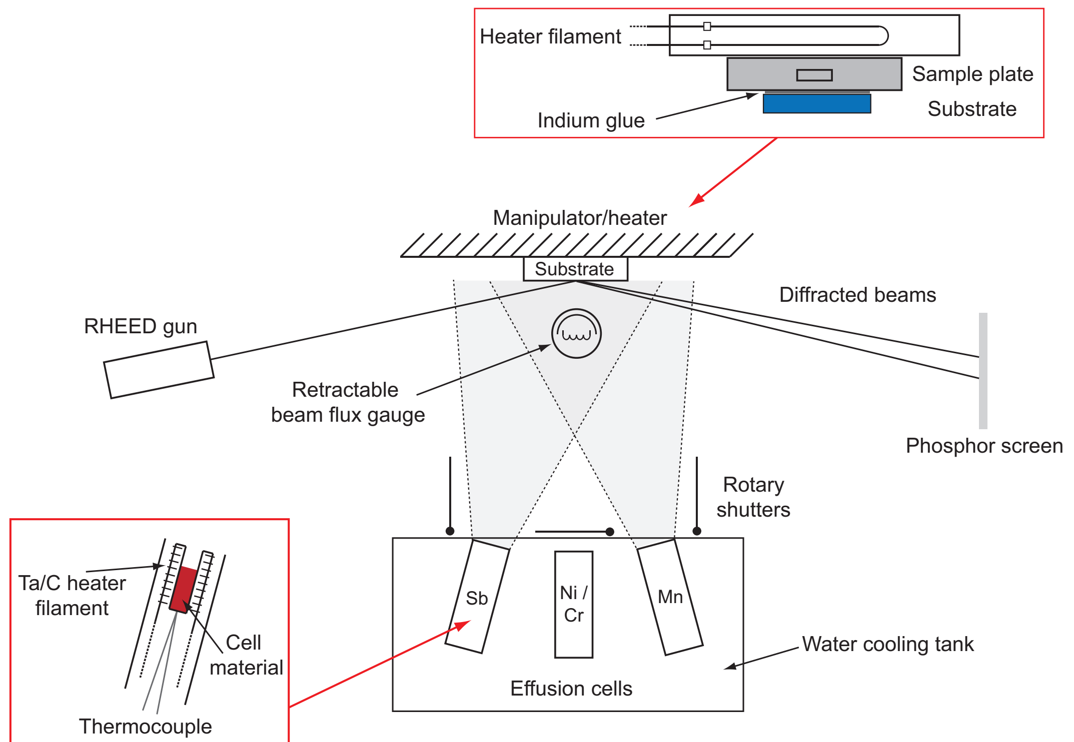

Figure 2.1: Schematic representation of the Warwick MBE growth chamber. Effusion cells containing Mn, Ni, Cr and Sb are located at the base of the chamber and are directed towards the manipulator. A retractable beam flux gauge is used to measure the beam equivalent pressure directly in the beam path. The inset in the bottom left shows a simplified diagram of the general construction of a radiative effusion cell indicating the heater filament, thermocouple and source material. The inset in the top right illustrates the construction of the manipulator and heater. Indium glue is used to affix samples to the sample plates, which are radiatively heated from behind using a metal filament.

nitrogen molecule is ∼70 nm, whilst at 10^{-9} mbar the mean free path is ∼100 km [39]. When compared to the size of a typical ultra-high vacuum (UHV) chamber (∼1 m) the sublimated/evaporated material experiences a very small number of collisions and so results in the formation of 'beams'. An additional benefit of using UHV is the reduced contamination of surfaces and the subsequent inclusion of impurities into growing films. This is crucial for the growth of semiconductors where the presence of a relatively small number of impurities can dramatically alter the electronic properties [54].

The setup of a typical MBE chamber is shown in Figure 2.1 and illustrates the layout of the Warwick growth chamber used to produce the samples discussed

throughout this thesis. This particular geometry enables the use of reflection high-energy electron diffraction (RHEED) during growth in order to study the roughness and the structure of a surface, and provides in-situ determination of sample quality and behaviour. Further detail on RHEED is given in Section 2.2.1. The substrate is attached to a sample plate, or holder, and is located in a manipulator capable of both rotating and heating the substrate during growth. The effusion cells, located at the bottom of the schematic in Figure 2.1, consist of a ceramic crucible, usually constructed of either pyrolytic boron nitride or alumina (Al_2O_3), which contains the source material and a method for heating this material. Heating is then achieved through one of two methods, either radiatively using a refractory metal filament wrapped around the crucible or directly via electron bombardment (e-beam heating). The behaviour of the source material vapour pressure with temperature is given by the Clausius-Clapeyron equation

$$P = P_0 \exp\left(\frac{-\Delta H}{\mathrm{R}T}\right) \tag{2.1}$$

where P is the beam flux as measured using an ion gauge located in the path of the beam, ΔH is the enthalpy of evaporation or sublimation (dependent upon source material), R is the molar gas constant and T is the absolute temperature of the source. It is then the value of ΔH which dictates the type of heating method used, typically for the transition metals (Ni, Fe, Co) the value of ΔH is large, for example the value of ΔH_{sub} for Ni is 428 kJ/mol [55]. Therefore, high temperatures ($>$1000 K) are required to generate appreciable vapour pressures and this favours the use of e-beam heating in order to achieve the required temperatures. However, for Group V elements, such as antimony or arsenic, radiative heating via a filament is able to generate beam pressures of up to 1×10^{-6} mbar due to the much lower value of ΔH for these materials. The temperature of the cell material is monitored via a thermocouple in physical contact with the base of the crucible and a PID feedback loop is then used to maintain the desired temperature and flux.

The resulting molecular beams are directed toward, and subsequently impinge upon, a substrate surface where they are free to interact. Following the arrival of an

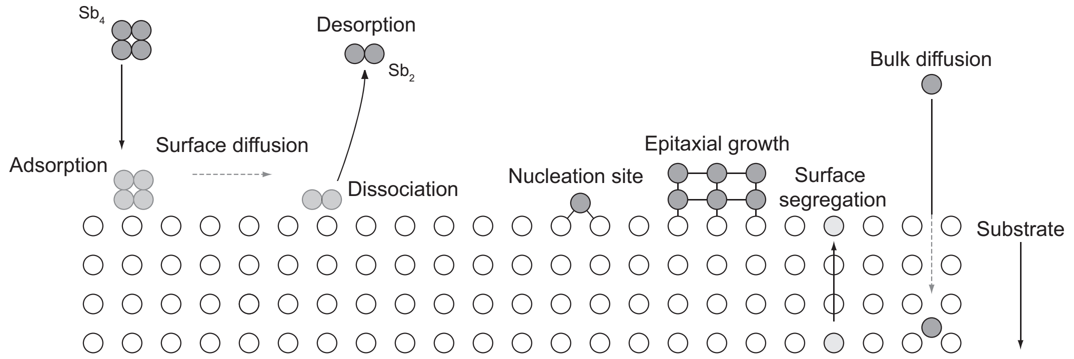

Figure 2.2: Representation of the atomistic surface processes that can take place during growth.

incident atom or molecule at a surface, several different processes can occur and these are illustrated in Figure 2.2 [56]. The rate, R_{surf}, at which these processes occur is given by an Arrhenius-like relationship

$$R_{\mathrm{surf}} = R_0 \exp\left(\frac{-E_{\mathrm{a}}}{\mathrm{k_B} T}\right) \tag{2.2}$$

where R_0 is the attempt rate of the process and is related to the lattice vibration frequency of the adsorbed atom. The activation energy of the process is denoted by E_{a}, $\mathrm{k_B}$ is the Boltzmann constant and T is the absolute temperature.

Following the arrival of an atom at the surface, there is a probability that it will remain on the surface and become adsorbed. This is known as the 'sticking coefficient' or 'sticking probability'and its value is dependent on both the atom/molecule species and the surface composition. The adsorption of atoms onto a surface falls into two broad categories. The first is physisorption and is characterised by weak van der Waals-like forces. The second occurs when an atom undergoes an electron exchange process and becomes chemically bonded to the surface, it is then said to be chemisorbed. Due to the increased temperature of the substrate, incident atoms are free to desorb into the vacuum and so there is also an effective loss of atoms which can act to reduce the growth rate. The benefit of elevated substrate temperatures is the increased diffusion of atoms across the surface until they reach nucleation sites. It is also possible for adsorbed molecules to dissociate (shown by the breaking of the Sb tetramer into dimers) and the resulting

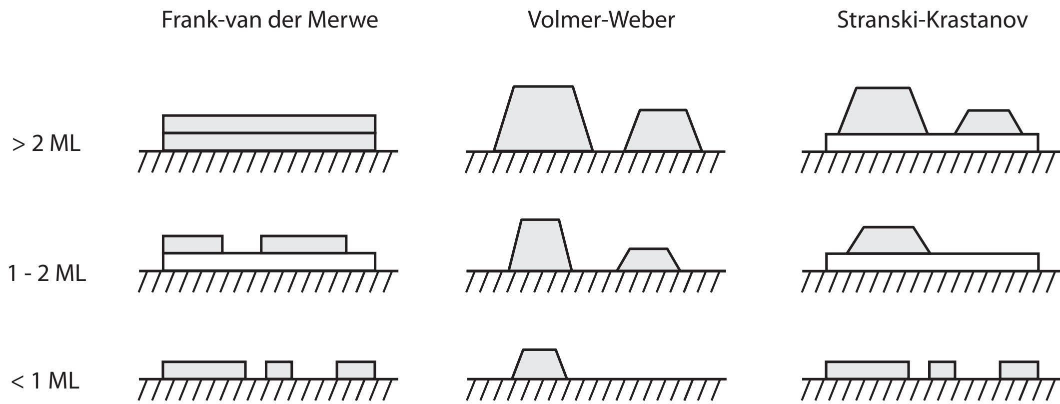

Figure 2.3: Schematic illustrating the three idealised epitaxial growth modes: Frank-van der Merwe (layer by layer growth), Volmer-Weber (3D island growth) and Stranski-Krastanov (wetting layer with 3D island growth).

fragments may then desorb into the vacuum. Equally, an adatom has a probability of being desorbed related to the substrate temperature, with increasing temperatures increasing the probability of surface atom loss. Layer growth then proceeds through the chemisorption of atoms at nucleation sites and, in itself, can be split into two categories depending upon whether the growing layer is the same as the substrate (homoepitaxy) or different (heteroepitaxy). Additionally, it is possible for T_{sub} to provide sufficient energy to overcome the activation barriers for surface and bulk diffusion processes, in which case reactive growth can take place.

There are three idealised modes for the epitaxial growth of thin films and these modes are shown schematically in Figure 2.3. The first is layer by layer, or Frank-van der Merwe, growth which is the preferred mode for thin films since the next monolayer of material forms only after the first has finished. This results in sharper interfaces and reduced surface roughness, both of which are highly desirable in device applications. The second is Volmer-Weber growth and this mode involves the formation of 3D islands on the surface. The final mode is Stranski-Krastanov growth and is an intermediate mode consisting of 3D islands with a wetting layer. The growth mode that dominates on a surface is dependent upon the balance between the surface energies of the substrate,

the overlayer and the interface between them [56].

The effect of strain on the growth mode can be significant, particularly for systems where there is a large lattice or structural mismatch. The lattice mismatch (f_i) along direction i for crystal structures with similar symmetries can be defined as follows [57]:

$$f_i = \frac{a_{si} - a_{oi}}{a_{si}} \tag{2.3}$$

where a_s and a_o are the in-plane lattice parameters of the substrate and overlayer, respectively. Note that for $f_i < 0$ the overlayer is under a *compressive* strain and for $f_i > 0$ it is under a *tensile* strain. In systems that are closely matched, $|f_i| < 1$ %, the growing material will, up to a critical thickness h_C, follow the in-plane spacing of the substrate in a Frank-van der Merwe growth mode. This is known as *pseudomorphic* growth and is typically exploited in the production of high electron mobility devices constructed from III-V semiconductors [52] due to the reduced number of interfacial defects. As the mismatch between the overlayer and substrate increases, the value of h_C rapidly decreases due to the increased strain energy in the growing layer. This strain is relaxed at h_C through the formation of defects and misfit dislocations. For large mismatches it is possible for Stranski-Krastanov growth to occur and this can result in the formation of quantum dot structures [58, 59]. Mismatch can also occur when the crystallographic symmetry of the substrate and overlayer is different, as is the case for MnSb on GaAs(001). Large mismatches occur along all of the major symmetry directions due to the different symmetries of the overlayer (hexagonal for MnSb) and the substrate (cubic for GaAs) [60]. The resulting MnSb film is then orientated $(1\bar{1}01)$ in order to minimise the mismatch.

It should be noted that these modes are highly idealised and growth often consists of a mixture of modes, dependent upon the conditions at the surface. The primary factor that influences the dominant growth mode is the relative strength of the atom-atom and atom-surface interactions, as mentioned previously. However, additional processes such as reactivity, substrate temperature, growth conditions and strain also change the

behaviour. As an example, reactivity between substrate and the incident atom species leads to a new growth mode whereby islands grow *into* the substrate. This mode is termed endotaxy and has been observed in the growth of MnSb on both GaSb [61] and InP [62].

As the growth of MnSb is III-V like [62], and is performed under Sb-rich conditions, its growth rate is proportional to the integrated Mn flux, which depends upon the measured Mn beam flux. Throughout this thesis, thickness values for MnSb layers are estimated by scaling the growth rate by the measured Mn beam equivalent pressure.

Warwick growth chamber

The MnSb samples studied during this thesis were grown using a compact MBE chamber located at the University of Warwick. The system consists of the growth chamber, a surface preparation and analysis chamber, and a fast entry chamber for sample loading. The growth chamber is equipped with Mn, Sb_4, Cr and Ni sources. The first three of these sources make use of radiative heating to evaporate the source material, while the Ni effusion cell uses e-beam heating to evaporate from a rod source. The MBE chamber is equipped with a 15 kV RHEED electron gun, operated at 12.5 keV, which is used to monitor the surface reconstruction throughout deposition. Beam pressures are measured using a retractable beam flux gauge (BFG) located at sample height. The surface analysis and preparation chamber features an scanning tunnelling microscope (STM) in addition to an ion sputter gun used for sample preparation. The growth chamber and surface analysis chambers both feature manipulators capable of heating samples to temperatures of 500 °C.

Beam equivalent pressure ratio

An important quantity in MBE is the ratio, J, of the beam equivalent pressures (BEPs) of the constituent elements and for MnSb it is defined as the ratio of the Sb

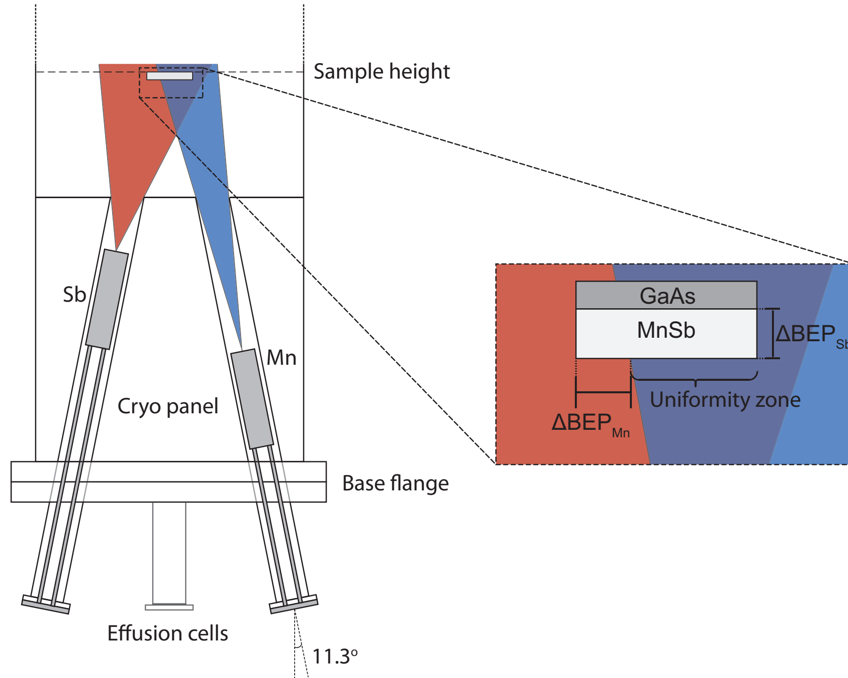

Figure 2.4: Illustration of the Warwick MBE chamber (left hand panel), indicating the offsets in the cell heights within the feedthroughs. The right hand side illustrates how the inhomogeneity of the beam equivalent pressure of Mn varies both across and throughout a sample. The uniformity zone highlights the region where the value of $J_{\mathrm{Sb/Mn}}$ is optimum.

flux to the Mn flux, such that

$$J_{\mathrm{Sb/Mn}} = \frac{\mathrm{BEP_{Sb}}}{\mathrm{BEP_{Mn}}}.$$

Here the BEP for a given element is the difference between the measured flux from the appropriate cell and the background pressure in the growth chamber. Prior to growth, the beam fluxes of both cells are allowed to stabilise, typically over a 30 minute period, and the desired $J_{\mathrm{Sb/Mn}}$ value is then obtained by altering the Sb cell temperature.

The effects of J on the growth of samples are significant and, in the case of MnSb, samples removed from the growth chamber often exhibit multiple surface morphologies, such that the surface consists of shiny and 'cloudy' regions that are visible by eye. Previous studies have shown that the cloudy regions are characterised by a mesa-like structure and are the result of high $J_{\mathrm{Sb/Mn}}$ values [28, 34]. This mixed surface

morphology is also seen on samples that have $J_{\mathrm{Sb/Mn}}$ values nominally in the optimal growth regime. On this basis, it is then worth briefly discussing the errors in $J_{\mathrm{Sb/Mn}}$.

Owing to the design of the growth chamber, the Mn cell lies further recessed into its feedthrough on the growth chamber in comparison to the Sb cell, as shown schematically in Figure 2.4. This results in a highly collimated beam and consequently the Mn flux varies significantly across the sample surface (denoted by $\Delta\mathrm{BEP}_{\mathrm{Mn}}$). Calibration studies of the beam shape profile [60] indicate that at approximately 5 mm away from the centre of the chamber the flux has decreased by a few percent, while at 10 mm from the centre the flux has decreased by $\sim$8 % relative to the central maximum. As samples are typically up to 10×10 mm^2 in size this represents a large variation in the local $J_{\mathrm{Sb/Mn}}$ value at the surface on the basis of the Mn spatial variation alone.

In contrast, the Sb spatial profile is highly uniform across the chamber due to its position further up the feedthrough. However, this introduces an additional complication as the cell is located closer to the shutter, which acts to reflect heat and increase the temperature of the material at the top of the crucible. The increased temperature results in a higher Sb flux compared to the initial value established when determining the value of $J_{\mathrm{Sb/Mn}}$. The elevated temperature of the upper material is not detected by the thermocouple as it is in contact with the base of the crucible and, when the shutter is opened, the material cools and so the measured Sb flux decays towards the originally measured value. As such, there are two primary sources of error in $J_{\mathrm{Sb/Mn}}$: the error in the Sb flux and the error in the Mn flux.

Considering the error in the Sb cell first. The time variation of the Sb flux, plotted in Figure 2.5, shows an exponential decay behaviour following opening of the shutter. The J value shown in the figure is scaled relative to the stabilised value of $J_{\mathrm{Sb/Mn}}$ measured prior to growth, while the red line is the result of fitting an exponential decay function which yields a time constant (τ) of 149 s. It should be noted that the time from opening the shutter is equivalent to the growth time and so, for samples that have a thickness less than $\sim 3\tau$ (for a 6 nm min^{-1} growth rate this is equal to

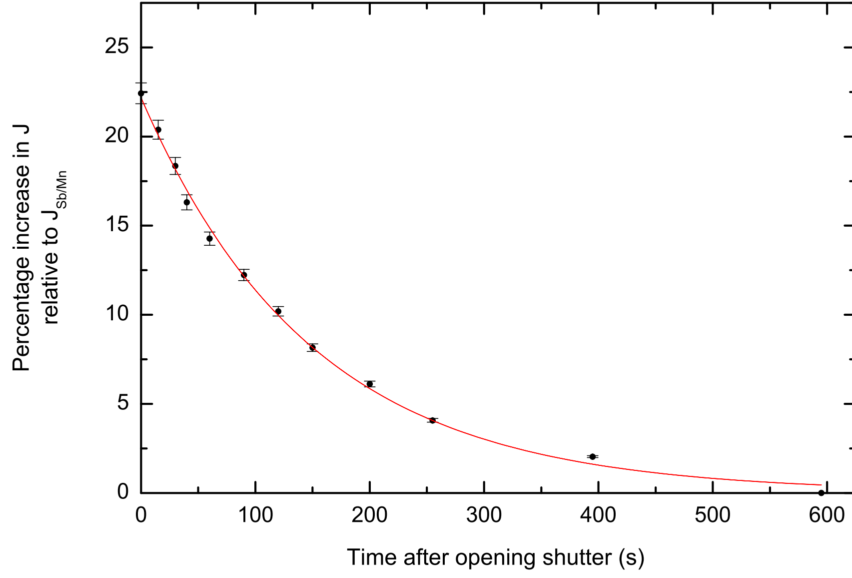

Figure 2.5: Behaviour of the Sb cell beam equivalent pressure with time. The vertical axis has been scaled relative to the stabilised value of $J_{Sb/Mn}$ measured prior to growth. The red line is an exponential fit to the data and indicates a time constant, τ, of 149 s.

45 nm), the actual J value will differ significantly from the value set prior to growth. A corrected J value, J_{corr}, can then be derived using the values obtained from the fit shown in Figure 2.5 and represents the time averaged J value for the entire film. On this basis, J_{corr} is then defined as

$$J_{corr} = \frac{1}{T}\int_0^{\mathrm{T}} J(t)\,\mathrm{d}t \tag{2.4}$$

where $J(t)$ is the value of J at time t after opening the shutter and T is the total deposition time. As the behaviour of the Sb BEP follows an exponential decay, as seen in Figure 2.5, the functional form of $J(t)$ can be represented as

$$J(t) = J_{Sb/Mn}\left(1 + \Delta J_0 \exp\left(\frac{-t}{\tau}\right)\right) \tag{2.5}$$

where ΔJ_0 is the fractional change in J at 0 s and from fitting is found to be 0.221 ± 0.04. A value for J_{corr} can then be calculated by substituting Equation 2.5 into Equation 2.4 and integrating between 0 and T. Following substitution of the limits, J_{corr} is given by

$$J_{corr} = \frac{J_{Sb/Mn}}{T}\left(T - \Delta J_0 \tau \exp\left(\frac{-T}{\tau}\right) + (\Delta J_0 \tau)\right). \tag{2.6}$$

As an example, for a 150 nm thick sample grown with $J_{\mathrm{Sb/Mn}} = 6.6$ for a total time of 1500 s the value of J_{corr} is 6.76, a 2.4 % correction. However, for a 10 nm sample grown using the same $J_{\mathrm{Sb/Mn}}$ over a time of 100 s, the value of J_{corr} is then 7.66 and represents a 16 % correction. Consequently, it can be seen that the actual value of J differs significantly from the desired value in the case of thin samples.

The uncertainty in J_{corr}, ΔJ_{corr}, can then be found by differentiating Equation 2.6 and so has the form

$$\Delta(J_{\mathrm{corr}}) = \left(\frac{J_{\mathrm{Sb/Mn}}}{T}\right)\left(1 - \exp\left(\frac{-T}{\tau}\right)\right)\Delta t \tag{2.7}$$

where Δt is the error in the growth time and includes the time required to close the shutters in addition to any measurement errors in the growth time, this value is approximately equal to 2 s. An additional source of error arises from the measurement uncertainty in the Sb BEP owing to the limited precision of the digital ion gauge controllers used on the growth chamber and the percentage uncertainty is observed to vary between 1 and 10 %. For the typical growth values used in this thesis, $\mathrm{BEP}_{\mathrm{Sb}} = 6.6\times10^{-7}$ mbar, and so the uncertainty is of the order 1.5 %.

The second major source of error is from the lateral inhomogeneity of the Mn flux at the sample surface due to collimation effects. Calibration studies suggest that the Mn flux is relatively constant over a small width of $\sim$ 5 millimetres near the centre of the chamber. However, it varies more rapidly at distances greater than this such that over variations in flux of approximately 7.5 % are observed over the typical width of a sample. As the flux is observed to *decrease* this will act to drive J_{corr} upwards. The uncertainty in J_{corr} is then asymmetric as the variation of the Sb flux will decrease the value of J_{corr} while the Mn flux variation increases it.

2.2 Electron diffraction techniques

2.2.1 Reflection high-energy electron diffraction

In RHEED, electrons of between 8 and 20 keV impinge upon a surface at grazing incidence, with an angle of between 1° and 6°, and the resulting diffracted beams are projected onto a phosphor screen. As a result of the scattering geometry used, such that the electron beam is perpendicular to the direction of the molecular beams, this technique is ideally suited for use in MBE chambers, as shown in Figure 2.1. Consequently, the behaviour of thin films can be monitored in real-time during growth. It is possible to extract both structural information, in the form of the surface periodicity and the in-plane lattice parameters, as well as the morphology of the surface. The presence of 3D islands, increased surface roughness or even the level of crystallinity of a material can all be deduced from the observed diffraction patterns.

The interaction of the incident electron beam results in the formation of scattered beams. As the diffracted beams have undergone elastic scattering, the energy of the scattered electrons must be conserved such that

$$|E_{\mathrm{f}}| = |E_{\mathrm{i}}| \tag{2.8}$$

where E_{f} and E_{i} are the final and incident energy of the scattered electron. Noting that the momentum of a particle is related to its energy via Equation 2.9a

$$E = \frac{\hbar^2 k^2}{2\mathrm{m_e}} \tag{2.9a}$$

$$|\mathbf{k}_{\mathrm{f}}| = |\mathbf{k}_{\mathrm{i}}| \tag{2.9b}$$

where $\mathbf{k}_{\mathrm{f}}$ and $\mathbf{k}_{\mathrm{i}}$ are the final and initial wavevectors of an electron, respectively. The conservation of momentum, and the interaction of the diffracting electron with the 3-dimensional (3D) reciprocal lattice, dictates that $\mathbf{k}_{\mathrm{i}}$ can only change by a discrete amount

$$\mathbf{k}_{\mathrm{f}} = \mathbf{k}_{\mathrm{i}} + \mathbf{G}_{ijk} \tag{2.10}$$

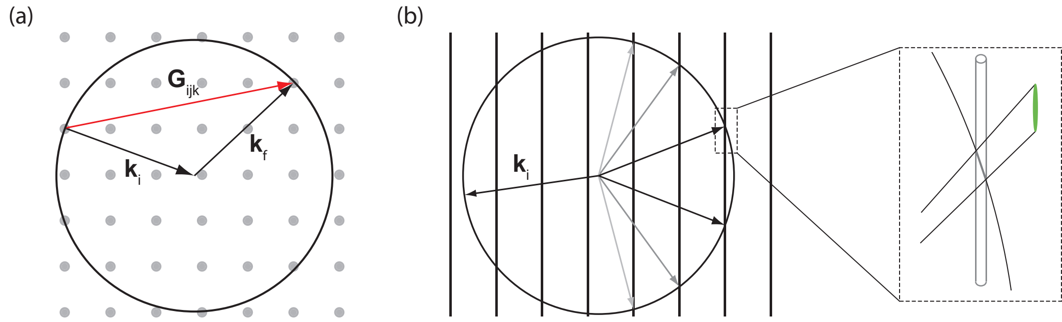

Figure 2.6: Ewald sphere construction for (a) 3D reciprocal lattice and (b) 2D reciprocal lattice, also shown is the intersection of the Ewald sphere with the reciprocal lattice rods resulting in the formation of streaks.

in which $\mathbf{G}_{ijk}$ is a lattice vector of the 3D reciprocal lattice. Solutions to Equation 2.10 can be represented graphically using the Ewald sphere construction, as shown in Figure 2.6. The Ewald sphere is constructed by drawing a vector, of length $|\mathbf{k}_\mathrm{i}|$, originating from a reciprocal lattice point. Following this, a sphere of radius $|\mathbf{k}_\mathrm{i}|$ is drawn centred on the head of the vector and all points which then lie on the surface of the sphere meet the diffraction conditions and so satisfy Equations 2.8-2.10.

At a surface, the loss of periodicity perpendicular to the surface results in the reciprocal lattice points forming infinitely long rods, which are also perpendicular to the surface. Accordingly Equation 2.10 reduces to the following form

$$\mathbf{k}_\mathrm{f} = \mathbf{k}_\mathrm{i} + \mathbf{G}_{ij} \tag{2.11}$$

where $\mathbf{G}_{ij}$ is now a vector of the 2D reciprocal lattice. In this case the Ewald sphere reduces to a circle and its construction is shown in Figure 2.6(b), all points that lie on the perimeter of the circle then fulfil the diffraction conditions. At the energies used in RHEED the Ewald sphere is much larger than the width of the reciprocal lattice rods and so the intersection between the Ewald sphere and the reciprocal lattice rod is nearly tangential. In the case of a perfect surface, the resulting pattern consists of a series of spots where the rods intercept the Ewald circle. However, due to contamination, thermal diffuse scattering and finite-size disorder the rods gain a finite width and so the

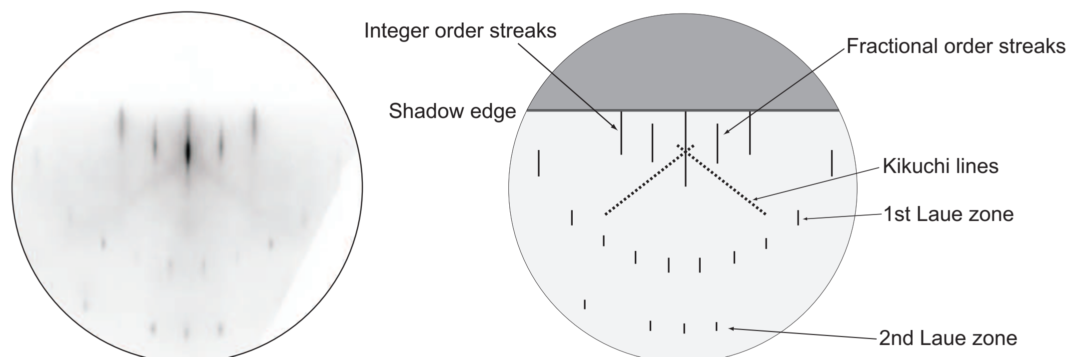

Figure 2.7: RHEED pattern obtained from a MnSb(0001) surface with the electron beam orientated along the $[11\bar{2}0]$ direction showing a $(2\times)$ periodicity. The schematic on the right hand side of the figure highlights the key features of the pattern.

intersection results in the formation of streaks, as indicated in Figure 2.6. Additionally, the absence of a monochromatic electron source gives rise to a range of incident wavevectors although the width arising from the source is often much lower than the effect of surface disorder [63].

RHEED pattern interpretation

The interpretation of RHEED patterns can be complex owing to the large number of phenomena which can occur when the electron beam strikes the surface. An example RHEED pattern, with a corresponding schematic, is shown in Figure 2.7. The more intense streaks, labelled as the integer order streaks, arise due to diffraction from rows of atoms in bulk-like positions, while the fainter fractional order streaks are from surface reconstruction features. The grazing incidence of the electron beam ensures the surface specificity of RHEED and so the observed streaks correspond to the crystal quality in the top few nanometres. Diffraction features are also observed on the lower edge of the phosphor screen and these correspond to additional Laue zones, these occur when the Ewald sphere intersects higher order reciprocal lattice rods. Finally, the faint features (shown as thin dotted lines in Figure 2.7) are known as Kikuchi lines. While streaks are formed from elastically scattered electrons, the Kikuchi features arise due to inelastically

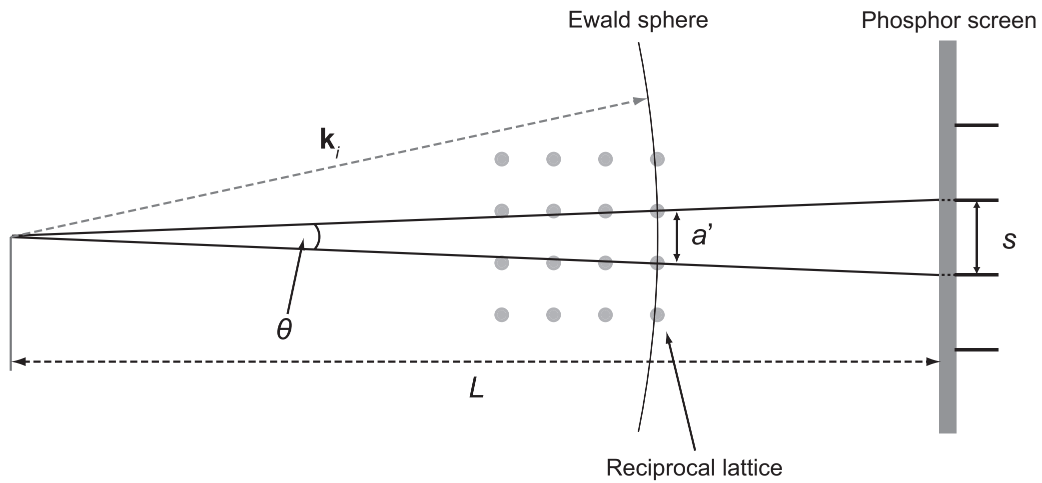

Figure 2.8: Geometric construction used when determining lattice parameters from RHEED patterns. The left hand side shows the reciprocal space correlation between the Ewald sphere and the corresponding diffracted beam directions. The right hand side shows the observed streak pattern.

scattered beams acting as incident beams inside the crystal. These additional beams are able to diffract from bulk planes and, as such, Kikuchi features are another measure of crystallinity and provide information on the quality of the layer. As these lines arise from bulk-like diffraction they can be used to align the crystal along high symmetry directions as they are unique to the orientation of the crystal under study.

Of primary interest in RHEED is the spacing and number of streaks present in any given diffraction pattern. The presence of fractional order streaks indicates that the surface has reconstructed in some way and that the surface periodicity is different from that of the bulk. The example pattern shown in Figure 2.7 has a single fractional streak between the integer streaks and is indicative of a $(2\times)$ periodicity. Rotation of the sample about the surface normal is required in RHEED in order to fully determine the surface reconstruction. For square symmetric surfaces, as on the III-V(001) surfaces, then a rotation of the sample by 90° is required to fully determine the reconstruction. On surfaces with hexagonal symmetry, such as MnSb(0001) or III-V(111), a rotation of only 30° is necessary to determine the reconstruction.

It is possible to derive the in-plane lattice parameters from the observed integer

streak spacing. From the Ewald sphere construction and using the small angle approximation the angle between two diffracted beams, θ, arising from neighbouring reciprocal lattice points is given by (using the small angle approximation)

$$\tan\theta = \theta = \frac{a'}{k_i} \tag{2.12}$$

where a' is the reciprocal lattice spacing. A schematic of this construction is shown in Figure 2.8 and from this it can be seen that θ is equivalent to the streak separation, s, divided by the camera length, L. The reciprocal lattice spacing can then be written as

$$a' = \frac{k_i\ s}{L}. \tag{2.13}$$

The reciprocal lattice parameter is inversely related to the real space lattice parameter, as shown in Equation 2.14a, and so the real space parameter is determined by the relationship in Equation 2.14b

$$a = \frac{2\pi}{a'} \tag{2.14a}$$

$$a = \frac{2\pi\ L}{\sin\phi\ k_i\ s} \tag{2.14b}$$

here the spacing relation has been generalised for non-square surfaces where the angle between the primitive lattice vectors, denoted by ϕ in Equation 2.14b, has been accounted for. For the growth chamber used in this thesis the RHEED gun was operated at 12.5 keV, such that k_i is 5.76×10^{11} m^{-1}, and the camera length is 280 mm. On this basis, the in-plane spacing of the [110] direction of GaAs (3.99 Å) would correspond to a streak spacing of 7.63 mm while for MnSb (a = 4.128 Å) it is 7.39 mm and so these in-plane separations can readily be distinguished. The determination of streak spacings in this thesis was performed by using a standard digital camera to obtain images of the diffraction pattern and then taking line profiles across the images using the Igor Pro data analysis software (WaveMetrics, Inc.). A conversion from pixels (in the images) to millimetres was performed through the use of two phosphor squares, of known separation, affixed either side of the RHEED screen flange. Note that, in addition to measurement uncertainties on the phosphor screen digital images, the uncertainty in the lattice can

also vary due to the difficulty in determining the area of the sample illuminated by the electron beam. For an 8×8 mm^2 sample, this can affect the camera length by ± 4 mm and results in a variation of the lattice parameter by ± 1.4 %.

Finally, of interest when calculating the size of the terraces present on the surface, the incident angle of the beam can be determined from the separation of the straight-through beam and the specular reflection, such that $\theta_\mathrm{i} = \theta_\mathrm{out}$. In RHEED the specular reflection is located in the zeroth Laue zone and so the radius of this zone can be used to determined the incident angle from the following relation [63]

$$R = L \tan \theta_\mathrm{i} \tag{2.15}$$

where R is the radius of the zeroth Laue zone, L is the camera distance and θ_i is the angle of incidence. The incident angle has been calculated using an InSb(001) sample, the RHEED pattern used to determine the incident angle is shown in the top panels of Figure B.1 and corresponds to the pattern with the electron beam directed along the $\langle 1\bar{1}0 \rangle$ direction. Using this pattern and knowing that R is 29 mm and L is 280 mm, an angle of incidence of 5.97° is found. Although this angle is quite steep, and is a result of maximising the size of the homogeneity zone for growth, it also acts to reduce the beam footprint on the sample and so reduces the magnification errors associated with beam spot movement. Note that in the XRD results presented in Chapter 4 the incident angle is denoted by α_i and that, for both RHEED and XRD, the angle is measured from the surface plane rather than the surface normal.

Types of RHEED pattern

It is worth briefly discussing the RHEED patterns observed from samples of varying surface roughness and crystallinity. A key quantity here is the *transfer width*, which is the largest possible distance over which interference can be detected [64]. For atomically smooth samples with large terraces (greater than the transfer width) the observed RHEED patterns will consist of concentric rings of spots, corresponding to diffracted beams arising from each Laue zone. For surfaces that consist of terraces that

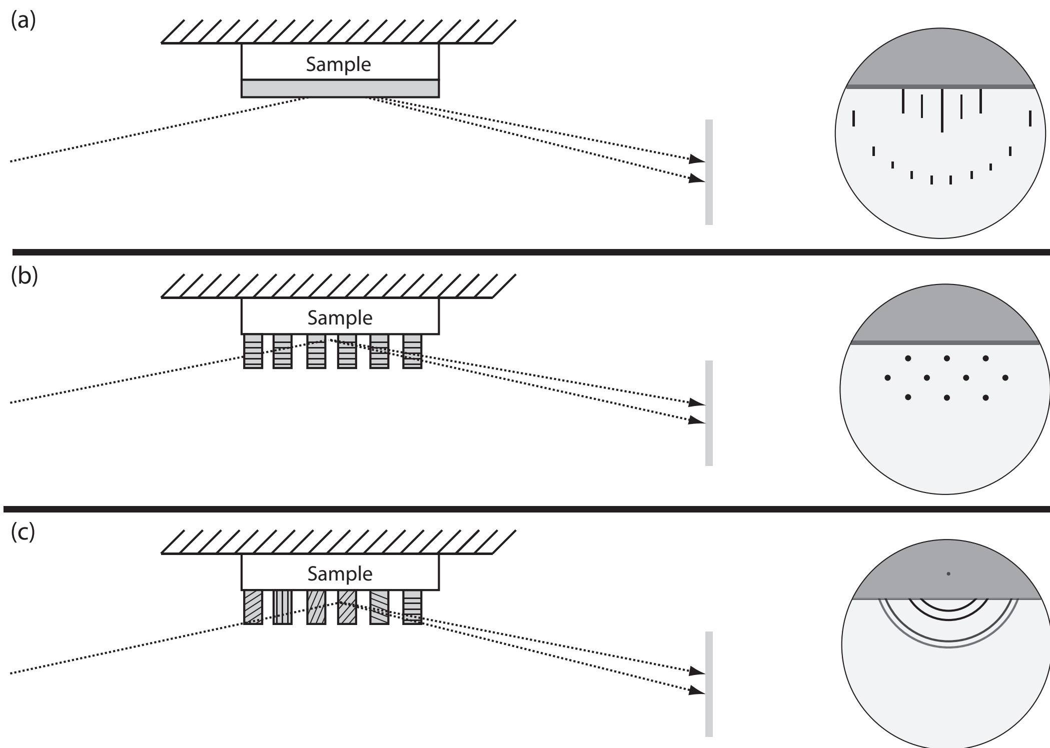

Figure 2.9: Schematic highlighting the types of surface crystal features and the RHEED patterns that result from them. (a) Surface diffraction from a smooth surface where the terrace width is less than the transfer width of the RHEED, giving rise to streaks on the phosphor screen. (b) Transmission diffraction through single crystal 3D asperities, which act to project the bulk 3D reciprocal lattice and so forms a 'spotty' pattern. (c) Transmission diffraction through 3D polycrystals, giving rise to diffraction rings which correspond to the various planes in the crystal.

are comparable in size to the transfer width then the pattern is seen to be streaky, as illustrated in Figures 2.7(a) and 2.9(a). This arises as a consequence of interference between neighbouring terraces due to the path length, and subsequent phase, difference between them due to their varying heights. In this case incoherent scattering causes the reciprocal lattice rods to broaden and so streaks are observed, as demonstrated in Figure 2.6(b). Typical values for the transfer width range between 1500 and 5000 Å dependent upon the experimental set-up and surfaces consisting of terraces of 500 nm or smaller will result in streaky patterns, even if the terraces themselves are atomically flat.

As the roughness of a surface increases, or if a 3D growth mode dominates, then the morphology will come to be dominated by asperities and 3D islands. If the lateral dimensions of the islands are smaller than the inelastic mean free path (IMFP) of the incident electron beam, which is approximately 15–20 nm at 12.5 keV, then transmission diffraction will be observed. Transmission diffraction acts to project the bulk reciprocal lattice and so the Ewald sphere is constructed as in Figure 2.6(a). The resulting pattern consists of circular spots as shown in Figure 2.9(b) and can be used to identify the crystal structure of the islands. However, this type of pattern only occurs for crystalline samples, for polycrystalline samples the rotational disorder inherent in the layer leads to the diffracted beams forming circular patterns, each of which corresponds to a particular crystal plane. An illustration of this type of pattern is shown in Figure 2.9(c). The lattice spacing analysis used for surface diffraction also applies to these types of patterns and so useful structural information can still be extracted.

2.2.2 Low-energy electron diffraction

The formalism used to describe RHEED is also applicable to low-energy electron diffraction (LEED). In LEED, electrons of energy 20–200 eV are incident upon a sample surface and the back-scattered diffracted beams are viewed on a phosphor screen. Surface specificity is ensured by the low energy of the electrons, which have IMFP values in the range 2–10 Å and so limit the probing depth to this range. Additionally, the change from grazing to normal incidence results in a plan-view projection of the reciprocal lattice/Ewald sphere intersection which has the advantage that the full periodicity of the surface reconstruction can be observed in a single image. This is particularly useful when studying rotated domain structures or more complex reconstructions. As with RHEED, finite-size disorder on the surface, in the form of domains smaller than the transfer width, give rise to broadened reciprocal lattice rods. However, in the case of LEED, the transfer width is significantly less than in RHEED and ranges between 30 and 100 Å over the energy range typically used [65]. As a consequence LEED is less

sensitive to the surface morphology and the presence of 3D surfaces features cannot readily be deduced.

2.3 Microscopy techniques

2.3.1 Scanning tunnelling microscopy

The invention of the STM by Binnig and Rohrer [66], and the subsequent growth of the field of scanning probe microscopy, has led to its establishment as an essential tool for surface scientists. Scanning tunnelling microscopy (the designation 'STM' equivalently represents the microscope itself) is a real space imaging technique utilising the phenomena of electron tunnelling to measure the topology of a surface. An atomically sharp tip, located on a stage consisting of several piezoelectric crystals, is brought to within a few angstroms of a surface and raster scanned across the sample. A bias voltage is held between the sample and tip and the resultant tunnelling current is recorded. The vacuum gap between the tip and the sample acts as a rectangular potential and so solutions to the Schrödinger equation have the form [39]

$$\psi = \exp\left(\pm\kappa z\right) \tag{2.16a}$$

$$\kappa = \frac{\sqrt{(2m\phi)}}{\hbar} \tag{2.16b}$$

where z is the tip-sample separation and ϕ is the effective local work function. From this it can be seen that the tunnelling current, which is proportional to ψ, is exponentially dependent on the separation and so thus provides a sensitive measure of the surface topology. However, the requirement for this tunnelling current is that the sample must be either conducting or semiconducting, such that it is possible for electrons to tunnel into and out of the material. This imposes the constraint that insulating materials cannot be imaged in STM.

The two primary modes of operation in STM vary which quantity, the tip-sample separation (height) or tunnelling current, is held constant during scanning. In constant

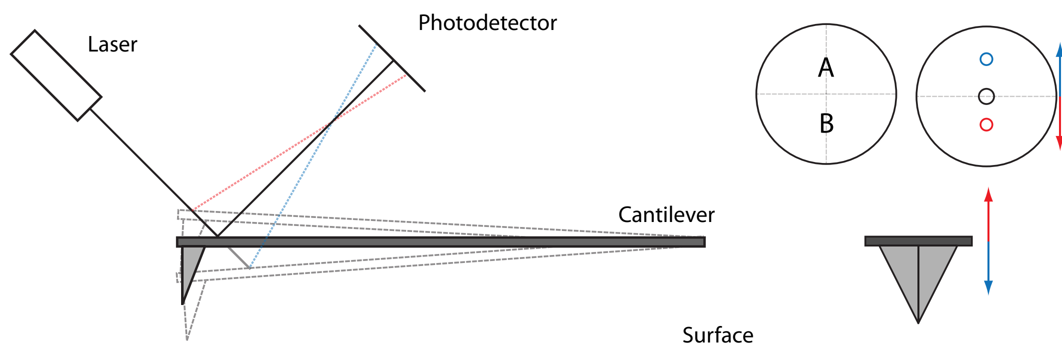

Figure 2.10: Schematic of the optical detection of cantilever movement as used in AFM. The cantilever is deflected up and down due to changes in surface topography and a photodetector is used to determine the direction of deflection through the movement of a reflected laser spot (as illustrated on the right hand side of the figure).

height mode, the tip-sample separation is maintained at a fixed value of z and the variation in the tunnelling current as the tip is scanned across the surface is measured. In constant current mode a feedback loop is applied to the piezoelectric crystals controlling the tip in order to maintain a constant tunnelling current, the variation in the piezoelectric motor movement is then recorded and used as a measure of the surface height variation. The advantage of constant current mode lies in the fact that there is active feedback involved in tip movement, such that any asperities or other large surface features can, in principle, be avoided thus reducing tip damage.

2.3.2 Atomic force microscopy

The inability of the STM to image insulating surfaces led Binnig et al. [67] to develop the atomic force microscope (AFM). Consequently, imaging of a surface with a lateral resolution of better than 10 nm and a vertical resolution of less than 1 Å is possible without the additional complexity of UHV conditions, although UHV AFMs are capable of atomic resolution. The ability to study non-conducting surfaces is especially useful in the case of oxidised surfaces, such as those observed following removal of a sample to the atmosphere.

In AFM a sharp tip, typically 10–25 nm across at the apex and located at the

end of a soft cantilever, is brought within a few angstroms of a surface such that any forces that act on the tip cause a deflection away from the equilibrium position of the cantilever. There are several methods for measuring this deflection, although the most common is through the use of a laser beam reflected from the back of the cantilever onto a four zone photodetector, as illustrated in Figure 2.10 (for simplicity only two photodetector zones, A and B, are shown). Deflection of the cantilever results in the laser spot moving on the photodetector and the difference in intensity between the top (A) and bottom (B) halves of the detector indicate the deflection of the cantilever and, consequently, the force experienced by the tip. It should be noted that the tip can also be 'twisted' by forces at the surface and so the difference in intensity between the left and right sides of the photodetector provide a measure of this deflection.

There are two primary operating modes in AFM: contact and tapping. In contact mode, the tip is brought into physical contact with the surface and raster scanned using a feedback loop to maintain a constant deflection. In tapping mode, the tip is maintained at a fixed distance from the surface and the cantilever oscillated just above its resonant frequency. Any forces acting on the tip will alter the amplitude of oscillation and so by using a feedback loop to maintain a constant amplitude the topography of the surface can be determined.

All images in this thesis were obtained using an Asylum Research MFP-3DSA AFM operating in tapping mode.

2.3.2.1 Interpretation of atomic force micrographs

In Chapter 3, AFM is used to determine the volume of islands distributed on the surfaces of III-V semiconductors. To this end, it is worth discussing the methodology used in the analysis of atomic force micrographs and the values derived from them. Figure 2.11 depicts atomic force micrographs of the surface of a NiSb(0001) thin film [68] in three stages: (a) the raw, unprocessed, image (b) following 'flattening' of the image and (c) with an applied mask.

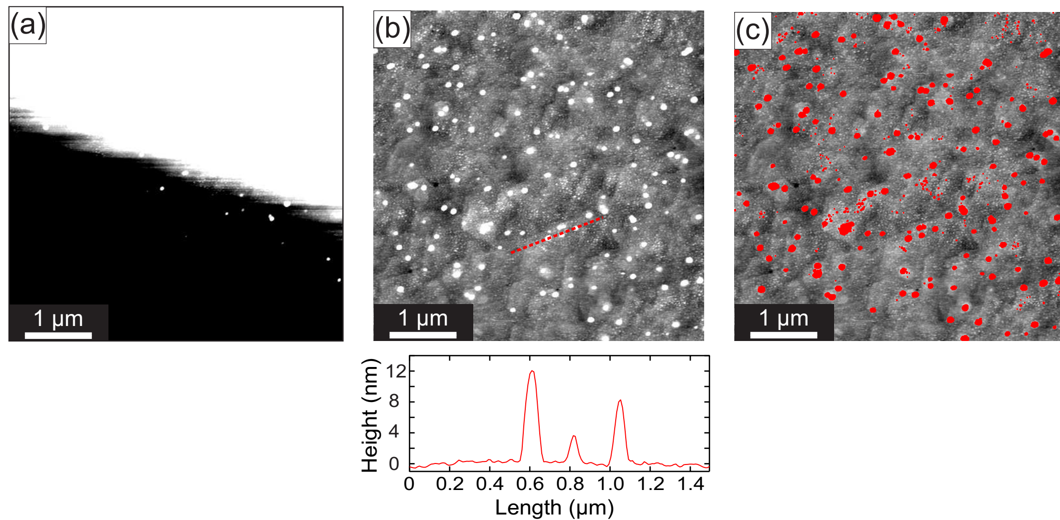

Figure 2.11: Example AFM of a NiSb(0001) thin film showing (a) an unflattened, raw, image (b) the same image following application of a flattening procedure and (c) the calculated image mask (inverted) using a threshold height of 1 nm.

The raw images obtained from the microscope consist of an array of height (z) values, combined into a two-dimensional array which specifies a pixel (and subsequently a distance) position, these images can then be wholly processed using the Asylum Research software written for the Igor Pro data analysis software (WaveMetrics, Inc.). The raw images, as shown in Figure 2.11(a), typically demonstrate significant tilting, as seen from the strong variation in height between the lower left and upper right areas of the image (black represents lower areas of the sample while white represents higher regions). This tilt arises due to the presence of debris on the rear of the sample, in the case of the scan presented in panel (a) the tilt is $\sim$0.89° and is likely due to some remaining indium glue from the sample mounting process.

In order to determine the morphology and root mean square (RMS) roughness of the surface a flattening process is used to account for any tilt present. This is typically performed by subtracting a function from the image and the simplest flattening function is a polynomial, with order varying between 0 and 3, and so ranges from a constant offset across the sample to a point-by-point offset. However, the Asylum Research software

offers an additional automated routine which initially performs a first order polynomial flattening and then calculates a mask, determining which features lie above the plane of the sample, and subsequently re-flattens the image. This procedure is iterated until no further changes are observed, an example of an image flattened using this method is shown in panel (b), note that this image is the flattened equivalent of panel (a).

The benefit of using a first order polynomial is that it maintains the true heights of the surface better in comparison to the higher order polynomials, which can introduce artifacts due to the nature of the functions. For example, these higher order polynomials can result in artificial tilts on a local scale that preclude the comparison of feature heights from across the entire sample surface. In addition, the presence of large features (such as contamination or debris) when flattening a surface can significantly alter the calculated tilt and so introduce additional height errors. These are typically observed as 'shadows' on either side of large features along the scan directions and are most common for flattening processes that independently flatten each scan line in the image.

Following this flattening process, the morphology of the surface can now be seen and the presence of crystallites on the surface is evident. From the image it is possible to extract line profiles, illustrating the topology of the surface along a particular direction and distance, and the RMS roughness. An example line profile corresponding to the dashed line shown in panel (b) is shown below the flattened image and highlights the size of the crystallites present on the surface. This is a typical use of the line profile feature and shows the crystallites have heights of between 3 and 12 nm, and have lateral extensions of $\sim$150 nm.

The roughness of the surface can then be determined by calculating the RMS value of the height values across the image. Due to the random distribution of heights on the surface, the RMS is a good measure of the roughness owing to its ability to cope with height values that vary both positively and negatively about a zero point. From panel (b) it can be seen that the presence of crystallites (and other, similar, surface features) will affect the calculated RMS value. In order to remove the contribution

from the crystallites to the roughness, it is possible to mask them and therefore remove their contribution to the RMS roughness of the underlying surface. Panel (c) shows a typical image with the crystallites masked (although the mask is inverted for clarity), the cut-off value of the mask was set at 1 nm and therefore heights above this value will not be included in the calculation. This leads to an RMS roughness of 0.4 nm, while with the crystallites included the roughness is 0.93 nm. This is a significant increase in the roughness and so demonstrates the influence that surface features can have on the measured roughness, necessitating the use of a mask. An additional benefit of using a mask is that it provides a natural method for integrating the volume of a region above a critical height threshold. One caveat of this is that surface roughness contributions to the volume can affect the resulting value. Choice of a value above the RMS roughness can minimise the additional volume integrated but care is required for islands with heights that are comparable to the RMS roughness. Using panel 2.11(c) as a graphical example the volume of the masked area is a good approximation to the volume of the crystallites.

2.3.3 Transmission electron microscopy

While techniques such as AFM and scanning electron microscopy can be used to readily understand the morphology of a surface, they provide limited direct information on the quality of the overlayer or the interface formed with the substrate. In this regard, transmission electron microscope (TEM) is a powerful tool capable of imaging an entire film and performing structural, and spectroscopic studies of these overlayers. In TEM, electrons are accelerated to energies of between 60 and 400 keV and directed through a series of electron lenses towards the sample. Of primary interest for this study is the direct imaging of the overlayer due to the scattering of the incident electron beam. In this situation, regions of decreased thickness (or density) result in a smaller amount of scattering of the beam and so these regions appear lighter. In the case where the primary transmitted electron beam is used to generate the image, the imaging mode is

known as *bright field imaging* and all of the TEM images presented in this thesis were obtained in this way. A second mode of operation was used to generate the selected area diffraction patterns (SADPs) images. Analogously to other diffraction techniques these can be used to determine the crystallographic properties of microscopic regions of a thin film.

2.4 X-ray techniques

2.4.1 X-ray photoelectron spectroscopy

The characterisation techniques listed so far have focussed on the structural properties of thin films. However, these techniques do not provide information regarding the chemical composition of a sample surface. Although TEM provides the opportunity for elemental specificity through the use of energy dispersive X-ray spectroscopy (EDS), dedicated techniques such as X-ray photoelectron spectroscopy (XPS) provide improved energy resolution and a greater level of information regarding chemical states in the sample. In XPS, incident x-ray photons are used to excite bound electrons from a sample into the vacuum. These electrons are then collected and the resulting spectrum can be analysed in order to determine the elemental species present and their relative concentrations.

In order to remove an electron from the core levels of an atom to the vacuum, the incident photon energy supplied must be greater than the binding energy, E_{b}, of that electron. The ejected photoelectrons then have a kinetic energy, E_{k}, related to the difference between the incident photon energy, $\hbar\nu$, and the binding energy of the core level. This simple model is known as Koopman's theorem and is given by

$$E_{\mathrm{k}} = \hbar\nu - E_{\mathrm{b}} - \phi \qquad (2.17)$$

where E_{b} is the single electron binding energy and ϕ is the work function of the sample. However, this is never observed as the formation of a core hole results in two relaxation

processes taking place. The first is the relaxation of the excited atom's core electrons to lower energy states due to the presence of the increased positive potential created by the core hole, giving rise to an *intra-atomic* relaxation potential. A similar effect can occur with the conduction electrons, especially so for the highly mobile conduction electrons found in metals, which then also acts to reduce the change in potential observed by the core electrons. This is an *inter-atomic* relaxation and so a more accurate description of the photoelectron energy can then be given by

$$E_{\mathrm{k}} = \hbar\nu - E_{\mathrm{b}} + E_{\mathrm{a}} + E_{\mathrm{r}} - \phi \tag{2.18}$$

where E_{a} is the intra-atomic relaxation energy and E_{r} is the inter-atomic relaxation energy. It should be noted that there are two pathways that lead to the filling of the core hole: Auger electron emission and X-ray fluorescence. In Auger emission an electron of a lower binding energy 'drops' down to fill the core-hole and in doing so causes the emission of an electron from a different energy level, the kinetic energy of this electron is then related to the energy levels involved in the transitions. In X-ray fluorescence, as with Auger emission, an electron with a lower binding energy drops down to fill the core hole and results in the emission of an X-ray photon.

Surface specificity in XPS is achieved due to the short IMFP, $\lambda(E_{\mathrm{k}})$, of electrons in solids at the kinetic energies measured during an XPS experiment. Values for the IMFP can be calculated using the TPP-2M equation derived by Tanuma, Penn and Powell [69], and typically vary between 5 and 30 Å. The surface composition of a sample can then be determined from the peak areas of appropriately chosen elemental core levels. Each of these levels gives rise to peaks in the spectra and subsequently need to be normalised according to several factors: the scan dwell time (D_{s}), the number of scans (n_{scan}), the atomic sensitivity factor (a_{asf}) and the probing depth, which depends on $\lambda(E_{\mathrm{k}})$. The area under the peak, A^{P}, is given by

$$A^{\mathrm{P}} \approx \int C(z)\ \exp\left(\frac{-t}{\sin\theta\ \lambda(E_{\mathrm{k}})}\right)\ \mathrm{d}z \tag{2.19}$$

where $C(z)$ is the concentration profile for that element in the surface region, t is the

thickness of the surface and θ is the take-off angle (TOA) between the sample and incident photon beam. Note that by reducing the TOA the probing depth decreases and so the scans become more surface sensitive, this effect is particularly useful during the studies of sub-monolayer deposition or segregation. The concentration profile strongly affects the area of the peak, being a direct measure of the number of atoms present in the surface region. It is possible to simulate appropriate structures and calculate concentration profiles for these; however, this is time consuming and results in non-unique solutions. For the purposes of simple stoichiometry determination, it is valid to note that the peak area for a uniform profile concentration, where $C(z)$ is constant, is proportional to $\lambda(E_k)$. Using this simplification the normalised peak area, I^P, is given by

$$I^P = \frac{A^p}{a_{asf}\ \lambda(E_k)\ n_{scan}\ D_s}. \tag{2.20}$$

This method is applicable for the calculation of surface stoichiometries using the integrated areas of the core levels. However, further information can be obtained via the detailed fitting of peak shapes. The presence of different bonding environments alters the distribution of electrons between atoms and in doing so induces a shift in the binding energy of core electrons. This can be explained through electronegativity arguments, such that if one atom in the bond pair has a higher electronegativity then it has a greater affinity for the electrons within the bond. This results in an increase in electron density around the more electronegative atom and so induces a screening effect. The remaining core electrons will then see a decreased nuclear charge and the core electron orbitals relax, leading to a decrease in binding energy. The opposite is also true for the less electronegative atom which has a corresponding increase in binding energy. In this way, the relative energy change of a chemical shift can be determined and the bonding environments of an element investigated. The peaks then observed in XPS spectra are the convolution of several chemically shifted peaks and can be fitted using software. The peaks are represented as Voigt functions, which are convolutions of Lorentzian and Gaussian functions, where the Lorentzian component arises from the intrinsic lineshape

Element	Core level	Binding energy (eV)
Mn	3p	48
Sb	4d	33
Ga	3d	19
As	3d	43
Ge	3d	29

Table 2.1: Binding energies for the elements relevant to this thesis, all values have been taken from Reference [71] and the energies given correspond to the highest spin-orbit split binding energy present for that level.

of the photoelectron peak and the Gaussian is due to instrumental broadening. The fitting proceeds by varying the full-width at half-maximum (FWHM), centre position and Lorentzian to Gaussian mixing ratio, these fits are then judged by a χ^2 least squares residual measure of fit. Through this, the chemical environment of an atomic species can be investigated and its bonding configurations determined.

All XPS spectra presented in this thesis were taken using the Science City XPS (Omicron GMBH) located at the University of Warwick using a monochromated Al K_α source, the data was subsequently analysed using the CasaXPS fitting software [70].

Further to the discussion on the need to normalise using $\lambda(E_k)$, in this thesis the shallow core region (10 - 80 eV) is used as the primary region for the determination of the surface stoichiometry. In this energy range the IMFP does not vary strongly and so enables a straightforward comparison of elemental ratios. Additionally, the scanning of a sample is greatly simplified by considering the fact that the elements relevant to this thesis all have core levels present in this energy range, as outlined in Table 2.1.

2.4.2 X-ray diffraction

In RHEED and LEED, the scattering of electrons from the near-surface region results in the formation of diffracted beams. Equivalently, the scattering of X-rays from the electrons of atoms in a solid results in the formation of diffracted beams. In X-ray diffraction (XRD) the intensity of the scattered beams is dependent upon the path difference between neighbouring scatterers, such that diffraction occurs when the

distance between the scatterers is an integer multiple of the photon wavelength. This relationship is expressed using Bragg's law [72] and is given by

$$n\lambda = 2d_{hkl}\sin(\theta_{\mathrm{B}}) \tag{2.21}$$

where λ is the photon wavelength, d_{hkl} is the separation of the lattice planes defined by the Miller indices hkl and θ_{B} is the angle between the incident X-ray beam and lattice planes (the Bragg angle). Here n is the order of diffraction, it is convenient to define a new lattice plane separation, $d'_{hkl} = \frac{d_{hkl}}{n}$, such that n is omitted from Equation 2.21. As an example, in the cubic system the second order reflection would be labelled the (002) and so has a lattice spacing equal to half that of the (001) reflection.

One disadvantage of the Bragg equation is the λ dependence, which precludes direct comparison between datasets taken using photons of different energy. This dependency can be removed by considering the scattering vector, $\mathbf{Q}$, of scattered photons and the geometric construction for this is shown in Figure 2.12. This formalism acts to transform the measured scattering data from angular space to reciprocal space. The transforms are given by

$$|\mathbf{Q}| = \begin{pmatrix} Q_{\mathrm{x}} \\ Q_{\mathrm{y}} \\ Q_{\mathrm{z}} \end{pmatrix} = \begin{pmatrix} \frac{4\pi}{\lambda}\sin\left(\frac{\omega}{2}\right)\sin\left(\theta - \frac{\omega}{2}\right) \\ 0 \\ \frac{4\pi}{\lambda}\sin\left(\frac{\omega}{2}\right)\cos\left(\theta - \frac{\omega}{2}\right) \end{pmatrix} \tag{2.22}$$

where the wavevector of the photon, $|\mathbf{k}|$, has been substituted by $\frac{2\pi}{\lambda}$, while θ and ω are the incident and scattering angles, respectively, as shown in Figure 2.12.

For the case of symmetric diffraction, where $\omega = 2\theta$, the above transforms simplify such that

$$|\mathbf{Q}| = Q_{\mathrm{z}} = \frac{4\pi}{\lambda}\sin\left(\frac{\omega}{2}\right) \tag{2.23}$$

In general, the use of the scattering vector is advantageous as reflections arising from a family of lattice planes are evenly spaced in Q and are multiples of one another related by n. Substitution of Equation 2.23 into Bragg's law (Equation 2.21) yields the relation

$$d_{hkl} = \frac{2\pi}{|\mathbf{Q}|} \tag{2.24}$$

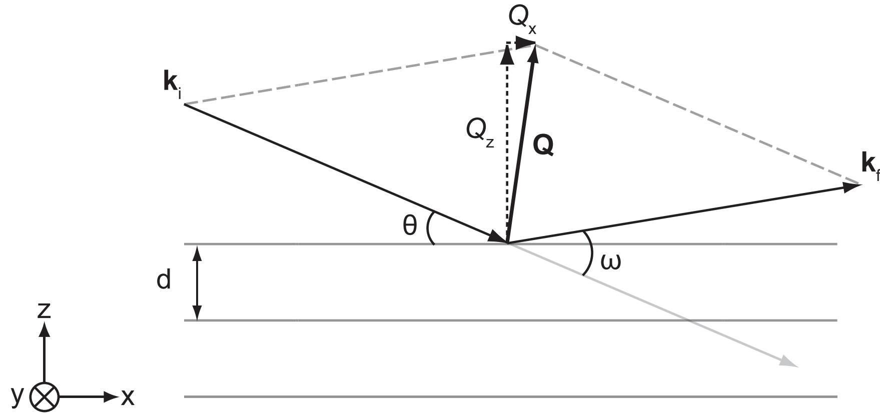

Figure 2.12: Geometric construction of the scattering vector, **Q**, in X-ray diffraction.

and so, in addition to being independent of the experimental set-up, the lattice parameter of a material can be determined directly.

Systematic extinctions and forbidden reflections

Within the kinematical approximation the intensity of a diffracted beam is governed by the structure factor [72]:

$$F_{hkl} = \sum_{J} f_n \; e^{2\pi \mathrm{i}(hu_n + kv_n + lw_n)} \tag{2.25}$$

where f_n is the atomic scattering factor, hkl are the Miller indices of the scattering planes and (u_n, v_n, w_n) are the fractional co-ordinates of the J atoms within the unit cell. Considering the body-centred cubic (bcc) structure, which has an atomic basis of (0,0,0) and $(\frac{1}{2},\frac{1}{2},\frac{1}{2})$, the scattering factor reduces to

$$F_{hkl} = e^{2\pi \mathrm{i}\cdot 0} + e^{2\pi \mathrm{i}\cdot \frac{1}{2}(h+k+l)} \tag{2.26a}$$

$$F_{hkl} = (1) + (-1)^{(h+k+l)} \tag{2.26b}$$

and so for values of $h + k + l$ that are odd there are no reflections, while for an even combination a reflection is allowed.

In comparison, the atomic basis for the zincblende structure consists of atom A at (0,0,0) and atom B at $(\frac{1}{4},\frac{1}{4},\frac{1}{4})$. Although the form of the structure factor is similar to that of the bcc case outlined above, the presence of two different elements requires the use of two values of f_n and so the resulting structure factor is:

$$F_{hkl} = f_A + f_B \left((-1)^{\frac{1}{2}(h+k+l)}\right) \tag{2.27}$$

where f_A and f_B are the atomic scattering factors for elements A and B, respectively. Consequently, hkl must consist of all even, or all odd, values for a reflection to be allowed while all other combinations of hkl are forbidden. Note that the differing values of f_A and f_B result in some forbidden reflections being allowed due to a small difference in their respective values.

2.4.3 Interpretation of X-ray diffraction data

Several types of dataset can be collected in XRD through a combination of sample and detector movement. Each of these provides different information about the sample ranging from film orientation and lattice parameters, to the in-plane behaviour of the film. The following section outlines the parameters that can be obtained from the various types of scans performed in XRD, making use of high resolution XRD of NiSb as an example. Further information on NiSb thin films can be found in References [34, 68]. The scans presented in this thesis were obtained from the X22C beamline at the National Synchrotron Light Source (NSLS), Brookhaven National Laboratory. Samples were aligned on the beamline in a two-axis setup with all subsequent scans performed in a triple-axis mode, with the third axis defined using a Ge analyser crystal. The incident energy was selected using a Si(111) monochromator and the incident beam was slit defined prior to the sample.

2.4.3.1 Coupled ω-2θ scans

Coupled movement between the sample and detector, such that $\Delta\omega = \frac{\theta}{2}$, results in symmetric diffraction conditions with $|\mathbf{Q}|$ probing the planes parallel to the

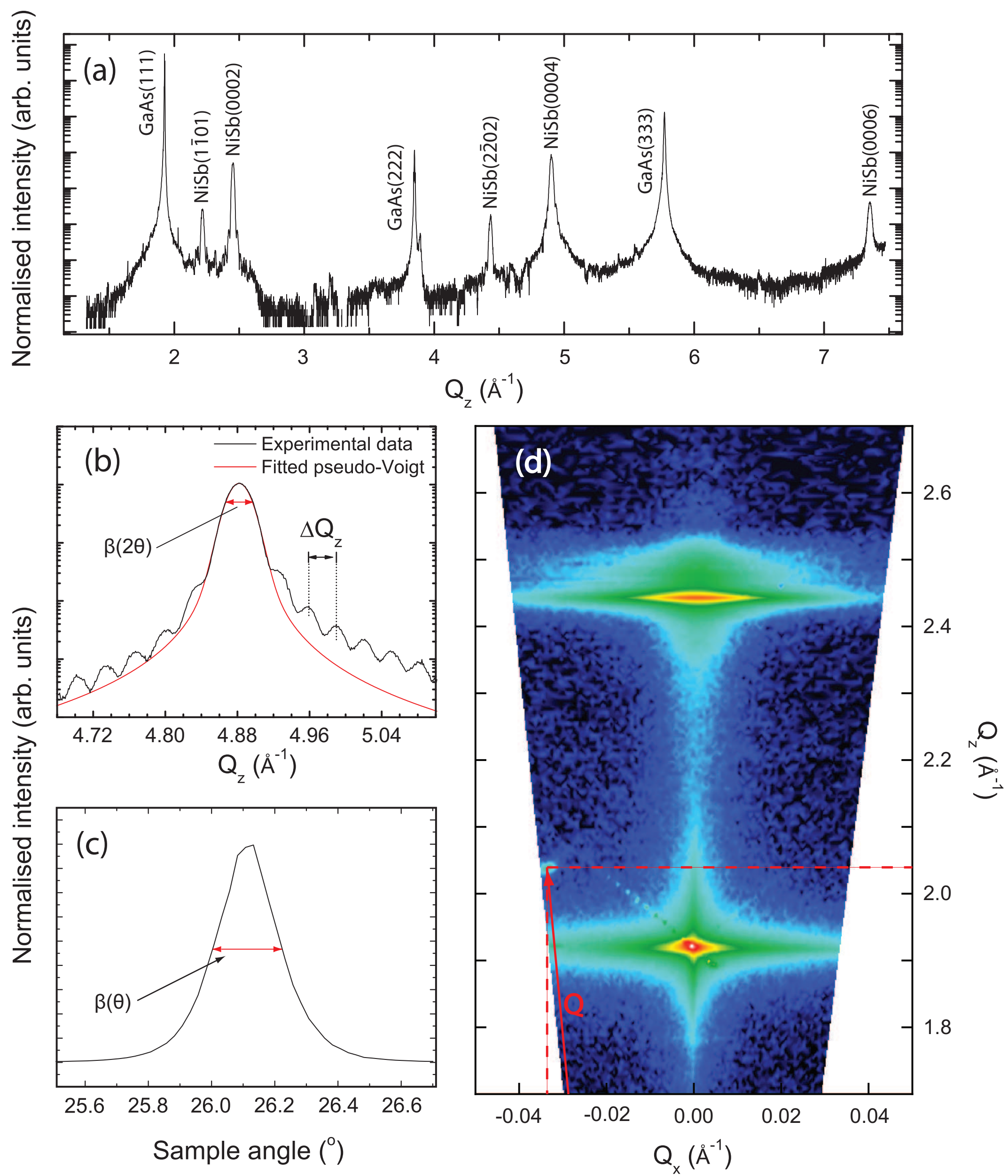

Figure 2.13: NiSb example diffraction data showing (a) symmetric ω-2θ data, (b) a close in view of the NiSb(0004) reflection, (c) rocking (ω) curve of the NiSb(0004) reflection and (d) a reciprocal space map around the GaAs(111) and NiSb(0002) reflections.

surface normal. This yields information on the growth orientation of a thin film, in addition to enabling determination of the out-of-plane lattice parameters. An example of a long ω-2θ scan, converted to Q_z, is shown in Figure 2.13(a), peaks arising from the substrate and the NiSb thin film have been labelled appropriately. Note that the intensity of the scans has been normalised to the incident X-ray flux.

A close up of the NiSb(0002) peak is shown in panel (b), the red line indicates a pseudo-Voigt function fitted to the data. From this fit both the centre and FWHM of the peak, denoted by $\beta(2\theta)$, can be obtained. Also of interest is the presence of thickness fringes which arise due to interference between beams scattered from the upper (surface) and lower (substrate/thin film) interfaces in the sample. Bragg's law is equally applicable here, although d is now equal to the distance between the interfaces. Equation 2.24 can then be used to determine the total layer thickness. The value of ΔQ for the sample shown in Figure 2.13 is 0.015(1) Å^{-1} giving a layer thickness of 41.8(3) nm. Additionally, the roughness of the interfaces plays a crucial role in determining the presence of these thickness fringes. High levels of roughness act to randomise the path difference between the interfaces and so reduce the intensity of the observed fringes. It can also be seen that as the thickness increases the value of ΔQ decreases and so for thick samples it can be difficult to adequately determine the sample thickness.

Lattice parameter determination

The relationship between $|\mathbf{Q}|$ and d_{hkl} can be used to determine the lattice parameters of a material. For hexagonal materials, such as NiSb and MnSb, the relation between the lattice spacing [73], d_{hkl}, and the lattice parameter, a, is

$$\frac{1}{d_{hkl}^2} = \frac{4}{3}\left(\frac{h^2 + hk + k^2}{a^2}\right) + \frac{l^2}{c^2}. \tag{2.28}$$

Substituting Equation 2.28 into Equation 2.24 leads to

$$|\mathbf{Q}|^2 = \frac{4\pi^2}{a^2}\left[\left(h^2 + hk + k^2\right) + \left(\frac{l^2}{(c/a)^2}\right)\right] \tag{2.29}$$

where a and c are the material lattice parameters parallel and perpendicular to the basal plane, and c/a is the ratio of these parameters. For reflections that contain no h or k components (the 000l planes) then the c lattice parameter can be simply deduced. It is then possible to use, for (000l) orientated films, a combination of ω-2θ scans and in-plane measurements to first obtain the c parameter and then refine a. Alternatively, the c/a ratio may be used as a fitting parameter in a minimisation routine to simultaneously obtain values for a and c.

The lattice parameters presented in this thesis have been determined using a χ^2 minimisation method under the assumption of a height offset resulting in a 2θ offset. This offset is relative to the incident beam and results in an error in d with the following form [72] [72]

$$\frac{\Delta d}{d} = -\frac{D\cos^2\theta}{R\sin\theta} \tag{2.30}$$

where d is the interplanar spacing, D is the displacement of the specimen along the diffraction-plane normal and R is the radius of the diffractometer. In order to offset the measured 2θ values, conversion from a planar spacing to angle is required. Rearranging and differentiating Bragg's law (Equation 2.21) yields

$$\frac{\Delta d}{d} = -2\frac{\cos\theta\Delta\theta}{\sin\theta} \tag{2.31}$$

where $\Delta\theta$ and Δd are the change in Bragg angle and interplanar spacings, respectively. Substitution of Equation 2.31 into the left hand side of Equation 2.30, and simplifying, gives the functional form of the angular offset

$$\Delta\theta \propto \cos\theta \tag{2.32}$$

Consequently, an angular offset of the form $2\theta - C\cos(\frac{2\theta}{2})$ has been used, where C is a fitting parameter accounting for a constant 2θ offset due to the alignment of the Ge analyser (which is of the order of $5\times10^{-3\circ}$) as well as the height offset. The uncertainty in the lattice parameter was found by determining the extent of the $\Delta\chi^2 = 1$ contour and further information on this method can be found in Reference [74].

Although the NiSb data presented in Figure 2.13(b) has been fitted using a pseudo-Voigt function, the MnSb data presented in this thesis was fitted using a Pearson VII function. The Pearson VII function better represents the MnSb data obtained from X22C and has the additional benefit that the width of the function represents the true FWHM of the peak.

Scherrer and Williamson-Hall analysis (grain and crystallite size)

For a perfect crystal, diffracted beams should emerge exactly at the Bragg angle and the resulting pattern would consist of a series of delta functions. However, both the finite size of the sample and the presence of defects as well as the instrumental resolution cause the observed peaks to have a measurable width.

For the case of a perfectly parallel, monochromatic, beam the broadening of the diffraction peak due to a finite sample size, $\beta(2\theta)$, is governed by the Scherrer equation

$$\beta(2\theta) = \frac{\kappa\lambda}{\tau\cos\theta_{\mathrm{B}}} \tag{2.33}$$

where $\beta(2\theta)$ is the FWHM of the peak (equivalent to the broadening), κ is a constant, λ is the wavelength of the incident X-rays and τ is the particle size. Strictly, τ is the average size of the scattering domains in the sample (denoted as the crystallite size throughout this thesis) and is typically smaller than the total thickness of the sample. The constant, κ, shown in Equation 2.33 is known as the shape factor and depends upon the assumed shape of the crystallites and the functional form of the diffraction peak. Throughout this thesis the value of the shape factor has been fixed at 0.88 to represent a Lorentzian lineshape, this is valid for Pearson VII functions with shape factors (η) that are close to 1. During fitting η is kept as close to 1 as the fit will allow.

In addition to the finite-size broadening discussed above, the presence of a strain dispersion in the sample also results in broadening. If an applied strain is uniform over a large distance, typically greater than the diffracting domain size, then it is termed a macrostrain. If the applied strain is, instead, non-uniform it acts over smaller length scales, typically less than the diffraction domain size, and is then termed a microstrain.

Strains over both length scales can be present in the same sample and result in asymmetric peaks, although the effects from each are readily separated. A macrostrain acts to change the lattice spacing of an entire crystallite and consequently any resulting diffraction peaks are observed to rigidly move position. Microstrains result in the formation of multiple d spacings and so a range of spacings, Δd, will be observed. The Bragg angle for each of these spacings is then only slightly different from the strain-free spacing and so a broadening of the diffraction peak is observed.

The contribution of Δd to the FWHM of the diffracted peak can be obtained by differentiating Bragg's law (Equation 2.21)

$$\beta(2\theta) = 2\frac{\Delta d}{d}\tan\theta_{\mathrm{B}}. \tag{2.34}$$

Typically, peak broadening arises due to both finite-size effects and strain. The total broadening, $\beta(2\theta)$, will then be the sum of Equations 2.33 and 2.34:

$$\beta(2\theta)\cos\theta = \frac{K\lambda}{\tau} + 2\frac{\Delta d}{d}\sin\theta \tag{2.35}$$

where $\frac{\Delta d}{d}$ is the fractional change in the lattice parameter (d, although in the case of symmetric diffraction from NiSb(0001) or MnSb(0001) films the ratio $\frac{\Delta c}{c}$ is more useful) and is known as the strain dispersion. As this accounts for both tensile and compressive strains, the maximum strain change in the lattice parameter is half $\frac{\Delta d}{d}$.

Of interest is the angular dependence of the strain component of the broadening, which is absent in the finite-size contribution. Consequently the strain and size components of the broadening can be separated by plotting $\beta(2\theta)$ $\cos\theta$ against $\sin\theta$. In this case the strain dispersion is obtained from the gradient while the intercept yields the grain size (distinct from the Scherrer *crystallite* size). These values, and their associated uncertainties, were determined using the least-squares method outlined above.

2.4.3.2 Rocking curves (ω scans)

Real crystals exhibit defects and non-uniform crystal structures which alter the in-plane characteristics of a film. This in-plane structure can be investigated using 'rocking

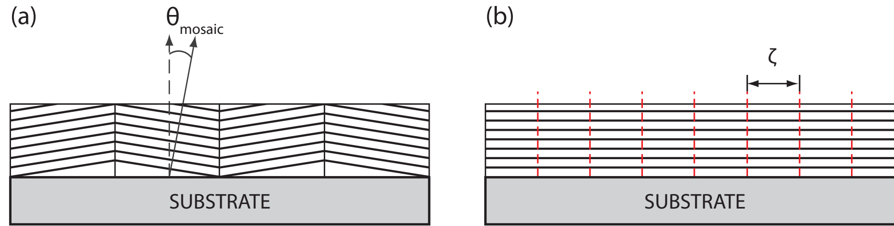

Figure 2.14: Illustrative diagrams showing (a) a mosaic dominated crystal structure highlighting the tilted mosaic crystallites and (b) a correlation length dominated structure. In panel (a) the average angular deviation of the overlayer from the substrate surface normal is termed θ_{mosaic}. In panel (b) the characteristic periodic lateral defect lengthscale is denoted by ζ.

curves', whereby the position of the detector is fixed and the sample is 'rocked' in ω. If the sample consists of small crystallites which are tilted with respect to the average surface normal of the film then it is said to have a *mosaic* dominated structure. A sample with periodic lateral defects is said to have a *correlation length* dominated structure. Figure 2.14 shows simple examples of these structures. The mosaic dominated case is presented in panel (a) and the relative average angular deviation, or tilt, of the mosaic crystallites has been denoted by θ_{mosaic}. A correlation length dominated structure is shown in panel (b) and the periodic defect lengthscale is represented by ζ.

A plot of the FWHM of the rocking curve against diffraction angle, often given in terms of increasing Bragg reflection, in angular and reciprocal space can be used to determine if the in-plane structure is dominated by either of these structures. A film with a correlation length dominated growth mode would be expected to behave as a series of well-aligned crystallites (with respect to the substrate surface normal) and so the rocking curve width will not vary in Q_{x}. Consequently, as Q_{x} exhibits a Bragg angle (2θ) dependency, as shown in Equation 2.22, the rocking curve width will remain constant in Q but necessarily vary in angle. A mosaic dominated film structure consists of grains that have a fixed angular distribution about the surface normal direction that is independent of the scattering angle and so constant angle behaviour, with a corresponding variation in Q, will be observed. A typical NiSb(0004) rocking curve is shown in Figure 2.13(c) and the FWHM of the curve is denoted by $\beta(\theta)$, note that NiSb films are observed to

be constant in θ and so are mosaic dominated.

The presence of a purely mosaic structure is indicative of Frank van der Merwe growth (layer-by-layer), while a correlation length dominated structure indicates Volmer-Weber growth (islands). A mixture of both structure types thus indicates that growth proceeds via the Stranski-Krastanov mode. As explained in Section 2.1 it should be noted that these modes are idealised and that the association here is equally as idealised.

2.4.3.3 Reciprocal space maps

Finally, it is possible to construct two-dimensional reciprocal space maps (RSMs) by collecting a series of rocking curves or coupled scans. These RSMs can probe either symmetric or asymmetric diffraction conditions depending upon whether the Bragg reflection under study is symmetric or asymmetric. In order to construct a symmetric RSM, which probes the lattice planes parallel to the surface of the sample, a series of rocking curves, each offset from one another by a value of $\Delta\omega$, are collected at a fixed detector angle. Using these scans, and the transforms presented in Equation 2.22, an RSM can be constructed in Q space from the angular values measured on the diffractometer. An asymmetric reciprocal space map is more complex as it probes reciprocal space around a series of planes that are not aligned parallel to the surface normal. In this case, a series of coupled ω-2θ scans are collected with an ω offset, which acts to bring the asymmetric reflection into the diffraction conditions. As with the symmetric RSM case the Q transforms can then be used to generate a map in Q space.

Figure 2.13(d) shows a typical symmetric RSM about the NiSb(0002) reflections. It is evident that the in-plane and out-of-plane structure shown in the ω-2θ and rocking curves is also visible here. There are several additional pieces of information that can be obtained from RSMs that are not evident from typical symmetric scans. The first is the presence of powder diffraction features, which appear as bands of intensity at fixed Q_z which are featureless in Q_x. The NiSb($1\bar{1}01$) crystallites observed in panel (a) have this structure when mapped [34], although it should be noted that in the sample used to

generate panel (d) no $(1\bar{1}01)$ crystallites were found to exist. Secondly, it is possible to determine both the in- and out-of-plane lattice parameters by calculating the scattering vector, $\mathbf{Q}$, for a particular reflection. An example of this is shown in panel (d), where the red solid line indicates the scattering vector and the dashed red lines are the Q_x and Q_z values. From this it can be seen that the scattering vector, and consequently the lattice d spacing, can be calculated using the simple relation $\mathbf{Q}^2 = {Q_x}^2 + {Q_z}^2$ and, in conjunction with direct out-of-plane measurements, the in-plane lattice parameter(s) can be determined.

2.5 Bulk magnetometry

The bulk magnetometry measurements presented in Chapter 5 were obtained using a superconducting quantum interference device (SQUID) magnetometer. The SQUID magnetometer consists of a superconducting ring containing two 'weak links', known as Josephson junctions, which are both made from thin insulating layers. The sample is inserted into the centre of the ring and changes in the sample magnetisation, either due to the presence of an applied field or due to varying sample temperature, lead to changes in the resistances of the Josephson junctions. These changes in resistance can then be used to determine the magnetisation of the sample.

There are two types of magnetometry measurements presented in this thesis: M-H and M-T. The first type, M-H, measures the change in magnetisation of the sample with varying applied field and are commonly known as hysteresis loops. Several values can be extracted from these loops: the saturation field, which is the applied field value at which the magnetic moment per atom (and hence the total magnetisation) reaches a maximum; the saturation magnetisation (M_s); and the coercive field, which is the field at which point the loop changes sign. The second type of measurement, M-T, measures the change in magnetisation as a function of sample temperature and from the observed behaviour the Curie temperature, T_C, can be inferred.

Chapter 3

Manganese on III-V semiconductor surfaces

3.1 Introduction

In the creation of spintronic devices based on magnetoelectrical effects, layered combinations of ferromagnetic and semiconducting materials are of significant interest. Understanding the behaviour of the interfaces between these layers is crucial for high-efficiency spin injection. The effects of reactivity and diffusion may act to reduce the spin polarisation of an injected current through the introduction of defects. For example, the deposition of Fe on GaAs leads to the formation of $Fe_3Ga_{2-x}As_x$ layers with magnetisations lower than that of bulk Fe [16]. Studies performed using DFT [75] on the effect of the atomic ordering of these layers reveals the introduction of minority spin states at the Fermi level. The presence of minority states, in conjunction with the reduced magnetisation of the layer, reduce the polarisation of an injected current and so limit the effectiveness of devices constructed from these materials.

The presence of a reconstruction prior to growth additionally constitutes a change in the atomic structure of a surface and so could radically alter the resulting interface.

The behaviour of Fe/GaAs [76] shows a strong structural dependence on the initial GaAs reconstruction, while the properties of magnetic oxide layers strongly depend on the starting reconstruction of the MgO or Al_2O_3 substrates [77]. Thus the atomic ordering of the interface, and consequently the reconstruction of the substrate, strongly affects the properties of thin films. As an example, in the growth of MnSb/GaAs(111)B by pulsed laser deposition, a pre-layer of Mn improved the crystallinity of films hundreds of nm thick [78]. For MnSb layers on GaAs(001), layers grown on the (2×4) reconstruction exhibited magnetic anisotropy in the sample plane, while layers grown on the (4×6) reconstruction were magnetically isotropic (when grown at $T_{sub} = 50$ °C) [79].

This chapter presents studies of the interaction of monolayer quantities of Mn with a range of reconstructed InSb and GaAs surfaces. The effects of Mn on the surface morphology were investigated using a combination of RHEED, STM and ex-situ AFM. On InSb, no Mn-InSb surface alloys or reconstructions form, although Mn removes Sb from the surface reconstruction and so results in the formation of islands. In contrast, a new reconstruction forms on GaAs with a (2×2) periodicity. The behaviour of these surfaces is then discussed in terms of bulk thermodynamic quantities and the presence, or absence, of surface reconstructions.

3.2 Experimental Details

The RHEED and STM experiments detailed in this chapter have been performed using two UHV chambers. The Warwick MBE chamber, described previously in Chapter 2, was used for the RHEED study of the Ga-rich GaAs(001)-(4×6) surface in addition to the RHEED and STM studies of the reconstructed InSb surfaces. This chamber is referred to as the Warwick MBE chamber. A second chamber, located at the National Centre for III-V materials (University of Sheffield), was used to study the As-rich GaAs reconstructions. The Sheffield chamber consists of a conventional III-V growth chamber attached to a UHV STM and full details of the system can be found in Reference [80].

In the Warwick MBE, InSb and GaAs substrates were mounted onto stainless

steel sample plates using an In/Ga/Sn eutectic and indium glue. Surface debris was then removed by chemical degreasing using an acetone, isopropanol and water wash cycle followed by drying with nitrogen. Samples were loaded into the vacuum chamber and prepared by ion bombardment and annealing (IBA) cycles. InSb substrates were ion bombarded for eight minutes followed by a one-hour anneal at 300 °C, while GaAs substrates were ion bombarded for ten minutes followed by a one-hour anneal at 480 °C. Buffer layer growth under Sb (In) rich conditions, or exposure to the relevant elemental fluxes at 300 °C, was used to provide the required surface reconstructions on InSb. Here In-rich growth is defined as where the ratio of Sb flux to In flux is less than one ($J_{\mathrm{Sb/In}} < 1$), while Sb-rich growth occurs when $J_{\mathrm{Sb/In}} > 1$. No difference in the quality of the RHEED patterns was observed between the as-grown and as-cleaned samples, and so no distinction has been made between the two preparation methods in this chapter. GaAs substrates prepared in the Warwick MBE exhibit only the Ga-rich reconstructions due to the tendency of IBA cycles to preferentially remove the Group V element. The absence of an As effusion cell meant that the As-rich reconstructions were inaccessible and precluded the growth of buffer layers. The sharpness of the streaks observed in the RHEED following cleaning, in addition to the presence of intense Kikuchi features, suggests that the as-cleaned samples are of sufficient quality for deposition. After RHEED studies, samples were removed from the Warwick MBE and imaged using AFM. It should be noted that no special precautions were taken to prevent surface oxidation during transport for imaging.

In the Sheffield MBE samples were mounted in a custom holder, with sample heating performed using a ceramic heating plate, and loaded into the vacuum. Cleaning was then performed via thermal oxide desorption under an As_4 flux before growth of a 500 nm buffer layer using As-rich conditions. Samples were then cooled under decreasing As_4 flux so as to stabilise the desired surface before transfer to the STM.

Following preparation of the desired surface reconstruction, Mn was deposited at fixed substrate temperatures of 280 °C for InSb and 300 °C for GaAs. The deposition

rate was fixed at 0.005 ML s^{-1} of Mn, where 1 ML is defined as 6.25×10^{14} cm^{-2} and is equal to the surface atom density of GaAs(001). Samples were observed using RHEED in order to determine the transition coverages, and at these coverage values a 'burst' deposition methodology was employed. This involved the use of 4 s bursts of Mn, achieved by opening the Mn cell shutter for the required time, at a fixed substrate temperature of 280 °C (InSb) or 300 °C (GaAs), followed by growth interrupts of approximately 10 minutes, in order to observe any RHEED pattern changes that occur. At the substrate temperatures used, any changes in the reconstructions due to annealing are slow, for example via Group V desorption, and so any observed changes can be attributed solely to the deposition of Mn. In both the Warwick and Sheffield chambers, deposition was halted to allow for transfer to the STM for imaging. All STM images are shown in filled states at constant current. The tunnelling conditions used were: sample bias -3 to -4 V, with tunnel currents of 0.2 to 1 nA.

3.3 Results

3.3.1 InSb

The effect of manganese on three InSb crystal faces was investigated in the Warwick MBE, the orientations studied were (001), (111)A and (111)B. Each of these surfaces exhibits a range of reconstructions depending on the value of $J_{Sb/In}$ and substrate temperature, the composition of these reconstructions is shown in Table 3.1.

The In-rich c(8×2) exhibits a complex structure incorporating both surface and sub-surface dimers [42]. The c(4×4) is the most Sb-rich reconstruction and consists of a missing dimer along the [110] direction. This results in three Sb dimers on top of a bulk-like Sb layer. The a(1×3) reconstruction is a disordered analogue to the c(4×4), with a reduction in surface Sb content leading to the breaking of surface dimers. With the exception of the InSb(001)-a(1×3), all of the reconstructions listed in Table 3.1 were used as starting surfaces prior to Mn deposition.

Table 3.1: Reconstructions of InSb surfaces. The ideal elemental content is given in ML for the top layer of the reconstruction. Sb rich reconstructions are denoted by an asterisk ($*$).

	Surface	Reconstruction	In content (ML)	Sb content (ML)	Ref.
InSb	(001)	c(8×2)	0.84	-	[42]
		a(1×3)$*$	-	1.66	[81]
		c(4×4)$*$	-	1.75	[82]
	(111)A	(2×2)	0.75	-	[83]
		$(2\sqrt{3}\times 2\sqrt{3})$R30°$*$	0.50 In	0.25	[84]
	(111)B	(3×3)	0.44	0.22	[85]
		(2×2)$*$	-	1.75	[83]

On the In-rich InSb(001)-c(8×2), InSb(111)A-(2×2) and InSb(111)B-(3×3) surfaces, the deposition of Mn resulted in no changes to the periodicity up to coverages (θ_{Mn}) of 1 ML. At higher coverages the intensity of the integer and fractional streaks decreased, characteristic of roughening or disorder on the surface. Some weak transmission features were also observed and are believed to be due to the formation of 3D islands on the surface.

The Sb-rich surfaces of InSb exhibited different behaviour, characterised by a change of periodicity as observed in the RHEED. These changes took place simultaneously with Mn deposition and occurred at coverages that were consistent between samples. The RHEED patterns observed during deposition for the (001), (111)A and (111)B surfaces are shown in Figures 3.1, 3.2 and 3.3, respectively. The (001) surface exhibited two reconstruction changes. The first, at $\theta_{\mathrm{Mn}} = 0.1$ ML, resulted in the initially c(4×4) changing to a less intense a(1×3). This pattern persisted up to a coverage of $\theta_{\mathrm{Mn}} = 0.35$ ML, above which a second transition, to a slightly spotty c(8×2) pattern, was observed. The transmission features arising from these surfaces were stronger in intensity than those seen on the In-rich surfaces. On the (111)A substrate a single transition was observed to occur at $\theta_{\mathrm{Mn}} = 0.05$ ML, where the Sb-rich $(2\sqrt{3} \times 2\sqrt{3})$R30° changed to a (2×2). On (111)B, the initially (2×2) surface transformed into a (3×3) at $\theta_{\mathrm{Mn}} = 0.1$ ML. On all orientations, a mixture of initial and final reconstructions were observed at the transition coverage.

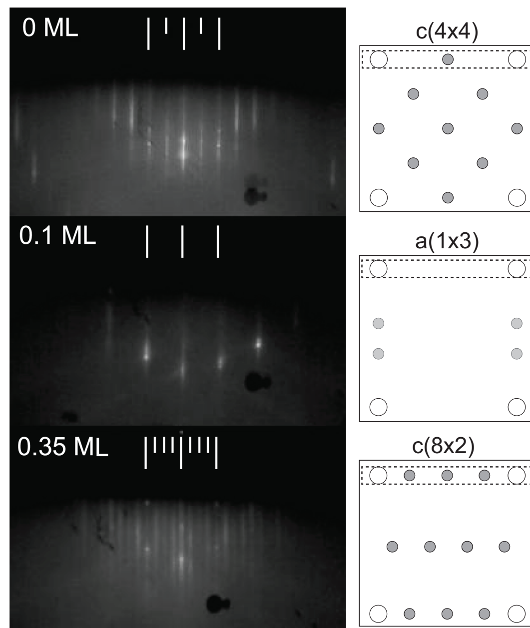

Figure 3.1: RHEED patterns observed along the $[1\bar{1}0]$ direction on the InSb(001) surface. The long (short) white lines indicate integer (fractional) streaks. Two reconstruction transitions are observed. From c(4×4) to a(1×3) at 0.1 ML and a(1×3) to c(8×2) at 0.35 ML. Also shown are the reciprocal space patterns giving rise to the diffraction features observed in the images. The dashed box highlights the crystallographic direction observed while the white (grey) circles correspond to integer (fractional) features.

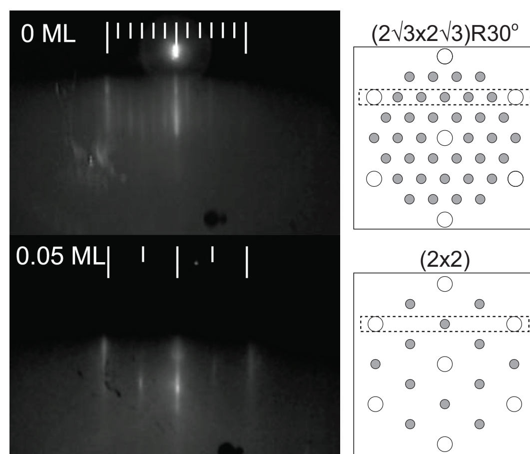

Figure 3.2: RHEED patterns observed along the $[\bar{1}\bar{1}2]$ direction on the InSb(111)A surface. The long (short) white lines indicate integer (fractional) streaks. A single reconstruction transition is observed from $(2\sqrt{3}\times2\sqrt{3})$R30° to ($2\times2$) at 0.05 ML. The explanatory symbols are as in Figure 3.1.

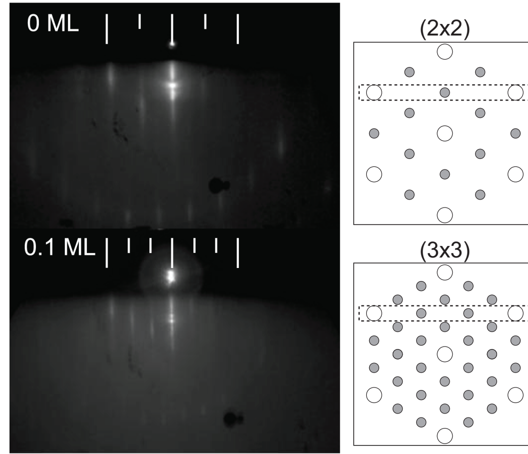

Figure 3.3: RHEED patterns observed along the $[\bar{1}\bar{1}2]$ direction on the InSb(111)B surface. The long (short) white lines indicate integer (fractional) streaks. A single reconstruction transition is observed from (2×2) to (3×3) at 0.1 ML. The explanatory symbols are as in Figure 3.1.

Table 3.2: Stoichiometry changes observed on the Sb terminated surfaces of InSb. ΔSb is defined as the change in Sb content during a transition, while ΔIn is the corresponding change of In content. The transition points correspond to those shown in Figure 3.4.

Transition Label	Surface	Transition	ΔSb (ML)	ΔIn (ML)
A	InSb(001)	c(4×4) → a(1×3)	-0.09	-0.16
B	InSb(111)A	$(2\sqrt{3}\times2\sqrt{3})$R30° → (2×2)	-0.25	+0.25
C	InSb(111)B	(2×2) → (3×3)	-0.53	+0.44
D	InSb(001)	c(4×4) → c(8×2)	-1.75	0

The relationship between Mn coverage (θ_{Mn}) and the change in Sb content (Δ_{Sb}) is shown in Figure 3.4. Points A, B, C and D correspond to the reconstruction transitions outlined in Table 3.2, these values are derived from the surface layer contents given in Table 3.1. It is worth noting that Δ_{Sb} is not precisely defined as real surface structures are not ideally stoichiometric. For example, the c(4×4) structure can include heterodimers which reduce the Sb content [86, 87] and increase In content, while the a(1×3) structure can accommodate a large stoichiometry range [81]. Although the uncertainty in Δ_{Sb} is large, a clear linear relationship between θ_{Mn} and Δ_{Sb} can be seen.

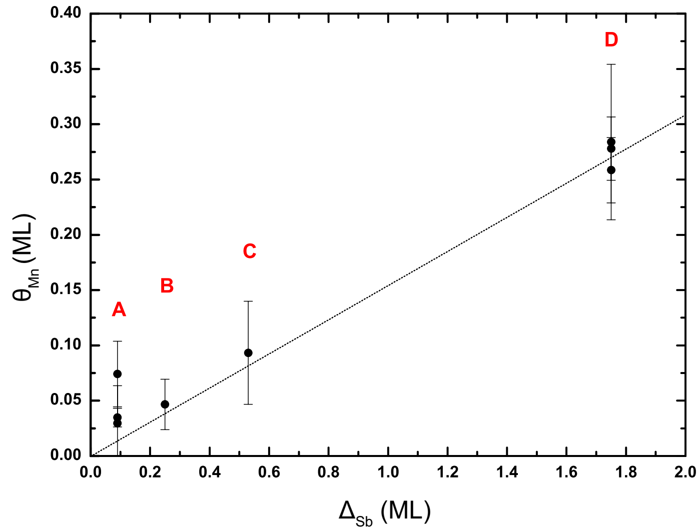

Figure 3.4: Mn coverage (θ_{Mn}) required to change reconstruction for the InSb surfaces as a function of Sb content (Δ_{Sb}). The transitions A, B, C and D are as labelled in Table 3.2.

At higher Mn coverages the presence of faint transmission spots in the RHEED is observed, indicative of the formation of 3D islands on the surface. To this end, samples of InSb(001) were investigated using in-situ STM and, where imaging was difficult due to the formation of larger islands, by ex-situ AFM. Figure 3.5 shows the morphology of the Sb-rich c(4×4) and In-rich c(8×2) surfaces. Panels (a) and (b) show STM for the clean c(8×2) and c(4×4) surfaces, respectively. The c(8×2) surface features squarer terraces with a high step density, while the c(4×4) surface exhibits meandering terraces. Of interest is the reappearance of the anisotropic terraces following 0.4 ML of Mn on the c(4×4) surface, shown in panel (c). The morphology of this surface is similar to that observed on the c(8×2) and is in agreement with the observed RHEED pattern.

Typical AFM images of the c(4×4) and c(8×2) surfaces following 1.0 ML of Mn are shown in panels (d) and (e), respectively. On the Sb-rich surface, panel (d), an increased density of irregularly shaped islands with heights of approximately 25 nm and basal diameters of between 150 and 300 nm can be seen. An additional distribution of smaller islands is also present on the surface with heights varying between 2 and

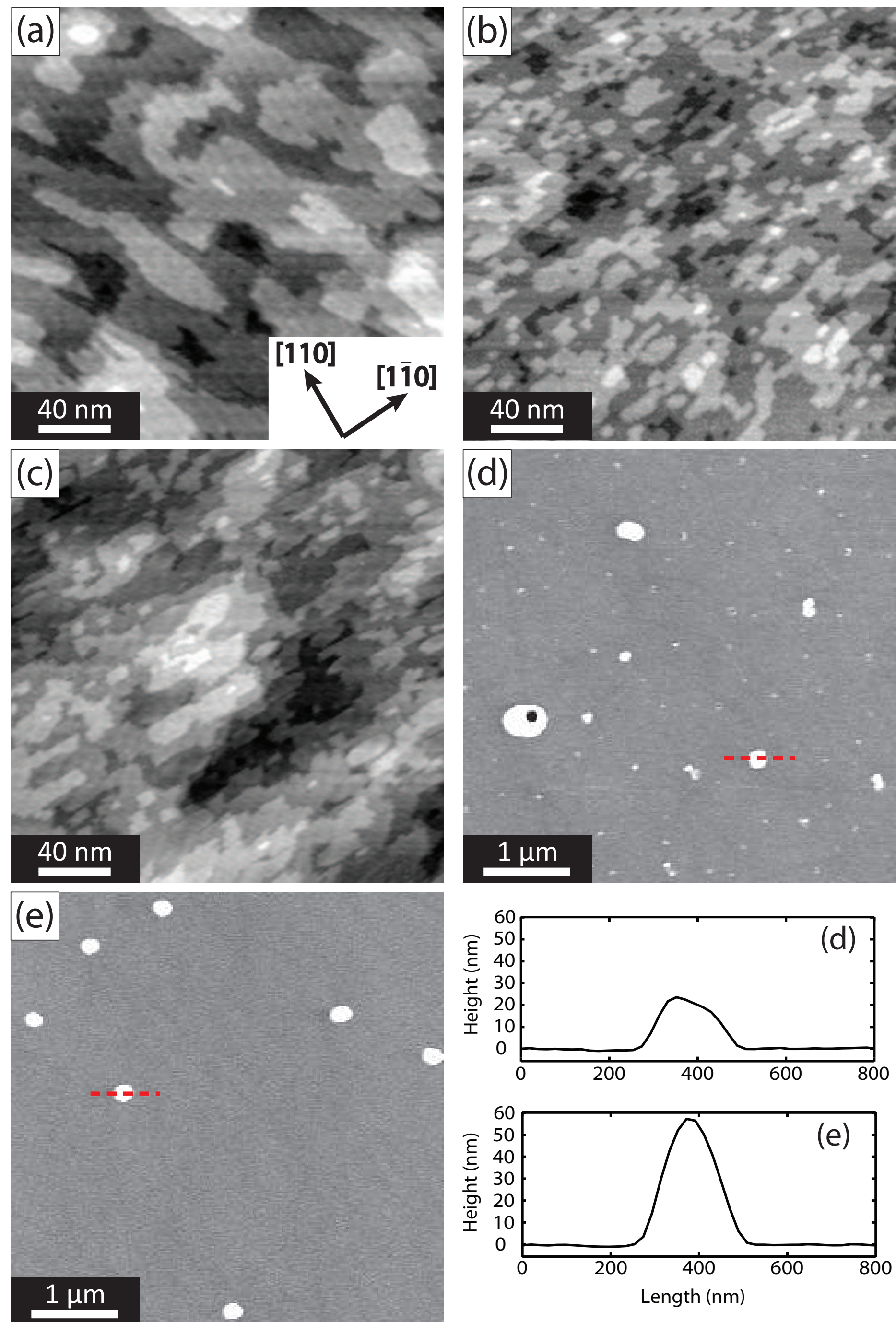

Figure 3.5: Surface morphology of InSb(001) surfaces before and after Mn deposition. Panels (a) and (b) show in-situ STM of the clean c(8×2) and c(4×4) surfaces, respectively. Panel (c) shows the c(4×4) following 0.4 ML of Mn. AFM images of the surface, and line profiles for typical large islands, following 1 ML of Mn are shown for the (d) c(4×4) and (e) c(8×2) surfaces.

Table 3.3: Reconstructions on the GaAs(001) surface. The ideal elemental content is given in ML for the top layer of the reconstruction and the As rich reconstructions are denoted by an asterisk ($*$).

	Surface	Reconstruction	Ga content (ML)	As content (ML)	Ref.
GaAs	(001)	(4×6)	1.00	0.08	[89]
		β2(2×4)$*$	-	0.75	[90]
		c(4×4)$*$	-	1.75	[86]

5 nm. The number density for the large islands is 2.6×10^7 cm^{-2} while for the smaller islands it is 3.0×10^8 cm^{-2}. The corresponding average nearest-neighbour distances are (640±30) nm and (35±2) nm. In contrast, on the In-rich surface the islands are more uniformly shaped and distributed with heights of approximately 60 nm and base diameters of 200 nm. For this surface the island number density is 3.2×10^7 cm^{-2} and the average nearest-neighbour distance is (1.45±0.07) μm. Line profiles across two islands are shown in the bottom right panel and correspond to the red dashed line shown on the equivalently labelled micrographs. It is evident that on the Sb-rich surface the islands are less uniform and have lower heights than those found on the In-rich surface.

From the obtained AFM images, the total island volume can readily be deduced and subsequently used to calculate a layer equivalent thickness (LET). The LET is defined as the thickness of a layer formed by equivalent layer-by-layer growth of the total volume of the islands. These volumes were obtained using the Asylum Research macros provided for the Igor Pro data analysis software and were then converted to monolayer values by scaling according to 1 ML of Mn producing a layer thickness equivalent of 0.28 nm [88]. The LET of the islands on the c(8×2) surface was found to be (1.10±0.06) ML, while on the c(4×4) surface it was found to be (1.92±0.2) ML.

3.3.2 GaAs

Three starting reconstructions on the GaAs(001) surface have also been investigated: (4×6), β2(2×4) and c(4×4). The stoichiometry of these reconstructions is outlined in Table 3.3 and, analogously to InSb, distinct Ga- and As-rich reconstructions

can be obtained though sample cleaning or epitaxial growth. The Ga-rich (4×6) reconstruction is observed following IBA cycles without access to As flux, as in the Warwick MBE chamber. This surface is thought to have a complex structure consisting of surface and sub-surface dimers [89]. The As-rich surfaces can be obtained through growth under As-rich conditions ($J_{\mathrm{As/Ga}}$ >1) or exposure to an As flux at elevated substrate temperature. The (2×4) reconstruction is typically seen during epitaxial growth and has several structural forms which differ in the extent of As dimerisation in the surface. Under the conditions used in this study the resulting structure is best described by the $\beta 2$ model [48]. The most As-rich surface is the c(4×4), which exhibits a similar structure to the c(4×4) observed on InSb. There are two phases reported on this surface [86]. The α phase consists of Ga-As heterodimers and the β phase consists of As-As dimers, both phases feature a common bulk-like As layer beneath them. Due to the preparation conditions used in this study the observed phase is the c(4×4)α.

Figure 3.6 shows RHEED patterns before and after deposition of 0.30 ML of Mn on the GaAs(001)-(4×6) surface. Panel (a) shows the pattern observed with the RHEED beam aligned along the $[1\bar{1}0]$ direction, while panel (b) shows the pattern with the electron beam along the [110] direction. For both (a) and (b) the upper image shows the clean substrate prior to deposition, highlighting the (4×6) structure, and the lower image shows the pattern following deposition of 0.30 ML of Mn. The elongated central fractional streak observed in the top panel of Figure 3.6(b) is the result of a (4×2) structure coexisting with the (4×6) structure, which results in the long $\frac{1}{2}$ / $\frac{3}{6}$ streak observed. At $\theta_{\mathrm{Mn}}{\sim}$0.24 ML the initially (4×6) RHEED pattern changes to include weak features of a (2×2) structure, with a complete change in reconstruction (no further coexistence of patterns) at $\theta_{\mathrm{Mn}} = 0.30$ ML. At coverages beyond this value, the pattern begins to degrade and incommensurate transmission diffraction is observed.

The morphology of the GaAs(001)-(4×6) surface following Mn deposition ($\theta_{\mathrm{Mn}} \sim$ 1.35 ML) was investigated using AFM and is presented in Figure 3.7. At larger scan sizes, (5 μm × 5 μm), the surface is mostly flat with a low density of 3D islands present.

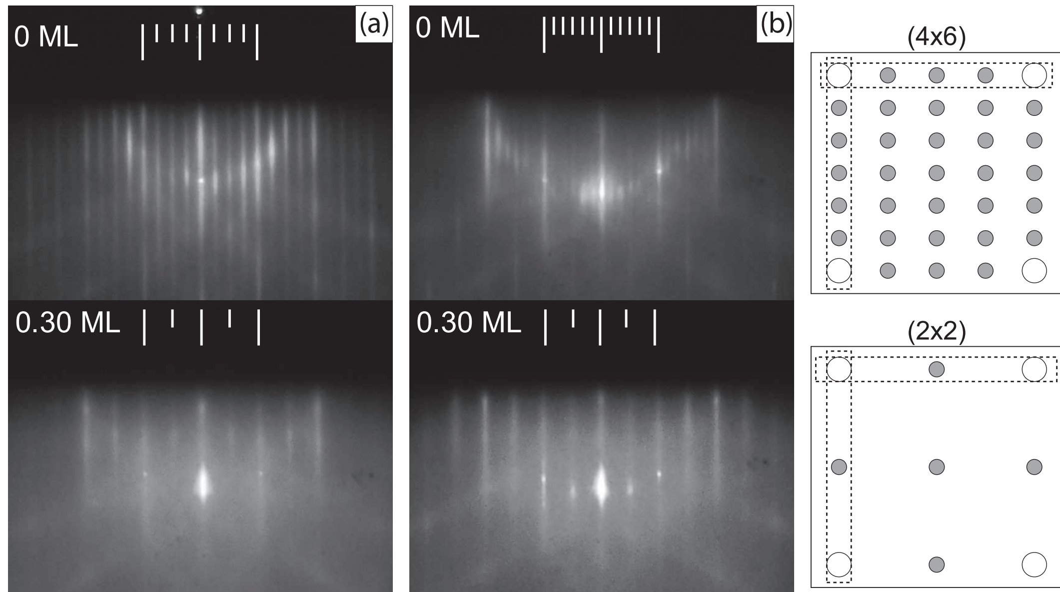

Figure 3.6: RHEED pattern observed along the (a) [1$\bar{1}$0] and (b) [110] of the GaAs(001) surface. The long (short) white lines indicate integer (fractional) streaks. A single reconstruction change is observed from (4×6) to (2×2) at 0.30 ML. Also shown are the reciprocal space patterns giving rise to the diffraction features shown. The dashed boxes highlight both of the crystallographic directions observed, the white (grey) circles correspond to integer (fractional) features.

At smaller scan sizes, (1 μm × 1 μm), the presence of a second island size distribution becomes apparent, these smaller islands are approximately 2 nm in height and 25 nm in diameter. The calculated LET of these islands corresponds to (0.82±0.16) ML of Mn. Figure 3.7(c) is a section profile corresponding to the black line shown in panel (b) and illustrates the general shape of the islands. It should be noted that the integration of island volumes on this surface is less reliable due to the difficulty in masking the islands to avoid substrate roughness contributions.

The As-rich (2×4) and c(4×4) surfaces were studied using STM and the images obtained are shown in Figures 3.8 and 3.9, respectively. Figure 3.8(a) shows the clean (2×4) surface and from this image the As dimer rows, which are orientated along the [1$\bar{1}$0] direction, can be seen. Following deposition of 0.8 ML of Mn, Figure 3.8(b), the original (2×4) structure has been disrupted and a co-existing (2×n) structure develops.

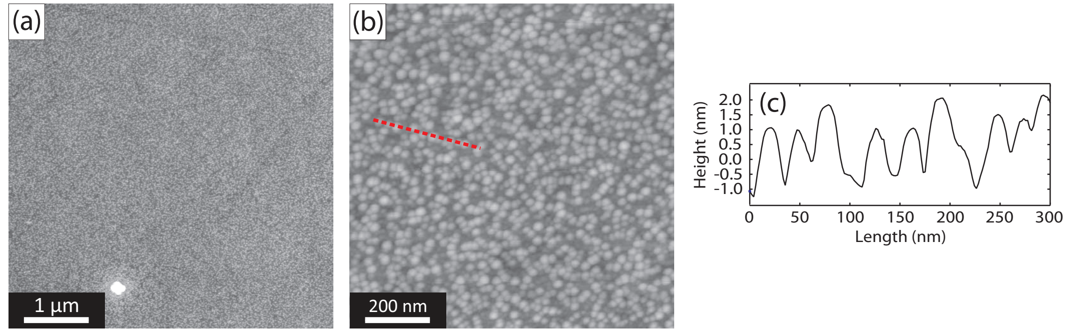

Figure 3.7: Surface morphology from AFM of GaAs(001)-(4x6) substrate following Mn deposition with scan sizes of (a) 5 μm × 5 μm and (b) 1 μm × 1 μm. The section profile shown in panel (c) corresponds to the line profile shown on image (b).

With increasing θ_{Mn} (1.2 ML), Figure 3.8(c), the ordering of the (2×n) improves and rod-like features, aligned along the [110] direction, form on the surface. A similar effect is observed during the growth of InAs quantum dots on GaAs under As-deficient conditions [91] and is attributed to the formation of Group III rich reconstruction domains. Finally, at high coverages of Mn (1.8 ML in Figure 3.8(d) and 2.4 ML in Figure 3.8(e)) the density and size of the islands increases. The height of the 3D islands is approximately 2 nm at the highest coverage $\theta_{\text{Mn}} = 2.4$ ML, with lateral extensions of greater than 40 nm.

The c(4×4) surface follows the same general trends as those seen on the (2×4). STM of the clean surface is shown in Figure 3.9(a), with the characteristic brickwork pattern of surface dimers clearly visible. At $\theta_{\text{Mn}} = 0.8$ ML, Figure 3.9(b), the (2×n) periodicity appears, although it is more disordered than for the equivalent Mn coverage on the (2×4) surface. At $\theta_{\text{Mn}} = 1.2$ ML, Figure 3.9(c), the surface island density has increased in addition to a greater number of rods visible on the surface. Finally, at $\theta_{\text{Mn}} = 1.8$ ML (Figure 3.9(d)), the surface has degraded substantially and features a large number of irregularly shaped islands. The size of the islands ranges between 1.5 and 2 nm at $\theta_{\text{Mn}} = 0.8$ ML, to between 2.5 and 4 nm at $\theta_{\text{Mn}} = 1.2$ ML. The behaviour of the islands and rod features on this surface is identical to those on the (2×4) surface, although a greater level of disruption is observed due to the higher initial As content.

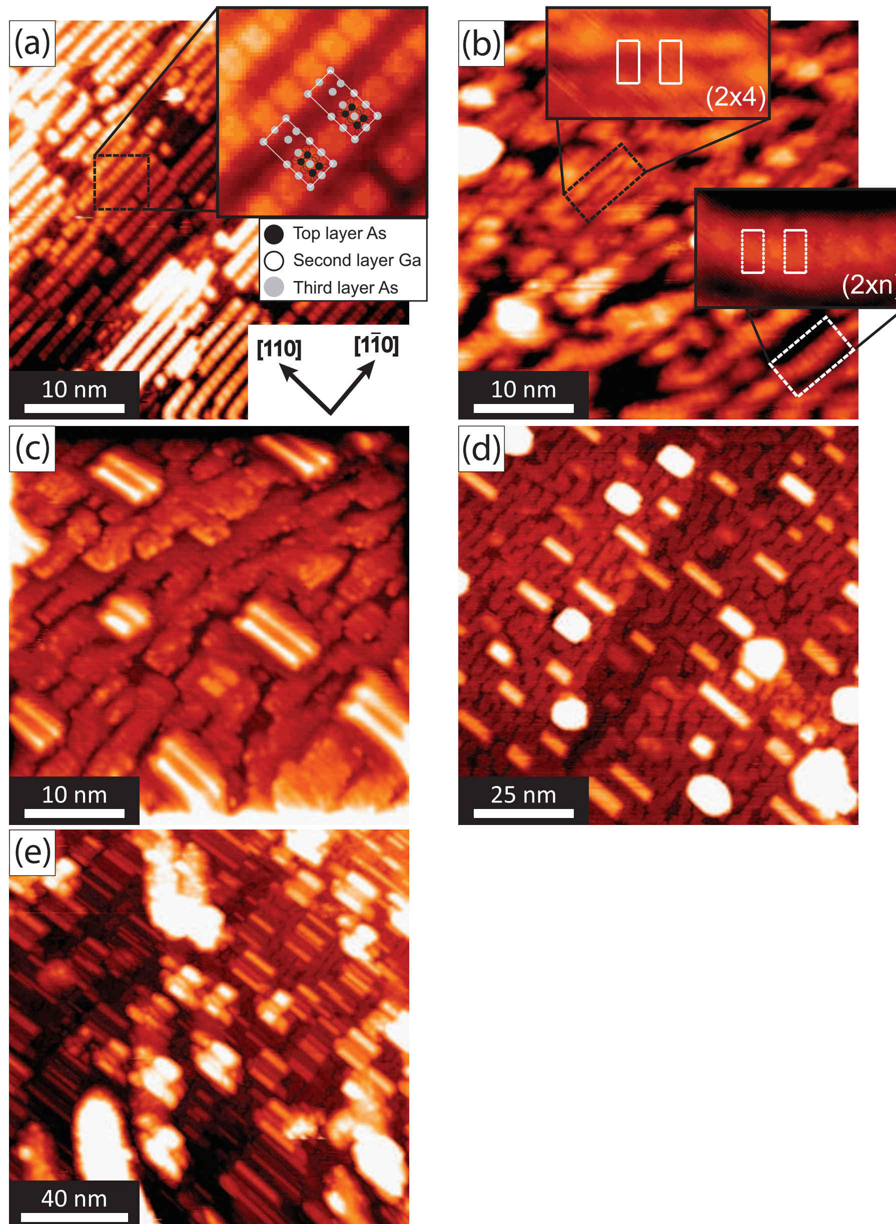

Figure 3.8: Morphology of the GaAs(001)-β2(2$\times$4) surface from STM at (a) 0 ML (clean surface), the inset shows a close up of the β2(2$\times$4) reconstruction alongside the structural model, (b) 0.8 ML, (c) 1.2 ML, (d) 1.8 ML and (e) 2.4 ML. Increasing Mn coverage results in the coexistence of (2$\times$4) and disordered (2$\times n$) regions, zoomed images of these regions are shown in the insets. In addition, the formation of irregularly shaped islands, consisting of a $MnAs_x$ alloy, and rod-like features due to Ga-rich surface structures is observed.

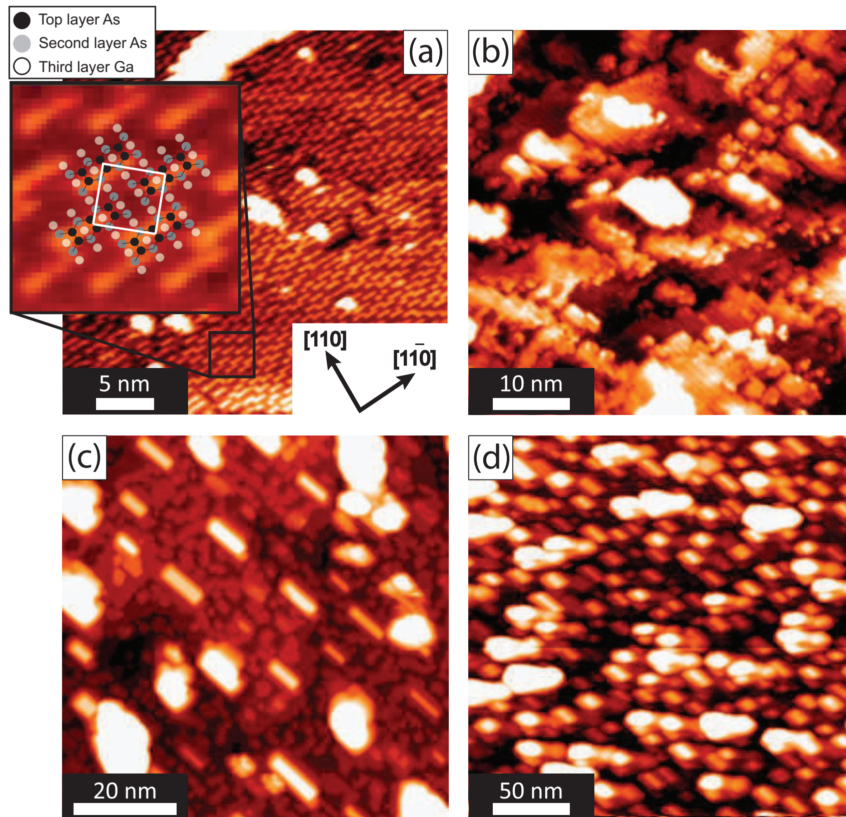

Figure 3.9: Morphology of the GaAs(001)-c(4x4) surface at (a) 0 ML (clean surface), (b) 0.8 ML, (c) 1.2 ML and (d) 1.8 ML. As on the (2×4) surface, increasing Mn coverage results in a disordered (2×*n*) structure. The formation of rods and islands is quicker on this surface due to the increased As content relative to the (2×4) surface.

3.4 Discussion

3.4.1 Thermodynamics

The reconstructions observed on InSb following Mn deposition are all characteristic of clean InSb surfaces and the transitions are all from the Sb-rich to In-rich surfaces as θ_{Mn} increases. The simplest explanation for this behaviour is the removal of Sb from the surface by Mn, thereby forming a new, lower Sb content reconstruction. Evidence for this process can be seen by considering the transitions seen on InSb(001). The first transition, from c(4×4) to a(1×3), is consistent with a small reduction in surface Sb

resulting in disordered top layer Sb-Sb dimers, characteristic of the a(1$\times$3). The second transition is to the In-rich c(8$\times$2) and arises from disruption of the complete Sb layer below the dimers. As similar transitions are observed on the (111)A and (111)B surfaces, it is likely that this process is common to all InSb faces. In addition, the linear relationship observed in Figure 3.4 indicates that the efficiency of Mn-induced Sb removal is similar on the three low-index faces. The gradient of the fitted line is determined to be (0.16$\pm$0.02) and so suggests that one Mn adatom removes approximately 6 Sb atoms from the surface. At the substrate temperatures used in this study the rate of Sb desorption is low (in the absence of a Mn flux) and so, as both Mn and Sb atoms are unable to desorb from the surface it is concluded that Mn is driving the removal of Sb from the surface. The determined LET values, obtained from the AFM images shown in Figure 3.7, show that the total island volume is larger for the c(4$\times$4) surface [(1.92$\pm$0.2) ML] than on the c(8$\times$2) surface [(1.10$\pm$0.06) ML]. It would be expected for $\theta_{\mathrm{Mn}} = 1.0$ ML that, in the absence of Mn incorporation, the approximate island volume on the In-rich surface would be $\sim$1 ML and $\sim$2 ML for a fully reacted MnSb layer. The calculated LET values are consistent with this hypothesis and so Mn is not incorporated into the surface. It should be noted that the AFM images were obtained outside UHV and oxide formation may increase the apparent volume of the islands, explaining the LET $>$ 1 ML value observed for the In-rich surface. Under the assumption that no Mn is incorporated into the surface, and that 1 ML of Mn must be present in the islands (resulting from deposition), then the difference in volumes between the In-rich and Sb-rich surfaces must arise from Sb incorporated into the islands. A tentative estimate of the average atomic percentage of Mn in the islands can then be made on the basis of this volume difference. In this case the increased volume on the Sb-rich surface is due to incorporated Sb and for alloy islands having a composition of the form MnSb_x, the value of x is (0.73$\pm$0.07). This value is surprisingly low as the transition from c(4$\times$4) to c(8$\times$2) requires the loss of 1.75 ML of Sb and contradicts the gradient value calculated from Figure 3.4. However, it is plausible that any Sb remaining from the disruption of

Table 3.4: Enthalpies of formation for various binary compounds as discussed in the text.

Compound	ΔH_f (kJ/mole)	Reference
InSb	-30.5	[92]
MnIn	-11.0	[93]
MnSb	-35.0	[93]
GaAs	-71.0	[94]
MnAs	-65.0	[93]
MnGa	-34.0	[93]
AuIn	-21.0	[95]
AuSb	-13.0	[96]
InAs	-58.6	[92]
FeAs	-40.0	[97]
FeIn	+13.0	[97]

the reconstruction is able to desorb into the vacuum and so results in the In-terminated surfaces observed in the RHEED.

The reactivity of Mn with the Sb-rich surface may also explain the difference in the morphologies of the surface. On c(4×4), the distribution of island sizes is strongly bimodal with large islands having heights of ∼25 nm and smaller islands having heights of up to 5 nm. However, only a single island size distribution is observed on the c(8×2) surface and the heights of the islands are ∼60 nm. The large average nearest-neighbour distance on the In-rich surface, (1.45±0.07) μm, indicates that Mn adatoms are able to migrate large distances before interacting with additional adatoms or islands. In comparison, for the large islands on the Sb-rich surface, the average nearest-neighbour distance is (640±30) nm and for the smaller islands it is (35±2) nm. It is plausible that the nearest-neighbour separation of the smaller islands is the result of a low migration length (due to reactivity) and so would result in the formation of a high density of small, Sb-rich, islands. With increasing Sb removal, the migration length of Mn adatoms will increase towards that of the In-rich surface and so larger islands, which are more Mn-rich, can then form.

The behaviour of the Mn-InSb and Mn-GaAs systems can then be understood in terms of simple reaction processes. Models using bulk thermodynamic quantities to de-

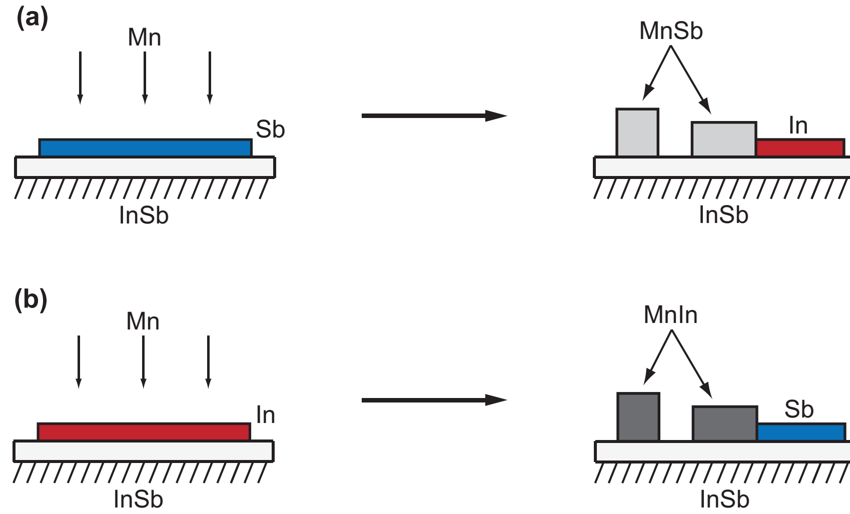

Figure 3.10: Simplistic schematic showing (a) the conversion of an Sb terminated InSb surface to an In surface with the formation of MnSb islands and (b) the conversion of an In terminated surface to an Sb surface with the formation of MnIn islands.

scribe the reactivity of interfaces have been successful for a range of metal-semiconductor systems [93, 98, 99] although little exists in the literature on the effect of surface reconstructions on these thermodynamic processes. The interaction of Sb- and In-rich InSb surfaces with Mn is shown simplistically in Figure 3.10 and can be represented by the following processes:

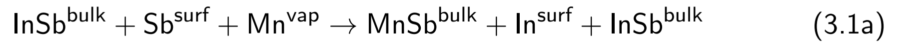

$$\mathrm{InSb^{bulk} + Sb^{surf} + Mn^{vap} \rightarrow MnSb^{bulk} + In^{surf} + InSb^{bulk}} \tag{3.1a}$$

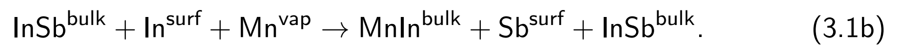

$$\mathrm{InSb^{bulk} + In^{surf} + Mn^{vap} \rightarrow MnIn^{bulk} + Sb^{surf} + InSb^{bulk}}. \tag{3.1b}$$

Where terms with the superscript 'bulk' denote the relevant bulk crystals, the 'surf' superscript indicates the terminating atomic species and $\mathrm{Mn^{vap}}$ is the incident metal flux, in this case Mn. Using the relevant enthalpies of formation, ΔH_f, and the processes outlined above, the enthalpies of reaction, ΔH_R, for these processes can then be derived. The enthalpies of reaction for conversion from an Sb (In) terminated surface to an In (Sb) terminated surface, $\Delta H_\mathrm{R}{}^{(\mathrm{Sb/In \rightarrow In/Sb})}$, are given by

$$\Delta H_\mathrm{R}{}^{(\mathrm{Sb \rightarrow In})} = \Delta H_\mathrm{f}(\mathrm{MnSb}) - \Delta H_\mathrm{f}(\mathrm{InSb}) + \Delta H_\mathrm{SR} \tag{3.2a}$$

$$\Delta H_{\mathrm{R}}{}^{(\mathrm{In}\rightarrow\mathrm{Sb})} = \Delta H_{\mathrm{f}}(\mathrm{MnIn}) - \Delta H_{\mathrm{f}}(\mathrm{InSb}) - \Delta H_{\mathrm{SR}} \tag{3.2b}$$

where ΔH_{SR} is the energy difference between the In terminated and the Sb terminated crystal. The In-terminated surface is more stable in the absence of an Sb flux under UHV conditions [100] and so the absolute value of ΔH_{SR} is negative. This value can be approximated using DFT and the typical differences in calculated surface energies for the III-V semiconductors are up to 10 meV Å^{-2} or approximately 5–10 kJ/mole [101, 102, 49]. Using the enthalpies of formation given in Table 3.4 the value of $\Delta H_{\mathrm{R}}{}^{(\mathrm{Sb}\rightarrow\mathrm{In})}$ is then calculated to be -14.5 kJ/mole while for $\Delta H_{\mathrm{R}}{}^{(\mathrm{In}\rightarrow\mathrm{Sb})}$ it is +29.5 kJ/mole. Consequently, the reaction of Mn with an Sb terminated surface is exothermic and so occurs spontaneously, while the reaction of Mn with an In terminated surface will not occur spontaneously. It is worth noting that the enthalpies of formation do not strongly depend upon temperature [98]. The reverse process, in which the In-terminated c(8$\times$2) surface is converted to the Sb-terminated c(4$\times$4) surface has been observed in the deposition of Au on InSb. This difference in behaviour is attributed to the higher stability of AuIn compared to AuSb [103] (Table 3.4).

The behaviour of Mn with GaAs is more complex due to the combination of As removal (island formation) and Mn incorporation (new surface periodicity). This implies that ΔH_{SR} contains a contribution from the stability of the alloy reconstructions. The removal of As from the surface can be straightforwardly attributed to bulk thermodynamics: the enthalpies of reaction are $\Delta H_{\mathrm{R}}^{(\mathrm{As}\rightarrow\mathrm{Ga})}$ = -4.0 kJ/mole and $\Delta H_{\mathrm{R}}^{(\mathrm{Ga}\rightarrow\mathrm{As})}$ = +47.0 kJ/mole. Therefore, for values of $\Delta H_{\mathrm{R}}{}^{(\mathrm{B}\rightarrow\mathrm{A})} = \pm 10$ kJ/mole, as in the case of Mn-GaAs, the contribution from ΔH_{SR} is critical in determining if Group V removal is exothermic.

From these observations some general comments on the conversion of Group V terminated surfaces can be made. For a metallic element, M, deposited onto a III-V surface, $\mathrm{A_{III}B_{V}}$, conversion of the $\mathrm{B_V}$-rich surface will be preferred if $\Delta H_{\mathrm{f}}(\mathrm{MB_V}) < \Delta H_{\mathrm{f}}(\mathrm{MA_{III}})$. The reverse is also true, such that if $\Delta H_{\mathrm{f}}(\mathrm{MA_{III}}) < \Delta H_{\mathrm{f}}(\mathrm{MB_V})$ then conversion of the Group III rich surface is preferred. Table 3.5 presents ΔH_{R} values

Table 3.5: Estimated enthalpies of reaction for the various metal/semiconductor combinations, the value of ΔH_{SR} has been taken to be 10 kJ/mole.

M (metal)	AB (semiconductor)	$\Delta H_R{}^{(B\rightarrow A)}$ (kJ/mole)	$\Delta H_R{}^{(A\rightarrow B)}$ (kJ/mole)
Mn	InAs	-16.4	+57.6
Mn	InSb	-14.5	+29.5
Mn	GaAs	-4.0	+47.0
Au	InSb	+7.5	+19.5
Fe	InAs	+8.6	+81.6
Fe	GaAs	+21.0	+63.0

for the various metal-semiconductor systems discussed so far. However, the absolute values for $\Delta H_f(MA_{III})$ or $\Delta H_f(MB_V)$, when combined with Equations 3.2b and 3.3 do not always correctly predict the preferred conversion process. For example, the removal of As, and the corresponding formation of In droplets, has been observed on the In-rich c(8×2) surface of InAs during Mn [104] deposition. However, the behaviour of this system is relatively complex and, below 300 K, the formation of MnAs was observed, while at ~530 K the formation of an $In_{1-x}Mn_xAs$ alloy occurred. From the calculated values, the conversion of the In-terminated surface is not favoured for Fe-InAs although, on the basis of photoemission measurements, Hricovini et al. [104] attribute the process of substitution to the increased strength of the Mn-As bond relative to that of the Mn-In bond.

It is worth briefly discussing the effects of ΔH_{SR} on the behaviour of a surface. In the simplest approximation it is the energy difference between the Group V and Group III terminated surfaces in the absence of a Group V flux. On the basis of chemical potential arguments, calculated using DFT, the value of ΔH_{SR} typically varies between 5 and 10 kJ/mole. When estimating the values of ΔH_R presented in Table 3.5 a value for ΔH_{SR} of 10 kJ/mole has been used. If the lower limit of 5 kJ/mole is instead used, then the value of $\Delta H_R{}^{(As\rightarrow Ga)}$ is no longer negative and so the conversion is not spontaneous. However, as mentioned earlier, if an alloy reconstruction forms on the surface then the value of ΔH_{SR} will have an additional contribution from this alloy reconstruction. As

an example, the behaviour of the surface energy of the GaAs(001)-(2×2)-Mn structure has been studied using DFT by Zhang et al. [105]. Their calculations suggest that, at $\theta_{\mathrm{Mn}} = 0.25$, the minimum surface energy varies by approximately 3.75 kJ/mole as the surface moves the from As-rich limit to the Ga-rich limit. The minimum value of ΔH_{SR} for the Mn-GaAs system is then 8.75 kJ/mole and consequently the value of $\Delta H_{\mathrm{R}}^{(\mathrm{B}\rightarrow\mathrm{A})}$ becomes negative. They note that for increasing θ_{Mn} a minimum in the surface energy occurs for a Ga-rich surface, indicating that the removal of As is an energetically favourable process. The behaviour of ΔH_{SR} is complex and will be a function of the As and Mn concentrations at the surface, varying as both As is removed and Mn is incorporated into the surface.

3.4.2 Surface reconstructions

As ΔH_{SR} is influenced by the presence of reconstructions, it is worthwhile considering the atomic details of the surface reconstructions discussed in this chapter. Although DFT can be used to optimise the atomic geometry of a surface, it is costly in terms of computational time and so we will use the GECR to explore how different III-V reconstructions offer different pathways to alloy and island formation. The GECR, outlined in Section 1.4.2, have been proposed as a guide to narrowing the range of possible reconstructions in metal-semiconductor systems. According to the GECR Mn will act as a donor on GaAs and so will prefer interstitial sites in order to maximise its local co-ordination. Once located at an interstitial site, the Mn adatom will then donate its two 4s electrons and, consequently, the local structure will reconstruct according to the ECR. The (2×4) structure is the smallest ECR compliant structure possible for III-V(001) surfaces [46], while a (2×2) structure requires two additional electrons (relative to the (2×4)) which are provided by the Mn adatom. The following section outlines the effects of surface reconstructions on the behaviour of III-V surfaces in the presence of metal fluxes.

From the thermodynamic arguments presented above, it can be seen that the

strength of the Mn-As bond is greater than that of the Mn-Ga bond. It is therefore plausible to assume that Mn will be able to substitute for surface atoms and that this will prefer to replace Group III atoms in order to maximise the number of Mn-As bonds. The substitution of Mn into the reconstruction could then serve as a nucleation point for the formation of Mn-As islands. It should be noted that although the substitution of Mn into the reconstruction can act to form islands, it is highly likely that defects on the surface, such as vacancies or dislocations, will instead offer more energetically favourable nucleation sites. The substitution of Mn into the reconstruction presents an alternative method, that can take place simultaneously with growth at defects, for the creation of pseudomorphic Mn pnictide islands. However, the presence of good quality RHEED patterns indicates that the surface consists of a greater number of ordered reconstructions sites relative to defect sites.

In order for a substitution to remain energetically favourable it must be GECR compliant as the energy penalty for excess charge on the surface is large [47]. Accordingly, the substitution of a Group III atom will require 1 electron (Mn provides 2 while Ga/In provides 3) and the substitution of a Group V atom requires 3 electrons (Mn provides 2 while As/Sb provides 5). In all cases Mn incorporation at an interstitial is required to reduce the electron deficit. For the c(4×4) structure, which is Group V terminated, it is not possible to reduce the unit mesh to a (2×2) structure with incorporation alone, as we now show.

Mn substitution into c(4×4) surfaces

Structural studies of the InSb(001)-c(4×4) surface made using STM [106] indicated that vacancies were present in the Sb dimer rows. However, the GaAs(001)-c(4×4) is observed to contain heterodimers and these are then proposed to explain the observed vacancies on the InSb(001) surface. As the STM images presented in the InSb work were obtained using filled-states tunnelling conditions, which probes the filled dangling bonds present on the Group V atoms, then the empty dangling bonds of the Group

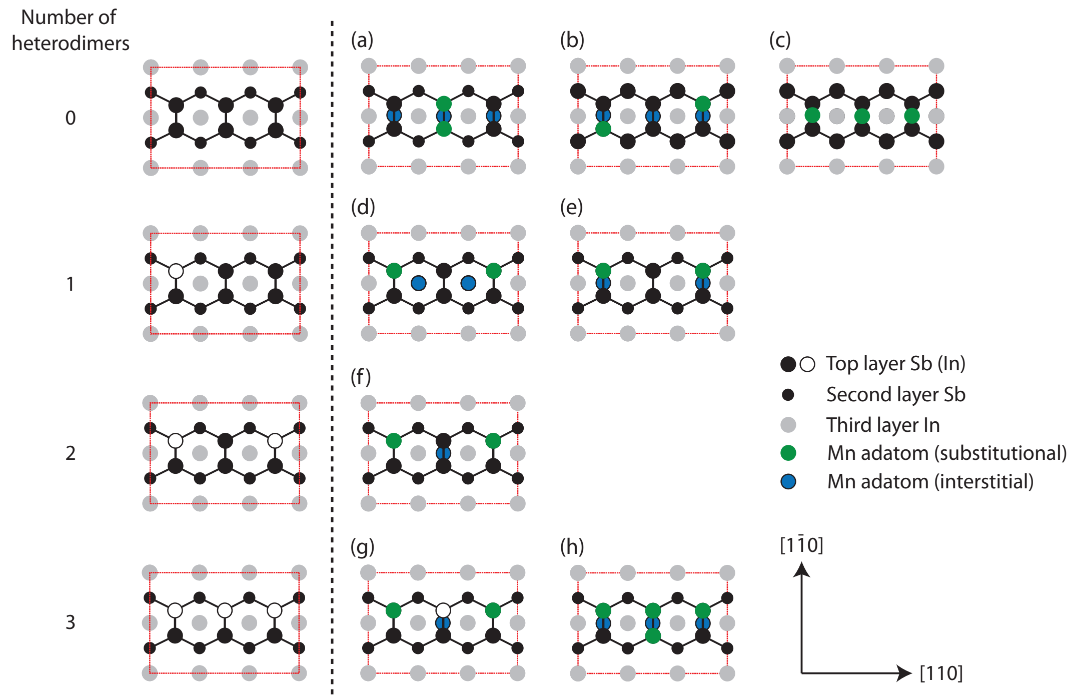

Figure 3.11: GECR compliant surface structure models for Mn substitution into the c(4×4) surface. The models for a completely Group V terminated surface include (a) Mn-Mn dimer formation, (b) partial dimer substitution and (c) Mn top bonded to existing Group V dimers. For a single heterodimer mixed Group III/Group V substitutions are possible but feature sub-surface Mn in either (d) an interstitial bridge site beneath a dimer or (e) interstitial hollow site between two dimers. For double and triple heterodimers models (f) and (g) are Group III substitutions while model (h) is partial substitution of two dimers with the formation of a Mn-Mn dimer. The models included do not represent all possible substitutions, although all non-repeating models have been shown. The red dashed box highlights the (2×4) unit cell.

III atoms will not be observed and so appear as vacancies in the image. The presence of heterodimers on InSb(001) is further corroborated by DFT studies [87] that suggest that heterodimers are a common feature of the c(4×4) reconstruction on the III-V semiconductors.

To this end, several models for Mn substitution into the c(4×4) structure, with a varying number of heterodimers, have been considered and are shown in Figure 3.11. Note that for simplicity only the triple dimer row building block of the reconstruction has been shown. The models feature three main structural motifs: Group III substitution, Group V substitution and 'bridge' bonding (resulting in the formation of two Mn-As

Table 3.6: Number of Mn adatoms substituted into In or Sb sites (n_{In},n_{Sb}), number of interstitial Mn adatoms ($n^{\text{int}}_{\text{Mn}}$) and the total number of Mn adatoms present ($n^{\text{tot}}_{\text{Mn}}$) for the models presented in Figure 3.11.

Model	n_{In}	n_{Sb}	$n^{\text{int}}_{\text{Mn}}$	$n^{\text{tot}}_{\text{Mn}}$
Charge excess/deficit	-1 e^-	-3 e^-	+2 e^-	
(a)	0	2	3	5
(b)	0	2	3	5
(c)	0	0	0	3
(d)	1	1	2	4
(e)	1	1	2	4
(f)	2	0	1	3
(g)	2	0	1	3
(h)	3	1	3	7

bonds). Substitution of Mn into the reconstruction follows a straightforward relationship between the number of substituted In/Sb atoms and the number of interstitial atoms and is given by

$$n_{\text{In}} + 3n_{\text{Sb}} = 2n^{\text{int}}_{\text{Mn}} \tag{3.3}$$

where n_{In} and n_{Sb} are the number of substituted In or Sb atoms and $n^{\text{int}}_{\text{Mn}}$ is the number of interstitial Mn adatoms. The number of substituted atoms and the total number of Mn atoms incorporated into the reconstruction, $n^{\text{int}}_{\text{Mn}}$, are given in Table 3.6.

On a completely Sb terminated surface, with no heterodimers, the GECR requires the substitution of two Sb atoms, with the incorporation of three interstitial Mn atoms in order to balance the surface charge. The substituted Mn atoms can then form either a Mn-Mn dimer, as in model (a), or partially substitute into two dimers, as in model (b). With increasing heterodimer content the surface requires less interstitial Mn in order to undergo substitution. Models (d) and (e) exhibit mixed species substitution with the requirement of two interstitial Mn per triple dimer row. These models differ in the location of the interstitial Mn adatoms, with model (d) being based on a bridge site and (e) based on a hollow site. Models (f) and (g) consist of partial substitution of two heterodimers, requiring only a single interstitial Mn and so are likely the preferred

models at low θ_{Mn}. Model (h) is highly Mn rich and exhibits two partial substitutions in addition to the formation of a Mn-Mn dimer. Finally, model (c) is proposed in light of similar structures observed during the deposition of Co onto GaAs(001)-c(4×4) [107] where deposited metal atoms are chemisorbed on top of the dimers. Note that GECR compliant substitution does not change the periodicity of the observed structures and that only a breaking of dimers will lead to a change in reconstruction. In the case of InSb(001) this results in the formation of the a(1×3) structure and so no (2×2) reconstruction forms. These models suggest that the formation of Mn-As bonds can take place on the surface during Mn deposition and so multiple substitutions can act as nucleation sites for MnAs_x islands. If the substitution of surface atoms is occurring then we would expect to see the formation of islands orientated along the As dimer direction on GaAs. However, no clear evidence for orientated islands can be seen and the surface consists of co-existing regions of (2×4) and (2×n) with some small islands. Further STM studies, or in-situ scanning tunnelling molecular beam epitaxy, at intermediate Mn coverages, $\theta_{\text{Mn}} \leq 0.25$ ML, would enable observation of the substitution process.

Reducing the Group V content of the InSb(001)-c(4×4) surface leads to the formation of the a(1×3) structure and, as the reconstructions share a common structural building block, it is likely that heterodimers are also present on a(1×3) surfaces. Consequently, similar substitution processes will occur although the presence of double dimer rows restricts the models presented in Figure 3.11 that feature three interstitial Mn and so models (c) and (h) are no longer applicable. However, on the GaAs(001)-c(4×4)β surface, a reduction in Group V content leads to the formation of the c(4×4)α structure and consequently the number of heterodimers increases enabling more substitutions.

There are several limiting factors to the incorporation of Mn on the c(4×4) surface, the first is the energy associated with the formation of interstitial Mn. Theoretical calculations by Erwin and Petukhov [108] for GaAs(001) surfaces predict that the bridge site, located between two dimers (as shown in Figure 3.11(d)), is energetically preferred. This favours models with less than 3 interstitial Mn adatoms (models (d) – (g)) and so

limits the total number of substitutions possible on the surface. A small barrier of 0.2 eV is necessary to separate the dimers and at the substrate temperature used for GaAs in this study the probability of Mn separating the dimers is approximately 2 %. However, the equivalent value is unknown for InSb and no value has so far been reported in the literature. The second barrier is the energy cost associated with substitution of atoms in the reconstruction. This process is likely related to the bulk enthalpies described above and consequently it might be expected that the rate of substitution is higher on InSb due to the lower estimated enthalpy. The bulk thermodynamics also dictates the removal of the Group V element from the surface and acts to remove the number of possible substitution sites during the formation of islands.

Mn substitution into (2×4) surfaces

Further reduction in the Group V content of the GaAs(001)-c(4×4) results in the (2×4) structure. As the β2(2×4) structure features no heterodimers, substitution is only possible through the removal of As and Figure 3.12 shows the possible substitution pathways on this surface. Panel (a) shows the β2(2×4) structure, which consists of two surface dimers and one trench dimer. Note that it is expected that the height difference between the surface and trench dimers prevents charge transfer between the them. Consequently, an interstitial Mn located beneath the trench dimer will provide electrons to that dimer only and so a maximum of two interstitial Mn are supported in this structure. Panel (b) shows a GECR compliant (2×2) structure for $\theta_{\mathrm{Mn}} = 0.25$ ML with a single interstitial Mn and is based on the model of Colonna et al. [109]. The model shown in panel (c) involves the substitution of one surface As and a Ga atom located beneath the dimer, requiring two interstitial Mn. Panel (d) involves two top bonded Mn atoms, replacing the existing surface dimers. It can be seen that a GECR compliant substitutional structure requires the substitution of sub-surface Ga atoms and so consequently needs to overcome the large energy barrier associated with breaking the As-As surface dimer. The top bonding model, illustrated in panel (d), can also

provide a nucleation point for subsequent island growth. Note that top bonding of Mn is possible for all three dimers and does not require any interstitial Mn, making it a relatively favourable process for this reconstruction. Following the formation of the structures discussed above, the remaining (2×2) sub-unit (containing the trench dimer) can also accommodate an interstitial or top-bonded Mn and, if Ga and As atoms migrate to these sub-units, so similar $(2\times n)$ structures could form in this other sub-unit. As this process is dependent on mobile surface atoms then this may explain the disorder observed on the As-rich surfaces. In summary, the number of substitutions possible on the surface is limited to those that either break As-As dimers, which is energetically unfavourable, or that prefer bonding atop of an As-As dimer. This reduces the total number of substitution pathways available on this surface. Based on the STM observations presented in Figures 3.8 and 3.9 it can be seen that the island density is lower for the (2×4) surface than for the c(4×4) surface (for the same value of θ_{Mn}). One explanation for this is the reduced number of substitution pathways, which act to minimise the rate at which substitution can occur. If island growth then proceeds through the reaction of incident Mn and mobile surface As, arising from disruption of the surface reconstruction, then the formation rate for islands will be greatly reduced.

The formation of a (2×2) structure on GaAs is possible due to the incorporation of an interstitial Mn, as shown in Figure 3.12(b). However, this reconstruction does not occur on InSb and instead a reduction in Group V content leads to the formation of the a(1×3) structure, which features the same basic dimer motif as the c(4×4). It should be noted that the two dimer unit present in the a(1×3) structure could behave analogously to the (2×4) structure, although no evidence of a (2×) periodicity was observed in the RHEED. Further Mn deposition leads to the In-rich c(8×2) and so it is likely that no alloy reconstruction forms. On this basis it appears that the presence of the (2×4) reconstruction is crucial to the formation of alloy reconstructions. The (2×4) structure is common to several III-V semiconductors, including GaP, InP, InAs and AlAs [49, 110] and investigation into the behaviour of these surfaces with Mn would

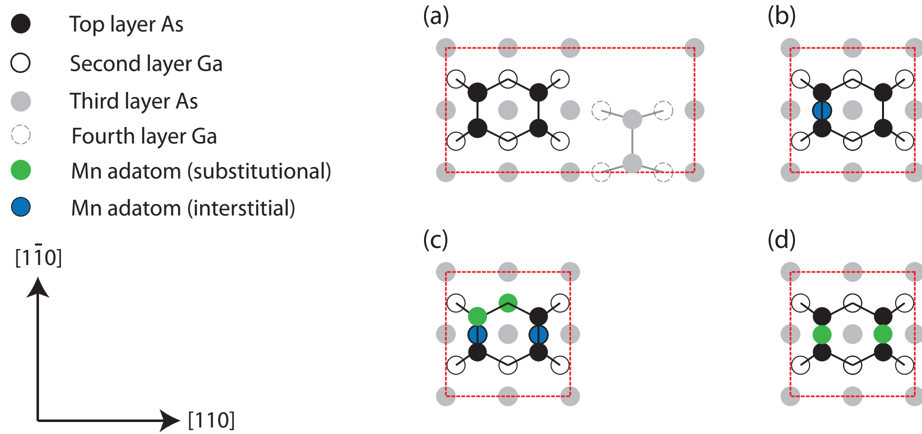

Figure 3.12: GECR compliant surface structure models for the (a) clean GaAs(001)-β2(2×4) surface (b) (2×2) model at θ_{Mn} = 0.25 ML (c) (2×2) mixed Ga and As substituted surface and (d) atop bonded Mn (replacing the dimer). The red dashed boxes indicate the (2×4) unit cell while the solid black box is the (2×2) unit cell. Atom types are as labelled in the figure.

determine if the (2×4) does indeed promote alloy reconstruction formation.

The Mn induced (2×2) reconstruction observed on the initially (4×6) GaAs(001) surface has not been previously reported. Simple (2×2) models that are GECR complaint can be built using Ga dimers or heterodimers on top of a bulk-like As layer. However, further structural characterisation, such as atomic resolution STM is required before structural models for the Mn-induced reconstruction can be proposed, especially in light of the complexity of the starting (4×6) structure.

3.5 Conclusions

The effect of Mn on several reconstructed surfaces of InSb and GaAs has been investigated using a combination of RHEED, STM and AFM. The In-rich surfaces of InSb are unreactive while the Sb-rich surfaces undergo transitions to reconstructions characteristic of clean InSb surfaces. On both surfaces, 3D islands form and layer equivalent thickness calculations indicate that on the In-rich surface they consist of elemental Mn, while on the Sb-rich surface they are comprised of a $MnSb_x$ alloy with

x estimated to be (0.73±0.07). On GaAs, a (2×2) alloy reconstruction is observed using RHEED (Ga-rich surface) and in STM (As-rich surface), although the resulting structure is poorly ordered on the As-rich surfaces and only a (2×n) periodicity is seen. Islands and 'rod' features also occur on the As-rich surface and the rod features are likely composed of Ga-rich reconstructions, indicative of As-deficient conditions and so suggest that significant As removal occurs.

The removal of Sb/As from the surface has been attributed to bulk thermodynamics and the resulting enthalpies of reaction are found to predict the direction of conversion (Group V to Group III) for InSb. For GaAs, the value of $\Delta H_{R}^{(As \rightarrow Ga)}$ is found to be close to zero and so the contribution from the alloy reconstruction energy to ΔH_{SR} is seen to be significant, resulting in a value of -7.75 kJ/mole and so conversion of the surface occurs as observed.

No direct method for the formation of a (2×2) structure from the c(4×4) and a(1×3) structures has been found, although simple interstitial Mn incorporation leads to the formation of a (2×2) structure on the (2×4) surface. The absence of a (2×4) structure on InSb is then proposed as the reason why no alloy reconstruction is observed on InSb.

The substitution of Group III and Group V atoms into c(4×4) and β2(2×4) surfaces is proposed. The extent of substitution depends on the number of available Mn interstitial sites and the presence of heterodimers in the reconstruction. For the c(4×4) surfaces, which can accommodate up to 3 heterodimers, the number of substitution pathways is large. In contrast, the β2(2×4) structure, with no heterodimers, has no straightforward substitution pathways and this may explain the difference in the observed island density between the two surfaces. The formation of Mn-As and Mn-Sb bonding environments implies that dimers consisting of substituted Mn act as nucleation sites for subsequent MnAs/MnSb growth, the transition from 'local surface alloy' to epitaxial island then requires an additional source of Group V atoms, either from mobile surface atoms or an incident flux.

Chapter 4

Characterisation of MnSb thin films

4.1 Introduction

In Chapter 3 the reaction of Mn with GaAs surfaces was investigated and it was proposed that the formation of Mn-As bonds in the reconstruction act as nucleation points for the formation of larger islands. It is highly likely that such bonds are formed at the interface during the growth of MnSb on GaAs and so lead to the formation of MnSb islands. Work performed by Dr Stuart Hatfield [60] indicated that the growth of MnSb proceeded by the nucleation, and subsequent coalescence, of islands in agreement with the observations made in the previous chapter. However, TEM studies have also revealed the presence of different polymorphs of MnSb within these thicker films. Zincblende and wurtzite structures were seen in addition to the normal niccolite phase for films with thicknesses greater than $\sim$100 nm. These polymorphs are of interest for spintronic applications due to their high spin polarisation and robust half-metallic ferromagnetism. Nonzero-temperature DFT indicates that c-MnSb is half-metallic for temperatures greater than 350 K and so is a promising candidate for room temperature spintronics [23]. Figure 4.1(a) shows a bright-field TEM image of a polymorphic MnSb film showing the formation of large polymorph crystallites near the surface. Figure 4.1(b) shows a high resolution TEM (HRTEM) image (far right of the panel) highlighting the

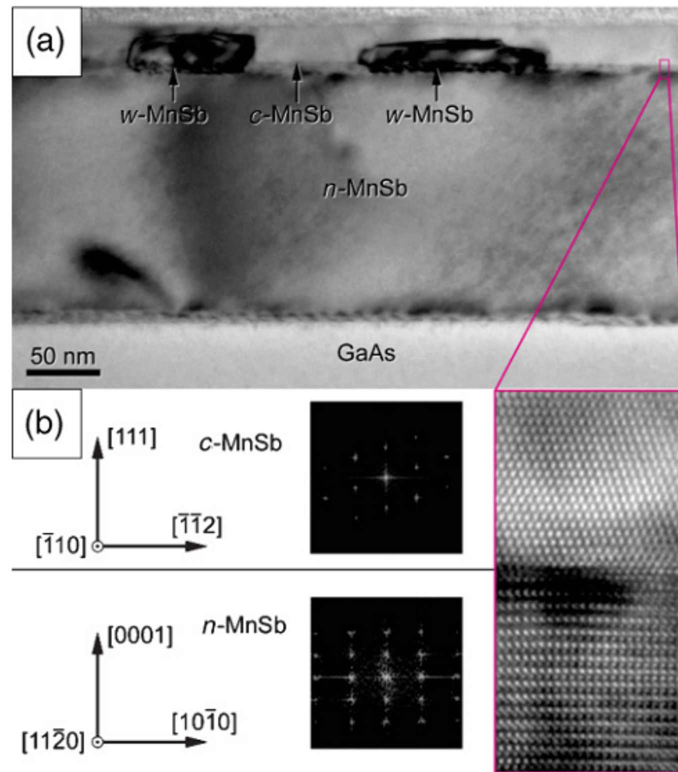

Figure 4.1: TEM images of MnSb films on GaAs(111) substrates showing (a) typical bright-field image, with the presence of polymorphs crystallites observed near the surface of the layer (as indicated by the labels) and (b) Fourier transforms of the highlighted regions alongside HRTEM images showing the sharp interface between n-MnSb (bottom) and c-MnSb (top). Reproduced from Reference [23].

sharp interface between the niccolite and cubic phases, also shown are Fourier transforms of the upper and lower regions of the image indicating their relative crystallinity. The lattice parameters of the various phases were determined from SADP measurements on the sample shown in Figure 4.1 and the values are given in Table 4.1 [23].

Of continued interest is the behaviour of the polymorphs with the growth parameters. For example, are there values of $J_{\mathrm{Sb/Mn}}$ or sample thickness where polymorph formation is maximised and any strain in the crystallites minimised? Although the spin polarisation at the Fermi level in n-MnSb is only 18 % it is possible to envisage a situation whereby the polarisation of an injected current is increased above the n-MnSb

Table 4.1: Lattice parameters of MnSb polymorphs determined from SADP measurements on the sample shown in Figure 4.1, the uncertainty of the values presented is ± 0.5 %.

Polymorph	*a* lattice parameter (Å)	*c* lattice parameter (Å)
n-MnSb	4.115	5.769
c-MnSb	6.502	-
w-MnSb	4.291	7.003

value by the presence of the half-metallic crystallites [23]. Increasing the polymorph content of these films is then a key first step in increasing the potential polarisation of n-MnSb films. A reduction in strain will straightforwardly lead to a reduced number of defects and grain boundaries and so minimises scattering losses arising from these features. Although structural properties, such as the lattice parameters, can be determined from SADP measurements there are two key issues with this analysis. The first is the long preparation times required to produce electron transparent samples. The second is the small probe area, ranging from a few hundreds of nanometres to a few micrometres. As this is comparable to the size of the crystallites it limits the number of sampled crystallites and so compromises quantitative analysis of the polymorphs. It is therefore advantageous to study films with a technique that requires less preparation time and that can average over a significant proportion of the film. It is worthwhile noting that this averaging effect can reduce the reliability of the determined parameters (including the local strain of individual crystallites) for the cubic and wurtzite polymorphs due to the small size of the crystallites relative to the beam footprint. To this end, high resolution XRD (HRXRD) has been used to study the structural properties of polymorphic MnSb films.

In this chapter, the growth parameters of MnSb(0001) films are outlined in Section 4.2 and the crystallinity of the samples is briefly discussed with regards to the RHEED patterns obtained. Following this, the presence of polymorph crystallites, as determined from symmetric diffraction data, is presented and some of the problems faced are discussed. Section 4.4 presents the XRD characterisation work carried out

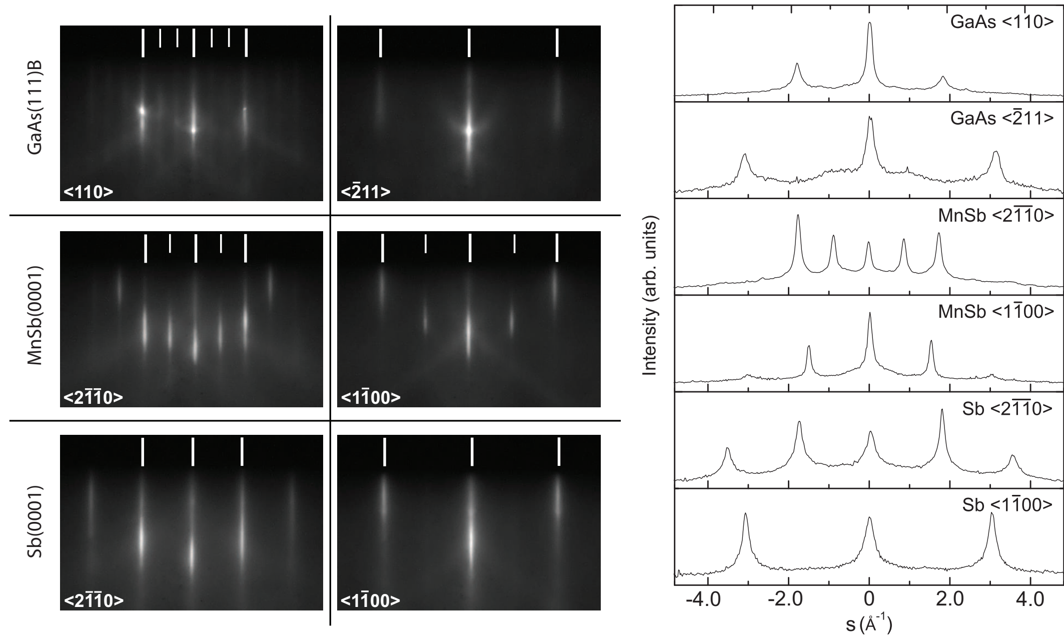

Figure 4.2: RHEED patterns obtained from a 150 nm MnSb film grown on a GaAs(111)B substrate. The top panel shows the GaAs(111)B-td(1×3) reconstruction observed following IBA. The middle panel shows the MnSb(0001)-(2×2) structure observed throughout growth. Finally, the bottom panel shows a h-Sb(0001)-(1×1) reconstruction obtained during deposition of the Sb cap. The right hand panel shows line profiles for each of the patterns.

on the three polymorphs in an attempt to determine the growth characteristics of the crystallites. Finally, Section 4.5 introduces some preliminary work using asymmetric RSMs to determine the in-plane lattice parameters of the polymorphs and to investigate any possible trends in polymorph content with growth parameters.

4.2 Growth of MnSb(0001) thin-films on GaAs substrates

This section focusses on the growth of MnSb thin films grown using MBE on GaAs(111)B substrates. The GaAs substrates were prepared using the method outlined in Section 3.2. The RHEED pattern observed following cleaning was a td(1×3), characterised by a (3×) periodicity along the $\langle 110 \rangle$ direction and a (1×) periodicity along the $\langle \bar{2}11 \rangle$ direction, and is shown in Figure 4.2.

The growth conditions of MnSb were initially determined by Hatfield and then further optimised with the introduction of a multiple-stage growth methodology [34]. The MnSb samples used in this study were then grown using a two-stage recipe with the following conditions:

- $J_{\mathrm{Sb/Mn}} = 6.2$–7.9
- $T_{\mathrm{sub}} = 350(\pm10)$ °C (first-stage) and $420(\pm10)$ °C (second-stage)
- $t = 60$ s (first-stage) and $t \geq 3$ minutes (second-stage).

A two-stage growth methodology was adopted in order to avoid the non-planar surface morphologies observed at high $J_{\mathrm{Sb/Mn}}$ values ($>$9) [28]. However, for $J_{\mathrm{Sb/Mn}}$ values between 6.5 and 7.3 (within the optimised region) a sharp and intense (2×2) reconstruction was observed and typical patterns for this surface are shown in the central panels of Figure 4.2. Although it should be noted that during the early stages of growth faint facet and transmission features were seen on the integer and fractional streaks. For samples with thicknesses less than 20 nm a single growth stage with a substrate temperature of $T_{\mathrm{sub}} = 420$°C was used. The RHEED patterns observed for single stage samples were similar to those observed during the first (low temperature) stage of the two-stage method, with the transmission features fading with increasing deposition time. An Sb capping stage was used for some samples in order to prevent oxidation of the surface. During this stage the Sb cell flux was held at the growth value and a $T_{\mathrm{sub}} \leq 250$°C was used with deposition times of $<$ 2 minutes, resulting in cap thicknesses of between 2 and 5 nm. Despite the relatively large lattice mismatch with MnSb ($\frac{a_{\mathrm{MnSb}}-a_{\mathrm{Sb}}}{a_{\mathrm{MnSb}}} = -4.36$ %) the caps display streaky RHEED (shown in the bottom panel of Figure 4.2) and exhibit the same symmetry as the MnSb layer. On this basis, the Sb caps are thought to be orientated Sb(0001)∥MnSb(0001), throughout this chapter the Sb cap is referred to as h-Sb denoting the hexagonal setting of the rhombohedral Sb crystal structure [111].

Using the profiles shown in Figure 4.2, the FWHM of the integer order streaks can be determined. From this width the size of the scattering domains parallel to the

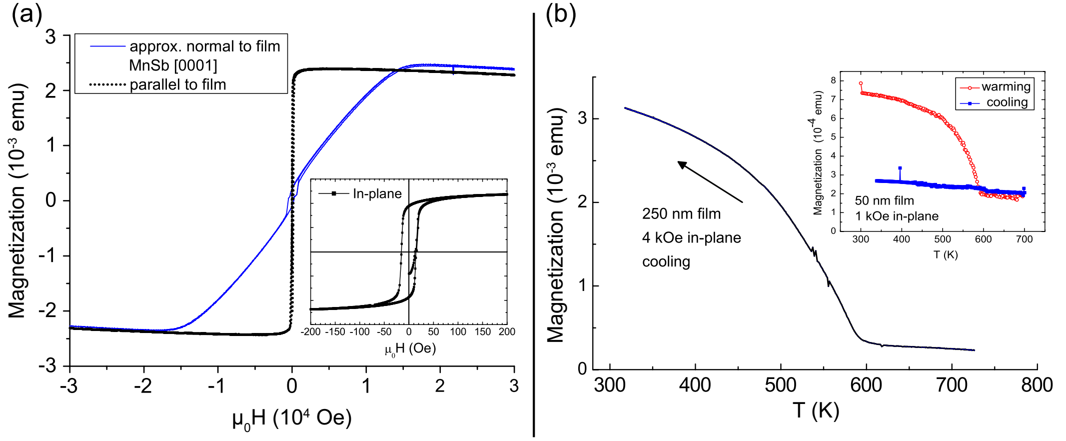

Figure 4.3: Magnetometry measurements of MnSb on GaAs(111)B substrates. Panel (a) shows hysteresis loops (measured in-plane, black, and out-of-plane, blue) for a 1 μm thick MnSb layer. Panel (b) shows *M*-*T* measurements for two MnSb layers, the main curve shows the behaviour of the film during cooling (with an applied field of 4 kOe) while the inset demonstrates the behaviour during both heating and cooling. Note that panel (a) was obtained using a vibrating sample magnetometer while panel (b) was obtained using a SQUID magnetometer. Reproduced from Reference [17].

surface, $L_{||}$, can be estimated using the following relation [112]

$$L_{||} = \frac{2\pi}{\Delta\phi_{\mathrm{f}}\ k\ \sin\theta_{\mathrm{i}}} \tag{4.1}$$

where $\Delta\phi_{\mathrm{f}}$ is the angular width of the streak, k is the magnitude of the incident wavevector and θ_{i} is the incident angle. The integer streak FWHM determined from Figure 4.2 is 9.5×10^{-4} radians giving a domain size of 110 nm which is in agreement with previous STM studies [28]. The sharp streaky patterns observed in the RHEED, in addition to the large terrace widths present on all samples, show the films to be of high crystalline quality.

The magnetic properties and surface stoichiometry of MnSb thin films grown using the above methodology have been studied previously by Aldous et al. [17] and Hatfield et al. [28], respectively. Thin films of MnSb are found to be ferromagnetic with a Curie temperature of (589$\pm$5) K, and both *M*-*H* and *M*-*T* measurements are presented in Figure 4.3. The in-plane (with the applied field perpendicular to the *c*-axis) coercive field of the 1 μm thick sample was determined to be (14.7$\pm$0.5) Oe

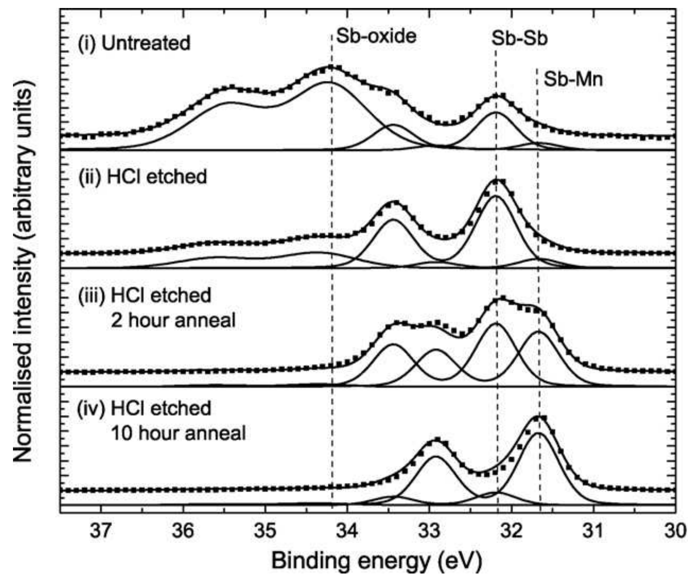

Figure 4.4: XPS Sb 4d spectra for a 100 - 300 nm MnSb film, both the experimental data (points) and fitted peaks (lines) are shown. Panel (i) is from an untreated (as-loaded) sample. Panels (ii)-(iv) are following a HCl etch and then annealed at 410 - 430 °C for (ii) 0 hours, (iii) 2 hours and (iv) 10 hours. Reproduced from Reference [28].

while the saturation magnetisation was calculated as being $(3.1\pm0.5)\mu_{\mathrm{B}}$ per Mn atom. Figure 4.3(b) illustrates temperature-dependent magnetisation behaviour of MnSb thin films, of particular interest is the effect of heating samples above 600 K. The inset of Figure 4.3(b) shows the behaviour of the sample magnetisation upon both cooling and heating with a loss of magnetisation observed when cooling from 700 K. This is believed to be due to the physical decomposition of the film during the heating cycle and is not due to oxide formation. Consequently, MnSb films should not be heated above this temperature in order to preserve their structural and magnetic properties.

Figure 4.4 shows XPS data for the Sb 4d region of an uncapped MnSb film with a thickness between 100 and 300 nm. The data presented was taken following a series of chemical etch and anneal cleaning cycles. It is evident that as-loaded MnSb samples are heavily oxidised, as can be seen from the significant Sb oxide component present in Figure 4.4(i). Following chemical etching using HCl and subsequent in-vacuo annealing (panels (ii) to (iv), in order of increasing anneal times of 0, 2 and 10 hours),

the Sb-oxide component decreases and a significant Sb-Mn bonding environment signal is observed. On the as-loaded sample the Sb oxide signal comprises 80 % of the total Sb 4d peak area while the remaining 20 % can be accounted for by Sb-Sb and Sb-Mn bonding environments. The binding energies for the Sb-Sb and Sb-Mn environments are 32.19 eV and 31.67 eV respectively, while the Sb oxide environment has a more variable binding energy due to the presence of multiple Sb oxides (Sb_2O_3, Sb_2O_4 and Sb_2O_5 [113]). Further details on the wet etch cleaning process for MnSb can be found in References [28] and [34].

Although electron diffraction, such as that presented in Figure 4.2, is ideal for the in-situ study of the growth surface it provides relatively low lattice parameter resolution ($\pm$0.1Å) and no effects arising from the formation of polymorphs have been observed in RHEED to date [34]. To this end, X-ray diffraction provides improved lattice parameter resolution and enables the study of the entire film thickness due to the large mean free path of X-rays.

4.3 Structural overview of MnSb polymorphs

As outlined previously, TEM studies of MnSb films show the presence of three crystal structures: cubic (c-MnSb), wurtzite (w-MnSb) and (n-MnSb) and the experimentally determined lattice parameters are given in Table 4.1. Note that the cubic phase was determined to be the zincblende structure from HRTEM although it is referred to as the cubic phase for simplicity. An initial study of the behaviour of the structural parameters of these polymorphs concluded that there were no obvious trends relating to $J_{\mathrm{Sb/Mn}}$ [34]. Although the presence of strained c-MnSb crystallites was determined from this data, the low intensities and absent higher order reflections precluded a more detailed analysis of the polymorph. Equally, the wurtzite polymorph was seen to be entirely absent in the majority of samples and, where present, the observed peaks were of low intensity. To this end, high resolution XRD (HRXRD) has been performed on beamline X22C at the NSLS to exploit the increased intensity available from this source.

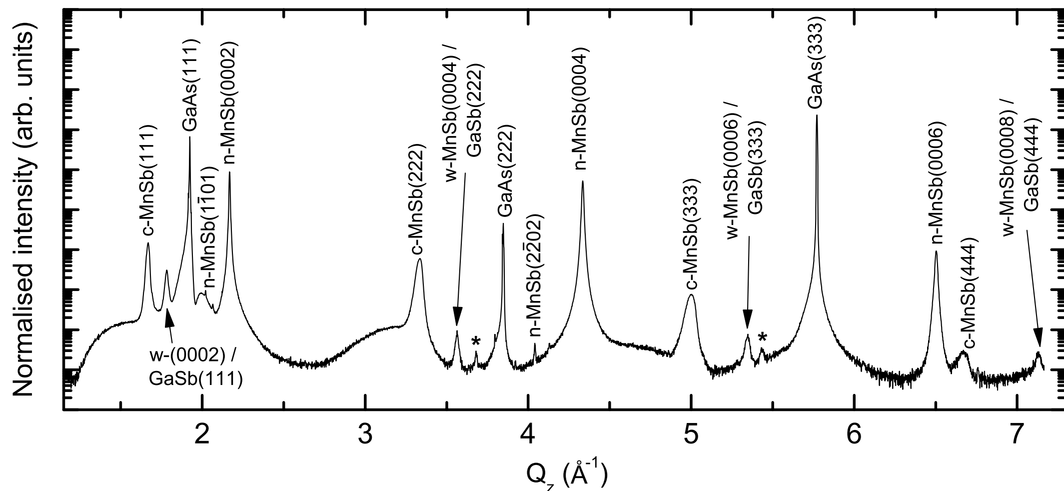

Figure 4.5: Symmetric XRD data for a nominally 180 nm thick MnSb film grown using a J_{corr} value of 7.05. Reflections originating from GaAs, n-MnSb, c-MnSb and w-MnSb/GaSb are all identified, in addition two reflections arising from MnSb(1$\bar{1}$01) crystallites are observed. Reflections marked by $*$ are unidentified and their origin is unknown.

Typical symmetric synchrotron HRXRD data for a 180 nm thick MnSb sample is shown in Figure 4.5. The most intense reflections are readily assigned to diffraction from the GaAs{111} and n-MnSb{0002} planes, while reflections arising from c-MnSb{111}, GaSb{111} or w-MnSb{0002}, and MnSb(1$\bar{1}$01) crystallites are also observed.

There are two unidentified peaks present at Q_z values of 3.681 and 5.434 Å^{-1} in Figure 4.5 and these are denoted by an $*$. Although these reflections cannot be indexed to any of the polymorphs and there exist four candidate origins for them. The first is the presence of stoichiometric compounds with increased Mn or Sb content, such as Mn_2Sb or $MnSb_2$. The growth of Mn_2Sb has been reported on GaAs(111) substrates, although the layers were found to be orientated $Mn_2Sb(002)\|GaAs(111)$ [114] and reflections from this family of planes do not account for either of the unknown reflections. The presence of $MnSb_2$ is rejected on the basis that it is only formed under high pressure conditions [115]. Secondly, the methods used to mount the samples for use in the growth chamber and for diffraction experiments provide sources of elemental In and Cu, respectively. However, no reflections from these two materials correspond to the unknown peaks.

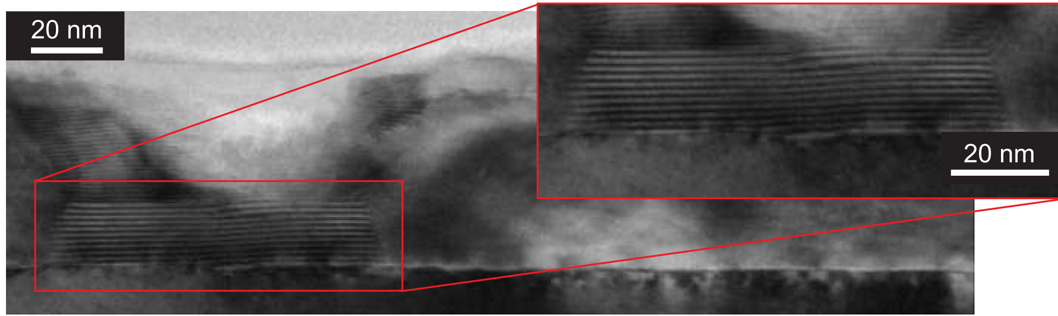

Figure 4.6: TEM image of the GaAs/MnSb interface revealing the presence of a large GaSb feature. The inset shows a zoom view of the crystallite.

Thirdly, although significant oxidation of the sample surface occurs following exposure to the atmosphere, resulting in MnO layers of ∼3–5 nm, no reflections from MnO could be attributed to the observed peaks. Finally, it is probable that the peaks arise from substrate reflections due to multiple scattering events, although this cannot be reliably determined as the reflections do not occur for all samples.

The presence of GaSb 'huts' at the MnSb/GaAs interface has been observed in TEM (confirmed by SADP measurements) and an example of such a feature is shown in Figure 4.6. The inset shown in Figure 4.6 indicates that the GaSb crystallites are approximately 20 nm in height and so are readily observed in the symmetric diffraction data presented in Figure 4.5. The origin of these huts is likely to be the reaction of incident Sb with Ga droplets on the GaAs surface, which form as a result of the IBA cycles used to clean the substrates. This reaction occurs on the substrate surface during the co-deposition of Mn and Sb, and so the GaSb structures are located at the MnSb/GaAs interface. Although the optimum growth temperature of GaSb is higher than that of MnSb, the large Sb overpressure compensates for this and so results in the formation of single crystal islands [116]. The ambiguity in differentiating between w-MnSb and GaSb features arises from the similar *d*-spacings of their respective crystallite orientations. Using the lowest index reflections present as an example, the GaSb huts are observed to be orientated (111) and the calculated *d*-spacing is 3.520 Å ($a_{\mathrm{GaSb}} = 6.096$ Å [117])

while w-MnSb crystallites are orientated (0002) giving a d-spacing value of 3.502 Å ($c_{\text{w-MnSb}} = 7.003$ Å). These spacings differ by $\sim$0.5 % and, due to stoichiometry variations and strain effects, are complex to reliably separate and analyse.

A similar situation occurs between reflections from c-MnSb(111) and h-Sb(0003) crystallites. The relevant d-spacings are 3.754 Å ($a_{\text{c-MnSb}} = 6.502$ Å) for c-MnSb and 3.758 Å ($c_{\text{Sb}} = 11.274$ Å [111]) for h-Sb. These spacings differ only by 0.1 % although it is straightforward to avoid this overlap by studying uncapped samples.

4.3.1 J dependence of the polymorphs

It can be seen from Figure 4.5 that HRXRD can be used to identify the presence and structure of MnSb polymorphs. It is then informative to briefly consider the relative polymorph content of a film against the primary growth parameter J_{corr} (the methodology for calculating J_{corr} was outlined in Section 2.1). The top panel of Figure 4.7 shows an illustrative schematic of the polymorph content (strong compared with weak) with varying J_{corr} for a range of MnSb films. Note that this only illustrates the presence of polymorphs and not the absolute content. The bottom panel then shows five θ-2θ scans of MnSb samples with the polymorph peak positions labelled. The definition of a 'strong' polymorph presence is that the peak height of the lowest index reflection available for a polymorph is greater than $10\times$ the background signal. A 'weak' presence is then defined as having less than $10\times$ the background counts but the peak is still readily identifiable. The two shaded regions indicate regions of non-optimal J_{corr} values. Samples grown using values in these regions often have non-optimal surface morphologies, with low J_{corr} samples (termed '*Sb-limited growth*') exhibiting Mn-rich surface features. At higher J_{corr} values (termed '*Non-planar growth*') a mesa-like morphology forms consisting of large terraces (>1 μm) separated by trenches with depths equivalent to the film thickness. The numbers displayed on each of the scans in the top panel correspond to the sample points labelled equivalently in the bottom panel. The first point to note is the difference between samples with nominally identical J_{corr} values, where the pres-

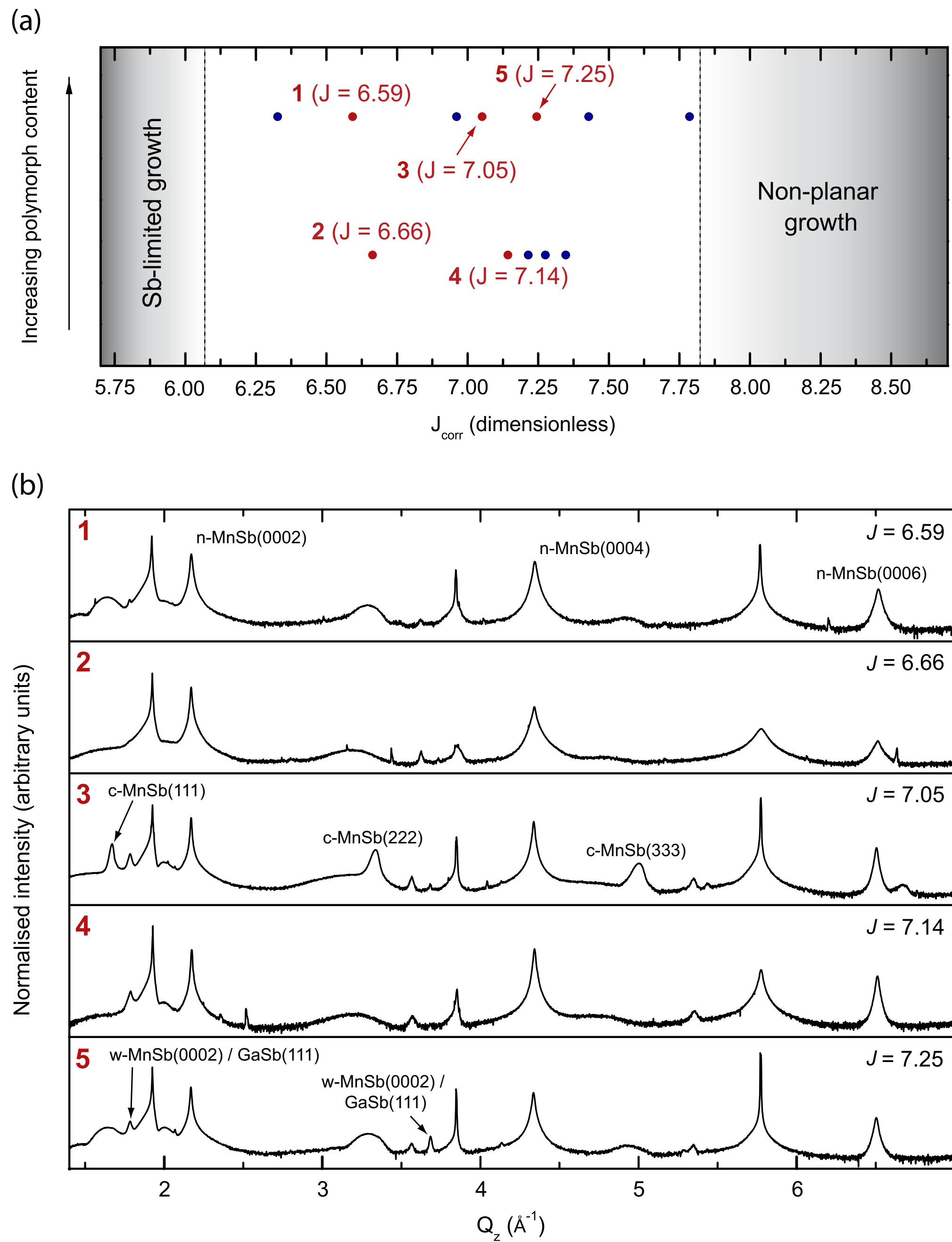

Figure 4.7: Panel (a) shows the relative polymorph content, 'strong' or 'weak', of several MnSb films. It can be seen that all of the films considered contain polymorphs and that the majority of samples are strongly polymorphic. Panel (b) shows symmetric XRD diffraction data for five MnSb films, labelled as in (a), of varying J_{corr} and the reflections arising from n-MnSb, c-MnSb and w-MnSb/GaSb have been identified and labelled accordingly.

ence of the polymorph can vary significantly and is most likely a result of a per-sample variation in the Mn or Sb fluxes. This is observed between samples (1) and (2) where strong c-MnSb peaks are observed in (1) but are absent in (2). Conversely, strong cubic reflections are observed in scans (3) and (5), both of which have a 'strong' presence of polymorphs based on the top panel of Figure 4.7. This variation in samples is likely due to the lateral inhomogeneity in the Mn flux, as outlined in Section 2.1. All five samples are observed to have a broad feature on the lower Q_z side of the labelled c-MnSb(222) position which suggests that strained c-MnSb exists in the majority of samples. As such, the polymorph presence and content varies significantly between samples, although all samples are observed to be polymorphic in some way.

In the following sections the behaviour of the lattice parameter and strain dispersion of the polymorphs are investigated as a function of grain size, J_{corr} and Mn flux. The behaviour of the predominant niccolite (n-MnSb) phase is considered first as it is the predominant phase present in MnSb thin films. Subsequently the behaviour of the cubic (c-MnSb) and wurtzite (w-MnSb) phases are discussed.

4.4 Structural characterisation of MnSb polymorphs

Although J is a critical growth parameter, it is observed to have no significant effect on the presence or apparent amount of a particular polymorph. However, all three polymorphs are observed to co-exist within films and, consequently, it is essential to study the niccolite polymorph (which comprises the majority of the film) first in order to understand the crystal 'framework' that the other polymorphs reside in. From the TEM presented in Section 4.1, it can be seen that the cubic and wurtzite polymorphs exist within the upper regions of a layer and constitute only a small proportion (<1 %) of the film. Due to their location, the c-MnSb and w-MnSb crystallites will be strongly influenced by the structural properties (mosaic, grain size, strain) of the n-MnSb. There are several variables that can affect the growth and formation of the polymorphs: the layer thickness, the lattice parameter and the strain dispersion within the film grains.

Addressing the importance of the layer thickness first, the polymorphs were observed to form in the upper regions of samples (typically after hundreds of nanometres of growth) although the number of samples imaged using TEM is relatively low and so a more comprehensive study of the thickness dependence is required. Although a variation in the lattice parameter will occur due to the presence of strain, it can also arise from changes in stoichiometry which aid in generating stacking order faults that may then aid the formation of polymorphs.

4.4.1 Niccolite MnSb

High resolution data has been collected for 19 MnSb thin films with thicknesses ranging from 2 to 300 nm and with $J_{\mathrm{Sb/Mn}}$ values between 6.2 and 7.9. It is worth briefly noting the difference between $J_{\mathrm{Sb/Mn}}$ and J_{corr}. The value of $J_{\mathrm{Sb/Mn}}$ is determined prior to growth and is set by fixing the fluxes of the Mn and Sb cells, while J_{corr} is a corrected $J_{\mathrm{Sb/Mn}}$ value that takes into account the spatial and temporal inhomogeneities of the cells. The benefit of using J_{corr} in this study arises from the correction of the value for the layer thickness (and cell behaviours) in addition to better representing the average value of J throughout the layer as observed by the X-ray beam. The n-MnSb c lattice parameter of each layer was determined from the positions of the n-MnSb(0002), (0004) and (0006) reflections. The 2θ FWHM were then subsequently used for Scherrer and Williamson-Hall analysis in order to determine the grain size (thickness) and strain dispersion within the n-MnSb crystallites present in these layers.

Lattice parameter behaviour of n-MnSb

Figure 4.8 shows the relationship between the measured lattice parameter and the grain size, as determined from Williamson-Hall analysis. The first thing to note is that the values are centred around an average c_{MnSb} parameter of 5.791(1) Å, in good agreement with the reported bulk value of 5.789 Å [78, 118] (indicated by the red dashed line). The second point to note is the increased lattice parameter for thinner samples,

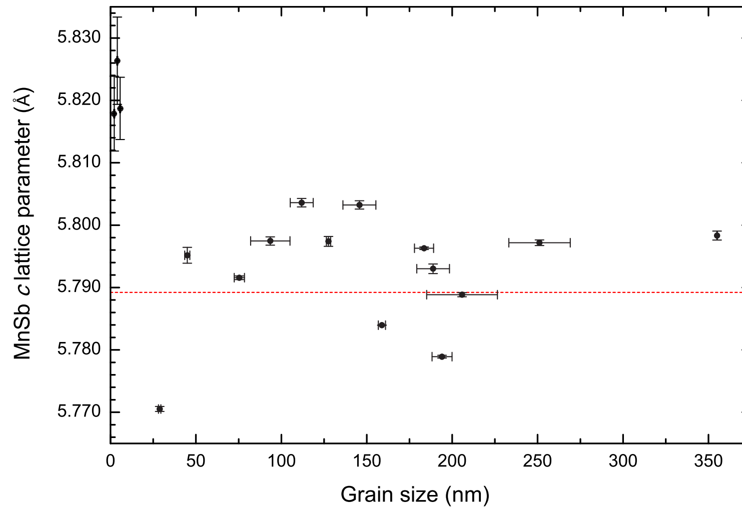

Figure 4.8: Variation of the n-MnSb c lattice parameter as a function of grain size (determined from Williamson-Hall analysis). The red dashed line indicates the published bulk c parameter of 5.789 Å.

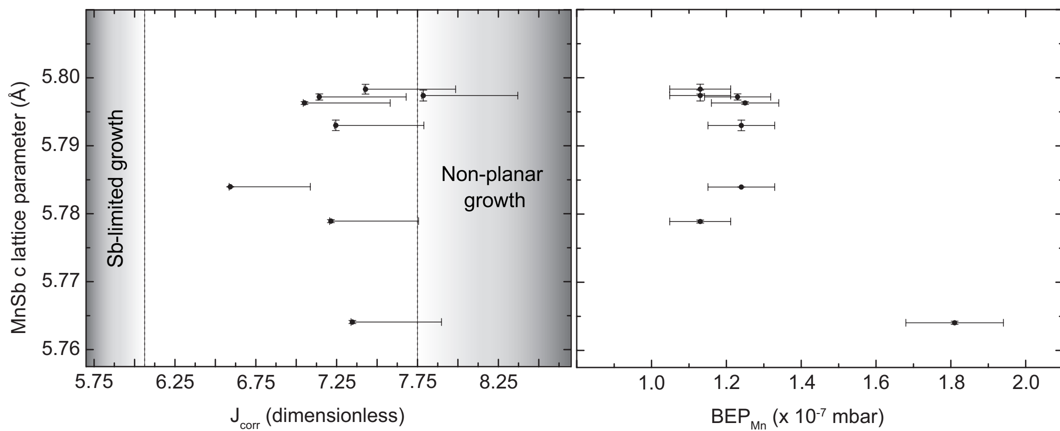

Figure 4.9: Variation of the n-MnSb c lattice parameter (for films >125 nm thick) as a function of J_{corr} (left panel) and Mn flux (right panel), BEP_{Mn}, which is proportional to the growth rate. The shaded regions in the left hand panel indicate non-optimal growth conditions.

which is indicative of epitaxial strain to the substrate.

For fully relaxed samples, with thicknesses greater than 125 nm, a comparison of the calculated c lattice parameters with J_{corr} and the growth rate can be made which is independent of any thickness effects. This relationship is shown in the left hand panel of Figure 4.9, while the right hand panel indicates the behaviour of the c parameter

with Mn flux, which is representative of the growth rate.

No clear trend between the c lattice parameter and J_{corr} or the growth rate were observed, supporting the observations from Figure 4.7. However, the variation observed in the lattice parameter is significantly larger than the calculated uncertainties and could be attributed to varying stoichiometry between samples. For low values of J_{corr} it is possible that the Mn-rich growth conditions would result in the incorporation of excess Mn into the niccolite structure and so act to change the observed c lattice parameter [26]. Studies on bulk crystals by Chen et al. [119] suggest that for approximately two percent of excess Mn the absolute change in c is $\sim$0.05 Å. As such, the observed variation in c lattice parameter seen in Figure 4.8 could be attributed to variations in the sample stoichiometry. Figure 4.10 shows the apparent level of polymorph, based on the information obtained for the bottom panel of Figure 4.7, plotted against the c lattice parameter, the vertical dashed line indicates the bulk parameter. For increasing Mn content a *decrease* in the c parameter is observed and so suggests that the majority of films actually exhibit a slight deficit in Mn concentration. The change in parameter associated with a change in stoichiometry leads to the presence of internal strains within the niccolite crystal structure and these may act to promote polymorph formation. These internal strains can be studied using Williamson-Hall analysis of the peak positions and FWHM, as described in Section 2.4.3.1.

Williamson-Hall analysis

The analysis of the FWHM(2θ) values of a family of reflections can be used to determine the strain dispersion present in a thin film. Figure 4.11(a) shows a typical Williamson-Hall plot used to calculate the strain dispersion, while panel (b) shows the strain dispersion of n-MnSb crystallites as a function of grain size. It can be seen that the n-MnSb crystallites are relaxed for thicknesses greater than 125 nm, although some residual strain dispersion along the n-MnSb c axis ($\frac{\Delta c}{c}$) is present in layers up to 350 nm in thickness and its origin can be explained as follows. Firstly, the formation of

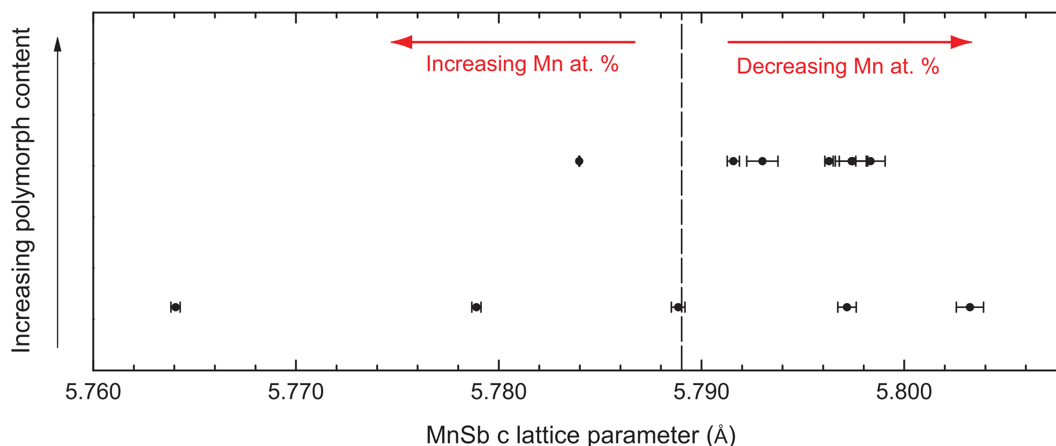

Figure 4.10: Apparent polymorph content as a function of n-MnSb *c* lattice parameter, the vertical dashed line indicates the bulk *c* lattice parameter. The arrows indicate the effect on the lattice parameter of increasing or decreasing Mn atomic percentage within the niccolite structure.

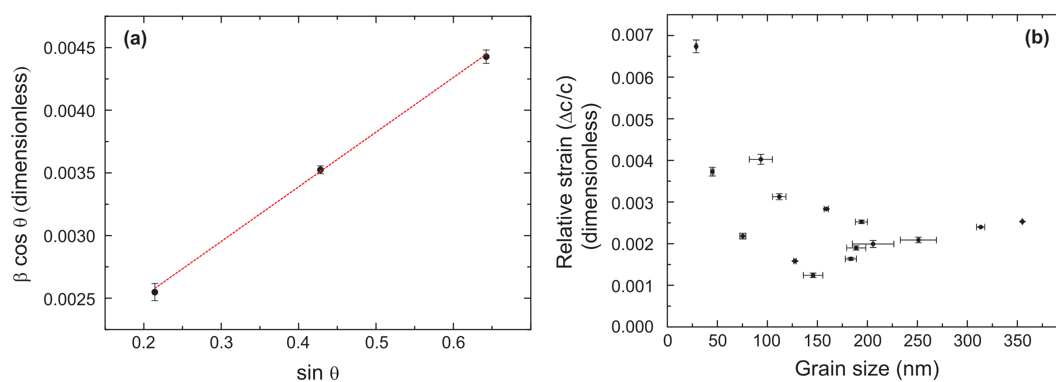

Figure 4.11: Panel (a) shows a typical Williamson-Hall plot for a 150 nm thick n-MnSb film, the linear increase in $\beta \sin\theta$ for increasing $\sin\theta$ is indicative of a strain contribution to the n-MnSb peak FWHM. Panel (b) shows the variation of the strain dispersion with sample thickness and indicates that thicker samples are highly relaxed with strain dispersions of $\sim$0.15 %.

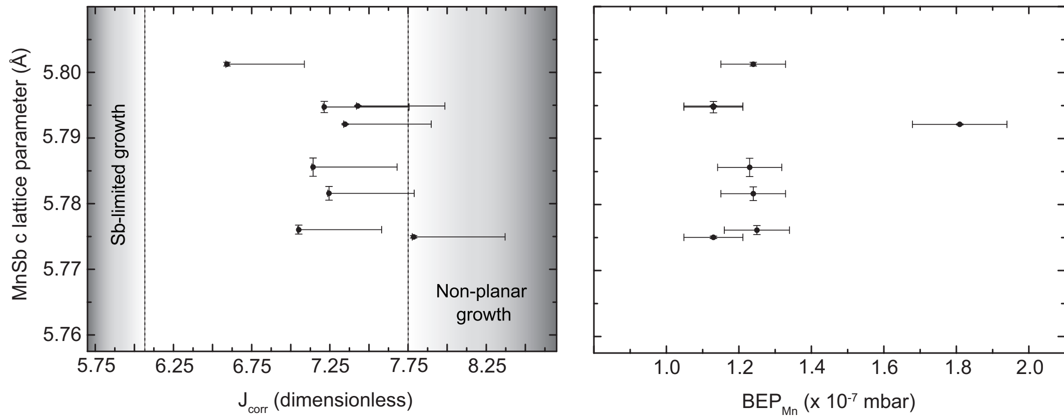

Figure 4.12: Strain dispersion behaviour for n-MnSb crystallites (in films >125 nm thick) as a function of J_{corr} (left panel) and Mn flux (right panel), BEP_{Mn}. Note that the shaded regions in the left hand panel indicate non-optimal growth conditions.

misfit dislocations acts to reduce some of the strain present in the overlayer due to the mismatch with the substrate. However, the dislocation network cannot accommodate all of the strain [57] and so some residual strain must be present. As the film thickness grows, relaxation can continue through the expansion, or formation, of defects in the additional layer material and so thicker films will have lower residual strains. Secondly, the small number of slip systems in the hexagonal close packed structure reduces the mobility of defects and so limits defect related relaxation. Finally, some additional strain is induced in the layer during cooling from the growth temperature owing to the different thermal expansion coefficients of GaAs and MnSb.

If the stoichiometry is varying with J_{corr} on a local scale then a change in lattice parameter away from the equilibrium value will result in the formation of internal strain fields. As the polymorph crystallites are observed to form within the n-MnSb framework then these local strain fields may induce the formation of polymorph crystallites. Figure 4.12 shows plots of residual strain against J_{corr} (left panel) and the growth rate (Mn flux, right panel). No clear trend is present for J_{corr}, while a mixture of strain values is observed for similar Mn fluxes. On this basis, the residual strain present in the layers is then due to the grain size in the film and the difference in expansion coefficients

between GaAs and MnSb. Residual strain will have the greatest effect on n-MnSb at low thicknesses and the following section outlines the behaviour of ultra-thin samples of MnSb.

Thickness evolution of n-MnSb

It can be seen from Figure 4.8 that the c lattice parameter of n-MnSb increases with decreasing thicknesses, h. This is unsurprising as in-plane compressive strain will force the a lattice parameter to match the GaAs a lattice parameter and so will correspondingly increase the c parameter through an approximately volume conserving distortion. This initial growth is pseudomorphic and occurs up to the critical thickness, after which the stored strain energy in the layer is minimised through the formation of misfit dislocations.

The behaviour of samples in the thickness range 2 - 30 nm have been investigated and symmetric diffraction data are presented for 2, 3, 5 and 30 nm samples in Figure 4.13. The figure shows both the (0002) reflection (left-hand side of the axis break) and the (0004) reflection (right-hand side of the axis break) regions. It is evident for the thinnest layers that finite-size broadening, in conjunction with the reduced scattering volume, causes the (0002) reflection to be low in intensity. The combination of this low intensity and the tails of the GaAs(111) reflection result in the formation of asymmetric peaks which are non-trivial to fit reliably. The high Q_z shoulder on the GaAs reflection could be attributed to strained n-MnSb and, due to its proximity to the GaAs, is strongly asymmetric. However, the presence of n-MnSb(0002) and Sb(0003) thickness fringes which coincide with the location of the shoulder (Q_z = 1.97 Å^{-1}) further complicate fitting.

Due to the complexity of the (0002) reflection region, the (0004) reflection has instead been used to determine the structural parameters of the layers. The benefit of using this reflection arises from the absence of any nearby peaks which confuse the analysis, the values determined by fitting the n-MnSb(0004) reflection are summarised

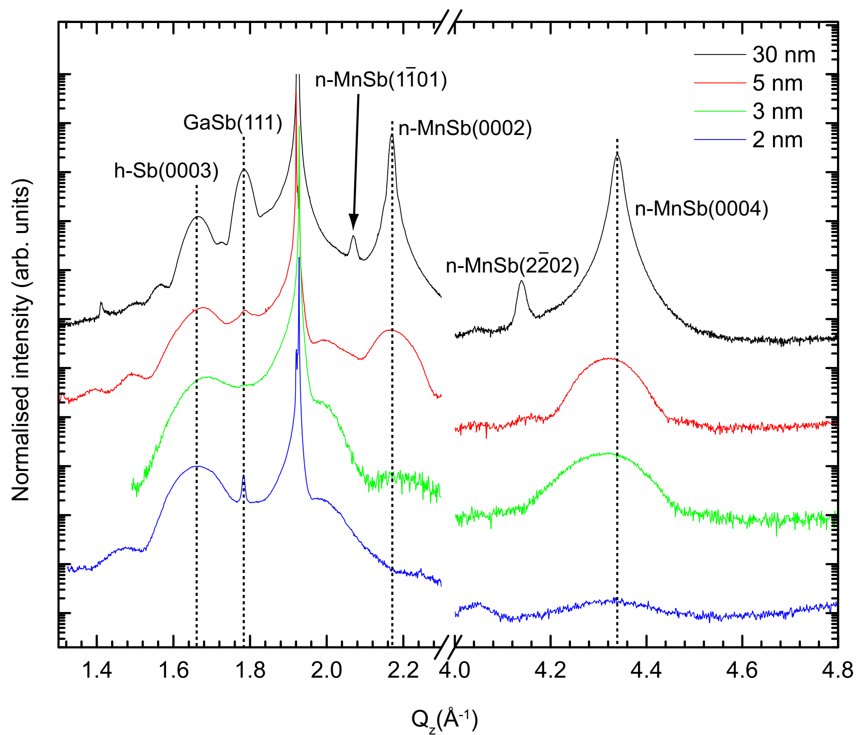

Figure 4.13: Symmetric diffraction data about the n-MnSb(0002) and (0004) reflection regions for samples with thicknesses of 30, 5, 3, and 2 nm (in order from top to bottom of figure), note that each scan is offset vertically for clarity. The vertical dashed lines indicate reflections from h-Sb(0003), GaSb(111) and n-MnSb(0002) while the presence of n-MnSb(1$\bar{1}$01) crystallites have only been observed for the 30 nm sample.

Table 4.2: Lattice parameters and crystallite size (from Scherrer analysis) obtained from fitting the n-MnSb(0004) peaks shown in Figure 4.13.

Thickness, growth est.(nm)	Q_z (Å^{-1})	c lattice parameter (Å)	Crystallite size (nm)
2	4.320(4)	5.818(5)	1.8(1)
3	4.314(5)	5.826(7)	3.6(1)
5	4.320(5)	5.819(6)	5.2(1)
30	4.339(1)	5.792(1)	31.8(4)

in Table 4.2. As seen from Figure 4.8 the c lattice parameters for the thin samples are larger than the bulk parameter by ∼0.5 %, while the crystallite sizes are similar to the expected sample thickness although they lie outside the uncertainty margins. One possible reason for this is that MnSb films with thicknesses less than ∼5 nm are known to consist of large islands that do not fully cover the surface [60]. The average island height will therefore be larger than if the film had grown in a continuous layer.

4.4.1.1 Rocking curve analysis

Although reliably separating the peak contributions from the (0002) region in the θ-2θ scans is complex, the in-plane structure of strained and unstrained n-MnSb would be expected to be different. As such, rocking curves can be used to distinguish between the strain states and are shown in Figure 4.14(a) for the 2, 3, 5 and 30 nm samples. The presence of two components with different FWHM, called 'narrow' and 'broad' in this discussion, is evident and indicates that there are two in-plane length scales contributing to the scattering.

The FWHM values derived from fitting the n-MnSb(0002) and n-MnSb(0004) rocking curves are given in Table 4.3. From these values, it can be seen that the FWHM of the 'narrow' component (shown in the insets in Figure 4.14) increases as a function of film thickness. This increase is likely due to the relaxation of the scattering crystallites and is corroborated by the absence of a narrow component for the 30 nm sample, which is expected to be relaxed. In contrast, no clear FWHM trend with thickness is evident for the 'broad' peak suggesting that at these thicknesses no additional relaxation takes place. From the measured widths, it is thought that the 'narrow' peak arises from strained pseudomorphic crystallites, while the 'broad' peak arises from relaxed crystallites. The increasing FWHM of the narrow component between 2 and 5 nm, in addition to the observed decrease in intensity relative to the 'broad' component, indicates that relaxation of these crystallites is rapid.

As outlined in Section 2.4.3.2 the formation of an island dominated structure

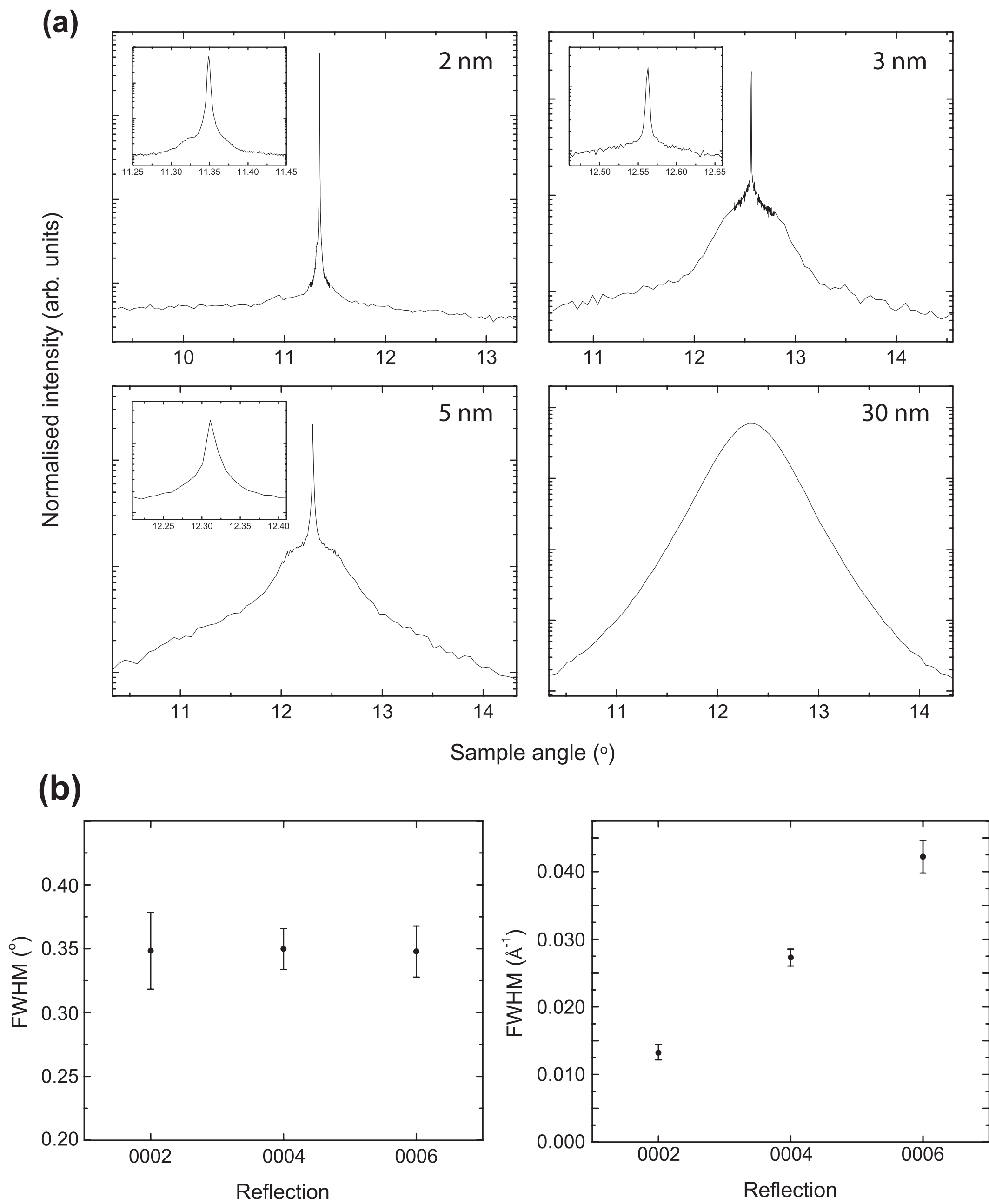

Figure 4.14: (a) Rocking curves for the n-MnSb(0002) reflection for 2, 3, 5 and 30 nm thick films. The main panels show wide-range scans indicating the presence of a broad component in the rocking curve, while the insets are zooms indicating the presence of a narrow component. Note that no narrow component is observed for the 30 nm sample. (b) The variation in the rocking curve FWHM of the n-MnSb{0002} family of reflections for a 180 nm thick film, showing the angular (left) and Q (right) dependence. A variation in Q but not in angular space indicates a mosaic dominated structure.

Table 4.3: θ and Q values for the FWHM of the 'narrow' and 'broad' rocking curves components observed for thin MnSb films. Note that no narrow component is observed for the 30 nm sample.

Thickness (nm)	GaAs FWHM (Å^{-1})	'Narrow' FWHM (Å^{-1})	'Broad' FWHM (Å^{-1})
	(0002) reflection		
2	$(9.35\pm0.07)\times10^{-5}$	$(1.06\pm0.05)\times10^{-4}$	$(1.43\pm0.2)\times10^{-2}$
3	$(1.02\pm0.07)\times10^{-4}$	$(1.47\pm0.03)\times10^{-4}$	$(2.45\pm0.03)\times10^{-2}$
5	$(1.00\pm0.03)\times10^{-4}$	$(2.93\pm0.02)\times10^{-4}$	$(2.56\pm0.04)\times10^{-2}$
30	$(2.36\pm0.03)\times10^{-4}$	-	$(2.00\pm0.04)\times10^{-2}$
	(0004) reflection		
2	-	-	-
3	-	$(3.21\pm0.2)\times10^{-4}$	$(4.61\pm0.08)\times10^{-2}$
5	-	$(5.34\pm0.08)\times10^{-4}$	$(4.88\pm0.08)\times10^{-2}$
30	-	-	$(3.88\pm0.07)\times10^{-2}$

Thickness (nm)	GaAs FWHM (°)	'Narrow' FWHM (°)	'Broad' FWHM (°)
	(0002) reflection		
2	$(2.97\pm0.02)\times10^{-3}$	$(3.04\pm0.01)\times10^{-3}$	$(4.1\pm0.2)\times10^{-1}$
3	$(3.00\pm0.2)\times10^{-3}$	$(3.81\pm0.01)\times10^{-3}$	$(6.3\pm0.1)\times10^{-1}$
5	$(2.77\pm0.07)\times10^{-3}$	$(7.72\pm0.04)\times10^{-3}$	$(6.7\pm0.1)\times10^{-1}$
30	$(6.60\pm0.09)\times10^{-3}$	-	$(5.3\pm0.3)\times10^{-1}$
	(0004) reflection		
2	-	-	-
3	-	$(4.2\pm0.02)\times10^{-3}$	$(6.1\pm0.1)\times10^{-1}$
5	-	$(6.9\pm0.1)\times10^{-3}$	$(6.7\pm0.1)\times10^{-1}$
30	-	-	$(5.0\pm0.3)\times10^{-1}$

results in the rocking curve FWHM remaining constant in Q but varying with θ, while the reverse is true for mosaic dominated growth. From the values presented in Table 4.3 both the narrow and broad components exhibit a mosaic structure. For the narrow component, this is due to the mosaic inherent in the substrate while for the broad component the behavior is dominated by the formation of misfit dislocations arising from the lattice mismatch between GaAs and n-MnSb ($\sim$3.2 %). Figure 4.14(b) shows the rocking curve FWHM behaviour (both in θ and in Q) with reflection for a 190 nm, indicating a mosaic of 0.35 $^\circ$ which is lower than for the thinner samples. This indicates that additional relaxation occurs as the sample thickness increases, although further study of intermediate film thicknesses are necessary to confirm this.

From the results presented above the initial growth of n-MnSb is thought to proceed through the formation of a pseudomorphic layer up to the critical thickness. Beyond this value, relaxation in the layer takes place through the formation of misfit dislocations and the generation of a mosaic structure (shown in Figure 2.14). The co-existence of both strained (pseudomorphic) and relaxed n-MnSb is observed in layers up to 5 nm thick. For samples greater than 30 nm in thickness no sharp component is seen and so the pseudomorphic layer is assumed to be completely relaxed. This growth progression is illustrated schematically for n-MnSb islands on GaAs in Figure 4.15, the top panel shows a sample where $h < h_C$ and the n-MnSb layer is pseudomorphic. As more material is deposited, localised growth leads to the formation of islands that have above average height. Consequently, when these regions reach h_C then relaxation occurs and misfit dislocations are formed, yielding the mosaic structure observed with a mosaic angle (related to the FWHM values given above) of θ_{mosaic}. A tentative estimate of the critical thickness of n-MnSb can then be made from Figure 4.14 on the basis of the change in intensity of the 'broad' component between 2 and 3 nm, and so h_C is within this range. However, the presence of islands, of varying thickness, complicates accurate determination of this value as islands that have $h > h_C$ can exist simultaneously with islands where $h < h_C$. Despite this, the critical thickness of n-MnSb on GaAs is observed

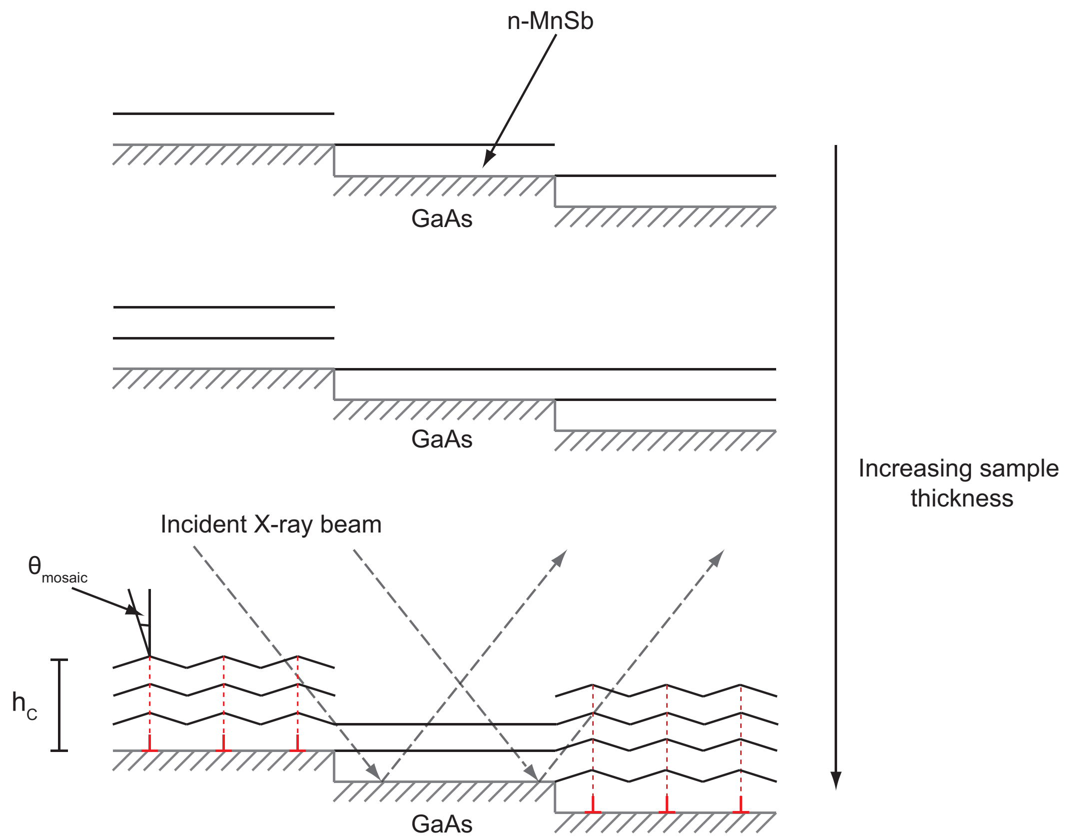

Figure 4.15: Schematic illustrating the progression of n-MnSb film growth via island formation and the subsequent relaxation of these islands. The inverted red 'T' shapes at the GaAs/MnSb interface indicate the position of misfit dislocations which give rise to the mosaic angle, θ_{mosaic}.

to be very low and a product of the large lattice mismatch. An estimate of the critical thickness can be made using the model of Matthews and Blakeslee [120] and is calculated to be 1.8 nm in the case of MnSb(0001) films on GaAs(111). Although this value is lower than the experimentally determined value of h_C the estimated thickness is calculated using a Poisson ratio of 0.33, more commonly used for the III-V semiconductors [57], and so may not be applicable to MnSb. The actual Poisson ratio for MnSb is currently unknown. Further structural studies of ultra-thin samples in this thickness range are therefore necessary to refine the value of h_C and separate out effects related to the island thickness.

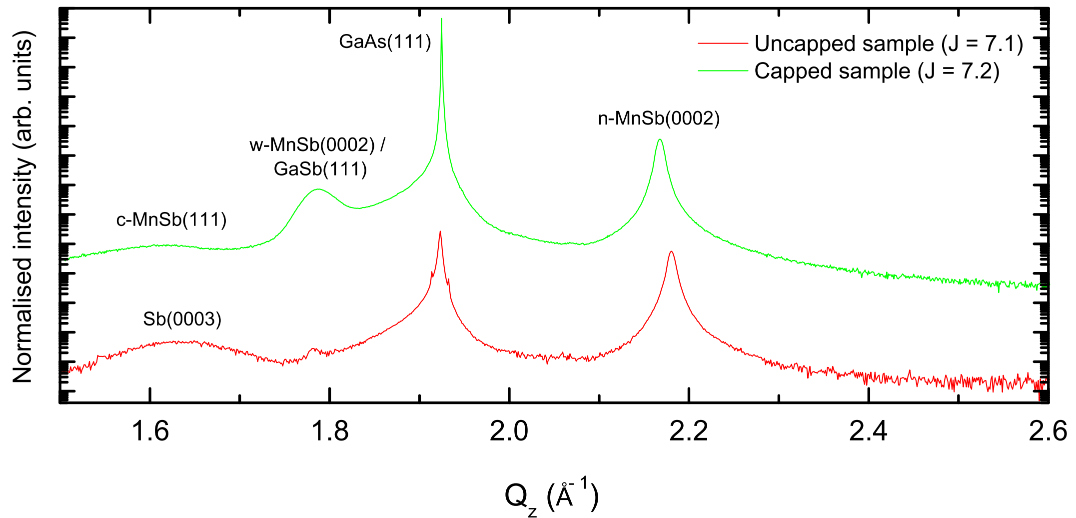

Figure 4.16: Typical XRD data showing a comparison between a capped (top) and uncapped (bottom) MnSb film in the region around the GaAs(111) reflection.

In summary, the n-MnSb framework is observed to relax at thicknesses greater than 3 nm and a mosaic of 0.35° develops as the film grows. The n-MnSb is observed to be structurally homogenous on a per-sample basis although the variation in the c lattice parameter suggests that the sample stoichiometry is variable. The mosaic structure of the film and the residual strain dispersion in thick films ($>$125 nm) of $\sim$0.15 % will influence the resulting structural properties of the polymorphs.

4.4.2 Cubic MnSb

The presence of zincblende MnSb crystallites is of great interest for spintronic applications due to their structural compatibility with cubic semiconductors and their high spin polarisations. However, the formation mechanism of the cubic polymorph is not yet fully understood. A key question is then: what effect do the growth conditions have on the structural properties of the polymorphs? This is a crucial first step in understanding why c-MnSb forms within n-MnSb thin films. As discussed in Section 4.3 the c-MnSb(111) and h-Sb(0003) reflections coincide and an example of this is shown in Figure 4.16. Here it can be seen that the peaks occur at identical positions and have

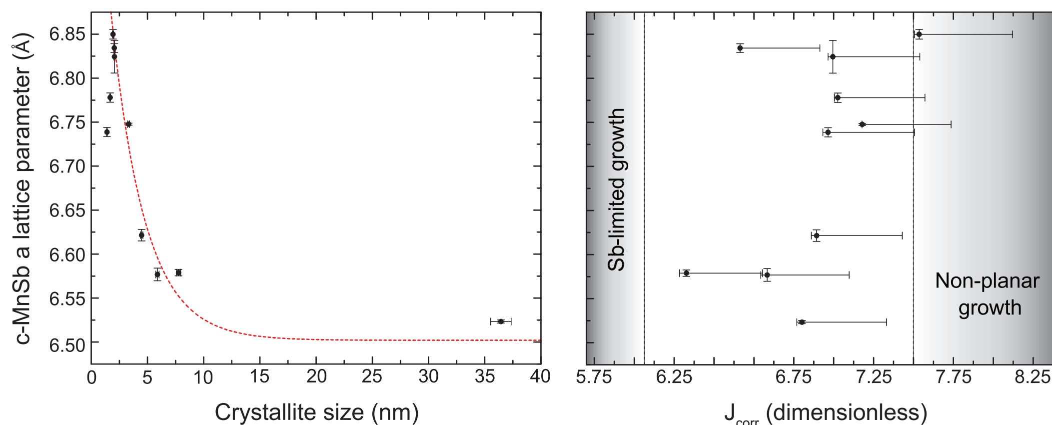

Figure 4.17: Variation in c-MnSb *a* lattice parameter as a function of crystallite size and J_{corr}. The red dashed line in the left hand panel is an exponential fit to the data using an offset of 6.502 Å, while the shaded regions in the right hand panel indicate non-optimal growth conditions.

similar shapes and FWHM. To this end, all of the samples studied in this section were uncapped to avoid the overlap of reflections.

If the strain and stoichiometry present in the n-MnSb framework were influencing the formation of cubic crystallites, then a comparison of the c-MnSb *a* lattice parameter with the n-MnSb *c* lattice parameter or strain should indicate the effect of the framework on the polymorph. However, no trends are observed between these parameters and one possible reason for this is an averaging over a wide range of J_{corr} due to the variation in $J_{Sb/Mn}$ over the sample. Typical strain energies are of the order 0.1 eV per formula unit [121] for mismatches of $\sim$16 % while the difference in total energy between the polymorphs is approximately 0.83 eV. As such, strain energy by itself cannot result in polymorph formation even when considering the large 10.2 % mismatch between c-MnSb and n-MnSb.

Figure 4.17 shows the *a* lattice parameter variation with cubic crystallite size (as determined from the lattice parameter determination methodology outlined in Section 2.4.3.1) and J_{corr}, note that Scherrer analysis has been used as the majority of samples only feature (111) and (222) reflections, providing unreliable fits when used for Williamson-Hall analysis. It is evident that the *a* lattice parameter relaxes with in-

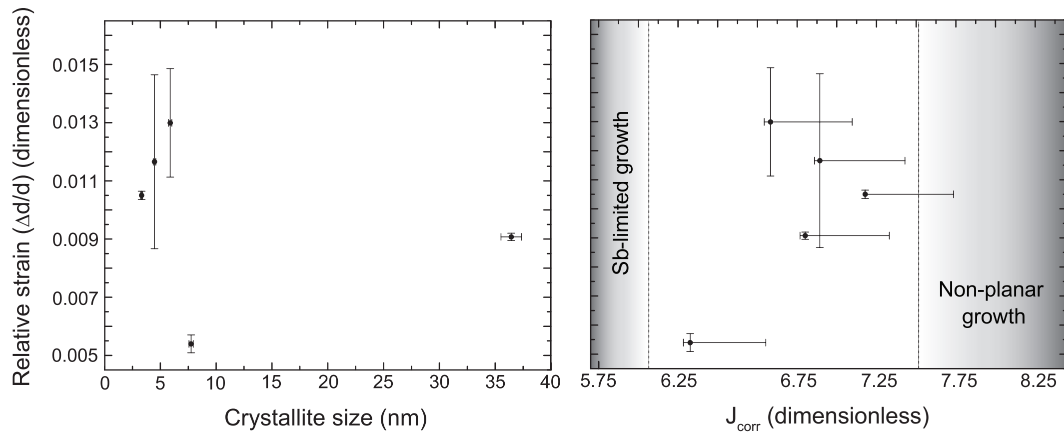

Figure 4.18: Strain dispersion behaviour for c-MnSb crystallites as a function of crystallite size and J_{corr}. The shaded regions in the right hand panel indicate non-optimal growth conditions.

creasing crystallite size towards a value of 6.5 Å, in agreement with the SADP value of 6.502 Å. An exponential fit to the data is presented in the left hand panel of Figure 4.17 and an estimated value of (3±1) nm for h_C was found from the decay constant of the fit. This value arises from the large mismatch between c-MnSb and n-MnSb of 10.2 % and is comparable to the value found for n-MnSb. No trend is seen in the behaviour of the *a* lattice parameter with J_{corr}, shown in the right hand panel of Figure 4.17. Additionally, no correlation is observed between the c-MnSb and n-MnSb lattice parameters, indicating that the presence of c-MnSb crystallites does not strongly influence the surrounding n-MnSb, which is unsurprising given the expected difference in polymorph quantities within the films. Given the large mismatch between c-MnSb and n-MnSb, it is expected that large strain dispersions will occur within the cubic crystallites. Figure 4.18 shows the strain behaviour with crystal size and J_{corr} from both plots it is evident that no clear trends occur. It should be noted that any conclusions drawn regarding the strain behaviour are limited due to the majority of samples missing several higher order reflections, which precludes the use of Williamson-Hall analysis. From the left hand panel of Figure 4.18 it can be seen that the crystallites are highly strained in comparison to the n-MnSb layer with strain dispersions of between 0.005 and 0.015 (0.5 – 1.5 %).

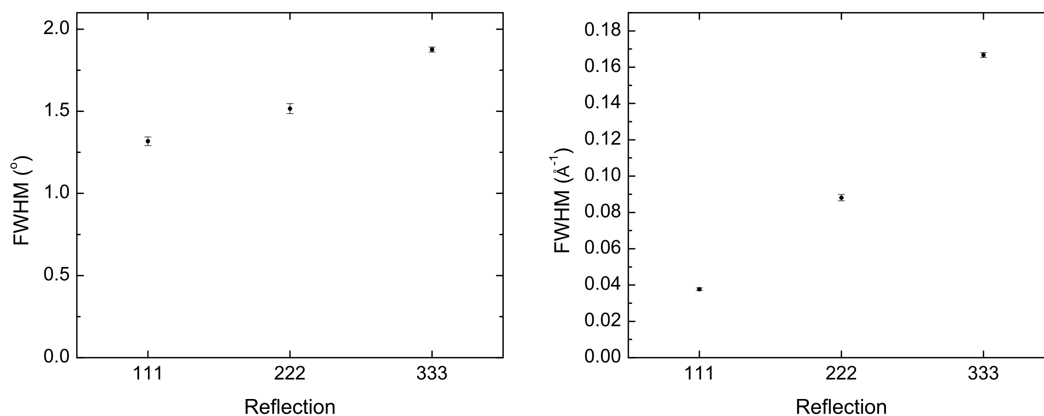

Figure 4.19: The variation of the rocking curve FWHM for the c-MnSb{111} family of reflections, showing the angular (left) and Q (right) dependence.

It is expected that the in-plane behaviour of the crystallites will be heavily influenced by the mismatch with the n-MnSb framework and will, in part, be influenced by the n-MnSb mosaic. Figure 4.19 shows the variation in the rocking curve FWHM values (shown in θ and Q) of the c-MnSb crystallites within a typical MnSb thin film. The rocking curves reveal FWHM θ values of between 1.2° and 1.9° and so the in-plane mosaic is much larger than that observed in n-MnSb. This increased mosaic is due to the increased strain from the large lattice mismatches that c-MnSb exhibits with the other MnSb polymorphs and GaAs. As both quantities are seen to vary with increasing diffraction angle (represented here by the (111), (222) and (333) reflections), then a correlation length and a mosaic structure dependence co-exist. The correlation length dependence arises from the size of the crystallites, which are considerably smaller than the X-ray coherence length, while the mosaic of the crystallites is influenced by both the mosaic of the n-MnSb layer and the increased formation of misfit dislocations due to the lattice mismatch. This, alongside the high levels of residual strain dispersion present, suggests that the crystallites are embedded within the n-MnSb framework and do not form exclusively at the top of the layer, as indicated by the TEM images presented in Figure 4.1. However, it should be noted that XRD does not have the same spatial resolution as TEM and, as such, no further conclusions can be drawn on the location of

the cubic crystallites within the film.

From the results presented above it can be seen that no significant trends between the lattice parameter, or strain dispersion, with either J_{corr} or grain size are present. The implication of this is that the thickness of the film and the growth conditions used do not strongly influence the formation of the cubic polymorph. Equivalently, c-MnSb crystallites are observed in nearly all of the samples studied, although no strong relationship between the growth conditions and the crystal quality of the polymorph are seen. It is evident that the crystallites themselves are under significant strain and could plausibly be embedded within a n-MnSb framework. However, the effect of strain on the half-metallicity of c-MnSb is currently unknown and further work, with an emphasis on DFT studies, may be necessary to determine the consequences of this strain. It is interesting to note that the *a* lattice parameter of c-MnSb (6.502 Å) is well matched to the lattice parameter of InSb (6.479 Å [117]) and so may provide a route for stabilising the growth of a layer composed entirely of the cubic polymorph. Further information on the preliminary growth of MnSb on InSb is presented in Appendix B.

4.4.3 Wurtzite MnSb

While the presence of c-MnSb has been conclusively identified from XRD measurements, w-MnSb crystallites have only been reliably identified on the basis of high resolution TEM experiments on a few samples. The difficulty in differentiating between the two materials on the basis of symmetric diffraction data means that a comparison of the *c* or *a* lattice parameters will reveal the same trends. However, it would be expected that the two materials would have different strain dispersions owing to their different formation points and so w-MnSb may exhibit a large strain dispersion due to the surrounding n-MnSb framework. As with c-MnSb, the absence of several higher order reflections means that the Scherrer analysis has been used to determine crystallite size.

Figure 4.20 shows the strain dispersion behaviour of the w-MnSb crystallites with

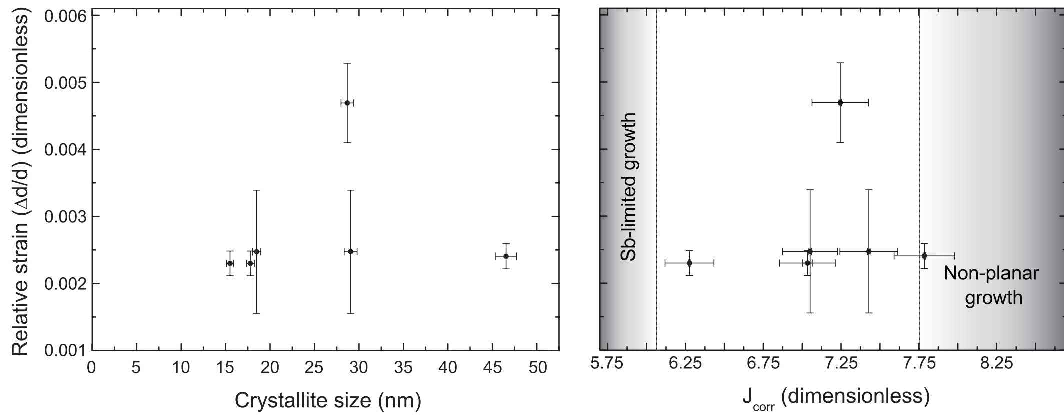

Figure 4.20: Strain dispersion behaviour of w-MnSb as a function of crystallite size (left panel) and J_{corr} (right panel). The shaded regions in the right hand panel indicate non-optimal growth conditions.

crystallite size and J_{corr}. No clear trend with either growth parameter is observed and, excluding a single outlier, the strain dispersion is constant around a value of 0.0025. As this observed value is relatively low and remains constant across a range of crystallite sizes, the origin of this peak is most likely relaxed crystallites. Through comparison with the cubic polymorph, which is seen to be highly strained due to the presence of the n-MnSb framework, it is likely that the primary contribution to the w-MnSb/GaSb diffraction peaks are from GaSb. Further evidence for this arises from the symmetric data obtained for the thin samples, as presented in Section 4.4.1 and in Figure 4.13, where for the 2 nm thick sample the size of the GaSb/w-MnSb inclusions is approximately 70 nm and is comparable to the feature size observed in Figure 4.6. On this basis it is likely that the reflections observed at these Q_z values consist almost entirely of scattering from GaSb.

4.4.4 Summary

On the basis of the results presented in Sections 4.4.1, 4.4.2 and 4.4.3 it is evident that θ-2θ scans are suitable for determining the structural properties of the crystallites present in these films. However, the presence of multiple phases that overlap reduces the effectiveness of analysis, as is evident in the case of w-MnSb/GaSb. Additionally,

Table 4.4: Summary of the samples studied using asymmetric RSMs in order to determine the in-plane lattice parameters and polymorph content of these films. Note that Samples A and C are uncapped.

Sample	J_{corr}	Grain size (nm)	Polymorph presence		Source used
			c-MnSb	w-MnSb	
A	6.81	115(9)	Yes	Yes	Lab source (Warwick)
B	7.03	75(3)	Capped	Yes	Synchrotron (NSLS)
C	7.21	194(6)	Yes	No	Lab source (Warwick)
D	7.35	313(4)	Capped	No	Synchrotron (Diamond)

ratios of the various polymorphs, which would indicate growth conditions that promote the formation of the polymorphs, cannot be obtained using the symmetric data as it represents a one dimensional slice through a three dimensional diffraction feature and so does not measure the true intensity of the feature. An alternative method for determining the ratios of the polymorphs is through the use of asymmetric reciprocal space maps, which then separate out reflections from the polymorphs (such that there is no overlap) and also provides a two dimensional area that can be integrated, resulting in more reliable ratios.

4.5 Reciprocal space map analysis

4.5.1 Polymorph identification

As outlined in Section 4.3, the difficulty in resolving w-MnSb and GaSb, in addition to c-MnSb and h-Sb, using symmetric data alone prevents a more complete analysis of the polymorphs. This section presents preliminary analysis of asymmetric RSMs with the aim of developing a methodology for the study of multi-phase MnSb samples. The reason for this is two-fold: firstly, analysis of the in-plane lattice parameters of thin samples is required for an understanding of the interface behaviour of heterostructures. Secondly, the ratio between the various polymorphs can be determined through the use of integrated peak intensities and so provide additional information on polymorph be-

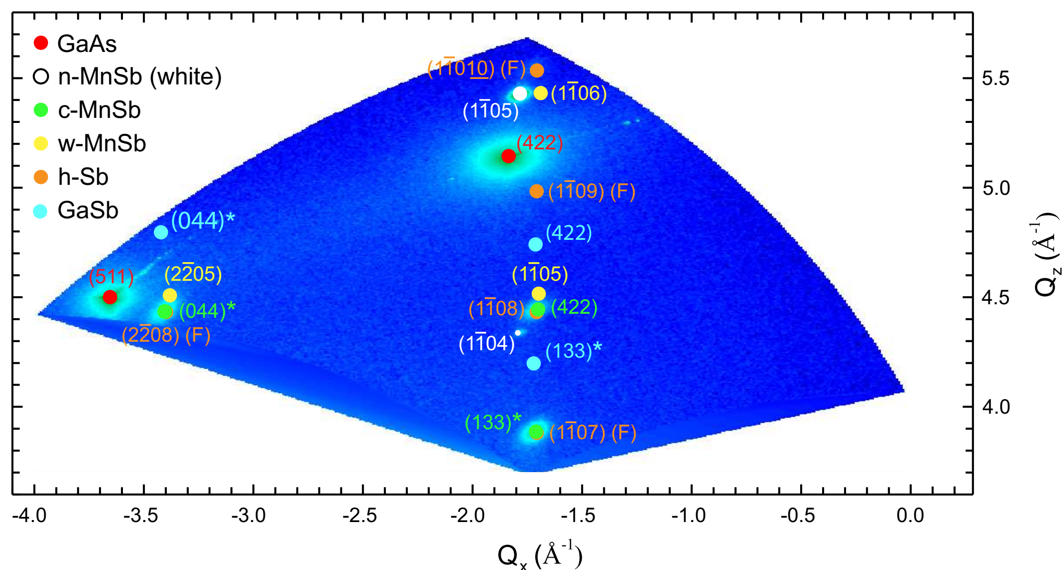

Figure 4.21: Asymmetric RSM for Sample A obtained around the GaAs(422) reflection. Also shown are reciprocal space nets for the allowed reflections of GaAs, n-MnSb, c-MnSb, w-MnSb, h-Sb and GaSb, note that the reciprocal space net for h-Sb includes the forbidden reflections which are denoted by (F) following the reflection indices.

haviour. Four samples have been studied using asymmetric RSMs and their details are given in Table 4.4.

Identifying the origin of the reflections present in a RSM is a necessary first step in determining both the lattice parameters and any relevant polymorph quantity ratios. Figure 4.21 shows a reciprocal space map around the GaAs (422) reflection for Sample A, reciprocal space nets have been generated using lattice parameters derived from symmetric diffraction and SADP data, and are overlaid on the map. The nets show all allowed reflections within the reciprocal space area studied, the exception to this is the forbidden h-Sb reflections shown which are discussed in more detail below. The Q value, and consequently the d spacing, of the observed reflections can be determined from the Q_x and Q_z positions using the simple trigonometric relation presented in Section 2.4.3. Note that Q_x and Q_z are defined relative to the GaAs(111) plane, such that reciprocal lattice vectors along the Q_z direction are of the form (111) and in the Q_x direction they are $(2\bar{1}\bar{1})$.

Due to the existence of multiple materials and crystal structures within the samples, the resulting reciprocal space maps are often complex. However, it is possible to index reflections originating from the substrate and n-MnSb polymorph rapidly due to their intensity and so any peaks remaining must originate from any polymorphs present in the layer. Of interest are the three features located at (Q_x,Q_y) positions, given in units of Å^{-1}, at (1.703,4.440), (1.697,3.883) and (3.399,4.432), which coincide with the positions of w-MnSb, h-Sb and c-MnSb reflections. It is straightforward to reject the presence of w-MnSb due to the absence of a feature at the $(1\bar{1}06)$ reflection position. Additionally the Q_z position of the w-MnSb net is derived from the symmetric diffraction data and so a systematic shift in the c parameter can be ruled out. In the case of h-Sb, it is more complex, as the $(1\bar{1}07)$, $(1\bar{1}08)$, $(2\bar{2}08)$ reflections all coincide with features in the map. However, the $(1\bar{1}07)$ and $(2\bar{2}08)$ reflections are forbidden and the presence of features at these positions is unexpected, therefore h-Sb is rejected on this basis. Consequently, the peaks are assigned to reflections from c-MnSb, the $*$ denotes that the reflections arise from crystallites that are rotated by 60° relative to the GaAs substrate. This acts to mirror the reciprocal net about the origin of reciprocal space and such a rotation occurs due to the difference in stacking orders between c-MnSb and n-MnSb. The cubic polymorph has an AaBbCc stacking order along the [111] direction (where capitalisation indicates atomic species and letter indicates the lattice site) while in n-MnSb it is AbAc along the [0001] direction. For an Sb terminated crystal, a change from an Ab to Ac layer results in a 60° rotation of the Sb bonds and so c-MnSb crystallites are able to nucleate on two different rotational domains.

In order to test the validity of using RSMs to measure the in-plane lattice parameter of the polymorphs, it is necessary to independently determine the in-plane lattice parameters. To this end, symmetric grazing incidence diffraction data have been collected for Sample A using beamline I16 at the Diamond Light Source (Rutherford Appleton Laboratory, UK) and are shown in Figure 4.22. Symmetric data is presented in panel (a) and indicates the presence of c-MnSb, w-MnSb (or GaSb) and n-MnSb

crystallites. Panel (b) shows an in-plane RSM obtained using a fixed incident angle geometry (α_i = 0.3°). The map was generated by first aligning the sample along the GaAs$\langle 2\overline{1}\overline{1}\rangle$ direction and then performing in-plane θ-2θ scans while rotating the sample about the surface normal (denoted by the angle ϕ). The angle of incidence was reduced to a value below the critical angle, resulting in a weak evanescent wave penetrating into the sample. This reduces the scattering depth (the depth at which the scattered intensity decreases to $1/e$) of the incident X-ray beam and so only the upper layers of the film are probed. The critical angle, α_c, of n-MnSb at the photon energy used (10 keV) is 0.44° and so the scattering depth (Λ_S), calculated using the methodology derived in Reference [122], is $\sim$12 nm. Under the assumption that the majority of detected intensity arises from within 3Λ_S then the effective probing depth is $\sim$36 nm, compared to the expected film thickness of 310 nm. Finally, panel (c) shows line scans at $\phi = 0°$, 30° and 60° from which values of the in-plane lattice parameters can be derived by using the fitting methodology used previously in this chapter. Note that the $\phi = 0°$ and 60° directions correspond to GaAs$\langle 2\overline{1}\overline{1}\rangle$ directions, while the $\phi = 30°$ direction corresponds to the GaAs$\langle 1\overline{1}0\rangle$ direction.

There are two interesting features to note from the in-plane data (Figure 4.22(b) and (c)): the first is the presence of pairs of reflections aligned along the high symmetry 0°, 30° and 60° directions; the second is the powder ring feature at $Q_{||}$ = 4.05 Å^{-1}. Considering the pairs of reflections first, the high $Q_{||}$ reflections in a pair arise from n-MnSb while the lower $Q_{||}$ features, denoted by arrows in panel (c), must then arise from polymorphs in the sample. The d-spacings of these reflections are given in Table 4.5, note that as the probing depth of the X-ray beam is less than the thickness of the film no reflections from the substrate are observed.

The presence of multiple materials complicates complete identification of the reflections in the in-plane map, although several candidate materials can be eliminated on the basis of the X-ray data presented so far. The presence of h-Sb is rejected due to absent reflections in the asymmetric RSM. The absence of any reflections associated

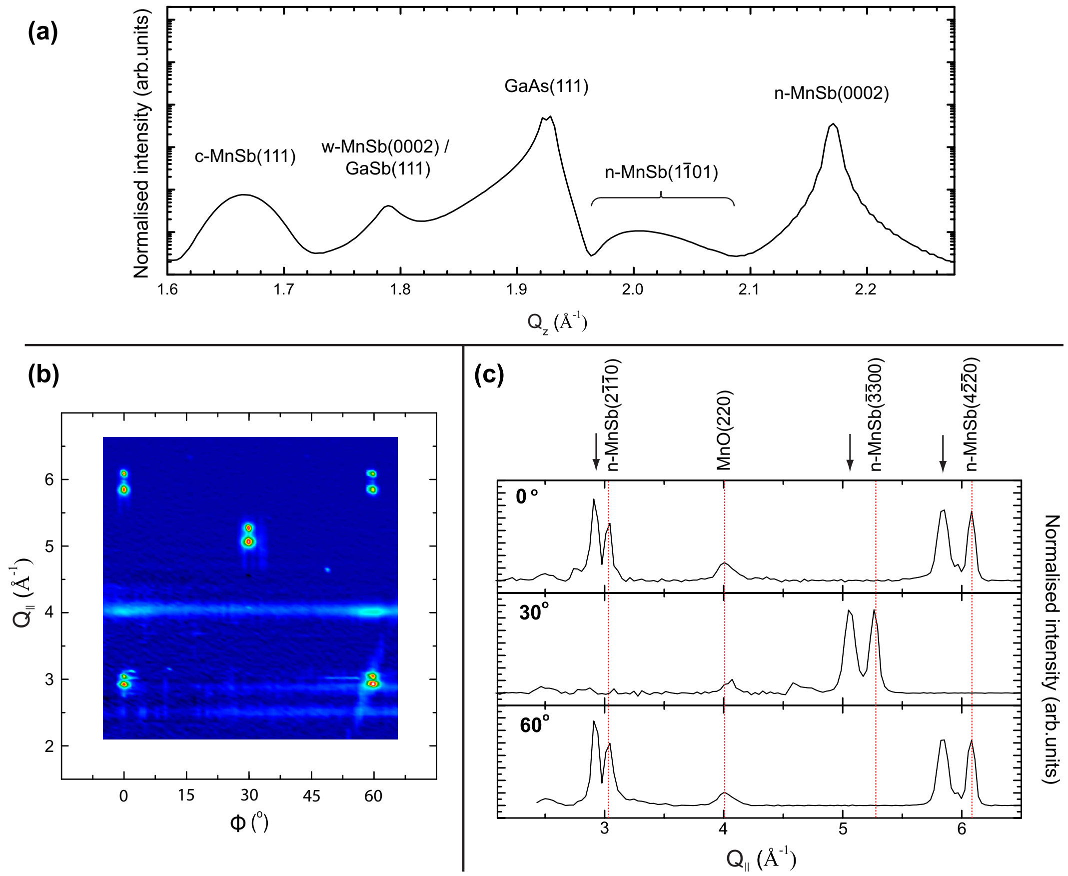

Figure 4.22: (a) Out-of-plane symmetric diffraction data for Sample A indicating the presence of GaAs(111) and n-MnSb(0002) reflections, in addition to reflections originating from c-MnSb(111) and w-MnSb(0002)/GaSb(111). (b) In-plane symmetric RSM for Sample A, ϕ is the azimuthal angle and corresponds to rotation about the surface normal. (c) In-plane symmetric θ-2θ scans along the 0° 30° and 60° high symmetry directions, the $\phi = 0°$ and 60° directions correspond to GaAs$\langle 2\bar{1}\bar{1} \rangle$ directions, while the $\phi = 30°$ direction corresponds to the GaAs$\langle 1\bar{1}0 \rangle$ direction.

Table 4.5: Candidate reflections for the in-plane symmetric θ-2θ scans presented in Figure 4.22(c). Shown is the azimuthal angle (ϕ), the $Q_{\|}$ value at which the reflection appears, the corresponding d-spacing and the corresponding reflection.

ϕ (°)	$Q_{\|}$ (Å^{-1})	d (Å)	Possible reflections
0	2.920(1)	2.152(1)	w-MnSb($2\bar{1}\bar{1}0$)
			h-Sb($2\bar{1}\bar{1}0$)
			GaSb(220)
			c-MnSb(220)
30	5.061(1)	1.242(1)	w-MnSb($3\bar{3}00$)
			h-Sb($3\bar{3}00$)
			GaSb(422)
			c-MnSb(422)
60	5.843(1)	1.076(1)	w-MnSb($4\bar{2}\bar{2}0$)
			h-Sb($4\bar{2}\bar{2}0$)
			GaSb(440)
			c-MnSb(440)

with the w-MnSb polymorph in Figure 4.21 suggest that no w-MnSb exists in the film. However, if w-MnSb is present then its large equilibrium energy will limit the thickness of any crystallites to a few unit cells. Such a low thickness would not be observable in the out-of-plane scattering, although the lateral extensions of these crystals would be large and so would give rise to intense peaks in the in-plane scattering. Note that the crystallites observed in the TEM are much larger than this, ∼30 nm thick, and so would be readily identifiable in the out-of-plane diffraction in addition to the RSMs, which is not the case for Sample A. As such, it is plausible that thin crystallites of w-MnSb could exist in the upper regions of the film. The presence of c-MnSb would be unexpected due to the large change in the in-plane lattice parameter (from 4.597 Å to 4.317 Å) required to observed the peaks at these $Q_{\|}$ values. From the symmetric data presented in Figure 4.17, the lattice parameter of c-MnSb tends towards 6.502 Å for large crystallites. Consequently, the in-plane (220) and (440) reflections would be expected at $Q_{\|}$ values of 2.733 and 5.466 Å^{-1} and these are not observed in the map. This value has been derived assuming a cubic structure with no strain, although if a

triclinic distortion occurs then it is plausible that an in-plane spacing equivalent to that of GaSb could result. Evidence of in-plane matching between GaSb and c-MnSb is observed in the RSM of Sample B, shown in Figure 4.23(a), where the reflections occur at identical value of Q_x. However, the most likely origin of the reflections is w-MnSb crystallites that are thin in the out-of-plane direction but have relatively large in-plane extents, and so are only observed in the grazing incidence scattering.

The powder feature located at $Q_{\|} = 4.05$ Å^{-1} is assigned to the (220) reflection from MnO crystallites (note that the sample was uncapped and so could therefore oxidise) and correspond to an *a* lattice parameter of 4.430(5) Å. As Sample A is uncapped, the formation of oxide layers is expected and layers of up to 5 nm in thickness have been observed on uncapped MnSb samples previously [17]. As the oxide forms at the surface, it is readily observed in a grazing scattering geometry. It is interesting to note the increased intensity of the powder ring along the 0° and 60° directions, this indicates a rotation of the MnO crystallite with respect to the GaAs substrate. However, as the oxide layer forms on the n-MnSb it is likely that the Ab/Ac stacking differences observed for c-MnSb also apply for the oxide and so give rise to multiple rotational alignments.

Using the data presented in Figure 4.22, the lattice parameters of the polymorphs observed in Figure 4.21 can now be derived. Additionally, the *d*-spacings for the reflections identified in Figure 4.21 can be calculated from Q and then by using this *d*-spacing value in Equations 2.28 and 2.29 the *a* and *c* lattice parameters can be determined. A summary of these values is presented in Table 4.6, note that the lattice parameters for the cubic polymorph are presented under the assumption of a rhombohedral distortion rather than a triclinic distortion.

The lattice parameters derived from the reciprocal space map reflections are, within experimental error, comparable to the values obtained from the symmetric and in-plane diffraction. The exception to this is c-MnSb, although the difficulty in obtaining a reliable fit for a rhombohedral fit indicates that some small distortion does occur in the cubic polymorph. It should be noted that any significant triclinic distortion would result

Table 4.6: Summary of the experimentally determined lattice parameters for Sample A from the diffraction data presented in Figure 4.22 (*'Sample A in-plane data'*) and from the asymmetric RSM shown in Figure 4.21 ('*Asymmetric RSM*').

	SADP		Sample A in-plane data		Asymmetric RSM		
Material	a (Å)	c (Å)	a (Å)	c (Å)	a (Å)	b (Å)	c (Å)
GaAs	-	-	5.653(1)	-	5.651(3)	-	-
n-MnSb	4.12(2)	5.77(3)	4.140(2)	5.789(1)	4.138(7)	-	5.789(1)
c-MnSb	6.50(3)	-	6.532(3)	-	6.51(2)	6.42(2)	6.42(2)

in previously forbidden cubic reflections being allowed, and as this is not observed, any distortion that does occur must be small. Consequently, the lattice parameters obtained from RSMs are similar to those measured by dedicated in-plane experiments and so a sufficient range of RSMs measurements would enable the in-plane structure of MnSb films to be quantified. It should be noted that a full quantitative analysis of Sample B, C and D has yet to be performed.

4.5.2 Quantitative polymorph identification

Having identified the origins of the peaks present in the RSM it is evident that the c-MnSb(133) and n-MnSb($1\bar{1}05$) reflections are sufficiently removed from neighbouring features such that no overlap occurs during integration of the intensities. To this end, integrated peak intensities for the n-MnSb($1\bar{1}05$) and c-MnSb(133) reflections have been calculated by considering a circular box, centred on the reflection maximum with a fixed radius of 0.07 $Å^{-1}$, following this the ratio of the intensities can be taken. Reciprocal space maps for Samples B, C and D are shown in Figure 4.23 and the resulting n-MnSb:c-MnSb ratios are given in Table 4.7. Note that as only a single reflection from each polymorph has been considered this is not a true measure of the relative polymorph content but is, instead, a useful metric for determining polymorph content trends between samples. Note that no c-MnSb(133) reflection is observed for Sample D and so a ratio of zero has been assumed.

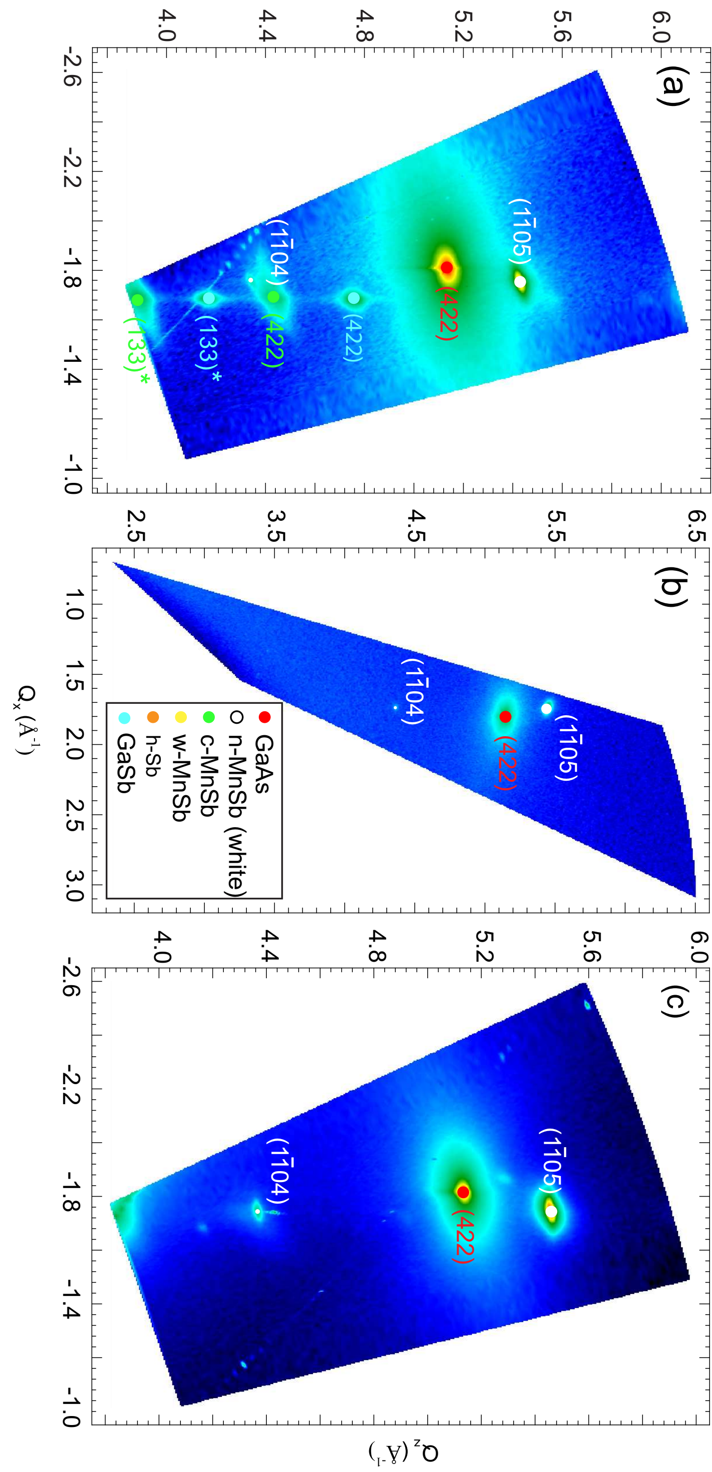

Figure 4.23: Asymmetric RSMs around the GaAs(422) reflection for Samples B, C and D. The reciprocal space nets show allowed reflections for GaAs, n-MnSb, c-MnSb, w-MnSb, h-Sb and GaSb.

Table 4.7: Calculated ratios of the c-MnSb(133) to n-MnSb($1\bar{1}05$) 2D integrated intensities, lattice parameters and J_{corr} values for Samples A through D as derived from the asymmetric RSMs shown in Figures 4.21 and 4.23.

Sample	n-MnSb:c-MnSb ratio	n-MnSb c lattice parameter (Å)	J_{corr}
A	0.023(1)	5.791(1)	6.81
B	0.013(1)	5.791(1)	7.03
C	0.00087(1)	5.779(1)	7.21
D	0	5.764(1)	7.35

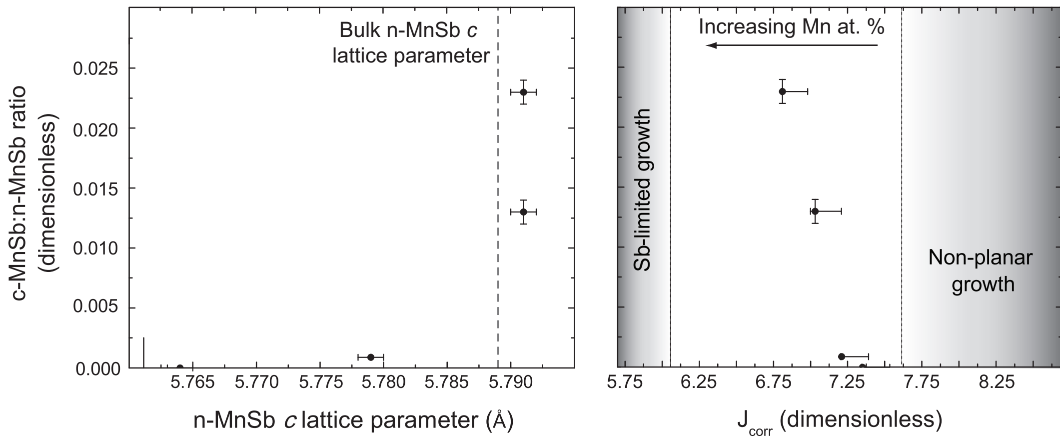

Figure 4.24: Variation in the n-MnSb:c-MnSb polymorph ratio as a function of the n-MnSb c lattice parameter (left panel) and J_{corr} (right panel).

Figure 4.24 shows the variation in c-MnSb:n-MnSb ratio as a function of n-MnSb c lattice parameter and J_{corr}. It can be seen that for samples with n-MnSb c lattice parameters larger than the bulk value of 5.789 Å the c-MnSb to n-MnSb ratio is larger. However, it is worth noting that the ratio decreases as J_{corr} increases, which is unexpected as larger values of J_{corr} result in an increased local Sb flux and so should cause an effective reduction in Mn content of a film.

Although only a small sample set has been studied, the relative ratios derived provide evidence for stoichiometry-based variation, indicated through lattice parameter variations, in the polymorph content. The maximum observed polymorph content

occurred for a c parameter of 5.791(1) Å which corresponds to the average value determined from Figure 4.8. As such, the optimum growth conditions presented in Section 4.2 give rise to the most strongly polymorphic samples. However, from the right hand panel of Figure 4.24, lower values of J_{corr} appear to promote the formation of MnSb polymorphs. This is unexpected if polymorph growth is due to the presence of a double-layered surface reconstruction with tetrahedral co-ordination, as proposed by Aldous et al. [23]. The presence of a double layer reconstruction could arise from either Sb segregation or excess Sb and the tetrahedral co-ordination of the layers would provide a route from a n-MnSb stacking order (AbAc) to either c-MnSb (AaBbCc) or w-MnSb (AaBb) stacking. These layer stacking orders are depicted graphically in Figure 1.3. As such, the observed trend of increased polymorph formation with lower values of J_{corr}, which would indicate a reduction in relative Sb concentration at the surface, is surprising. An alternative formation method for the polymorphs could arise from Ga segregation in MnSb films [123], which could lead to a tetrahedral bonding configuration between Ga and Sb (as in GaSb) at the surface. The subsequent substitution of Mn with Ga would then be required to form c-MnSb or w-MnSb and it is unknown if such a process is likely. However, the presence of this segregation would additionally lead to the formation of embedded polymorph and GaSb crystallites throughout the layer. The presence of embedded polymorph crystallites is suggested from the XRD data presented in this chapter, however it is not supported by the TEM data. The presence of small GaSb crystallites could reasonably be detected by XRD although the observed GaSb crystallite size, $\sim$20 nm, is entirely consistent with the size of the GaSb features observed at the interface rather than distributed throughout the film, which are not observed in the TEM.

Note that the large uncertainties observed for J_{corr} mean that a range of J values are investigated when using X-ray sources with large footprints. As the major uncertainty in J_{corr} is positive the trend of lower J_{corr} values promoting polymorph formation remains and so additional RSMs are needed in order to verify the tentative analysis presented

here.

As a result of the data presented above, it can be seen that asymmetric RSMs are a good method for determining both the lattice parameter behaviour for all materials present in a sample and their relative ratios. Additional difficulties arise from a practical point of view, the RSMs for Samples A and C were obtained using a laboratory source (Philips X'Pert PANalytical diffractometer) and took approximately 72 hours to collect. Samples B and D were instead studied using a synchrotron sources (NSLS and Diamond, respectively) and it can be seen that a greater range of polymorph reflections are present. The increased flux of synchrotron sources are therefore necessary to fully explore the polymorph behaviour and content of these films, especially with regards to the small w-MnSb crystallites observed. The ability to tune the energy, and consequently the wavelength, provides the opportunity to explore a larger region of reciprocal space and so would prove useful in the analysis of distortion with the cubic polymorph. Equally, additional reflections can be chosen in order to exclude, or include, reflections from a particular polymorph and so improve the identification of features in the map.

4.6 Conclusions

Films of MnSb, grown on GaAs(111) substrates, containing the niccolite, cubic and wurtzite polymorphs have been investigated using HRXRD. No strong trends in the structural properties of the polymorphs are observed with the growth parameters. Although the variation in the n-MnSb c lattice parameter indicates that the film stoichiometry changes from sample to sample, with the atomic Mn concentration changing by up to 2 %. Effective fluctuations in the local J-value drive the formation of internal strain fields which may then promote the growth of polymorphs within the n-MnSb framework. Due to the lattice mismatch with GaAs the n-MnSb crystallites are observed to quickly relax through the introduction of misfit dislocations and the resulting mosaic structure strongly influences the growth of the polymorph crystallites. Evidence for pseudomorphic growth is seen in MnSb thin films below 5 nm, although no polymorph

reflections were identified. However, the requirement of Sb capping these thin films, to prevent complete oxidation of the layer, results in the c-MnSb reflections being obscured and so further work is needed to explore polymorphism in these very thin films.

Crystallites of c-MnSb are observed to have large strain dispersions, which suggests that they are embedded within the n-MnSb framework although TEM images suggest that the polymorphs are located solely at the surface. On the basis of the asymmetric RSMs, the cubic crystallites are thought to experience either a rhombohedral or triclinic distortion. These distortions are expected to have a profound effect on the electronic and magnetic properties, although this is yet to be studied. Use has also been made of asymmetric RSMs in order to quantify the cubic polymorph content. This preliminary work suggests that using the optimised n-MnSb growth conditions results in films with the highest polymorph content. Tentative analysis then suggests that lower J_{corr} values promote the formation of the polymorphs although why these conditions promote the growth is currently unknown. Several methods for polymorph formation have been discussed: double-layered reconstructions leading to a change in stacking order, Ga segregation and strain. However, the double-layered reconstruction is not directly supported by the XRD data which indicates that the films are Mn rich (and so are Sb deficient). The segregation of Ga could result in the formation of Ga-Sb tetrahedral co-ordination which would facilitate a change in stacking order allowing the growth of the polymorphs. Although no evidence of GaSb, w-MnSb or c-MnSb crystallites are seen throughout the film as would be expected. Finally, the energy available from strain cannot account for the 0.83 eV difference in total energy between n-MnSb and c-MnSb or w-MnSb. Further studies, making use of additional RSMs, are then necessary in order to fully explore the growth phase space and determined the key parameters in the formation of the polymorphs.

Chapter 5

Heteroepitaxial growth of MnSb on Ge

5.1 Introduction

The use of III-V semiconducting substrates in the successful growth of Mn pnictides has been reported by several groups [62, 124] and is due to the excellent epitaxial compatibility observed between the materials. There are several benefits of using III-V substrates for spintronic applications, including the manipulation of spin currents through the Rashba effect [10, 125] and the ability to grow functional structures, such as quantum wells [126], for use in spin detection. However, the Group IV semiconductors, such as Si or Ge, are the dominant materials for technological applications and it is highly desirable to find materials that are epitaxially compatible with them.

The integration of the Mn pnictides with the Group IV semiconductors is attractive from a spintronics point of view due to the long spin lifetimes observed in Si [13] and the demonstration of spin transport in Ni/Ge structures [14]. The high Curie temperature of MnSb makes it a good choice for inclusion into magnetic heterostructures. However, the use of Si as a substrate is hampered by the large lattice mismatch, $\sim$7.5 %,

and the formation of interfacial silicides [127, 128] due to reactivity between the substrate and incident Mn flux. The lattice mismatch is reduced for Ge to 3.2 %, identical to that of the MnSb/GaAs system, and it is possible that the growth would behave similarly. The likely thermodynamic behaviour of the interface is unknown owing to limited data on the enthalpies of formation of the MnGe intermetallic alloys. Although Mn_5Ge_3 is observed to have the greatest thermodynamic stability based on observations made during the growth of Mn_xGe_{1-x} thin films [129]. To date, little work exists in the literature on the growth of MnSb films on Ge substrates and it is therefore worthwhile studying the combination of these two materials.

In this chapter, the growth of MnSb thin films on Ge(001) and Ge(111) is investigated. Firstly, cleaning of the substrates is outlined and a comparison of the observed electron diffraction patterns is made for Ge(001). The growth of MnSb/Ge(001) is then discussed in terms of the behaviour of samples during growth as characterised by RHEED. Subsequently, ex-situ structural, compositional and magnetic characterisation work is presented. Finally, preliminary work on the growth and characterisation of MnSb/Ge(111) is shown.

5.2 Surface preparation of Ge substrates

Cleaning of single element substrates is relatively straightforward due to the absence of preferential sputtering and their relatively high melting points. As such, the IBA method outlined for GaAs in Section 3.2 is applicable here. The Ge substrates used in this chapter are thin films, nominally undoped, and were grown via chemical vapour deposition (CVD) on Si substrates [130, 131]. Substrates of Ge, measuring approximately 8 mm $\times$ 8 mm, were mounted using spot-welded tantalum strips directly onto stainless steel sample plates. Samples were mounted in this fashion due to the high mobility of In glue on Ge, which would subsequently result in the disruption of the growth surface. The position of the Ta strips was chosen such that the high symmetry directions of the surface were accessible in the RHEED. Samples were cleaned using

an acetone, isopropanol and deionised water wash. Samples were then blown dry with dry nitrogen before being loaded into the vacuum chamber. All Ge substrates were cleaned using a one hour degas at 420 °C, followed by a 10 minute ion bombard and subsequently annealed for 40 minutes at 500 °C.

5.2.1 Electron diffraction

Ge(001)

Following cleaning, a double domain (2×1) LEED pattern was observed on the Ge(001) surface and is shown in Figure 5.1(a)(i). Panel (a)(ii) gives the corresponding schematic of the image and highlights the positions of the integer and fractional order spots. The (2×1) surface unit cell results from the formation of dimers [132, 133] and two domains occur due to the presence of $a/4$ steps which result in a 90° rotation of the dimer bond directions. Consequently, a mixture of (2×1) and (1×2) unit cells are present on the surface and the observed LEED pattern arises from diffraction from both domains. The RHEED pattern observed on this surface was (2×2), characterised by a (2×) periodicity along the ⟨110⟩ direction and a (2×) periodicity along the ⟨100⟩ direction which exhibited curved fractional-order streaks. This difference in reconstruction is surprising, as a (1×) periodicity would be expected along the ⟨100⟩ direction in RHEED, while a diffraction feature would be expected at the $(\frac{1}{2},\frac{1}{2})$ position in the LEED pattern, neither of which are observed. This apparent discrepancy in surface periodicity arises from the effects of the transfer width in LEED and RHEED compared to the size of the reconstruction domains present on the surface.

It is worth discussing the presence of additional reconstructions on the Ge(001) surface. The dimers of the (2×1) structure were found to be tilted with respect to the surface plane by STM studies and that 'flipping' between two tilt orientations occurred at room temperature [134]. Tilting of the dimers is thought to lower the surface energy by ensuring semiconducting behaviour [135] and so is favoured over symmetric (parallel to the surface plane) dimer structures. The presence of tilting then enables the formation of

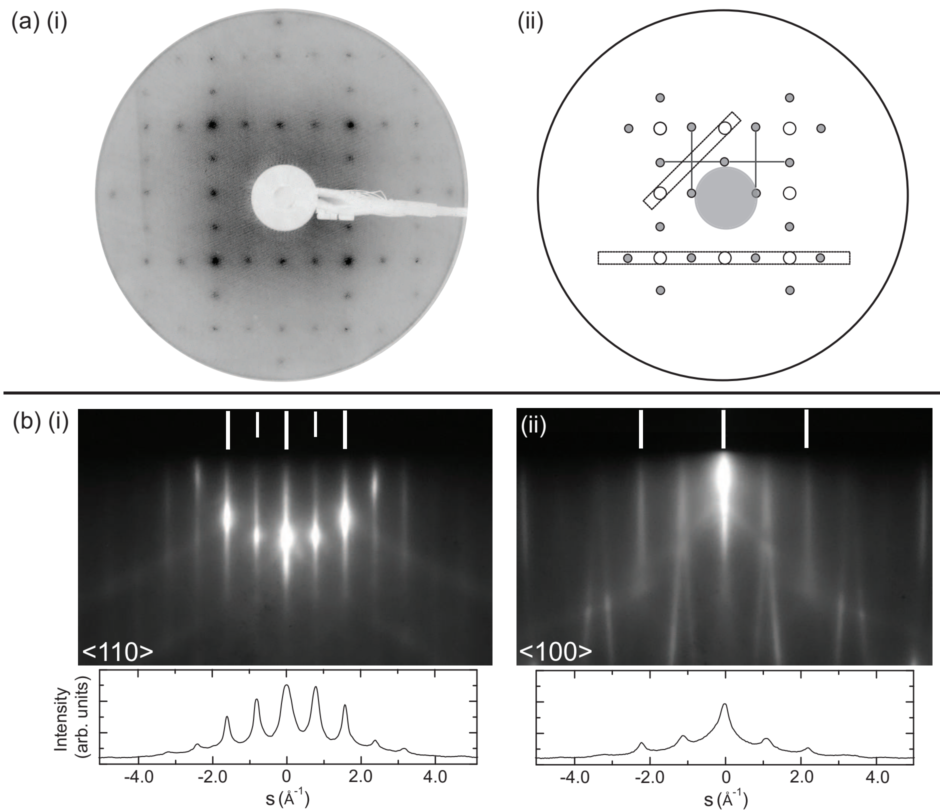

Figure 5.1: Electron diffraction obtained from a clean Ge(001) surface showing a (a)(i) 115 eV LEED pattern and (a)(ii) the corresponding schematic. Integer (fractional) spots are denoted by the small white (grey) circles, the dashed lines indicate the RHEED (shown in panel (b)) recording directions and the thin grey lines indicate the expected position of the intensity sheet streaks. Also shown are the RHEED patterns obtained with the electron beam orientated along the (b)(i) ⟨110⟩ and (b)(ii) ⟨100⟩ directions. Integer (fractional) streaks are denoted by the long (short) white lines.

higher-order reconstructions, relative to the (2×1), through the ordering of neighbouring tilts [136] and some example models for these higher-order reconstructions are shown in Figure 5.2. At room temperature, the thermally activated flipping of dimer tilts suppresses the formation of the larger unit cells and so the (2×1) structure is observed. The model for this structure is shown in panel (a), note that for simplicity the model has been produced using symmetric dimers, while panel (b) shows a side view of the surface indicating the two possible tilt orientations. At temperatures below 280 K the dimer tilts begin to order and two additional reconstructions are seen [136, 137]: (2×2)

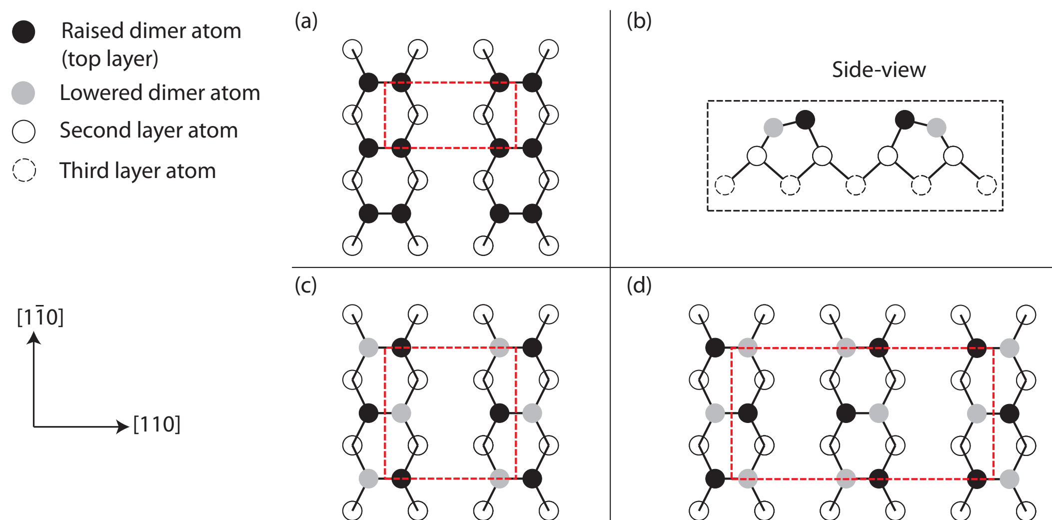

Figure 5.2: Surface structures of the Ge(001) surface (a) (2×1) with symmetric dimers, (b) side view of the (2×1) structure showing the two dimer tilt directions, (c) (2×2) structure due to in-phase tilt orientation and (d) c(4×2) structure from out-of-phase dimer tilts. The atoms are as labelled in the key.

and c(4×2). The models for these are then shown in panels (c) and (d), respectively. It is possible to envisage a situation where random tilt orientations result in the formation of domains of the larger reconstructions and, for sufficiently large domains, these would be visible in RHEED. On this basis, the curved fractional streaks along the ⟨100⟩ are thought to arise from the spontaneous formation of higher-order reconstructions.

The difference in the observed patterns, (2×1) from LEED and (2×2) from RHEED, can then be related to two factors: the transfer width of the techniques and the effective ordering of the dimers. The transfer width limits the largest possible distance over which interference can be detected and so determines the size of the domains that contribute to the diffraction. The size of the transfer width differs significantly between the techniques [112, 65], with values in RHEED ranging from 1500 Å to 5000 Å and in LEED between 30 and 100 Å. This results in coherent interference between domains on the surface occurring for RHEED but not for LEED.

The effect of the flipping of dimer tilts, in addition to the formation of domains

of the higher-order reconstructions, is to induce disorder along the dimer row directions. However, if the timescale of the dimer flipping is sufficiently short then the incident electron beam will see an average of dimer positions, such that they appear symmetric. A typical RHEED electron (at 12.5 keV) travels at ~0.2c and so across a transfer width of ~1500 Å the RHEED electron interacts with the surface for 2.5×10^{-15} s. The expected dimer flip time for Ge is approximately 1×10^{-6} s [138] and so the incident RHEED beam observes the surface in an effectively 'frozen' state. Coherent interference between the local ordered domains can then contribute to the diffraction. The presence of tilt disorder along the dimer rows then gives rise to 'sheets' of diffuse intensity in reciprocal space. These sheets are aligned perpendicular to the rows and arise due to the loss of periodicity and momentum conservation in the surface plane [139]. The presence of two dimer row directions rotated by 90° relative to one another then gives rise to the formation of two sheets of intensity. In LEED, as the incident beam is normal to the dimer rows, the Ewald circle acts to project the edges of the sheets and so streaks appear in the pattern. These are not observed in Figure 5.1(a)(i) and it is likely that the sample temperature results in an increased dimer flipping rate, and so suppresses the higher-order reconstructions.

Figure 5.3 shows a schematic for the intersection of the Ewald sphere with the intensity sheets when the electron beam is directed along the [100] direction. Note that directing the electron beam along the ⟨110⟩ directions results in only diffuse scattering from the sheets. The intersection of the Ewald sphere and the sheets at oblique angles produces circles of allowed diffraction conditions (shown in red). For an incident beam aligned along the ⟨110⟩ direction, these circles are rotated by 45° relative to the incident electron beam. The projection of these rotated diffraction circles onto the screen, in addition to the large Ewald sphere radius found in RHEED ($\sim5\times10^{11}$ m^{-1}), results in the formation of curved streaks as observed in Figure 5.1(b)(ii). Note that the spontaneous formation of higher-order reconstructions results in a (2×) periodicity along the dimer rows and so the curved streaks appear at half-order fractional positions.

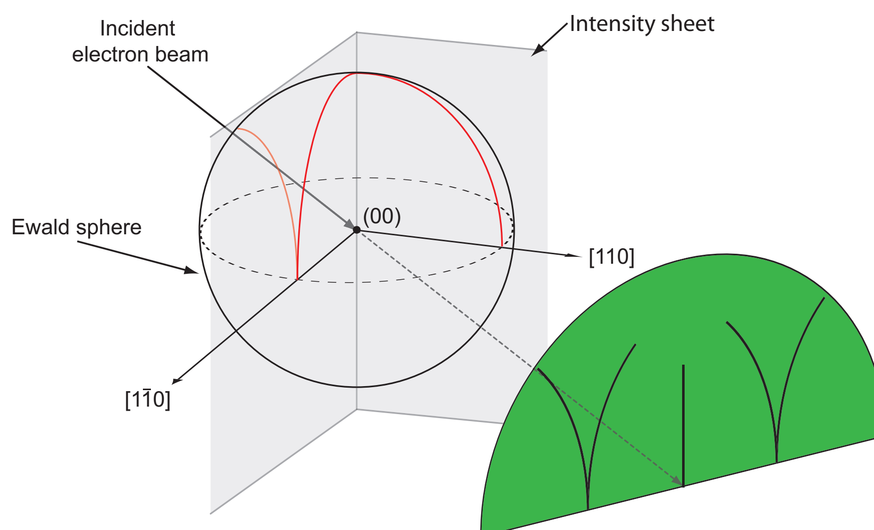

Figure 5.3: Schematic showing the intersection of the Ewald sphere with two sheets of intensity that are orientated along the $\langle 110 \rangle$ directions. The intersection of the sphere with the planes results in the formation of circles (indicated in red) and the projection of these onto the phosphor screen gives rise to curved streaks.

Ge(111)

On Ge(111) a triple-domain c(2×8) structure is observed following cleaning, the corresponding RHEED pattern and expected reciprocal space mesh for this surface are shown in Figure 5.4. The absence of the $\frac{1}{4}$ and $\frac{3}{4}$ streaks along the $\langle 110 \rangle$ direction is thought to be due to small structure factors arising from the symmetry of the unit cell [140]. The origin of the faint $\frac{1}{4}$ and $\frac{3}{4}$ streaks along the $\langle \bar{2}11 \rangle$ is currently unknown.

5.2.2 X-ray photoelectron spectroscopy

In order to test the efficacy of IBA cleaning cycles, pieces of Ge(001) and Ge(111) were studied by XPS. The samples were cleaned using the procedure outlined above, although the Ge(111) sample had the solvent wash stage omitted. Spectra for both

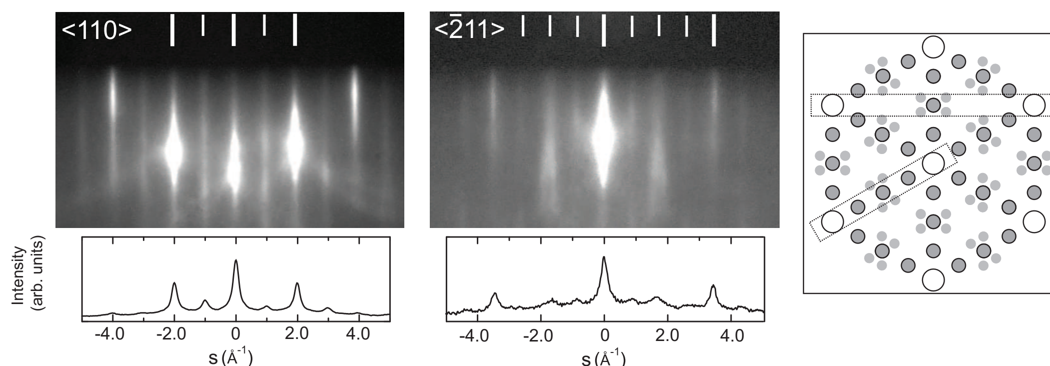

Figure 5.4: RHEED of a cleaned Ge(111) with the electron beam aligned along the $\langle 110 \rangle$ and $\langle \bar{2}11 \rangle$ directions showing the triple domain c(2×8) structure. The reciprocal space mesh for the structure is shown on the right. Large white circles represent integer streaks, grey circles with a black outline are $\frac{1}{4}$ features and the small grey circles with no outline are $\frac{1}{8}$ features. The dashed boxes indicate the RHEED recording directions.

substrate orientations are shown in Figure 5.5.

Figures 5.5(a) and (b) show O 1s spectra for the two substrate orientations before and after a single IBA cycle. Two features are common between the spectra: the broad Ge $L_3M_{23}M_{23}$ Auger centred at 533.8 eV and an O-O bonding environment component at 531.1 eV. An additional component is observed on the Ge(001) surface and is shifted by approximately 0.1 eV from the expected O-O binding energy. This small shift is indicative of bonding environments found in organic compounds [71] and so the peak is attributed to residue from the solvent wash. Following cleaning the Auger feature remains, although a small O-O component was observed on the (111) surface. This peak was thought to arise from misalignment of the sample rather than from re-contamination during cleaning. The C 1s region, shown in Figures 5.5(c) and (d), show a similar reduction in intensity following cleaning although not all of the adventitious carbon is removed. A shift towards ~284 eV is observed and is tentatively assigned to a Ge-C bonding environment [141].

Finally, two features are observed in the Ge 2p region (Figures 5.5(e) and (f)) that are worth mentioning. Firstly, the relative intensities of the oxide and elemental peaks are different between the samples. On the (001) surface, the as-loaded sample

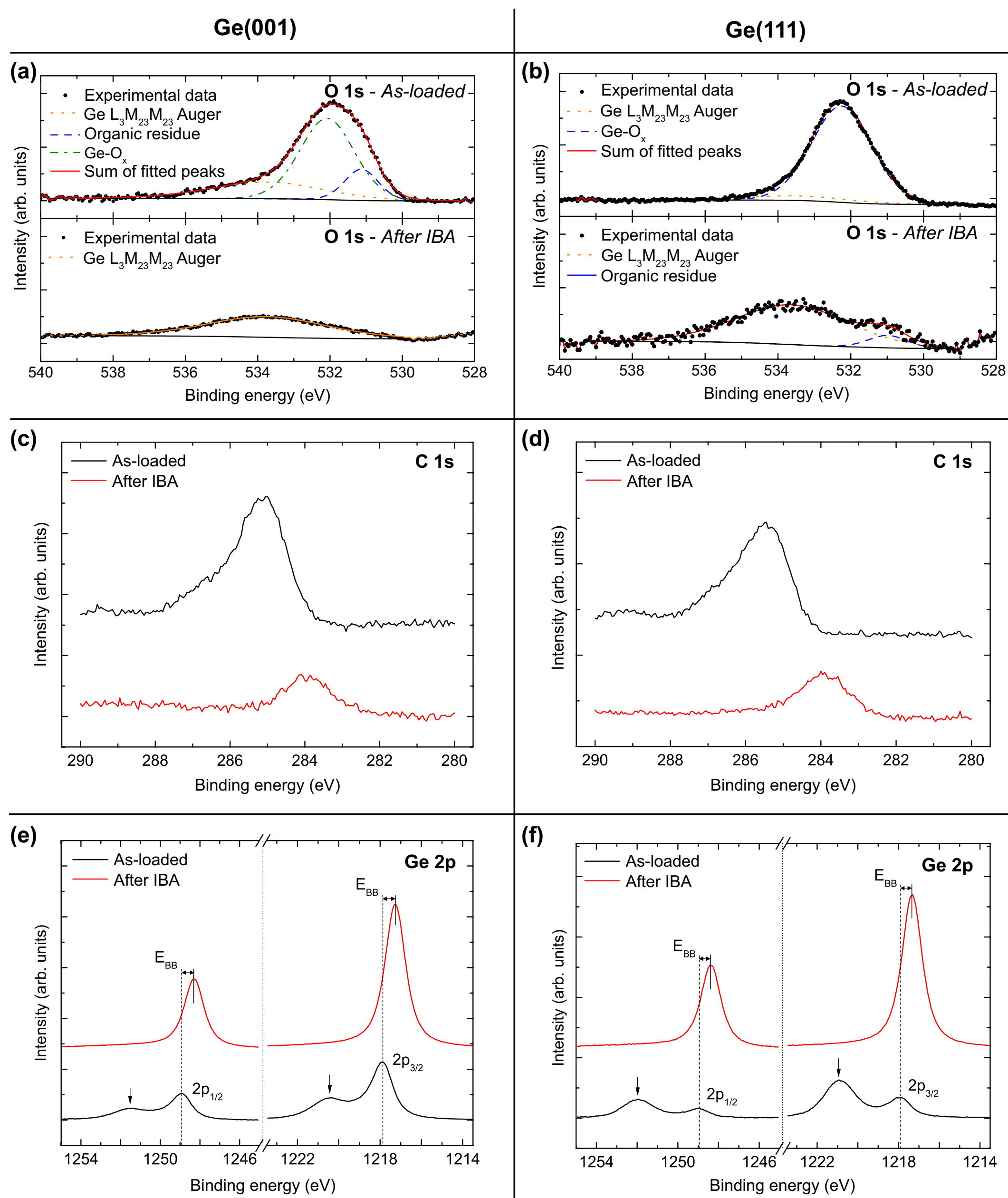

Figure 5.5: Top panels are fitted XPS spectra of the O 1s core level for (a) Ge(001) and (b) Ge(111), the components are as listed on the figure. Middle row panels are XPS spectra of the C 1s core level for (c) Ge(001) and (d) Ge(111). Finally, the bottom row panels show spectra for the Ge 2p core level of (e) Ge(001) and (f) Ge(111), the arrows denote the position of the GeO_2 peak.

features a smaller oxide component when compared to the as-loaded (111) surface. This is thought to be due to the use of a deionised water wash stage as the native oxide of Ge, GeO_2, is water soluble [142] and so removed during the ex-situ cleaning wash. Secondly, a shift of 0.63 eV is observed in the Ge 2p core level position for the (001) surface, and a 0.62 eV shift is seen on the (111) sample, between the as-loaded and cleaned sample. These shifts are denoted byE_{BB} in Figures 5.5(e) and (f), and are thought to arise from surface band bending. The use of IBA cycles, in conjunction with an ex-situ solvent washing stage, is seen to be effective in reducing surface contamination on Ge substrates. On this basis, and from the presence of sharp features in the electron diffraction, these surfaces are suitable for use in epitaxial growth. However, it should be noted that the effect of two reconstruction domains on the growth of MnSb thin films is unknown. Although the formation of multiple domains during the growth of MnAs on Si(001) substrates has been observed [18] and it is expected that a similar effect may occur during the growth of MnSb.

5.3 Growth of MnSb layers on Ge(001) substrates

Several MnSb samples of varying thicknesses have been grown on Ge(001) substrates. The substrates were cleaned using the method outlined in Section 5.2 and exhibited a double domain (2×1) pattern. The beam flux ratio, $J_{Sb/Mn}$, was fixed prior to growth while the substrate temperature, deposition time and number of growth stages were varied. The following range of conditions have been investigated:

- $J_{Sb/Mn} = 6.6 – 7.3$
- First-stage growth temperature, T_{sub} = (100 – 350) °C (this range also applies to single stage samples)
- Second-stage growth temperature, T_{sub} = (350 – 420) °C

Sample thicknesses were calibrated relative to the growth rate of MnSb on GaAs(111) substrates and subsequently scaled to the measured Mn beam flux. This yielded expected growth rates in the range 4–6 nm min^{-1}.

RHEED observations

For single-stage growth, the beginning of growth was characterised by the fading of the substrate streaks and new streaks, with a different spacing, subsequently appearing. Along the Ge[110] and [100] directions the streak separation decreased, while along the Ge[$1\bar{1}0$] the separation increased, the real space values corresponding to these separations are given in Table 5.1. The weak intensity of these new streaks indicated that the initial growth surface was rough although a weak dependence on T_{sub} was found with the streaks persisting for longer at lower temperatures. With increasing deposition, the streaky pattern faded and a complex transmission pattern appeared indicating a transition from planar to 3D growth.

For samples grown using a two-stage methodology, as outlined in Section 4.2, increasing first-stage T_{sub} resulted in transmission patterns that had greater intensity and exhibited a greater number of reflections. The sharpest features were observed for samples grown with a first stage T_{sub} of 300 °C, although no strong dependence on the second stage T_{sub} was observed. The presence of transmission features was found to persist in samples up to approximately 75 nm in thickness, although above this thickness the pattern faded rapidly. This is attributed to the formation of 3D islands with lateral extensions greater than the IMFP of the RHEED beam ($\sim$20 nm). Finally, the intensity and sharpness of the RHEED patterns was not observed to change over the $J_{\mathsf{Sb/Mn}}$ range investigated.

Figure 5.6 shows the RHEED transmission patterns for a sample grown using a single growth stage at $T_{\mathsf{sub}} = 350$ °C. Also shown are schematics highlighting separations that correspond to d-spacings that are present in n-MnSb and the corresponding real space values are given in Table 5.1. Note that the patterns along the [110] and [$1\bar{1}0$]

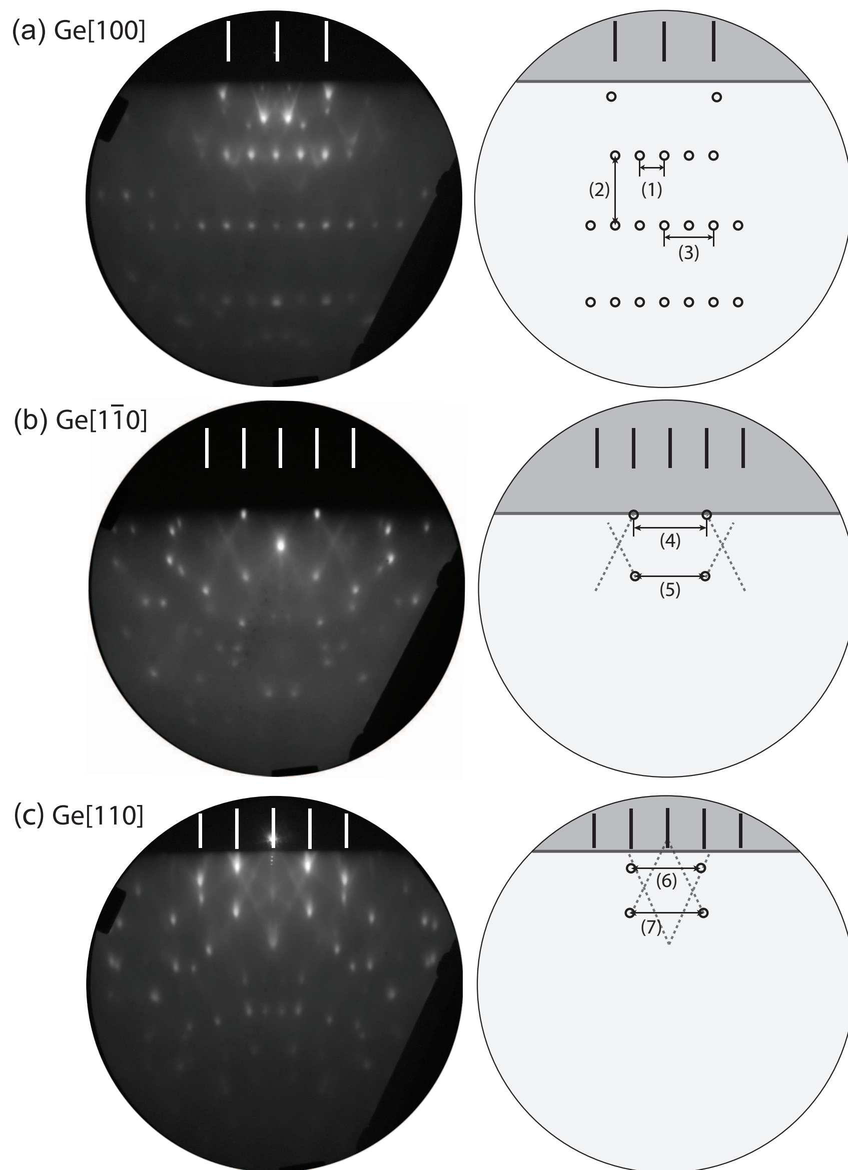

Figure 5.6: RHEED transmission patterns observed during the growth of MnSb on Ge(001). The electron beam is orientated along the (a) Ge[100] (b) Ge[1$\bar{1}$0] and (c) Ge[110] directions. Schematics highlighting the separations that have *d*-spacings corresponding to planes present in n-MnSb are shown on the right. Circles (crosses) denote the primary (secondary) patterns observed where appropriate while the dashed lines indicate the presence of facet streaks.

Table 5.1: Electron beam orientation (relative to the Ge substrate), schematic label and real space separations for MnSb/Ge(001) RHEED transmission features as labelled in Figure 5.6. Early-stage streaks denotes the separations determined for the streaks observed at the start of growth.

Electron beam orientation	Feature spacing label	Real space separation (Å)
[100]	(1)	5.84±0.2
	(2)	2.04±0.04
	(3)	2.90±0.06
	Early-stage streaks	2.90±0.06
$[1\bar{1}0]$	(4)	1.91±0.05
	(5)	2.02±0.06
	Early-stage streaks	4.12±0.08
$[1\bar{1}0]$	(6)	2.19±0.07
	(7)	2.08±0.06
	Early-stage streaks	3.82±0.07

directions are inequivalent but the patterns observed along the ⟨100⟩ directions were all identical. The absence of diffraction rings, and the sharpness of the observed spots, indicates that the layer is crystalline. No changes in the diffraction pattern were observed as the RHEED spot was moved across the sample surface indicating that the 3D growth is not due to local beam flux inhomogeneities.

The pattern observed along the Ge[100] direction, as shown in Figure 5.6(a), exhibits rectangular symmetry. From Table 5.1 it can be seen that the horizontal spacings are given by directions (1) and (3), while the corresponding real space separation of these features is (5.84±0.2) Å and (2.90±0.06) Å, respectively. While along the vertical axis of the screen, direction (2), the real space separation is (2.04±0.04) Å. These spacings are in agreement with transmission along the $[1\bar{1}00]$ direction of a MnSb$(11\bar{2}0)$ crystal, where the expected vertical separation is 2.064 Å ($a_{\mathrm{MnSb}}/2$) and the expected horizontal separation is 5.789 Å (c_{MnSb}). An illustration of transmission diffraction through a $(11\bar{2}0)$ orientated crystal is shown in Figure 5.7. It can be seen that the c axis lies in-plane and is larger than the average c lattice parameter value of 5.791 Å, as determined in Section 4.4.1. The observation of identical patterns along the [100]

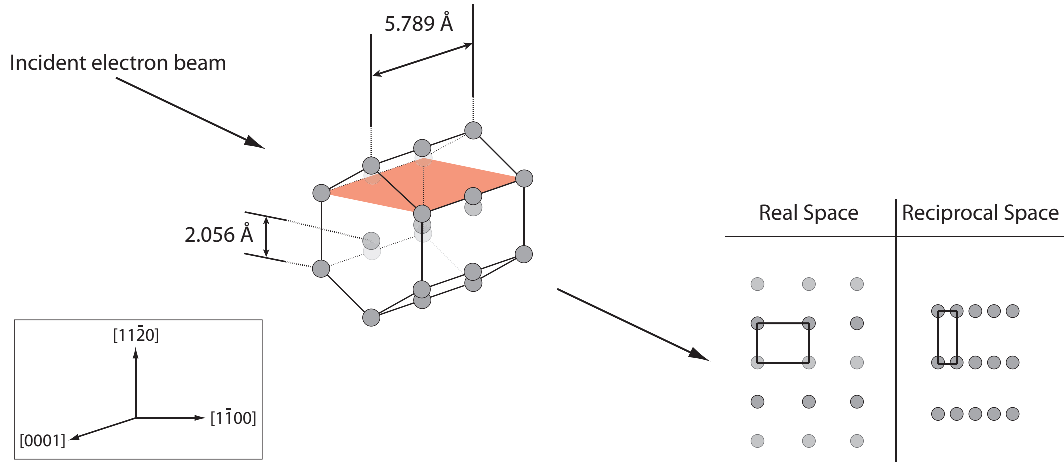

Figure 5.7: Schematic of transmission diffraction through MnSb(11$\bar{2}$0) crystallites, relevant d spacings are indicated on the crystal and the (11$\bar{2}$0) plane highlighted in red. On the right are illustrative patterns of the project real, and reciprocal, space patterns observed in the RHEED.

directions is indicative of two domains of MnSb(11$\bar{2}$0) crystallites and so transmission features arising from diffraction along the MnSb[0001] direction might be expected, although these are not observed. However, as the unit cell is elongated along the c axis it is possible that strain in this direction results in the loss of these reflections. On the basis of the RHEED observations presented here, the orientation of the features giving rise to the transmission diffraction is determined to be MnSb$\langle 0001 \rangle$ $\|$Ge$\langle 100 \rangle$ and MnSb$\langle 1\bar{1}00 \rangle$ $\|$Ge$\langle 100 \rangle$ for the two domains, with MnSb[11$\bar{2}$0]$\|$Ge[001].

With the electron beam orientated along the [110], or [1$\bar{1}$0], directions (Figures 5.6(b) and (c), respectively) the patterns are more complex. The separations labelled (4), (5), (6) and (7) appear common to both directions and have similar horizontal real space separations. These separations are in agreement with the d-spacing for the (1$\bar{1}$00) planes in MnSb ($a_{\mathrm{MnSb}}/2 = 2.064$ Å). However, this spacing cannot be accounted for by (11$\bar{2}$0) domains without a 30° rotation of the crystal about the [0001] axis. As such, these features remain unidentified although the symmetric nature of the pattern confirms the double domain structure of the layer. The growth of MnSb(11$\bar{2}$0) differs from the observed formation of MnSb(1$\bar{1}$01) on GaAs(001) [62] and has not been

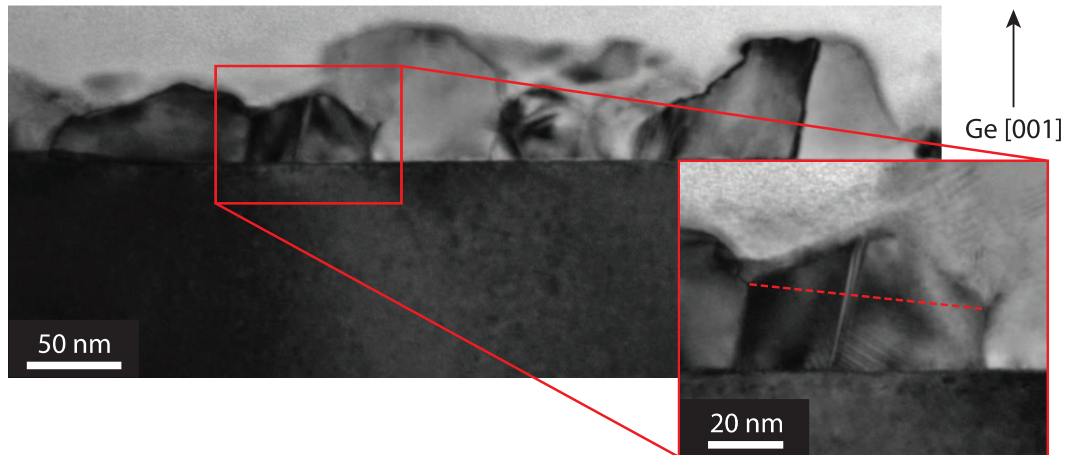

Figure 5.8: TEM image of a nominally 45 nm MnSb layer on Ge(001). The main image reveals the layer to be composed of islands and the inset shows a zoom view of a single crystallite, the red dashed line indicates the expected position of the $(11\bar{2}0)$ plane.

reported previously.

5.4 Characterisation of MnSb/Ge(001) samples

5.4.1 Transmission electron microscopy

Transmission electron microscopy has been used to investigate the structure and interfaces of MnSb/Ge(001) films. A typical image of a nominally 45 nm thick sample is shown in Figure 5.8. There are two points to note from this image: the first is that the interface is smooth with no large scale disruption over hundreds of nanometres. As such, the observed 3D growth is not due to reactivity between the MnSb overlayer and the Ge substrate. Second is the irregular structure of the layer and the presence of multiple crystallites, an example of which is shown in the inset of Figure 5.8, note the sharp interface between MnSb crystallite and the Ge substrate. These crystallites are observed to be tilted with respect to the expected $(11\bar{2}0)$ plane orientation, as indicated by the red dashed line on the inset image.

5.4.2 X-ray photoelectron spectroscopy

The TEM results presented in Section 5.4.1 indicate that the interface is sharp with no large scale intermixing occurring between the overlayer and the substrate. However, the presence of 1 ML of Ga has been observed on the surfaces of MnSb films grown on GaAs substrates [123]. A requirement of heterostructure applications is the formation of high quality, contamination free, surfaces in order to ensure compatibility with the deposition of further layers. The structural characterisation techniques presented thus far, RHEED and TEM, are unable to detect segregation at the monolayer level and therefore a preliminary XPS study is worthwhile to investigate the surface chemical properties of these films and to determine if Ge segregation occurs in the MnSb/Ge system.

Figure 5.9 shows XPS spectra for a nominally 70 nm thick uncapped sample, taken at 90° TOA, of the shallow core region and a close-in of the Sb 4d region. The shallow core region has been chosen on the basis that the IMFP for electrons in this energy range show little variation. Consequently, direct comparisons between peak areas within this energy range can be made and it is straightforward to analyse these shallow core levels for stoichiometry determination. However, the peak areas still have a dependence on atomic sensitivity factors that relate to the ease of ionisation of that core level. When comparing with higher binding energy core levels the IMFPs are required for normalisation in order to account for the differing probing depths of the photoelectrons. From the shallow core scan shown in panel (a), it can be seen that both Mn and Sb are present in the surface region while no signal from the Ge 3d core level is apparent. However, a small Ge 2p core level signal is observed, as shown in panel (b) and for a uniform surface coverage would be $\sim$2 % of the combined Mn, Sb and O signal and is surprisingly large. This would signify that segregation does occur although as the layer is irregular in structure (as observed by TEM) it is plausible that areas of the MnSb film will be sufficiently thin. If the sample thickness is less than three times the IMFP of the Ge 2p photoelectrons in MnSb, which corresponds to a layer thickness of

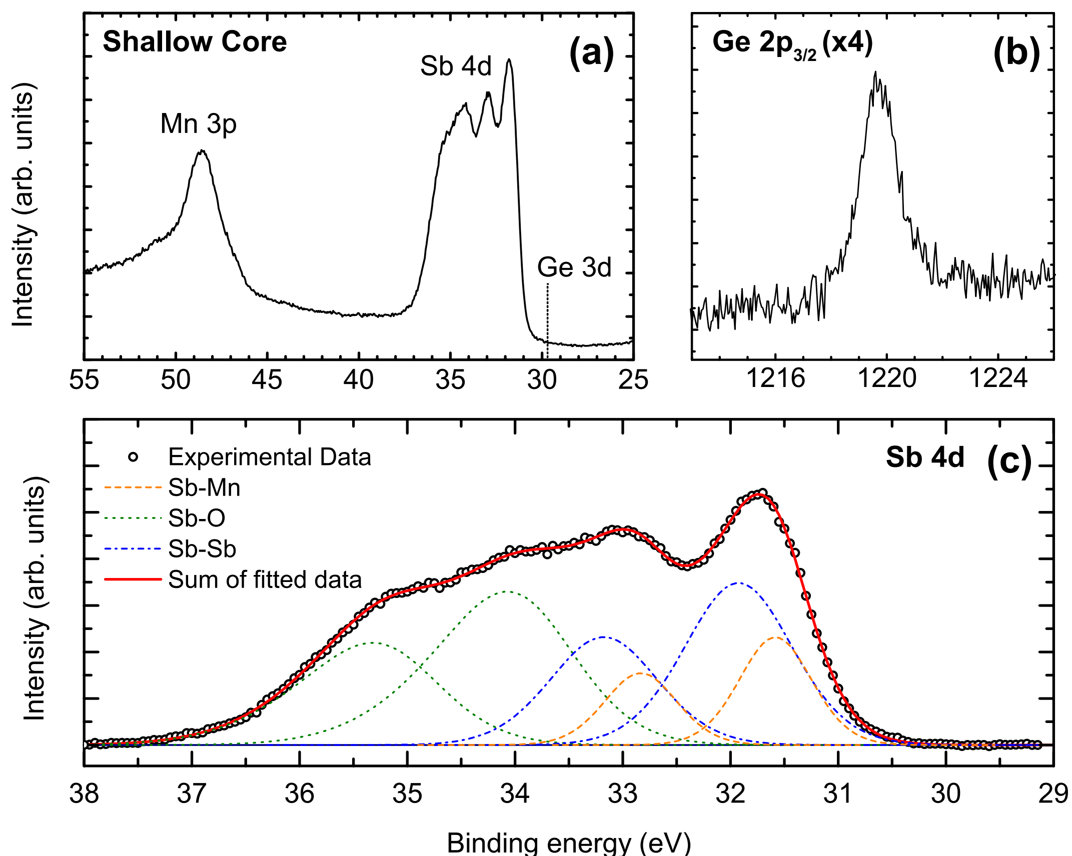

Figure 5.9: XPS spectra taken from an as-loaded 70 nm thick film grown on Ge(001). Panel (a) shows the shallow core region with the Mn 3p and Sb 4d core levels present while the Ge 3d core level is absent. Panel (b) is the Ge $2p_{3/2}$ core level. Panel (c) is the fitted Sb 4d region and indicates the presence of Sb-Mn, Sb-O and Sb-Sb bonding environments.

approximately 6 nm, then photoelectrons from the substrate will be detected. On this basis, it is difficult to ascertain if segregation occurs in MnSb/Ge(001) or if reduced layer thickness (or exposed substrate) is contributing to the observed signal based on XPS measurements alone. Additional take-off angle dependent work would enable a reduction in the probing depth and so would limit the number of photoelectrons from the substrate that would be detected.

Figure 5.9(c) shows the Sb 4d region for the sample. Following subtraction of a linear background, three doublets have been fitted and are assigned to Sb-Sb, Sb-Mn

and Sb-O bonding environments. The binding energies used to fit these peaks are given in Table 5.2 along with the chemical shifts relative to elemental Sb and the percentage breakdown of the Sb 4d core level. A chemical shift of -0.37 eV, relative to the Sb-Sb component, is found for the Sb-Mn environment, while a shift of 2.36 eV is found for the oxide peak. Note that the oxide peak was allowed a larger range of FWHM values in order to account for multiple oxides such as Sb_2O_3, Sb_2O_4 and Sb_2O_5 [113]. These shifts are in broad agreement with Hatfield et al., although the chemical shift for Sb-Mn determined here is somewhat smaller than previously observed. The values listed by Hatfield et al. for MnSb(0001) films on GaAs(111) were for samples that had been exposed to air for several days and had undergone significant oxidation while the studied sample had only been exposed for less than five minutes. Using the above fitting, in combination with total peak areas for the Mn 3p, C 1s and O 1s core levels, some conclusions can be drawn regarding the stoichiometry of these samples. Values for the normalised peak areas are given in Table 5.3 and from these results it is apparent that even after a few minutes of exposure to air the surface is heavily contaminated. This is unsurprising given the rough morphology of the films and the resulting large surface area, which will act to increase the rate at which the layer can be oxidised. However, in contrast to previous studies [28], the surface is Sb-rich with a ratio of Sb-to-Mn of (1.27 ± 0.03), although a significant proportion of the Sb signal arises from oxide environments (50.3 %). This is in contrast to air-exposed MnSb(0001) samples, where the surfaces are Mn-rich although it should be noted that these samples had been at atmosphere for several days or more. It is therefore plausible that the Sb-rich oxides are able to form first and that there is insufficient time for the Mn-oxides to form. Although it would be expected that the high reactivity of Mn, relative to that of Sb, would initially lead to the formation of Mn oxides and not Sb oxides.

Table 5.2: Peak fitting details showing the assigned bonding environment, binding energy, chemical shift relative to the Sb-Sb bonding environment and percentage breakdown of Sb bonding environments for a MnSb/Ge(001) sample. Values are taken from the fit shown in Figure 5.9(c).

Bonding environment	Binding energy $4d_{5/2}$ (eV)	ΔE (rel. to Sb-Sb) (eV)	Percentage
Sb-Sb	31.93	0.00	35.5
Sb-Mn	31.61	-0.32	14.2
Sb-O	34.29	2.36	50.3

Table 5.3: Normalised areas, and the corresponding percentage compositions, for the C 1s, O 1s, Mn 3p and Sb 4d core levels

Core level	Normalised Area	Percentage composition
C 1s	3164	15.4
O 1s	6634	32.3
Mn 3p	4732	23.1
Sb 4d	5982	29.2

5.4.3 X-ray diffraction

To check if the layer includes a significant presence of either MnSb(11$\bar{2}$0) crystallites or reacted material the sample studied in Section 5.4.2 has been investigated using XRD. Symmetric diffraction data is presented in Figure 5.10 and the intense peaks located at $Q_z = 4.45$ Å^{-1} and 4.63 Å^{-1} are readily indexed to Ge(004) and Si(004) reflections, respectively. The offset in 2θ was determined from the shift in the Si(004) peak relative to the expected bulk peak position and this offset was then used in calculating the Q_z values for the data. The value of the Ge lattice parameter has been calculated as 5.652(3) Å and this is indicative of a slight compressive strain of $\sim$0.1 %, which is in agreement with the relaxed lattice parameter of 5.654 Å found by Shah et al. [130]. An additional peak located at 6.90 Å^{-1} is observed, labelled MS in Figure 5.10, which corresponds to the Si(442) reflection and is attributed to multiple scattering from the edge of the substrate.

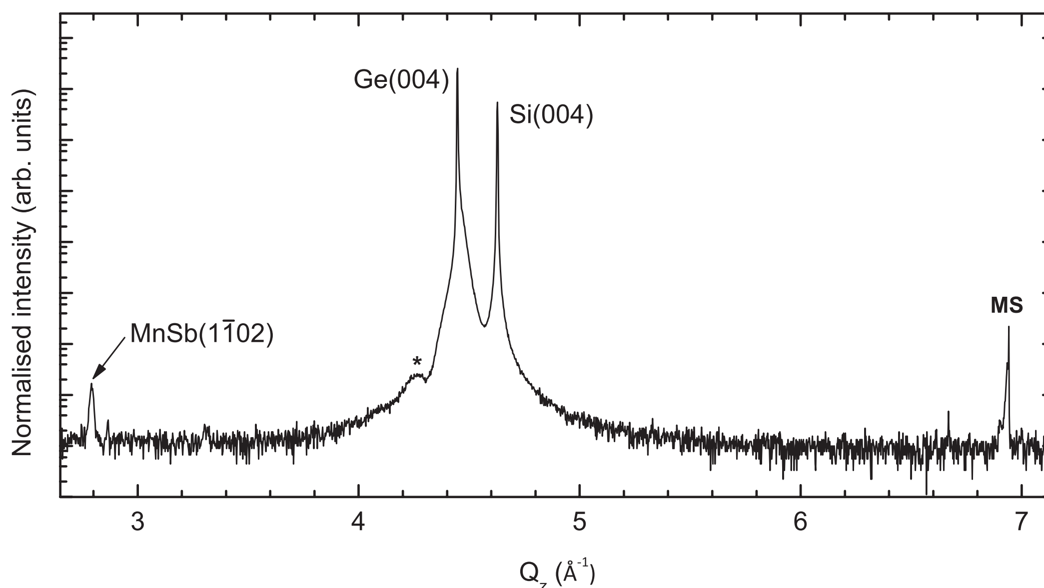

Figure 5.10: High-resolution XRD of a 100 nm thick MnSb layer acquired on beamline X22C at the National Synchrotron Light Source, Brookhaven National Lab. Reflections identified as originating from the substrate and overlayer are as labelled. The $*$ denotes an unassigned peak, believed to arise from the overlayer. The peak labelled MS is due to multiple scattering from the substrate.

Two reflections in the data presented in Figure 5.10 are thought to originate from the overlayer. The first is at $Q_z = 2.792$ Å^{-1}, which corresponds to a d-spacing of 2.250(8) Å, while the second is located at $Q_z = 4.265$ Å^{-1} with a d-spacing of 1.473(5) Å. Given that Mn, Sb and Ge are present in the sample the list of candidate materials is large and includes a range of Mn-Ge alloys. However, the presence of these Ge alloys can be ruled out on the basis of the TEM (where no interfacial alloys are observed to form) and XPS measurements (where no surface Ge signal is observed) presented in Sections 5.4.1 and 5.4.2, respectively. Consequently, based on examination of the predicted reflection positions and lattice parameters listed in Appendix A, there are only two candidate reflections applicable to the lower Q_z value peak: MnSb(1$\bar{1}$02) and $MnSb_2$(220). As $MnSb_2$ forms under high pressure conditions the peak is therefore assigned to MnSb(1$\bar{1}$02) crystallites. The FWHM of the peak is 0.21(1)$^\circ$ and so the crystallite size, determined using the Scherrer equation Equation 2.33, is (31$\pm$2) nm,

which is in broad agreement with the crystallites sizes observed in TEM.

For the peak at $Q_z = 4.265$ Å^{-1}, there are only two reflections that give rise to the appropriate d spacing: $Mn_2Sb(220)$ and $Mn_2Sb(203)$. As $Mn_2Sb(001)$ orientated films have been reported on GaAs(001) substrates [128] it is unlikely that either $Mn_2Sb(203)$ (with an oblique surface mesh) or (220) orientated films (with a rectangular surface mesh) would be observed on substrates with square symmetry. An alternative explanation is that it originates from Ge under tensile stress. However, the strain required for the shift in Q_z is 5.7 % and such a high strain value is likely to be unfavourable. A final possibility is diffraction from elemental Cu due to its use in the sample holders used on the X22C beamline. However, no reflections from elemental Cu correspond to the peak in question and so it remains unidentified.

It is then interesting to note that both MnSb($1\bar{1}02$) and ($11\bar{2}0$) crystallites are present in these layers. The absence of a ($11\bar{2}0$) reflection, which would be expected at $Q_z = 3.044$ Å^{-1}, is then surprising. One possible cause is tilting of the crystallites and an example of this can be seen in Figure 5.8 where the hexagonal crystallite is rotated approximately 6° away from the [$11\bar{2}0$] direction (the position of the ($11\bar{2}0$) plane is indicated by the red dashed line). Consequently, these scattering planes are not within the scattering vector direction and so cannot contribute to the scattering. A possible origin of the observed tilt is strain relaxation for thicknesses beyond h_C. A similar process is tentatively thought to occur during the growth of NiSb(0001) films on GaAs(111) substrates, where an interfacial layer, ~10 nm thick, of ($1\bar{1}01$) crystallites forms due to the actions of misfit dislocations on the NiSb structure. However, the strain is sufficiently low in the NiSb(0001)/GaAs(111) system that these crystallites do not propagate throughout the layer. Finally, the presence of ($1\bar{1}02$) and ($1\bar{1}03$) crystal orientations have been observed in NiSb films [34] and it therefore seems likely that the formation of ($1\bar{1}0l$) planes is an efficient method of reducing strain in these materials.

Reflections from both ($1\bar{1}02$) and ($11\bar{2}0$) crystallites have been identified in the growth of MnSb on InSb(001) and NaCl(001) substrates (diffraction data for these layers

is presented in Appendix B). The relative peak intensities of the two reflections differs between the substrates with growth on InSb resulting in the preferential formation of MnSb($1\bar{1}02$), while on NaCl the dominant orientation is ($11\bar{2}0$).

On the basis of electron and X-ray diffraction, it is thought that the growth of MnSb on Ge(001) results in the formation of two crystal orientations. The presence of MnSb($11\bar{2}0$) crystallites, aligned MnSb[0001]$\|$Ge[100] and MnSb[$11\bar{2}0$]$\|$Ge[010], is determined on the basis of RHEED measurements. It is likely that a second domain, with in-plane orientations of MnSb[0001]$\|$Ge[010] and MnSb[$11\bar{2}0$]$\|$Ge[100], is also present due to the two-fold symmetry of the Ge(001) double domain (2×1) reconstruction. In addition, the presence of crystallites orientated MnSb[$1\bar{1}02$]$\|$Ge[001] are observed in XRD, although as these crystallites could not be observed in the RHEED no in-plane orientation can be deduced.

5.4.4 Atomic force microscopy

The behaviour of the RHEED patterns during growth, alongside the observations made from the TEM, indicate that MnSb layers grown on Ge(001) consist of 3D islands. As the RHEED patterns fade for layer thicknesses nominally larger than 75 nm it is highly likely that the size of the islands continues to increase throughout growth, and so a key question is: does growth transition to a 2D mode with increasing coverage?

Samples of varying thickness have been studied using AFM and images of their surfaces are shown in Figure 5.11. The nominal thicknesses of the samples investigated are as follows: sample A is 5.5 nm, sample B is 27 nm and sample C is 70 nm. As the layer thicknesses increase the lateral and vertical dimensions of the islands also increase. The average height of the islands is 4 nm, 15 nm and 35 nm for samples A, B and C, respectively, while the lateral size of the islands increases from $\sim$75 nm for sample A to greater than 180 nm for sample C. As a consequence of this coarsening process, the layer continues to roughen throughout growth. The bottom panel of Figure 5.11 shows the RMS roughness of the surface as a function of layer thickness and demonstrates

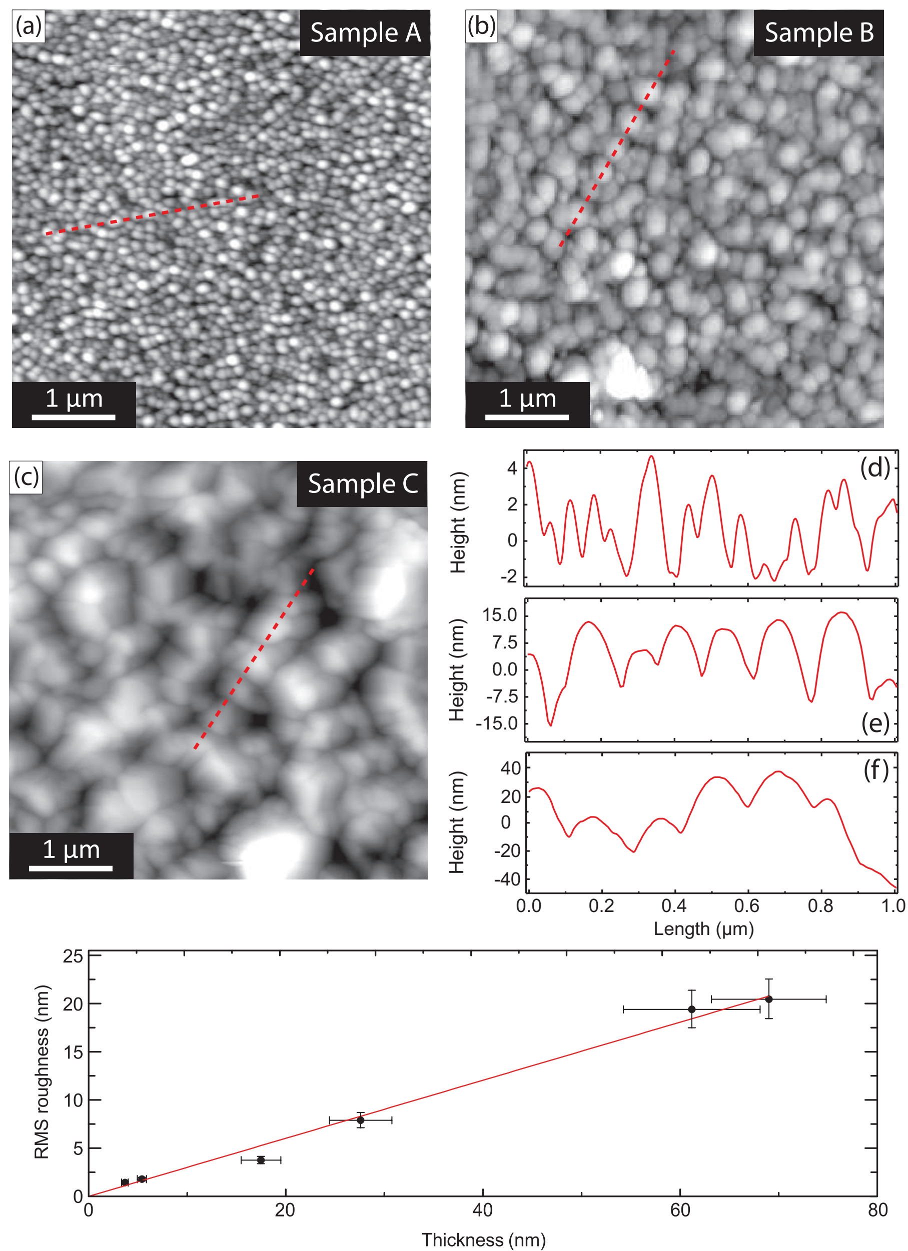

Figure 5.11: Atomic force micrographs of MnSb on Ge(001) at expected layer thicknesses of (a) 5.5 nm (b) 27 nm and (c) 70 nm. The corresponding section profiles are shown bottom right and correspond to (d) the 5.5 nm sample, (e) the 27 nm sample and (f) the 70 nm sample. Of note is the increasing island size with increasing layer thickness (progression from (a)–(c)), in all cases the samples are heavily islanded.

the linearly increasing roughness of the surface with increasing island size. Sample A exhibits an RMS roughness of (1.8±0.2) nm, sample B has a roughness of (7.9±0.8) nm and the roughness reaches (20.5±2) nm for sample C. A plot of RMS roughness for a given layer thickness is shown in panel (d) and the observed behaviour suggests that the islands will continue to grow and that, at the growth conditions studied, the layer will not transition to a 2D mode. Section profiles also show the islands become more rounded with increasing layer thickness, developing radii of curvature greater than 50 nm. This curvature is larger than the IMFP of the incident electrons in RHEED (~20 nm) and so explains the weakening of the transmission pattern for samples greater than 75 nm.

5.4.5 Magnetometry

Understanding the magnetic properties of MnSb is essential for its successful incorporation into Ge-based spintronic or magnetoelectronic devices. Previous studies of MnSb films have shown ferromagnetic behaviour with $T_C = 587$ K [17] and the easy axis in the basal plane. Hysteresis loops (M-H) and magnetisation versus temperature (M-T) curves were obtained at Warwick using a SQUID and are presented in Figure 5.12 for a sample with the surface normal aligned parallel to the applied field. Panel (a) shows a hysteresis loop acquired at 2 K between -20 and 20 kOe. The negative slope at high applied fields, above the saturation field of 8.5 kOe, is due to a diamagnetic contribution from the Ge substrate. The shape of the loop is characteristic of a hard axis response and exhibits a coercive field of (485±25) Oe. This value is significantly larger than the coercive field determined from measurements on MnSb(0001) films at Warwick of 300 Oe [60]. However, as the film is composed of small crystallites the coercivity might be expected to be large due to the difficulty in changing the magnetisation of small domains. The effective moment per Mn atom, μ_{Mn}, can be found using the following relation:

$$\mu_{\mathrm{Mn}} = \frac{M_{\mathrm{sat}}}{n_{\mathrm{Mn}}} \tag{5.1}$$

where M_{sat} is the saturation magnetisation and n_{Mn} is the number of Mn atoms present in

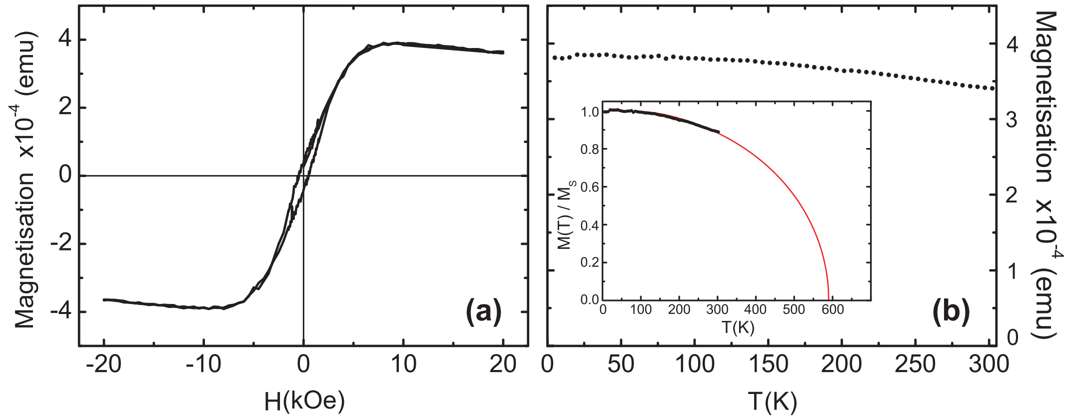

Figure 5.12: SQUID magnetometry of a 70 nm MnSb layer on Ge(001) substrate. Panel (a) shows a hysteresis loop (*M*-*H*) with the applied field aligned parallel to the *c* axis (out of the plane of the sample). The data was acquired at 2 K and the applied field was swept between -20 and 20 kOe. The shape of the curve is indicative of hard axis behaviour, while the coercive field is (485±25) Oe. Panel (b) shows a *M*-*T* plot for the same sample taken at a fixed applied field of 10 kOe, the inset shows a Brillouin function plot for $T_C = 590$ K and $J_{Mn} = 5/2$.

the sample. For a sample thickness of 70 nm a value for μ_{Mn} of $(3.5\pm0.4)\mu_B$ is obtained, which is in agreement with expected bulk value of $3.6\mu_B$ [143]. Panel (b) demonstrates the temperature dependence of the magnetisation between 5 and 302 K under an applied field of 10 kOe. From the decreasing magnetisation with increasing temperature the sample is ferromagnetic with a Curie temperature in excess of 300 K. Over the temperature range studied the effective moment of the system decreases by (12±1) % and when compared to the value of 7.5 % determined from the MnSb/GaAs(111) system indicates a possible reduction in the Curie temperature. However, shown in the inset is a plot of the Brillouin function for $J = 5/2$ and $T_C = 590$ K, from which it can be seen that the Curie temperature of the system is in good agreement with the expected bulk value of 587 K [17]. The magnetic measurements presented here show that layers of MnSb on Ge(001) are ferromagnetic with properties similar to MnSb thin films on GaAs substrates.

5.5 Growth of MnSb layers on Ge(111) substrates

The growth of MnSb on Ge(001) substrates is characterised by 3D growth, with a mixture of $(1\bar{1}02)$ and $(11\bar{2}0)$ crystallites although the ferromagnetic and chemical behaviour of the film are seen to be the same as films grown on GaAs substrates (see Section 4.2). It is expected that the improved symmetry match with the (111) face of Ge will result in improved growth. To this end, thin films of MnSb have been grown on Ge(111) substrates using a two-stage growth method with $T_{\mathrm{sub}} = 350/420$ °C and a $J_{\mathrm{Sb/Mn}}$ of 6.5. However, owing to the reduced availability of (111) orientated substrates a small sample set has been produced. As such, the work detailed below presents preliminary results on this system.

RHEED observations

The start of growth was characterised by the fading of the substrate streaks and the appearance of new streaks, with a different separation. However, unlike on Ge(001), these streaks persisted throughout growth. Some faint transmission spots and facets were observed on the integer order streaks during the first stage of growth but these faded during the second stage. Following growth a weak td(1×4) pattern appeared, indicative of an Sb rich MnSb(0001) surface. Typical RHEED patterns are shown in Figure 5.4. Panels (a) and (b) show the periodicities of the td(1×4) pattern along the [110] and $[\bar{2}11]$ directions. The presence of sharp integer and fractional streaks, in addition to multiple Laue zones and Kikuchi features, demonstrates that surface is highly crystalline. Additionally, the absence of transmission features following deposition of a thick film (hundreds of nanometres) indicates planar growth and the absence of 3D islands. The RHEED patterns have hexagonal symmetry and follow the same symmetry as observed on the Ge substrate. The measured separation of the streaks corresponds to a real space separation of 4.13(9) Å, which is in good agreement with the expected MnSb bulk *a* parameter of 4.128 Å.

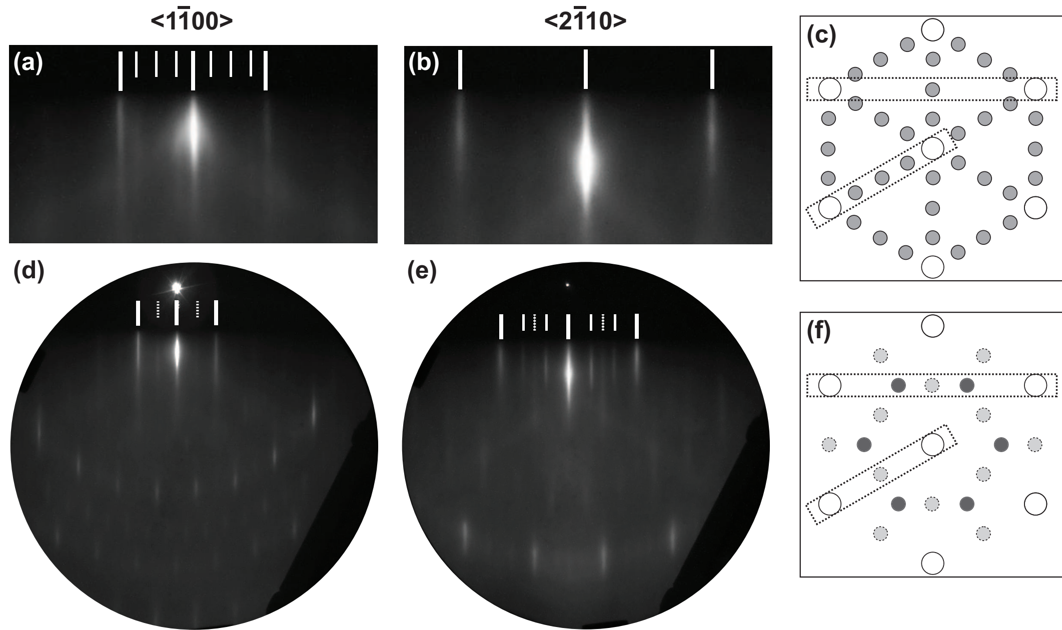

Figure 5.13: RHEED patterns obtained for a 70 nm MnSb thin film grown on Ge(111). Panels (a) and (b) show the td(1×4) pattern observed after growth was stopped and the sample was allowed to cool to <350 °C, while panel (c) shows the expected reciprocal space mesh. Panels (d) and (e) demonstrate the co-existing (2×2)/($\sqrt{3}\times\sqrt{3}$)R30° pattern observed following Mn deposition and subsequent annealing. while panel (f) is the expected reciprocal space mesh, dark grey circles indicate the ($\sqrt{3}\times\sqrt{3}$)R30° structure while the light grey arise from the (2×2) structure. The long (short) solid bars indicate the position of the integer (fractional) streaks for one of the co-existing reconstructions, while the dashed lines represent the second (if present).

After growth was stopped, samples were exposed to fluxes of Mn or Sb in order to determine if any additional reconstructions exist on the surface. When grown on GaAs substrates, MnSb(0001) has four reconstructions [62] and, in order of increasing Mn exposure, these are: td(1×4), (1×1), (2×2) and ($2\sqrt{3}\times2\sqrt{3}$)R30°. At temperatures above 350 °C, exposure to Sb results in the formation of a (1×1) structure, while below 350 °C a td(1×4) structure is observed. The behaviour of the surface is, initially, similar to MnSb(0001)/GaAs(111) with the formation of a (2×2) structure following exposure to Mn. However, with increasing Mn deposition time a metastable (6×4) structure appears, which is characterised by a (6×) periodicity along the [$\bar{2}$11] direction and a (4×) periodicity along the [110] direction. In the absence of Mn the pattern fades to

a (1×1) within tens of seconds and, as a result, could not be photographed. This pattern has been recently reported on NiSb [68] under similar metal-rich conditions. Increasing Mn exposure results in the appearance of a co-existing $(\sqrt{3}\times\sqrt{3})$R30° and $(2\sqrt{3}\times2\sqrt{3})$R30°. In all cases, annealing to temperature greater than 300 °C reverts the structure back to a faint (2×2) with weak $(\sqrt{3}\times\sqrt{3})$R30° features: an example of this pattern is shown in Figures 5.13(c) and (d). The presence of the (1×1) structure during growth is indicative of high $J_{\mathrm{Sb/Mn}}$ conditions [62]. The diffusion pathways of Mn adatoms on Ge(111) substrates were investigated by Zhu et al. [144] through the use of DFT calculations and it was found that segregation of Mn into the Ge(111) bulk is a favourable process. Segregation would then act to reduce the effective $J_{\mathrm{Sb/Mn}}$ value on the surface and so could explain the behaviour observed in the RHEED. As the values for T_{sub} and $J_{\mathrm{Sb/Mn}}$ are the same as those used for growth on GaAs(111), while the lattice mismatch is also very similar, it might be expected that the observed growth reconstruction would be the (2×2). Further work, including interface studies using TEM, is necessary in order to check the validity of this assumption and investigate the possibility of Mn segregation.

From the measured lattice parameter and the observed symmetry match between the substrate and epilayer, the orientation of the film is MnSb[0001]||Ge[111] with MnSb[$2\bar{1}\bar{1}0$]||Ge[110]. This is in agreement with previous work on the growth of MnSb and MnAs thin films on GaAs [145, 128] and MnAs on Si(111) [146].

5.6 Characterisation of MnSb/Ge(111) samples

5.6.1 X-ray photoelectron spectroscopy

Initial XPS studies have been performed to check the stoichiometry of the sample and to investigate the presence of Ge at the surface. Figure 5.14 shows shallow core XPS data for the sample shown in Figure 5.13 which was uncapped and had been exposed to air for several days. No sample preparation was performed after loading into the XPS

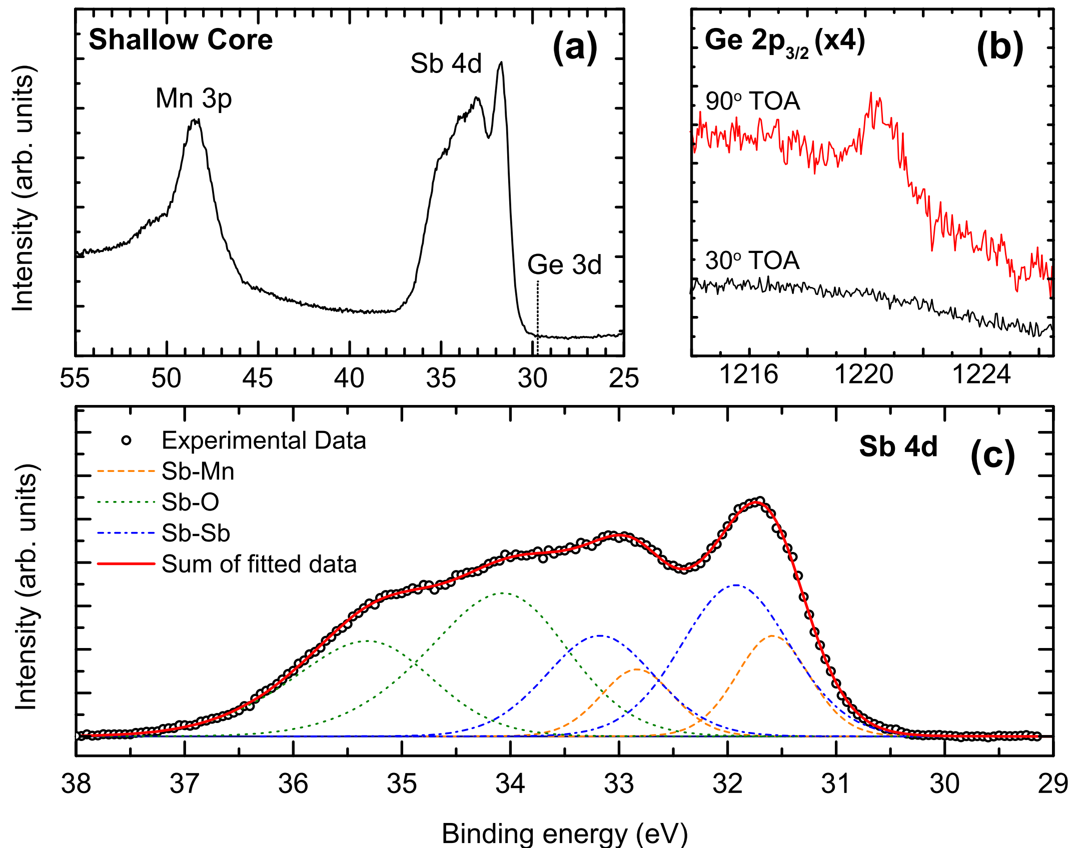

Figure 5.14: XPS spectra from an as-loaded 70 nm thick MnSb film grown on Ge(111). Panel (a) shows the shallow core region with the Mn 3p and Sb 4d core levels present while the Ge 3d core level is absent. Panel (b) is the Ge $2p_{3/2}$ core level showing 90° and 30° TOA scans. Panel (c) is the fitted Sb 4d region and indicates the presence of Sb-Mn, Sb-O and Sb-Sb bonding environments, the obtained shift of -0.34 eV between the Sb-Sb and Sb-Mn environments is similar to that observed on Ge(001) substrates.

chamber and so the scans are presented as-loaded. Figure 5.14(a) shows the shallow core region with the Mn 3p and Sb 4d core levels. As there is no Ge 3d signal present in the spectra, significant Ge surface segregation can be ruled out. Panel (b) shows the Ge 2p signal at 90° and 30° TOA, note that the increased atomic sensitivity of the Ge 2p core level (relative to the 3d core level) will result in an increase in observed intensity if Ge is present at the surface. However, the absence of any signal at 30°, which probes a smaller distance into the surface, confirms the absence of Ge segregation in MnSb

Table 5.4: Normalised area, and the corresponding percentage composition, for the C 1s, O 1s, Mn 3p and Sb 4d core levels.

Core level	Normalised Area	Percentage composition
C 1s	6989	25.3
O 1s	4813	36.8
Mn 3p	4030	21.2
Sb 4d	3174	16.7

films. The observed signal is then attributed to misalignment and so a small region of the sample that was obscured by the Ta strips during growth has been probed. In order to determine the stoichiometry of the surface region, total elemental peak areas were obtained. Following subtraction of a linear background from the measured spectra, the core levels (C 1s, O 1s, Mn 3p and Sb 4d) were then fitted using Voigt functions and the results of these fits are given in Table 5.4. It can be seen that the surface is strongly contaminated by C and O, and the Mn-to-Sb ratio is determined to be 1.27:1. The increased Mn content arises due to the preferential formation of Mn oxides relative to Sb oxides [28] and is characteristic of oxidised MnSb thin films on GaAs. Shown in Figure 5.14(c) is a close-up of the fitted Sb 4d region. As with MnSb/Ge(001), three doublets are required to fit the core level with the doublets corresponding to Sb-Sb, Sb-Mn and Sb-O_x bonding environments. The corresponding binding energies of the Sb $4d_{5/2}$ components are given in Table 5.5. The chemical shift between the Sb-Sb and Sb-Mn component is similar to that observed on MnSb/Ge(001) at 0.34 eV. Preliminary fits of the Sb 4d core level of decapped MnSb(0001) films on GaAs(111) reveal a shift of $\sim$0.4 eV, in broad agreement with the shift observed here. The Sb-O_x component shows a reduced shift as compared to MnSb/Ge(001), indicating the formation of more Sb-rich oxides.

The formation of a Mn-rich surface following exposure to atmosphere is consistent with the behaviour of MnSb on GaAs substrates, while the absence of a Ge signal is promising in terms of reduced segregation in MnSb layers.

Table 5.5: Peak fitting details showing the assigned bonding environment, binding energy and the chemical shift relative to the Sb-Sb bonding environment for a MnSb/Ge(111) sample. Values are taken from the fit presented in Figure 5.14.

Bonding environment	Binding energy $4d_{5/2}$ (eV)	ΔE (rel. to Sb-Sb) (eV)	Percentage
Sb-Sb	31.92	0.00	39.3
Sb-Mn	31.58	-0.34	14.0
Sb-O	34.07	2.15	46.7

5.6.2 X-ray diffraction

To confirm if the growth plane is MnSb(0001), XRD was performed on the sample that gave rise to the RHEED patterns shown in Figure 5.13. Figure 5.15 shows diffraction data from a 70 nm thick uncapped sample, the intense peaks are easily identified as belonging to the $\{111\}$ planes of Si and Ge, and the measured a_{Ge} lattice parameter is 5.655(1) Å, which is in agreement with the expected bulk value of 5.658 Å [147].

Table 5.6: Fitting details for the peaks observed in Figure 5.15. The obtained values for Q_z were used to determine the lattice parameter, while the FWHM values were used for Williamson-Hall analysis in order to determine the grain size.

Reflection	Q_z (Å^{-1})	FWHM (°)
(0002)	2.170(2)	0.117(2)
(0004)	4.340(3)	0.156(3)
(0006)	6.510(5)	0.236(3)

Three reflections arising from n-MnSb$\{0002\}$ planes have been identified and their associated values are shown in Table 5.6. The c_{MnSb} lattice parameter was determined to be 5.790(1) Å, while the grain size, obtained from Williamson-Hall analysis, yields a grain size of (89$\pm$2) nm. This value is larger than the film thickness derived from the growth rate. This discrepancy likely arises from the value of κ used in the grain size contribution to the Williamson-Hall analysis (Section 2.4.3.1). The exact value of κ depends upon the function used to represent the peak shape and, consequently, the

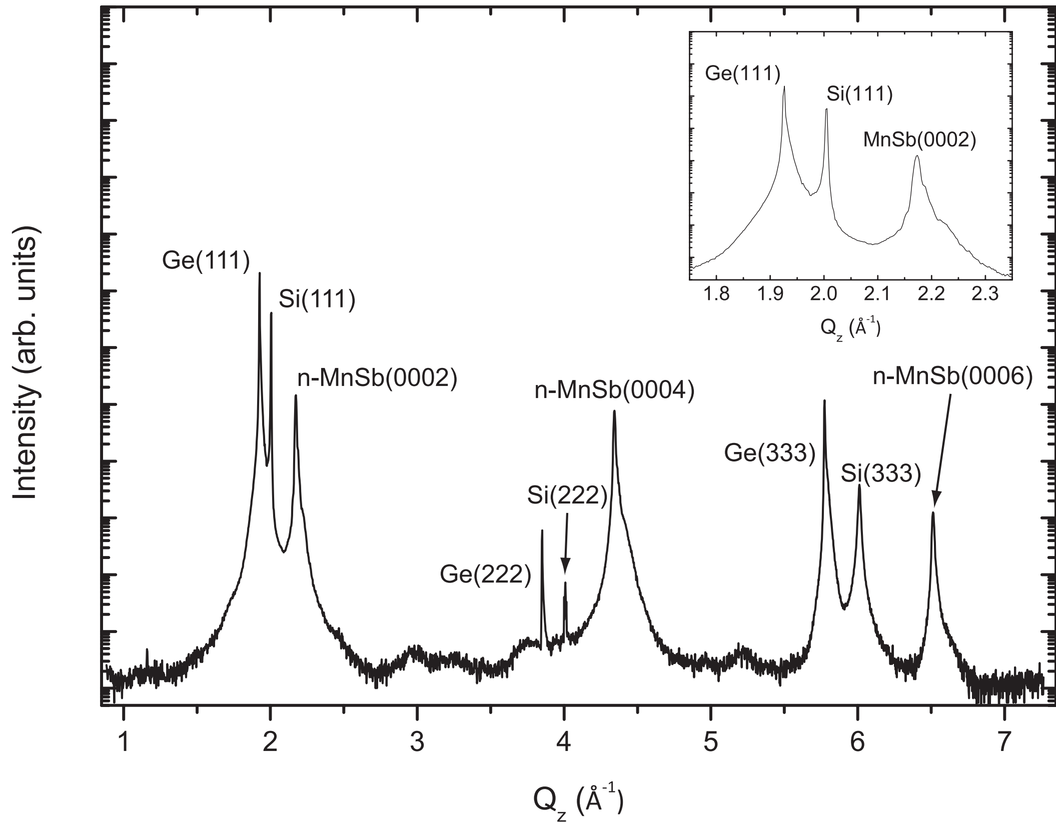

Figure 5.15: High-resolution XRD of a 70 nm MnSb(0001) layer grown on Ge(111) acquired at the NSLS. The inset shows a zoom around the MnSb(0002) reflection in the 1.75 Å^{-1} $\leq Q_z \leq$ 2.35 Å^{-1}. Reflections from the substrate and overlayer are as labelled in the figure.

presence of multiple strained peaks for the n-MnSb{0002} reflections, as shown in the inset of Figure 5.15, results in asymmetric peaks that are not perfectly represented by the Pearson VII function. As such, a systematic thickness offset is introduced into the grain size through the uncertainty in the value of κ. The derived c_{MnSb} lattice parameter is in good agreement with the average film value of 5.791 Å which was determined in Chapter 4.

The inset shows a zoom of the MnSb(0002) region for 1.75 Å^{-1} $\leq Q_z \leq$ 2.35 Å^{-1}. The Ge(111) reflection shows a strained shoulder towards the Si peak, while the (0002) reflection demonstrates a clear asymmetry towards higher Q_z values. This indicates a

reduction in c lattice parameter and, for a positive Poisson ratio (or appropriate elastic modulus), a volume conserving distortion may be taking place. This would result in an increase in the in-plane lattice parameter, although this is not observed in the RHEED. Under the assumption of a volume conserving distortion a change of $\sim$2 % in c (as observed in Figure 5.15) would correspond to an a parameter shift of $\sim$1 %, which is within the uncertainty of the RHEED (which is approximately 1.5 %). Consequently, any strain in these layers cannot be observed using RHEED alone and XRD is necessary to study the effects of strain, as demonstrated in Chapter 4. It is likely that the observed shoulder on the MnSb(0002) reflection (shown in the inset of Figure 5.15) originates from a strained layer buried in the film, possibly either at the interface or within the layer itself. However, it is currently unknown if this is a property of the layer or due to the non-optimal growth conditions used for the samples studied.

Of interest is the absence of reflections from MnSb polymorphs, Mn_xGe_y compounds or MnSb crystallites. It is possible that the polymorphs are an artifact of growth on GaAs and that this arises due to Ga segregation at the surface, which induces the formation of polymorphs through local stoichiometry variations (note that As segregation is not observed). However, as only a limited sample set has been investigated no strong conclusions can be made regarding the presence of polymorphs in MnSb layers on Ge substrates. Further structural investigations are therefore required to determine if the formation of polymorphs is related to the choice of substrate.

5.6.3 Atomic force microscopy

Figure 5.16 shows atomic force micrographs at scan sizes of 5 μm $\times$ 5 μm, shown in panel (a), and 15 μm $\times$ 15 μm, shown in panel (b). The sample, of thickness 70 nm, consists of flat-topped islands greater than 500 nm in width, with heights ranging between 10 and 25 nm, and an example profile across these islands is shown in panel (a). Larger image sizes reveal that the sample is uniformly covered in crystallites and the corresponding RMS roughness of the sample is approximately 7 nm, as derived from

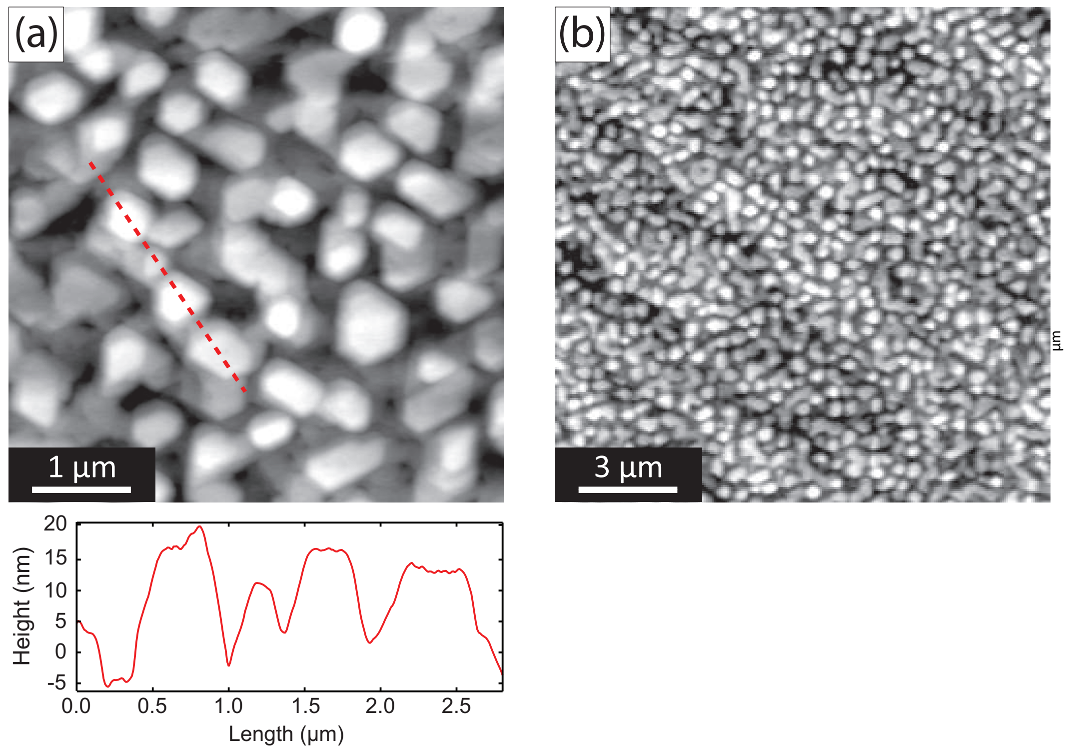

Figure 5.16: Atomic force micrographs of a MnSb(0001) thin film at scan sizes of (a) 5 μm × 5 μm (including section profile shown at bottom of panel) and (b) 15 μm × 15 μm. The surface consists of a mesa morphology structure and so is consistent with high $J_{\mathrm{Sb/Mn}}$ growth conditions. The RMS roughness for the sample, as derived from panel (b), is 7 nm.

panel (b). The steep sided hexagonal islands are very similar to the mesa morphology of MnSb/GaAs(111) layers grown under Sb-rich conditions. The islands observed here are significantly smaller than the mesa structures typically seen on high $J_{\mathrm{Sb/Mn}}$ MnSb/GaAs samples. In the case of MnSb/GaAs samples the height of the mesas can reach the thickness of the films (hundreds of nms), although it should be noted that both the islands seen here and the mesas are flat-topped. This is in agreement with the behaviour of the RHEED which indicates Sb-rich conditions and the observed streaky diffraction then arises from the flat tops of the islands.

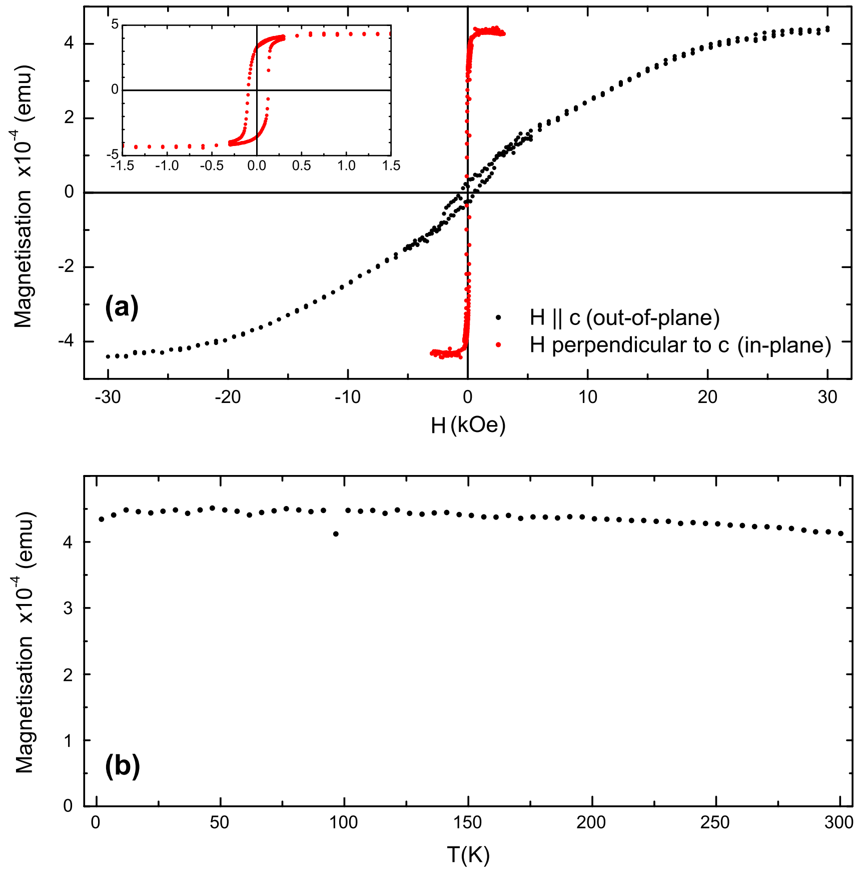

Figure 5.17: SQUID magnetometry of a 70 nm MnSb layer on Ge(111) substrate. Panel (a) shows hysteresis loops (*M*-*H*) obtained at 5 K with the applied field parallel (out-of-plane, black) and perpendicular (in-plane, red) to the *c* axis of MnSb. The inset shows a zoom of the loop for the field applied perpendicular to the *c* axis. Panel (b) shows the *M*-*H* behaviour of the sample.

5.6.4 Magnetometry

Figure 5.17 shows *M*-*T* and *M*-*H* plots for a MnSb(0001) film grown on Ge(111). Panel (a) shows hysteresis loops, obtained at 5 K, with the applied field perpendicular (coloured red and denoting in-plane magnetisation behaviour) and parallel (black, which denotes out-of-plane behaviour) to the *c*-axis. The inset shows a zoom of the hysteresis loop with the field applied perpendicular to the *c* axis. Uniaxial magnetic anisotropy is present in the film and the easy axis corresponds to the in-plane direction, which agrees with the behaviour of both thin films [17] and bulk crystals [143] of MnSb. An estimate

of the effective moment per Mn can be made using the film thickness of 70 nm and a value of $(3.3\pm0.3)\mu_B$ is found. The coercive field, H_c, along the easy axis is (111 ± 2) Oe while with the field along the hard axis it is (567 ± 30) Oe. These values are consistent with those derived for MnSb(0001) films grown on GaAs(111) substrates, where H_c along the easy axis is 14–200 Oe and is 300–500 Oe along the hard axis [17, 60]. Panel (b) shows the magnetisation behaviour as a function of temperature (H fixed at 30000 Oe) and indicates a Curie temperature in excess of 300 K, consistent with previous observations of MnSb thin films.

5.7 Conclusions

The growth of MnSb on Ge(001) and Ge(111) layers has been investigated over a range of T_{sub} and $J_{Sb/Mn}$ conditions. To characterise the substrate prior to the growth of MnSb, a combined RHEED and LEED study of the Ge(001)-(2$\times$1) structure has been performed. In LEED, the expected (2$\times$1) pattern is observed although a (2$\times$2) pattern is seen in RHEED. The half-order fractional streaks along the [100] direction are curved and are found to arise from disorder along the (2$\times$1) dimer rows. The presence of intense curved diffraction features in RHEED, compared to LEED, is attributed to the different transfer widths of the two techniques.

The growth of MnSb on Ge(001) is hampered by a three-dimensional growth mode which results in the formation of islands with two distinct crystallographic orientations: $(1\bar{1}02)$ and $(1\bar{1}20)$. The two crystallite orientations are observed either in XRD and RHEED, respectively, and the absence of $(1\bar{1}20)$ reflections in the XRD is thought to arise due to tilting of the crystallites with respect to the substrate. The origin of the 3D growth mode is not due to interfacial reactivity but is, instead, likely to arise from strain relaxation. Through comparison with NiSb thin films, the formation of $(1\bar{1}0l)$ orientated crystallites are proposed as an efficient strain relaxation mechanism in transition-metal pnictides.

Films of MnSb on Ge(001) are of low crystalline quality, however, the heteroepi-

taxial growth of MnSb(0001) occurs on Ge(111) substrates and is reported for the first time. The resulting high quality films have structural parameters that are comparable to films grown on GaAs(111) substrates, with an *a* lattice parameter of 4.13(9) Å and a *c* parameter of 5.790(1) Å. The growth conditions used for the production of high quality films on GaAs substrates are not transferable to Ge(111) and it is believed that Mn segregation into the bulk results in a higher effective $J_{\mathrm{Sb/Mn}}$. The films show the expected ferromagnetic behaviour and our results show the successful combination of a transition-metal pnictide with a Group IV semiconductor. The use of engineered Ge buffer layers on Si substrates, as a means of reducing lattice mismatch, is then a promising route for the incorporation of Mn pnictides into Si-based spintronics.

Chapter 6

Conclusions and future work

6.1 Conclusions

In this thesis a wide range of techniques have been used to study the structural, chemical and magnetic properties of MnSb thin films on both GaAs and Ge substrates. In addition, the effect of Mn on III-V semiconductor surfaces has been investigated and this is the focus of the first experimental chapter, Chapter 3.

A combination of RHEED, STM and AFM have shown that islands form on both In- and Sb-rich surfaces of InSb. Layer equivalent thickness measurements, performed using AFM, indicate that the islands on the In-rich surface consist of elemental Mn, while on the Sb-rich surface they are seen to be composed of a $MnSb_x$ alloy. However, on GaAs, the incorporation of Mn into the surface results in the formation of a (2×2) reconstruction. This process occurs simultaneously with the formation of $MnAs_x$ alloy islands and Ga-rich 'rod' reconstructions, which arise due to local reductions in the surface As content. On both GaAs and InSb surfaces the removal of Group V atoms from the surface, and the appearance of alloy islands, is predicted by bulk thermodynamics. However, the energy contribution of the surface and transition-metal induced reconstruction (if present) to the resulting enthalpies is significant and may have a profound effect on the behaviour of the surface. The substitution of Mn atoms into the $\beta2(2\times4)$

and c(4×4) surface reconstructions has been considered in terms of the presence of heterodimers in these reconstructions. As the $\beta2(2\times4)$ contains no heterodimers, a reduced number of incorporation pathways were found for this surface compared to the c(4×4) and so accounts for the difference in island densities between the two surfaces. Finally, the incorporation of Mn is proposed as a method for MnSb island formation. This has two consequences: the first is that substitution sites in the reconstruction can act to promote island growth during MnSb heteroepitaxy alongside the more commonplace defect-mediated nucleation. Secondly, the change in bonding environments will have a significant effect on the density of states (DOS) of the interface and so alter the transport properties of a spintronic devices constructed from these materials.

Chapter 4 presents an HRXRD investigation into the niccolite, zincblende and wurtzite phases of MnSb. The structure of MnSb films on GaAs can be thought of as consisting of a n-MnSb framework which could plausibly contain strained c-MnSb and ultra-thin w-MnSb inclusions embedded within. However, TEM studies indicate that the polymorphs are located in the upper regions of the film while the strain behaviour determined by XRD suggests that the crystallites are embedded within the majority n-MnSb layer. The n-MnSb framework is epitaxial to the GaAs substrate but is also observed to grow on GaSb islands located at the interface. The initial growth of MnSb on GaAs is seen to be pseudomorphic up to the critical thickness of $\sim$3 nm after which a mosaic of $\sim$0.4° forms due to the generation of misfit dislocations at the interface as the film relaxes. No significant trends with the $J_{\mathrm{Sb/Mn}}$ value were observed for the lattice parameter or strain dispersion values for any of the polymorphs. While this indicates little or no dependence on the growth parameters, it is highly likely that the X-ray beam is averaging over a large range of J values due to the uncertainty in the Mn flux. However, while no dependence on the Sb-to-Mn flux ratio is observed at macroscopic lengthscales it is likely that local J variations are driving stoichiometry changes. This results in the n-MnSb c lattice parameter varying and, through the use of asymmetric RSMs, the relative concentration of the c-MnSb polymorph is seen

to reach a maximum at the average film c parameter of 5.791(1) Å. This suggests that the optimum n-MnSb growth conditions are favourable for the formation of the polymorphs. However, the polymorph content appears to increase with decreasing J and so it may be possible to further increase the polymorph content of MnSb films through stoichiometry variation. The incorporation of highly spin polarised inclusions in the ferromagnetic n-MnSb framework could act to increase the net polarisation of the layer and this has implications for the applicability of MnSb as a spin polarising injection layer. Regarding the polymorph inclusions, the difficulty in resolving between GaSb and wurtzite MnSb reflections has so far limited a full analysis of this material. The use of asymmetric RSMs is an attractive method for gaining insight into this polymorph owing to the structural differences between the two materials. The c-MnSb crystallites present in the film are found to be significantly strained and as a result are likely to experience either a trigonal or rhombohedral distortion. The effects of such distortions on the half-metallicity are unknown at this time but could plausibly disrupt the half-metallicity of the cubic polymorph. Investigation into the effect of this strain on the magnetic behaviour of c-MnSb should be of interest for future theoretical studies. From an experimental point of view, the small lattice mismatch between c-MnSb and InSb, and the observation that InSb is unreactive in the presence of Mn, is promising for the use of InSb as a substrate for c-MnSb. However, preliminary studies, presented in Appendix B, reveal an absence of c-MnSb. As only a few samples have been grown it is necessary to further refine, and subsequently optimise, the growth conditions for the formation of this polymorph. In addition, the presence of Sb diffraction features may be obscuring the underlying c-MnSb reflections.

Finally, the growth of MnSb on Ge substrates has been investigated. The lattice parameter of Ge is very close to that of GaAs and it is expected that the growth of MnSb would be behave similarly. Additionally, the choice of Ge substrates avoids the segregation of Ga throughout the films and the formation of GaSb 'huts' at the interface. Prior to growth, the Ge(001) substrates were characterised through the use

of RHEED and XPS, before a combined LEED-RHEED study was made of the Ge(001)-(2×1) structure. The apparent discrepancy between the (2×1) pattern in LEED and the (2×2) observed in RHEED is discussed in reference to the presence of spontaneous dimer tilt ordering and the relative transfer widths of the two techniques. The growth of MnSb on Ge(001) results in low crystalline-quality films, which are seen to consist of a mixture of $(1\bar{1}02)$ and $(1\bar{1}20)$ orientated islands. The $(1\bar{1}20)$ crystallites are believed to be tilted, explaining their absence in the XRD data. Interfacial reactivity as the cause of the observed 3D growth mode is ruled out on the basis of TEM and XPS studies, which show the interface to be sharp and the surface to have a small Ge content, respectively. The observed Ge signal is believed to result from the irregular nature of the layers and that regions of the MnSb layer are sufficiently thin that photoelectrons from the substrate can be detected. Through comparison with NiSb thin films, the formation of $(1\bar{1}0l)$ orientated crystallites could then be an efficient method for strain relaxation in the transition-metal pnictides, although this is currently unconfirmed. Finally, the successful growth of MnSb thin-films on Ge(111) substrates is reported. The structural and magnetic properties of the films are comparable to those grown on GaAs(111), although no segregation of Ge is observed. As the Ge films are grown on Si substrates it is plausible that the Ge layer could be lattice matched to MnSb through the use of strain engineering. This then provides an attractive method for producing low defect MnSb layers for incorporation into Si-based spintronic devices.

6.2 Future work

There remain several questions regarding the MnSb polymorphs and their spintronic applications. These arise from both interfacial, for spin transport, and half-metallic polymorph, for high efficiency injection, considerations. Regarding the interface, the interaction of Mn with the surface of GaAs is seen to be reactive and the incorporation/substitution of Mn into the surface could act to form island nucleation centres during MnSb growth. High resolution STM of ultra-low coverages of both Mn

and MnSb would help to confirm if this process does occur, subsequent detailed structural studies on the Mn induced (2×2) on the Ga- and As-rich GaAs surfaces would yield possible atomic structures for the reconstructions. These could then be used as a basis, with focus on the likely positions of the Mn atoms, for determining the structure of the interface between GaAs and MnSb. Subsequently, through the use of DFT calculations, the electronic behaviour of the resulting interfaces could be calculated and investigated. The spontaneous removal of Group V atoms from the surface is reflected, to a first approximation, by bulk thermodynamics. However, the calculated enthalpies of reaction are often positive, even for the experimentally observed conversion pathway. Further investigation into the surface behaviour of Ni or Cr with additional III-V semiconductors would allow the effects of bulk thermodynamics to be more fully explored. The effect of particular reconstructions, such as the (2×4), could then be investigated across a wide range of III-V semiconductors.

The XRD studies presented in Chapter 4 indicate that the formation and growth of the MnSb polymorphs is seemingly unrelated to the growth parameters. However, the large variation observed in J_{corr} as a result of the Mn cell position remains a concern. To this end, it is worthwhile lengthening the Mn effusion cell in order to minimise the collimating effects. Equally, lowering the position of the Sb effusion cell to match the height of the Mn cell would reduce the temporal effects induced by the shutter proximity. These two modifications, alongside further XRD structural studies of MnSb thin films, may help to determine the true influence of J on the growth of c-MnSb and w-MnSb. Additionally, asymmetric RSMs will prove invaluable in determining the strain and the extent of polymorphism in these layers. Further study on the effects of T_{sub} during growth and the influence of post-growth annealing cycles may help to determine the thermodynamic properties of polymorph formation.

MnSb was successfully grown on Ge(111) substrates but growth on Ge(001) reveals the presence of 3D growth with two crystal orientations: $(11\bar{2}0)$ and $(1\bar{1}02)$. A wide range of techniques have been used to characterise the properties of these layers,

although only a relatively narrow range of growth conditions have been investigated. Studies of the growth at either extreme of the $J_{\mathrm{Sb/Mn}}$ range ($J \leq 4$ or $J \geq 10$) should be carried out in order to ascertain if 2D growth is feasible on (001) substrates. This is done with reference to the observation that values of $J \leq 8$ avoids the mesa morphology of MnSb layers grown on GaAs substrates. Although the growth of MnSb on Ge(111) was successful, the number of samples grown to date is limited. Additionally, the surface morphology of the films indicates a high $J_{\mathrm{Sb/Mn}}$ value. A more detailed growth study is necessary to optimise the growth conditions. Studies by XRD are also necessary in order to determine if polymorph formation does occur in layers grown on Ge, as they are not evident in the limited data presented in this thesis. Further studies of the MnSb/Ge(111) interface using HRTEM or scanning transmission electron microscopy (STEM), while making use of spectroscopic measurements, could be used to determine if Mn diffusion into the Ge substrate occurs and to subsequently map its spatial distribution.

There remains the opportunity for heteroepitaxial growth on additional substrates. The In-terminated InSb surfaces were seen to be unreactive under the deposition of Mn and so might be expected to provide good substrates for the growth of c-MnSb films. This is further corroborated by the excellent symmetry and small lattice mismatch (≤ 0.4 %) present between the two materials. Consequently, an in-depth growth study of these systems could provide a method for stabilising the growth of c-MnSb in thin film form. Additionally, the growth on ionic solids, particularly NaCl (lattice mismatch -3.5 %), may provide avenues for stabilising the polymorphs through a change in surface chemistry or strain. Preliminary results on the growth of MnSb on InSb and NaCl substrate are presented in Appendix B.

Appendix A

Predicted X-ray diffraction reflection positions

Indexing reflections from θ-2θ diffraction data

The XRD data presented in Chapter 4 features an extensive number of reflections arising from multiple materials, crystallites and polymorphs. A list of these materials, and their lattice parameters, is given in Table A.1. For materials with a cubic structure the predicted Q_z values are given in Table A.2. The zincblende structure (spacegroup $F\overline{4}3m$) is observed for GaAs, GaSb, InSb and c-MnSb, while rs-MnSb and NaCl have the rocksalt structure (spacegroup $Fm\overline{3}m$). The elemental semiconductor Ge has the diamond structure (spacegroup $Fd\overline{3}m$). Reflections for rs-MnSb have been calculated on the basis that the rare earth pnictides, such as ErSb [148], exhibit this structure and so it is feasible that MnSb could adopt this structure. The equilibrium lattice parameter of rs-MnSb has been calculated using the CASTEP DFT code and is found to be 5.600 Å. These calculations were performed by Dr Matthew Bradley at the University of Warwick, note that no spin polarisation constraints were placed on the calculation and that the resulting ground state is ferromagnetic. Similar studies have shown c-MnSb to be half-metallic while the present study indicated that rs-MnSb is not half-metallic.

Table A.1: Lattice parameters used to calculate the Q_z values for the XRD reflections given in Tables A.2 and A.3.

Material	*a* parameter (Å)	*c* parameter (Å)	% mismatch to GaAs	% mismatch to n-MnSb	Ref.
GaAs	5.653	-	0.00	-3.27	[31]
GaSb	6.096	-	7.27	4.23	[117]
InSb	6.479	-	12.75	9.90	[117]
NaCl	5.640	-	-0.23	-3.50	[92]
Ge	5.658	-	-0.09	-3.18	[147]
c-MnSb	6.502	-	13.06	10.21	[23]
rs-MnSb	5.600	-	-0.95	-4.25	DFT
n-MnSb	4.128	5.789	3.17	0.00	[118]
w-MnSb	4.291	7.003	6.85	3.80	[23]
h-Sb	4.308	11.274	7.21	4.18	[111]

The predicted Q_z values for the hexagonal materials (n-MnSb, w-MnSb and h-Sb) are given in Table A.3. The properties of niccolite MnSb (n-MnSb, spacegroup $P6_3/mmc$) were outlined in Section 4.4.1 and it is the primary structural form of the material in the bulk. The wurtzite polymorph of MnSb (spacegroup $P6_3mc$) is a mutual polytype of c-MnSb and differs in the stacking order. The zincblende structure has an AaBbCc stacking order, while the stacking order of wurtzite is given by AaBb. Here, the letter denotes the lattice site while capitalisation denotes atomic species occupation (A = Mn, a = Sb). A consequence of the polytypism is a small difference in the next-nearest neighbour distance of the two structures and, consequently, the difference in equilibrium energies of the two structures is small ($\sim 4\times10^{-3}$ eV [23]). It might then be expected that the cubic and wurtzite polymorphs would form in approximately equal quantities although, as outlined in Chapter 4, this is not observed. Finally, elemental Sb is rhombohedral in its bulk form (spacegroup $R\overline{3}m$) although a hexagonal setting can be constructed (h-Sb) [111] and is seen to be epitaxial to n-MnSb.

Additional, unidentified, reflections are present in the diffraction data shown in Figure 4.5. Several possible materials are thought to be the origin of these peaks, including: Mn_2Sb (P4/nmm), $MnSb_2$ (Pnnm), Cu ($Fm\overline{3}m$), In (I4/mmm) and MnO

Table A.2: Predicted Q_z values (for 10 keV X-ray photons with $\lambda = 1.24$ Å), given in units of Å^{-1}, for the cubic materials discussed in the text, dashes indicate systematic extinctions. It should be noted that the lowest index reflections inside the typical Q_z range studied ($0.883 \leq Q_z \leq 7.167$ Å^{-1}) are presented.

Lattice plane	GaAs	c-MnSb	rs-MnSb	GaSb	InSb	NaCl	Ge
(002)	2.223	1.933	2.244	2.061	1.940	2.228	-
(004)	4.446	3.865	4.446	4.123	3.879	4.456	4.442
(006)	6.669	5.798	6.668	6.184	5.819	6.684	-
(110)	-	-	-	-	-	-	-
(220)	3.144	2.733	3.173	2.915	2.743	3.151	3.141
(330)	-	-	-	-	-	-	-
(440)	6.288	5.466	6.347	5.830	5.486	6.302	6.282
(111)	1.925	1.674	1.943	1.785	1.680	1.930	1.923
(222)	3.850	3.348	3.886	3.570	3.360	3.860	3.847
(333)	5.775	5.022	5.829	5.355	5.039	5.789	5.770

Table A.3: Predicted Q_z values (for 10 keV X-ray photons with $\lambda = 1.24$ Å), given in units of Å^{-1}, for hexagonal materials present in MnSb thin-films, dashes indicate systematic extinctions. It should be noted that the lowest index reflections inside the typical Q_z range studied ($0.883 \leq Q_z \leq 7.167$ Å^{-1}) are presented.

Lattice plane	n-MnSb	w-MnSb	h-Sb
(0002)	2.171	1.794	-
(0004)	4.342	3.588	-
(0006)	6.513	5.382	-
$(1\bar{1}00)$	1.758	1.691	-
$(2\bar{2}00)$	3.516	3.382	-
$(3\bar{3}00)$	5.274	5.073	-
$(4\bar{4}00)$	7.032	6.764	-
$(11\bar{2}0)$	3.044	2.929	-
$(22\bar{4}0)$	6.088	5.857	-
$(1\bar{1}01)$	2.066	1.914	-
$(2\bar{2}02)$	4.132	3.828	-
$(3\bar{3}03)$	6.198	5.755	-
$(1\bar{1}02)$	2.793	2.466	-
$(2\bar{2}04)$	5.586	4.931	-
(0003)	-	-	1.672
(0006)	-	-	3.344
(0009)	-	-	5.016
$(00\underline{12})$	-	-	6.688

Table A.4: Lattice parameters used to calculate the Q_z values for the XRD reflections given in Table A.5.

Material	*a* parameter (Å)	*b* parameter (Å)	*c* parameter (Å)	Ref.
Mn_2Sb	4.074	-	6.545	[149]
$MnSb_2$	6.017	6.881	3.324	[115]
Cu	3.610	-	-	[111]
In	3.252	-	4.947	[111]
MnO	4.446	-	-	[150]

Table A.5: Predicted values of Q_z (for 10 keV X-ray photons with $\lambda = 1.24$ Å) in $Å^{-1}$ for materials trialled as potential sources of the unknown peaks in Figure 4.5. Values of Q_z highlighted in red are outside the typical angular range studied.

Lattice plane	Mn_2Sb	$MnSb_2$	Cu	In	MnO
(001)	0.960	-	-	-	-
(002)	1.920	3.780	3.481	2.540	2.826
(003)	2.880	-	-	-	-
(004)	3.840	7.561	6.962	5.080	5.652
(005)	4.800	-	-	-	-
(006)	5.760	-	-	7.620	8.478
(007)	6.720	-	-	-	-
(110)	2.181	1.387	-	2.732	-
(220)	4.362	2.774	4.924	5.464	3.997
(330)	6.543	4.161	-	8.196	-
(440)	8.724	5.548	9.848	-	7.994
(550)	-	6.935	-	-	-
(101)	1.817	2.159	-	2.312	-
(202)	3.634	4.318	4.924	4.624	3.997
(303)	5.451	6.477	-	6.936	-
(011)	1.817	2.099	-	2.312	-
(022)	3.634	4.198	4.924	4.624	3.997
(033)	5.451	6.297	-	6.936	-
(111)	2.383	2.345	3.015	-	2.448
(222)	4.766	4.690	6.030	6.026	4.896
(333)	7.149	7.035	9.045	-	7.344

($Fm\bar{3}m$) and the reasoning behind these choices is outlined in Section 4.3. Table A.4 lists the lattice parameters used in determining the predicted Q_z shown in Table A.5.

Appendix B

Heteroepitaxial growth of MnSb on InSb and NaCl

Introduction

This appendix outlines the preliminary studies performed on the growth of MnSb on InSb and NaCl substrates. This work was performed for two reasons: the first is the small lattice mismatch between c-MnSb and InSb of $\sim$0.4 %. The second is that strain engineering may provide an alternative method for promoting the growth of a single polymorph as an epitaxial layer. Firstly, the growth of MnSb on InSb(001) is discussed with reference to electron and X-ray diffraction data followed by the results obtained for growth on NaCl(001), although it should be noted that only a limited sample set has been produced for both substrates.

Growth of MnSb films on InSb(001)

The RHEED patterns from an InSb(001) sample following a single IBA cycle are shown in the top panels of Figure B.1 and show the presence of a c(8$\times$2) reconstruction. Some faint facet features can be seen along the $\langle 1\bar{1}0 \rangle$ direction along with the presence

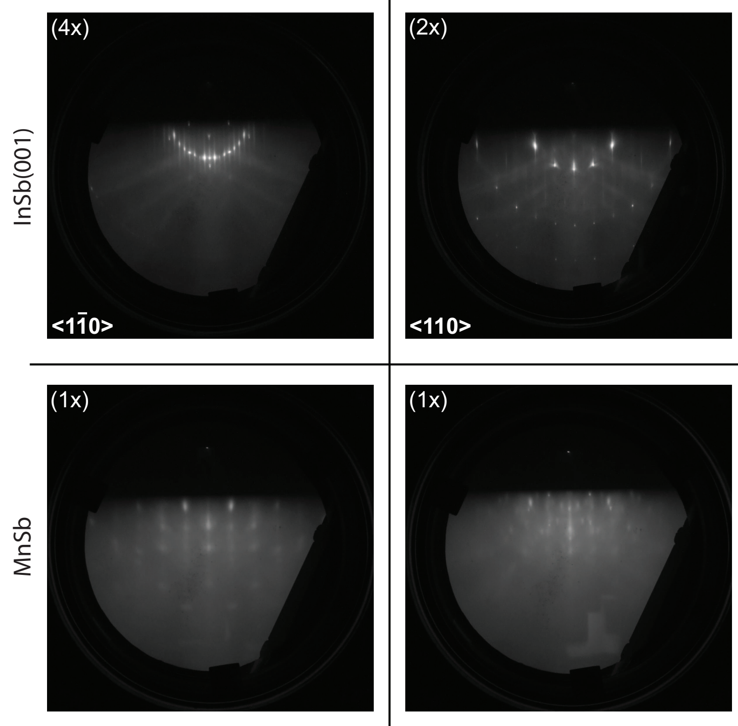

Figure B.1: RHEED patterns from a 5 nm MnSb film grown on an InSb(001) substrate. The top panel shows the InSb(001)-c(8×2) reconstruction observed following cleaning. The bottom panel shows the RHEED patterns following deposition of 5 nm of MnSb.

of strong Kikuchi features and multiple Laue zones. The bottom panels show the patterns following deposition of approximately 5 nm of MnSb using a $J_{\mathrm{Sb/Mn}}$ value of 6.6 with $T_{\mathrm{sub}} = 350$ °C. Note that the substrate temperature was decreased relative to growth on GaAs due to the lower non-congruent temperature of InSb. There are two features to note in these patterns: the first is the presence of faint streaks and second are the incommensurate transmission features, which are stronger along the InSb$\langle 110 \rangle$ direction. The early stages of deposition are characterised by a fading of the substrate streaks and the appearance of new streaks with a different spacing. For the patterns presented in Figure B.1, the spacing along the $\langle 110 \rangle$ direction is 4.1(2) Å while along the $\left\langle 1\bar{1}0 \right\rangle$ direction it is 4.6(1) Å. The expected value for InSb$\langle 110 \rangle$ is 4.58 Å and so this lower streak spacing along the $\left\langle 1\bar{1}0 \right\rangle$ direction is surprising but may arise from n-

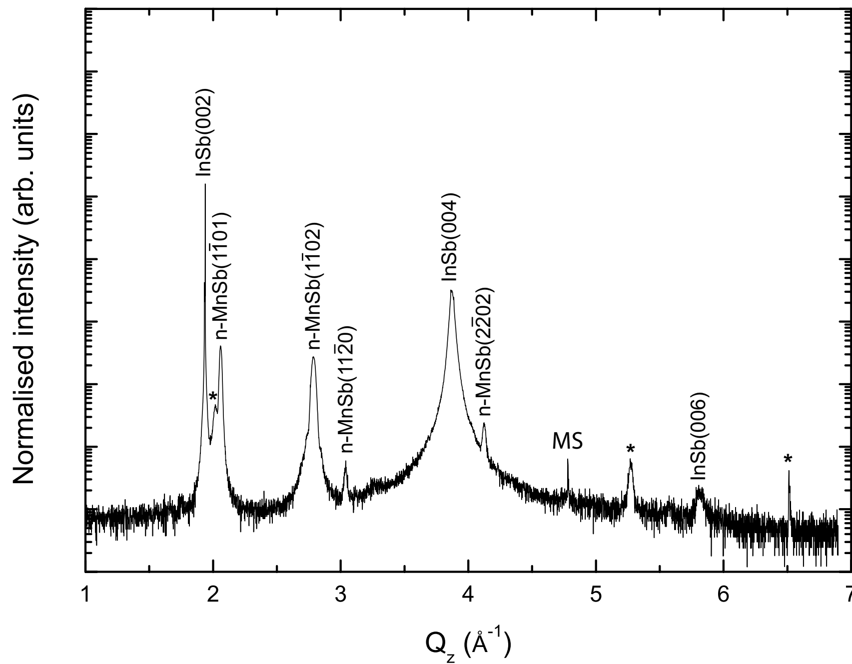

Figure B.2: Symmetric XRD data for a 5 nm MnSb film grown on InSb(001). Several reflections originating from n-MnSb (1$\bar{1}$01), (1$\bar{1}$02) and (11$\bar{2}$0) crystallites can be seen.

MnSb crystallites strained to the InSb. At the present time, analysis of the transmission patterns has not been performed and further study is necessary to fully identify all of the potential spacings.

Figure B.2 shows symmetric diffraction data for a 20 nm sample grown using the conditions given above. Substrate peaks are readily identifiable based on their intensity and several peaks remain that must then originate from the overlayer. It is interesting to note the presence of both (1$\bar{1}$02) and (11$\bar{2}$0) n-MnSb crystallites, in addition to (1$\bar{1}$01) crystallites. This supports the observations of multiple orientations during the growth of MnSb on Ge(001). Following comparison with the Q_z values listed in Appendix A, several unidentified peaks remain and these are denoted by $*$.

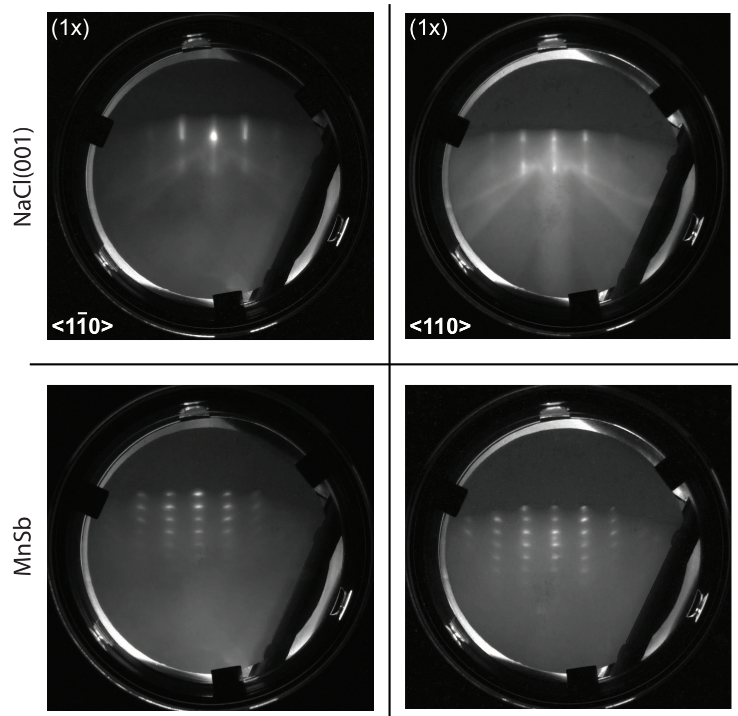

Figure B.3: RHEED patterns from a 20 nm thick MnSb film on NaCl(001). The top panel shows the NaCl(001)-(1×1) reconstruction observed following annealing. The bottom panel shows the RHEED patterns following deposition of 20 nm of MnSb.

Growth of MnSb films on NaCl(001)

The optimum cleaning procedure reported in the literature for NaCl(001) makes use of in-vacuo cleaving. However, the Warwick growth chamber is not equipped with a cleaving stage and so the UHV annealing method of Gaire et al. [151] has been used. Samples were initially cleaved in a dry nitrogen atmosphere before being mounted onto stainless steel sample plates using spot-welded tantalum foil and then loaded into the vacuum chamber. Once under vacuum, the samples were annealed at 420 °C for two hours and the resulting (1×1) RHEED patterns are shown in the top panels of Figure B.3. The transmission features present on the integer order streaks were observed over the entire sample surface and are likely the result of a poor initial cleaving. The MnSb film

was then grown using a $J_{\mathrm{Sb/Mn}}$ value of 6.4 with T_{sub} at 410 °C for five minutes, with an expected film thickness of 20 nm. Within a few tens of seconds of growth the initially streaky pattern faded and a transmission diffraction pattern appeared, which persisted throughout growth. The transmission patterns along the $\langle 110 \rangle$ and $\langle 1\bar{1}0 \rangle$ directions have similar spacings, with the horizontal feature separation equalling 4.3(1) Å and the vertical separation being 10.2(4) Å. The vertical separation of the features is larger than the maximum *d*-spacing possible in n-MnSb (the (0001) spacing at 5.789 Å). However, the horizontal separation is in agreement with the in-plane parameter of either h-Sb and w-MnSb, although no evidence of w-MnSb was observed in the diffraction data presented in Figure B.4. It is possible that the sticking coefficient of Mn is low on NaCl(001) surfaces and so the observed patterns could then originate from Sb-rich structures. However, the difference between the measured vertical separation (10.2 Å) and the h-Sb *c* lattice parameter (11.238 Å) means that the origin of this pattern is currently unknown.

Symmetric diffraction data from the sample discussed above is given in Figure B.4 and, as in the InSb(001) case, indicates the presence of multiple n-MnSb orientations. Of note is the reverse in relative intensity of the $(1\bar{1}02)$ and $(11\bar{2}0)$ reflections.

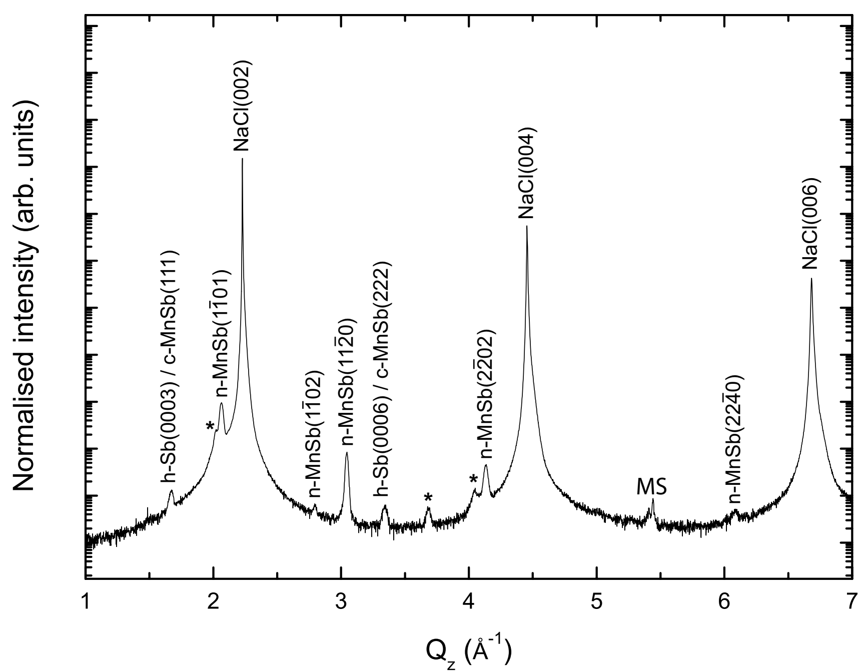

Figure B.4: Symmetric XRD data for a 20 nm MnSb film grown on NaCl(001). Several reflections originating from n-MnSb (1$\bar{1}$01), (1$\bar{1}$02) and (11$\bar{2}$0) crystallites, in addition to peaks arising from the Sb cap can be seen.

Bibliography

[1] K. Leosson, J. R. Jensen, W. Langbein, and J. M. Hvam, Phys. Rev. B. **61**, 10322 (1999).

[2] M. Hosomi et al., A Novel Nonvolatile Memory with Spin Torque Transfer Magnetization Switching: Spin-RAM, in *Electron Devices Meeting (IEDM), 2005 IEEE International*, pages 459–462, 2005.

[3] P. Packan et al., High performance 32nm logic technology featuring 2nd generation high-k + metal gate transistors, in *Electron Devices Meeting (IEDM), 2009 IEEE International*, pages 1–4, 2009.

[4] M. N. Baibich et al., Phys. Rev. Lett. **61**, 2472 (1988).

[5] G. Binasch, P. Grünberg, F. Saurenbach, and W. Zinn, Phys. Rev. B. **39**, 4828 (1989).

[6] S. Yuasa, T. Nagahama, A. Fukushima, Y. Suzuki, and K. Ando, Nat. Mat. **3**, 868 (2004).

[7] S. S. P. Parkin et al., Nat. Mat. **3**, 862 (2004).

[8] B. N. Engel et al., IEEE Trans. Mag. **41**, 132 (2005).

[9] W. Terui, H. Munekata, T. Hanna, and D. Yoshida, Phys. Status Solidi C **8**, 396 (2011).

[10] S. Datta and B. Das, Appl. Phys. Lett. **56**, 665 (1990).

[11] P. N. Hai, S. Ohya, M. Tanaka, S. E. Barnes, and S. Maekawa, Nature Lett. **458**, 489 (2009).

[12] D. Hägale, M. Oestrich, W. W. Rühle, N. Nestle, and K. Eberl, Appl. Phys. Lett. **73**, 1580 (1998).

[13] S. P. Dash, S. Sharma, R. S. Patel, M. P. de Jong, and R. Jansen, Nature Lett. **462**, 491 (2009).

[14] C. Shen et al., Appl. Phys. Lett. **97**, 162104 (2010).

[15] R. M. Stroud et al., Phys. Rev. Lett. **89**, 166602 (2002).

[16] A. Filipe, A. Schuhl, and P. Galtier, Appl. Phys. Lett. **129**, 129 (1997).

[17] J. D. Aldous et al., J. Phys-Condens. Mat. **14**, 146002 (2012).

[18] M. Tanaka, Semicond. Sci. Technol. **17**, 327 (2002).

[19] I. Žutić, J. Fabian, and S. D. Sarma, Rev. Mod. Phys. **76**, 323 (2004).

[20] T. Jungwirth et al., Phys. Rev. B. **72**, 165204 (2005).

[21] S. Dhar et al., Phys. Rev. B. **72**, 245203 (2005).

[22] R. A. de Groot and F. M. Mueller, Phys. Rev. Lett. **50**, 2024 (1983).

[23] J. D. Aldous et al., Phys. Rev. B. **85**, 060403 (2012).

[24] S. Mollet and S. J. Jenkins, J. Phys-Condens. Mat. **19**, 315214 (2007).

[25] C. N. Borca et al., J. Phys. Cond. Mat. **19**, 315211 (2007).

[26] T. Chen, J. C. Mikkelsen, and G. B. Charlan, J. Cryst. Growth **43**, 5 (1978).

[27] M. Nogami, M. Sekinobu, and H. Doi, Jpn. J. Appl. Phys. **3**, 572 (1964).

[28] S. A. Hatfield, J. D. Aldous, and G. R. Bell, Appl. Surf. Sci. **255**, 3567 (2009).

[29] G. C. Han, C. K. Ong, and T. Y. F. Liew, J. Magn. Magn. Mater. **192**, 233 (1999).

[30] T. Amemiya, Y. Ogawa, H. Shimizu, H. Munekata, and Y. Nakano, Appl. Phys. Express **1**, 022002 (2008).

[31] J. S. Blakemore, J. Appl. Phys. **53**, R123 (1982).

[32] B. T. M. Willis, Acta Cryst. **6**, 425 (1953).

[33] D. A. Ogarev et al., Inorganic Mater. **41**, 1320 (2005).

[34] J. D. Aldous, *Growth, Characterisation and Surface Structures of MnSb and NiSb Thin Films*, PhD thesis, University of Warwick, 2011.

[35] H. Akinaga and M. Mizuguchi, J. Phys-Condens. Mat. **16**, S5549 (2004).

[36] J. H. Zhao et al., Mat. Sci. Semicon. Proc. **6**, 507 (2003).

[37] G. Attard and C. Barnes, *Surfaces*, Oxford University Press.

[38] P. W. Tasker, J. Phys. C: Solid State Phys. **12**, 4977 (1979).

[39] D. Woodruff and T. Delchar, *Modern Techniques of Surface Science*, Cambridge University Press, second edition, 1999.

[40] R. L. Park and H. H. Madden, Surf. Sci. **11**, 188 (1968).

[41] G. P. Srivastava, Rep. Prog. Phys. **60**, 561 (1997).

[42] C. Kumpf et al., Phys. Rev. Lett. **86**, 3586 (2001).

[43] J. Falta, M. Tromp, M. Copel, G. D. Pettit, and P. D. Kirchner, Phys. Rev. Lett. **69**, 3068 (1992).

[44] L. Fishwick, M. Walker, M. K. Bradley, D. P. Woodruff, and C. F. McConville, Phys. Rev. B. **85**, 045322 (2012).

[45] A. Nagashima, M. Tazima, A. Nishimura, Y. Takagi, and J. Yoshino, Surf. Sci. **493**, 227 (2001).

[46] M. D. Pashley, Phys. Rev. B. **40**, 10481 (1989).

[47] J. E. Northrup and S. Froyen, Phys. Rev. B **50**, 2015 (1994).

[48] A. Ohtake, Surf. Sci. Rep. **63**, 295 (2008).

[49] W. Schmidt, Appl. Phys. A-Mater. **75**, 89 (2002).

[50] L. Zhang, E. G. Wang, Q. K. Xue, S. B. Zhang, and Z. Zhang, Phys. Rev. Lett. **97**, 126103 (2006).

[51] A. Y. Cho and J. R. Arthur, Prog. Solid. State. Ch. **10**, 157 (1975).

[52] T. Mimura, S. Hiyamizu, T. Fujii, and K. Nanbu, Jpn. J. Appl. Phys. **19**, L225 (1980).

[53] W. T. Tsang, C. Weisbuch, R. C. Miller, and R. Dingle, Appl. Phys. Lett. **35**, 673 (1919).

[54] P. Y. Yu and M. Cardona, *Fundamentals of Semiconductors*, Third edition, 2001.

[55] P. D. Desai, Int. J. Thermophys. **8**, 763 (1987).

[56] F. Bechstedt, *Principles of Surface Physics*, Springer-Verlag, Berlin, Heidelberg, Germany, 2003.

[57] J. E. Ayers, *Heteroepitaxy of Semiconductors: Theory, Growth, And Characterization*, CRC Press, Boca Raton, Flo., USA, 2007.

[58] V. L. Thanh et al., Phys. Rev. B. **58**, 13115 (1998).

[59] B. Elman, E. S. Koteles, C. J. P. Melman, J. Lee, and D. Dugger, Appl. Phys. Lett. **55**, 1659 (1989).

[60] S. A. Hatfield, *Heteroepitaxial Growth of MnSb on III-V semiconductor substrates*, PhD thesis, University of Warwick, 2007.

[61] W. Braun et al., J. Cryst. Growth **301–302**, 50 (2007).

[62] S. A. Hatfield and G. R. Bell, Surf. Sci. **601**, 5368 (2007).

[63] A. Ichimiya and P. I. Cohen, *Reflection High Energy Electron Diffraction*, Cambridge University Press, Cambridge, UK, 2004.

[64] J. M. V. Hove, P. Pukite, and P. I. Cohen, J. Vac. Sci. Technol. A **1**, 609 (1983).

[65] R. L. Park, J. E. Houston, and D. G. Schreiner, Rev. Sci. Instrum. **42**, 60 (1971).

[66] G. Binnig, H. Rohrer, C. Gerber, and E. Weibel, Phys. Rev. Lett. **49**, 57 (1982).

[67] G. Binnig, C. F. Quate, and C. Gerber, Phys. Rev. Lett. **56**, 930 (1986).

[68] J. D. Aldous et al., J. Cryst. Growth **357**, 1 (2012).

[69] S. Tanuma, C. J. Powell, and D. R. Penn, Surf. Interface Anal. **21**, 165 (1993).

[70] CasaXPS: Processing Software for XPS, AES, SIMS and More, `http://www.casaxps.com/`, Accessed: 25 July 2012.

[71] J. F. Moulder, W. F. Stickle, P. E. Sobol, and K. D. Bomben, *Handbook of X-ray Photoelectron Spectroscopy*, Perkin-Elmer Corporation, 1992.

[72] B. D. Cullity and S. R. Stock, *Elements of X-ray diffraction*, Prentice-Hall, New Jersey, 2001.

[73] B. E. Warren, *X-ray Diffraction*, Addison-Wesley Publishing Company, Inc, 1990.

[74] I. G. Hughes and T. P. A. Hase, *Measurements and their Uncertainties: A Practical Guide to Modern Error Analysis*, Oxford University Press, 2010.

[75] D. O. Demchenko and A. Y. Liu, Phys. Rev. B. **73**, 115332 (2006).

[76] G. Wastlbauer and J. A. C. Bland, Adv. Phys. **54**, 137 (2005).

[77] S. H. Cheung et al., Phys. Rev. B **85**, 045405 (2012).

[78] S. X. Liu, S. M. Bedair, and N. A. El-Masry, Mater. Lett. **42**, 121 (2000).

[79] H. Akinaga, S. Miyanish, W. V. Roy, J. D. Boeck, and G. Borghs, Appl. Phys. Lett. **73**, 3285 (1998).

[80] F. Bastiman, A. G. Cullis, M. Hopkinson, and M. Green, Growth and in vivo STM of III-V Compound Semiconductors, in *Microscopy of Semiconducting Materials 2007*, edited by A. G. Cullis and P. A. Midgley, volume 120 of *Springer Proceedings in Physics*, pages 471–476, Springer Netherlands, 2008.

[81] A. G. de Oliveira, S. D. Parker, R. Droopad, and B. A. Joyce, Surf. Sci. **227**, 150 (1990).

[82] P. John, T. Miller, and T. C. Chiang, Phys. Rev. B. **39**, 1730 (1989).

[83] A. Ohtake and J. Nakamura, Surf. Sci. **396**, 394 (1998).

[84] M. Nishizawa, T. Eguchi, T. Misima, J. Nakamura, and T. Osaka, Phys. Rev. B. **57**, 6317 (1998).

[85] J. Wever et al., Surf. Sci. **321**, L225 (1994).

[86] A. Ohtake and N. Koguchi, Appl. Phys. Lett. **83**, 5193 (2003).

[87] E. Penev, P. Kratzer, and M. Scheffler, Phys. Rev. Lett. **93**, 146102 (2004).

[88] B. Cordero et al., Dalton Trans. **21**, 2832 (2008).

[89] A. Ohtake, P. Kocán, K. Seino, W. G. Schmidt, and N. Koguchi, Phys. Rev. Lett. **93**, 266101 (2004).

[90] T. Hashizume, Q. K. Xue, J. Zhou, A. Ichimiya, and T. Sakurai, Phys. Rev. Lett. **73**, 2208 (1993).

[91] T. J. Krzyzewski, P. B. Joyce, G. R. Bell, and T. S. Jones, Surf. Sci **517**, 8 (2002).

[92] *CRC Handbook of Chemistry and Physics*, CRC Press, Boca Raton, Florida, 84th edition, 2003.

[93] F. R. de Boer, R. Boom, and A. R. Miedema, Physica. B. **113**, 18 (1982).

[94] *Thermochemical properties of pure substances*, Springer-Verlag, Berlin, Germany, 1973.

[95] Collaboration: Scientific Group Thermodata Europe (SGTE), Au-In. (ed.), SpringerMaterials - The Landolt-Börnstein Database (http://www.springermaterials.com)
.

[96] Collaboration: Scientific Group Thermodata Europe (SGTE), Au-Sb. (ed.), SpringerMaterials - The Landolt-Börnstein Database (http://www.springermaterials.com)
.

[97] R. Boom, F. R. D. Boer, A. K. Niessen, and A. R. Miedema, Physica B. **115**, 285 (1983).

[98] R. Pretorious, T. K. Marais, and C. C. Theron, Mater. Sci. Eng. **10**, 1 (1993).

[99] J. F. McGilp, J. Phys. C Solid State **17**, 2249 (1984).

[100] A. J. Noreika, M. H. Francombe, and C. E. C. Wood, J. Appl. Phys. **12**, 7416 (1981).

[101] C. Ratsch, W. Barvosa-Carter, F. Grosse, J. H. G. Owen, and J. J. Zinck, Phys. Rev. B. **62**, 7719 (2000).

[102] Q. K. Xue, T. Hashizume, and T. Sakurai, Prog. Surf. Sci. **56**, 1 (1997).

[103] M. Goryl et al., Vacuum **74**, 223 (2000).

[104] K. Hricovini et al., Appl. Surf. Sci. **212-213**, 17 (2003).

[105] S. B. Zhang et al., Phys. Rev. B. **69**, 121308 (2004).

[106] C. F. McConville et al., Phys. Rev. B. **50**, 14965 (1994).

[107] K. Lüdge et al., J. Vac. Sci. Technol. B **20**, 1591 (2002).

[108] S. C. Erwin and A. G. Petukhov, Phys. Rev. Lett. **89**, 227201 (2002).

[109] S. Colonna et al., J. Appl. Phys. **109**, 123522 (2011).

[110] K. Regiński, J. Muszalski, V. V. Preobrazhenskii, and D. I. Lubyshev, Thin Solid Films **54**, 54 (1995).

[111] J. Donohue, *The Structures of the Elements*, R.E. Krieger Publishing Co., Malabar, Flo., 1982.

[112] J. M. Van Hove, P. Pukite, P. I. Cohen, and C. S. Lent, J. Vac. Sci. Technol. A **1**, 609 (1983).

[113] F. Garbassi, Surface and Interface Analysis **2**, 165 (1980).

[114] H. Tatsuoka et al., Thin Solid Films **281**, 499 (1996).

[115] H. Takizawa, M. Shimada, Y. Sato, and T. Endo, Mater. Lett. **18**, 11 (1993).

[116] M. Yano, Y. Suzuki, T. Ishii, Y. Matsushima, and M. Kimata, Jpn. J. Appl. Phys. **17**, 2091 (1978).

[117] M. E. Straumanis and C. D. Kim, J. Appl. Phys. **36**, 3822 (1965).

[118] B. T. M. Willis and H. P. Rooksby, Proc. Phys. Soc. B **67**, 290 (1954).

[119] T. Chen, G. B. Charlan, and R. C. Keezer, J. Cryst. Growth **37**, 29 (1977).

[120] J. W. Matthews and A. E. Blakeslee, J. Cryst. Growth **27**, 118 (1974).

[121] H. J. Park et al., J. Cryst. Growth **27**, 118 (1974).

[122] H. Dosch, B. W. Batterman, and D. C. Wack, Phys. Rev. Lett. **56**, 1144 (1986).

[123] K. Ono, M. Shuzo, M. Oshima, and H. Akinaga, Phys. Rev. B. **64**, 085328 (2001).

[124] M. Tanaka et al., J. Vac. Sci. Technol. B **12**, 1091 (1994).

[125] W. Zawadzki and P. Pfeffer, Semicond. Sci. Technol. **19**, R1 (2004).

[126] R. Fiederling et al., Nature **402**, 787 (1999).

[127] S. Teichert, H. Hortenbach, and H.-J. Hinneberg, Appl. Phys. Lett. **78**, 1988 (2001).

[128] H. Tatsuoka et al., J. Appl. Phys. **10**, 5504 (1998).

[129] P. D. Padova et al., Surf. Sci. **601**, 4370 (2007).

[130] V. A. Shah, A. Dobbie, M. Myronov, and D. R. Leadley, Thin Solid Films **519**, 7911 (2011).

[131] A. Dobbie et al., Appl. Phys. Express **5**, 071301 (2012).

[132] R. E. Schlier and H. E. Farnsworth, J. Chem. Phys. **30**, 917 (1959).

[133] R. Rossman et al., Surf. Sci. **279**, 199 (1992).

[134] J. A. Kubby, J. E. Griffith, R. S. Becker, and J. S. Vickers, Phys. Rev. B. **315**, 6079 (1994).

[135] R. E. Schlier and H. E. Farnsworth, Phys. Rev. Lett. **43**, 43 (1979).

[136] S. D. Kevan, Phys. Rev. B. **32**, 2344 (1985).

[137] P. E. J. Eriksson, M. Adell, K. Sakamoto, and R. I. G. Uhrberg, Phys. Rev. B. **77**, 085406 (2008).

[138] J.-H. Cho and M.-H. Kang, Phys. Rev. B. **49**, 13670 (1994).

[139] P. Delescluse and A. Masson, Surf. Sci. **100**, 423 (1980).

[140] D. J. Chadi and C. Chiang, Phys. Rev. B. **23**, 1843 (1981).

[141] N. Tabet, M. Faiz, N. M. Hamdan, and Z. Hussain, Surf. Sci. **523**, 68 (2003).

[142] K. Prabhakarana and T. Ogino, Surf. Sci. **325**, 263 (1994).

[143] T. Okita and Y. Makino, J. Phys. Soc. Jpn. **25**, 120.

[144] W. Zhu, H. H. Weitering, E. G. Wang, E. Kaxiras, and Z. Zhang, Phys. Rev. Lett. **93**, 126102 (2004).

[145] S. A. Hatfield and G. R. Bell, J. Cryst. Growth **296**, 165 (2006).

[146] A. M. Nazmul, A. G. Banshchikov, H. Shimuzu, and M. Tanaka, J. Cryst. Growth **227–228**, 874 (2001).

[147] J. F. C. Baker and M. Hart, Acta. Cryst. **31**, 364 (1975).

[148] A. Guivarc'h, J. Caulet, and A. L. Carre, Electron. Lett. **25**, 1050 (1989).

[149] T. Kanomata, T. Kawashima, T. Kaneko, H. Takahashi, and N. Mori, Jpn. J. Appl. Phys. **30**, 541 (1991).

[150] A. P. Kantor, L. S. Dubrovinsky, N. A. Dubrovinskaia, I. Y. Kantor, and I. N. Goncharenko, J. Alloy Compd. **402**, 42 (2005).

[151] C. Gaire, F. Tang, and G.-C. Wang, Thin Solid Films **517**, 4509 (2009).